

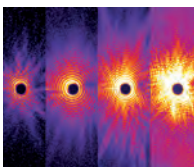
PHOTON SCIENCE 2016.

Highlights and Annual Report

Accelerators | Photon Science | Particle Physics

Deutsches Elektronen-Synchrotron
A Research Centre of the Helmholtz Association

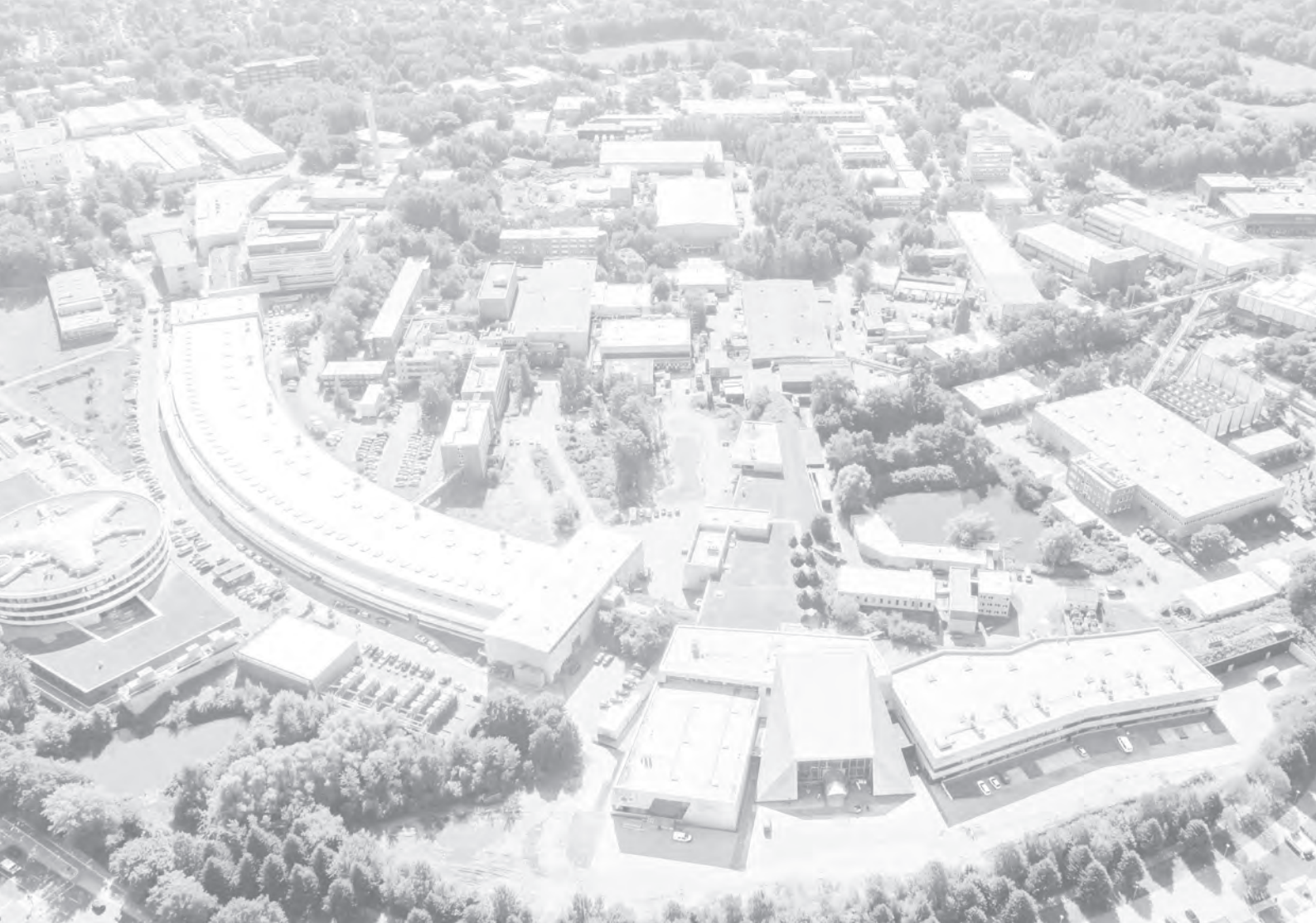




Cover

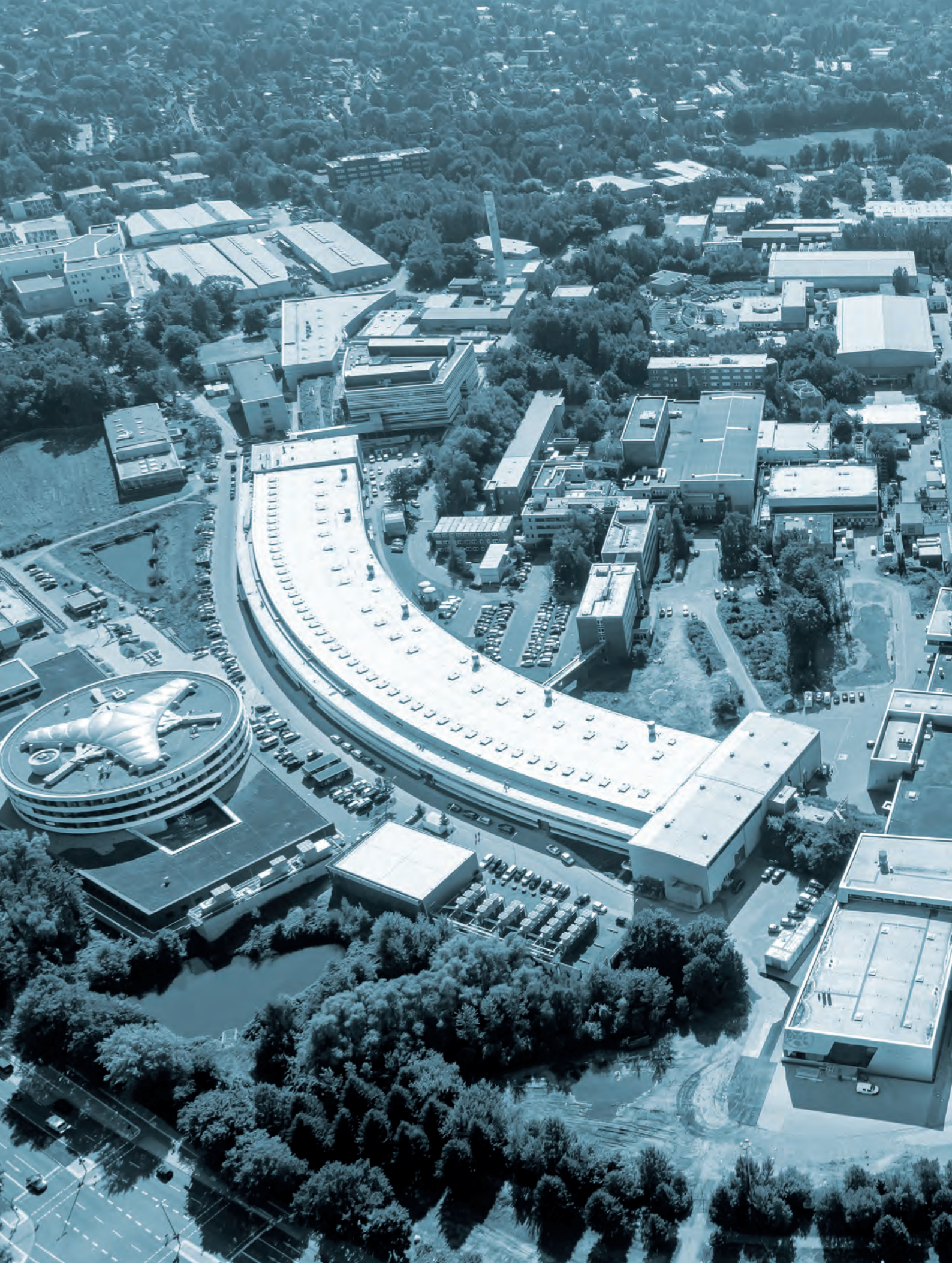
The diffraction images measured at FLASH are used to decode cluster size and FEL intensity of the events. The single-cluster measurements allow for a novel quality in laser-cluster interaction studies.

More information on these measurements can be found on page 72.



PHOTON SCIENCE 2016.

Highlights and Annual Report



Contents.

> Introduction	4
> News and Events	8
> Science Highlights	20
• Cultural and natural history	22
• Surfaces, thin films and interfaces	26
• Electronic and magnetic structure	34
• Structure and structural dynamics	44
• Life Sciences	56
• Atomic and molecular dynamics	72
• Science of X-ray sources - methods and developments	76
> Light Sources	88
> Campus and Collaborations	98
> Facts and Numbers	114

Publications.

The list of publications based on work done at DESY Photon Science is accessible online:
http://photon-science.desy.de/research/publications/list_of_publications/index_eng.html

DESY tries to keep this list as complete and as updated as possible, and relies on the support by all users, who are kindly requested to register their publications via DOOR (door.desy.de).

The year 2016 at DESY.

Chairman's foreword

*Dear Colleagues and
Friends of DESY,*

During the past years, Photon Science at DESY has developed into a powerhouse which attracts the best scientists from all over the world. This great success was achieved by the focused development of a world-leading research infrastructure and by the consistent buildup of an ambitious research profile.

The additional research opportunities offered by the modern beamlines at the second FLASH experimental hall and the two PETRA III extension halls are important to strengthen DESY's role in advanced materials design and biological research. We soon expect the start of the user operation at the European XFEL which will be the most powerful X-ray

free-electron laser worldwide, offering unique opportunities for fascinating science.

With the construction of the European XFEL drawing to a close, it is already a remarkable success story: Within only 6 years, the most advanced and most powerful linear accelerator was assembled in a tunnel from DESY to Schenefeld with no major delays and no major budget adjustments and without any major accident. I congratulate all European XFEL and DESY teams for this impressive achievement. On 6 October, the commissioning phase was launched in a festive celebration. We are all looking forward to the start of the XFEL operation for users in 2017.



Pushing the buttons uncovered the names 'Ada Yonath' and 'Paul P. Ewald' of the new PETRA III experimental halls: (from left)

Harsh Vardhan, India's Minister of Research, Edelgard Bulmahn, Vice-President of Germany's Bundestag, Olaf Scholz, First Mayor of Hamburg, Ada Yonath, Israeli Nobel laureate who conducted important research at DESY, Georg Schütte, state secretary at the Federal Ministry for Education and Research, John-Paul Davidson, grandson of Paul P. Ewald, Mikhail Rychev from the Russian Kurchatov Institute, Ulf Karlsson, head of the Swedish delegation of the Röntgen Angström Cluster and Helmut Dosch.



Tightened the final screws on the 3.4 kilometres long underground installation of the European XFEL: Hamburg's Senator for Science Katharina Fegebank (centre), Beatrix Vierkorn-Rudolph from the Federal Ministry for Education and Research (right), the Chairman of the European XFEL Management Board Massimo Altarelli (left) and Helmut Dosch (far left).

In the past years, DESY has appointed leading scientists in this field. In 2016, it was our pleasure to welcome Francesca Calegari from Milan, Nina Rohringer and Melanie Schnell, both from the Max Planck Society. They will boost DESY's expertise in important future science areas, i.e. ultrafast spectroscopy, nonlinear X-ray physics and the manipulation of the motion of molecules.

What needs to be accomplished in the coming years?

Photon Science at DESY critically hinges on the successful operation of PETRA III and FLASH for users. This also requires the advancement of the PETRA III and FLASH facilities to keep their world-leading position. For both facilities, DESY has set up project teams to devise the next generation of storage ring X-ray sources and LINAC-based X-ray lasers, respectively.

An upgrade of PETRA III, the diffraction-limited light source PETRA IV, will be exploiting novel technologies based on so-called multiband achromats which enables the achievement of unprecedented beam qualities and in turn innovative ways of exploring the structure and function of matter, materials and biomatter. It will be accommodated into the existing PETRA tunnel and thus aims for the most advanced facility worldwide at moderate construction costs. The FLASH upgrade plans, denoted FLASH2020, encompass new tunable undulators as well as options for seeding and cw operation.

Both facility developments must take into account the needs of the users who come from Europe and all over the world. In other words, the novel analytical technologies offered by PETRA IV and FLASH2020 need to be integrated into a European dimension. Along these lines, DESY launched already in 2015 the European process LEAPS (Luminous Electron Accelerators for Photon Science) which aims at a European roadmap as well as for a better integration of all European X-ray and X-ray laser facilities. The goal is to deliver a strategy document in the second



New leading scientists at DESY Photon Science: (from left) Francesca Calegari, Nina Rohringer and Melanie Schnell.

half of 2017 and to influence the upcoming European Framework Programme FP9.

DESY's X-ray facilities invite scientists from all over the world and from all scientific disciplines to carry out their research at highly specialised experimental stations. The challenge of the future is to unlock the innovation potential of these advanced and at the same time mature technologies. In 2016, we made important steps to foster further partnerships and cooperations with industry, in particular a new DESY unit 'Innovation and Technology Transfer' was established under the guidance of the newly appointed CTO Arik Willner.

All in all, Photon Science at DESY is well prepared to tackle the future challenges. My thanks go to the dedicated scientists at the beamlines and to all research and development groups and their staff who have been contributing to this wonderful success. ●

Helmut Dosch
Chairman of the DESY Board of Directors

Photon Science at DESY.

Introduction



Aerial view of the DESY site in September 2016 (from lower left to upper right corner: the PETRA III experimental hall 'Ada Yonath', the construction site of the CSSB building, the curved PETRA III hall 'Max von Laue', the experimental halls 'Kai Siegbahn' and 'Albert Einstein' adjacent to the PETRA III experimental hall 'Paul P. Ewald').

Dear Colleagues,

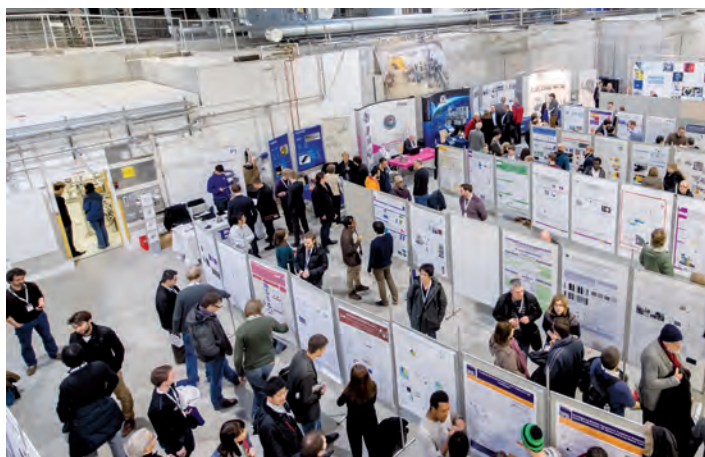
The year 2016 had a good start when the photon science community gave rise to a record with more than 1000 participants at the combined European XFEL – DESY Photon Science Users' Meeting for the first time. This event demonstrates the increasing attractiveness of Photon Science in Hamburg. DESY's tender to the hard X-ray synchrotron radiation source PETRA III was operating roughly 4000 h in 2016 after a longer winter shutdown needed for the installation of frontend components into the ring tunnel related to the PETRA III extension project. Many exciting scientific results could be achieved at PETRA III in 2016 with some of them highlighted in this brochure.

Since mid 2016 the first beamline in the new PETRA III experimental hall 'Paul P. Ewald' (north) is in full user operation and a second one will follow after the winter shutdown in spring 2017. Another four beamlines in the second new PETRA III experimental hall 'Ada Yonath' (east) are expected to see first beam during the year 2017, thus significantly expanding the experimental capabilities at PETRA III by installing additional beamlines. For the future a project group started the design work for an upgrade of PETRA III into a source that will be close to the diffraction limit in the harder X-ray regime – PETRA IV. With its large circumference of 2.3 kilometres, the storage ring PETRA is worldwide unique to achieve this ambitious

goal, enabling experimental techniques that can be described as being the ultimate hard X-ray *in situ* microscope exploiting nearly all possible X-ray contrast mechanisms at the nanoscale. For this design work a number of workshops are planned to take into account all possible input from the user community.

At FLASH significant progress has been achieved. For the first time, parallel user operation at both FLASH undulator lines FLASH1 and FLASH2 could be established. Due to the flexibility of gap tuneable undulators at FLASH2 various new FEL schemes could be realised also for the first time like reverse and quadratic tapering, higher harmonic lasing as well as frequency doubling. These schemes will open a number of future options for FEL experiments. Details can be found in the respective chapters of this annual report. In 2017 DESY will continue to complete the FLASH2 experimental capabilities by additional beamlines and a powerful pump-probe laser system. In addition, a project team is exploring options for upgrades of FLASH for higher repetition rates towards the ultimate goal of cw operation, that would be extremely beneficial to all low target-density experiments, called FLASH2020.

2016 was a decisive year for the European XFEL. After very successful commissioning of the injector during this year, cooling down of the entire 2 km long super conducting linear accelerator is planned for November/December. First experiments are planned for late spring 2017. European XFEL will not only be the XFEL with the highest electron and therefore highest photon energy, it will also for several years be the one with the highest repetition rate, enabling especially experiments on dilute targets hardly or not



DESY Photon Science Users' Meeting in January 2016: poster session in the PETRA III experimental hall 'Paul P. Ewald'.

possible at present day XFELs driven by normal conducting linear accelerators.

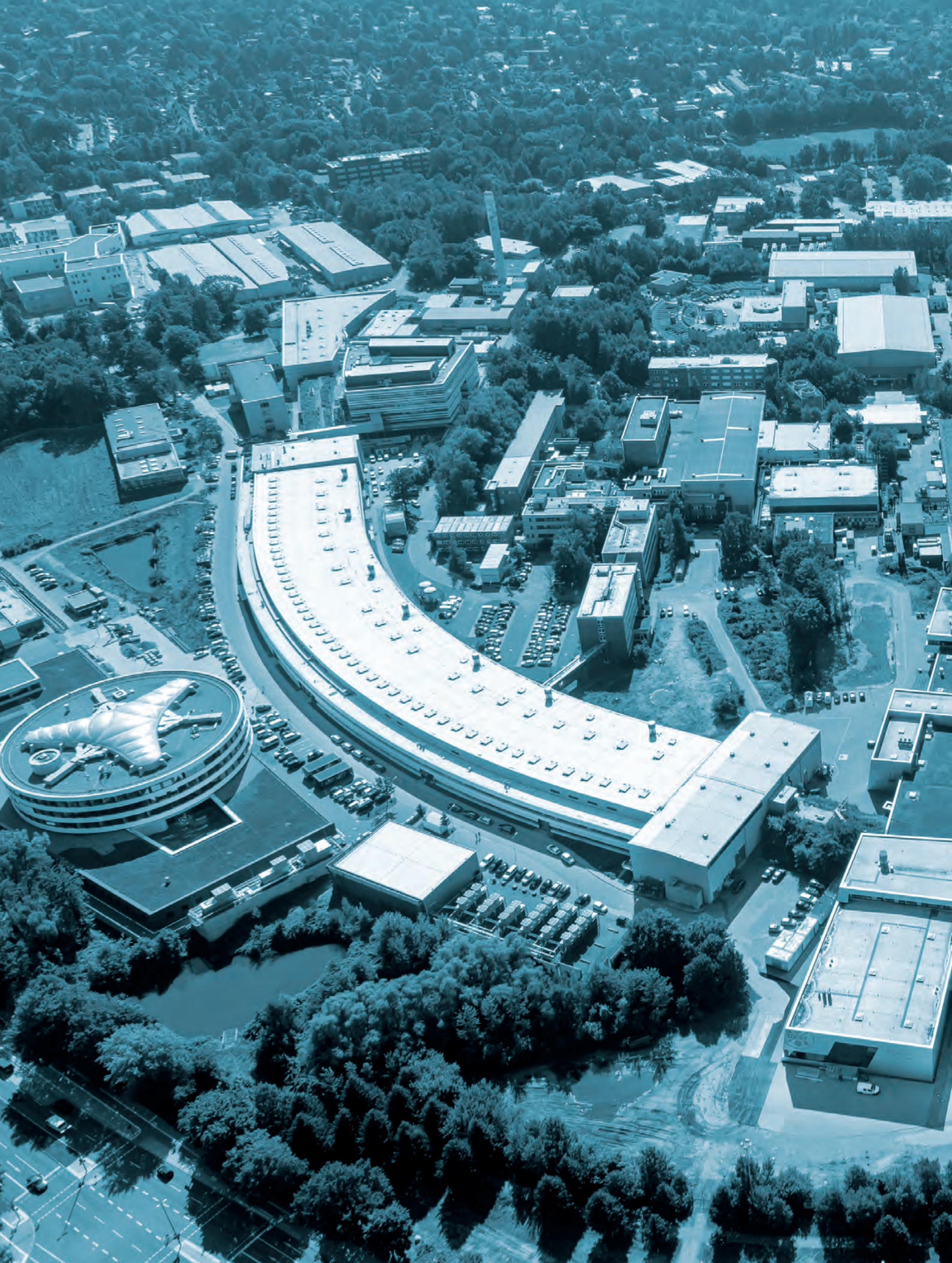
In-house research at DESY Photon Science, especially from CFEL, is heavily involved in the planning and establishing of experiments at European XFEL by leading or contributing to six user consortia for the realisation of dedicated experimental stations that also will be open to general users.

At present the Bahrenfeld campus on which DESY resides continues to develop rapidly. The new building for the Centre for Structural Systems Biology (CSSB), a cooperation of meanwhile 10 institutions in the field of infection research, is almost finished. Moving in is planned for spring 2017. Ground breaking for a new Photon Science Building, housing the DESY NanoLab, is planned for March 2017. The NanoLab will provide complementary methods for preparing, analysing and handling of samples for the users of the DESY photon sources and for in-house research scientists. Activities and instrumentation in the NanoLab are closely coordinated with the Centre for Hybrid Nanomaterials (CHyN) established by University of Hamburg on site. The corresponding building is close to completion. In addition, the construction work for the new buildings of the Max Planck Institute for Structure and Dynamics as well as for the Hamburg Advanced Centre for Bioorganic Chemistry (HARBOR) have started. On longer terms the University of Hamburg is planning to move almost its entire physics and chemistry departments and activities to the Bahrenfeld campus, which will certainly make the campus even more interesting for young students.

Despite all the construction and facility design and commissioning work users and in-house staff at the DESY Photon Science facilities and research laboratories have carried out exciting science besides numerous new technical developments. A selection can be found in this annual report – I hope you will enjoy reading it.

All these activities are only possible due to the dedication of all DESY staff as well as of our users and collaborators. I wholeheartedly thank all of them for the continued effort and support.

Edgar Weckert
Director Photon Science



News and Events.



News and Events.

A busy year 2016

January

21 January: Helmholtz International Fellow Award for John Spence

Each year the Helmholtz Association awards up to ten International Fellow Awards to distinguished foreign scientists. John C. H. Spence, professor at Arizona State University, has done pioneering work in the field of X-ray lasers. He is considered an outstanding expert of X-ray laser application especially to investigate the atomic structure of biomolecules. Furthermore, he is a world leading researcher in the development and application of electron microscopy at atomic-scale resolution.



John C. H. Spence is Professor at Arizona State University and Fellow of the British Royal Society.

27 – 29 January: Users' Meeting again breaks the attendance record

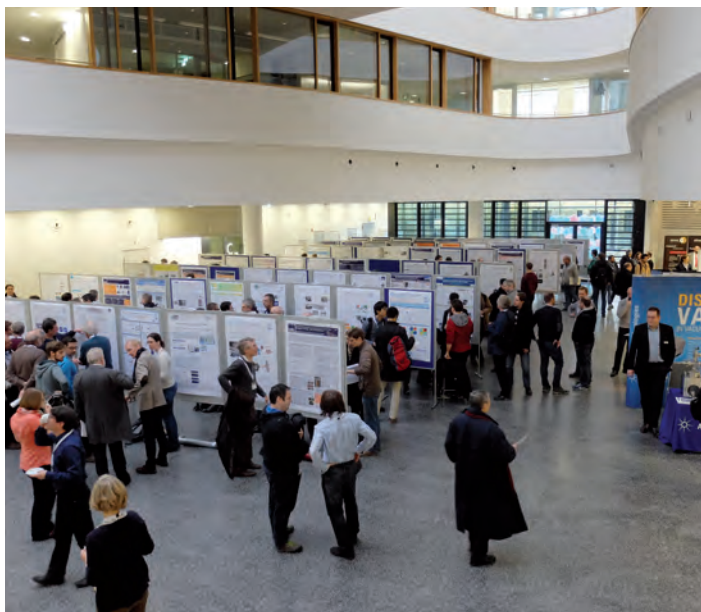
For the first time the number of participants of the annual joint European XFEL and DESY Photon Science Users' Meeting passed the 1000-mark. During the three-day meeting the participants discussed existing and future research prospects utilizing the brilliant X-rays from the free-electron lasers FLASH and European XFEL as well as from DESY's synchrotron radiation source PETRA III.



Around 1000 participants came to the DESY and European XFEL Users' Meeting 2016.

The first day was dedicated to European XFEL with project status reports, presentations about the planned scientific instruments, and talks on recent advances in FEL related science.

The morning of the second day was devoted to soft X-ray experiments at free-electron lasers and was especially addressing science at DESY's FLASH facility. Finally, the morning of the last day was reserved for the DESY Photon Science Users' Meeting with a general presentation by Edgar Weckert on the status of science with photons at



The poster session of the annual Users' Meeting in the CFEL building.

DESY, and talks about scientific and technical highlights achieved at the PETRA III storage ring. The main programme was complemented by 15 satellite meetings on various specific scientific and technical topics on the afternoon of the second day, a poster session with more than 350 contributions, and a vendor exhibition with more than 50 exhibitors.

March

2 – 4 March: 15th DESY Research Course

The series of DESY Research Courses started in 2001. The 15th DESY Research Course 'Soft Matter in the Light of Modern X-ray Sources' addressed topics like colloidal crystals and crystallisation in soft matter, complex fluids, soft matter surfaces and interfaces, colloidal glass transition, and biological soft matter. Special attention was paid to X-ray methods for soft matter characterisation. 90 participants – mainly master and PhD students, as well as young postdoctoral researchers – attended the talks and a poster session.

Soft Matter in the Light of Modern X-ray Sources

XV. Research Course on X-Ray Sciences
2-4 March 2016, DESY Hamburg

- > Molecular and colloidal glass formation
- > Colloidal crystals
- > Modern lightsources for Soft Matter characterization
- > Structure formation in polymer systems
- > Soft Matter surface and interfaces
- > Complex fluids

Soft Matter materials have become essential in modern every-day life. This family of materials ranges from colloidal dispersions, glasses, liquid crystals to gels, foams and biological macromolecules. In recent years, X-ray scattering has become a key technique to reveal structure and dynamics of Soft Matter materials. Especially with the advent of X-ray Free-Electron Laser sources and the last generation of storage rings new experiments extend our knowledge on structure and dynamics of these materials.

The 15th DESY Research Course will provide an introduction to the recent developments in the field of Soft Matter under X-ray light. Special attention will be paid on modern experimental techniques, scientific applications and connections to theory and simulation. The course addresses master and PhD students, young research fellows, as well as interested scientists.

Registration is free of charge and the number of participants is limited. Applications for this course should be made **not later than 26 February, 2016**.

Speakers:
V. Abelt (Hamburg), L. Järnsten (Düsseldorf), A. Phanou (CEA, CFEL), J. S. Pedersen (Aarhus), A. Petukhov (Utrecht), J. Russo (Tokyo), B. Ruta (ESRF, Grenoble), F. Schreiber (Tübingen), M. A. Schroer (DESY), A. Sepe (Fribourg), M. Sprung (DESY), M. Tolan (TU Dortmund)

Organizing Committee:
G. Grübel (DESY), F. Lehmkuhler (DESY), M. Kreuzer (DESY)
Contact: research-course-organ@desy.de

HELMHOLTZ ASSOCIATION PIER CUJ <http://researchcourse2016.desy.de>

The poster announcing the 15th DESY Research Course.

March

9 – 11 March:

Workshop on Diffraction Limited Storage Rings

Since the first use of synchrotron radiation for science in the late 1970s the brightness of synchrotron radiation sources has increased by a factor of 10000 every decade. This was possible by ever improving the storage ring emittance and the X-ray sources from bending magnets to undulators. With a new storage ring technology, the so-called multi-bend-achromat, which was pioneered by the MAX IV team in Lund (Sweden), the physical limit of synchrotron radiation, the so-called diffraction limit, is within reach even in the hard X-ray range. At the fifth Diffraction-Limited Storage Ring (DSLIR) Workshop about 140 scientists from more than ten synchrotron radiation sources worldwide came together at DESY to address science and technology of building and using this next generation of storage rings.

There is worldwide interest in upgrading existing storage rings as well as constructing new ones where the electron-beam emittance approaches the diffraction limit down to X-ray wavelengths of one Ångström. This workshop focused on both science and accelerator questions addressing new research opportunities and the hardware developments for the storage rings, optics, and instrumentation needed to carry out the science that these new sources will enable. At DESY it is planned to upgrade the synchrotron radiation source PETRA III into the ultra-low emittance source PETRA IV.



The participants of the workshop on diffraction limited storage rings.

April

8 April:

First user experiment at FLASH2

From the year 2011 to 2015 a second free-electron laser line, FLASH2, was realised at FLASH. This upgrade was intended to enable parallel operation for two user experiments located in the first experimental hall 'Albert Einstein' (FLASH1) and in the newly built hall FLASH2 which was named after the physicist Kai Siegbahn.

Now the first FEL beamline in the new hall has become operational and ready for user experiments. The first users were scientists from DESY who studied the fluorescence of plasma excitation in rare gas clusters as function of the cluster size.



View into the experimental hall 'Kai Siegbahn' with the two new FLASH2 beamlines FL24 and FL26.



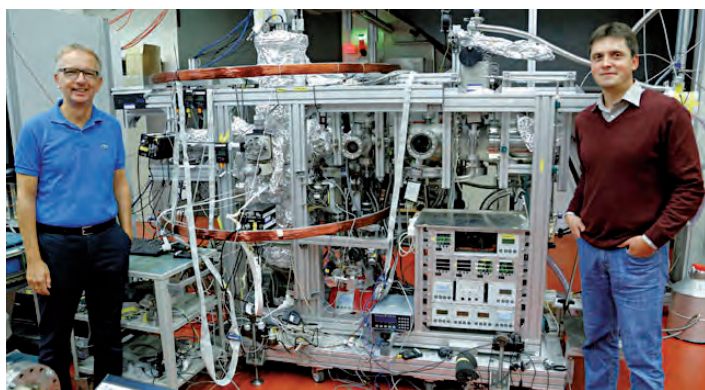
FLASH is the first X-ray laser worldwide which can serve experiments at two beamlines at the same time. The FLASH experimental hall 'Albert Einstein' (FLASH1, left) and the hall 'Kai Siegbahn' (FLASH2, right).

May

28 April: Helmholtz Prize awarded for science at FLASH

A team of five scientists led by Reinhard Dörner, professor at the Goethe University in Frankfurt am Main, was awarded the Helmholtz Prize in Metrology for work carried out with the help of DESY's free-electron laser FLASH. The prize is intended to promote science in the field of precision measurements in physics and technology; it is endowed with 20000 Euro. The group obtained the award for high-precision measurements using a special apparatus to study extremely weakly bound helium molecules.

Under special conditions two or even three helium atoms can form very weakly bonded helium molecules. Dörner and his colleagues, Till Jahnke, Maksim Kunitski, Jörg Voigtsberger and Stefan Zeller, succeeded in measuring the tiny binding energy of He₂ molecules with a precision of a few parts in a billion electron volts. They used a special reaction microscope COLTRIMS (Cold Target Recoil Ion Momentum Spectroscopy), developed at the Goethe University.



Reinhard Dörner (left) and Maksim Kunitski at the COLTRIMS experiment which was used to measure weak bonding of helium molecules. (credit: Uwe Dettmar)

29 May – 4 June: Third International Summer School of Crystallography

This year's third International Summer School of Crystallography (ISSC) at the Center for Free-Electron Laser Science CFEL was attended by 34 participants from 15 different countries. Main topics were the basic principles of crystallography, one of the most important tools for exploring the internal structure of materials. Scientists use computer programs to perform the task of calculating the arrangement of molecules or atoms from the diffraction patterns obtained by illuminating crystalline samples with X-rays. The school is intended to let the participants comprehend what these computer programs are actually doing. For this reason, it aims to provide the attendees, mainly PhD students, with a clear understanding of the mathematical foundations of the techniques being used. The participants learned how the tools work and how to tackle complex crystallographic challenges. As before, the organisers succeeded in engaging Carmelo Giacovazzo, an internationally renowned expert in the field of crystallography from the University of Bari as tutor supported by scientists from CFEL, DESY, CUI, European XFEL, and EMBL.



Participants of the International Summer School of Crystallography 2016.

June

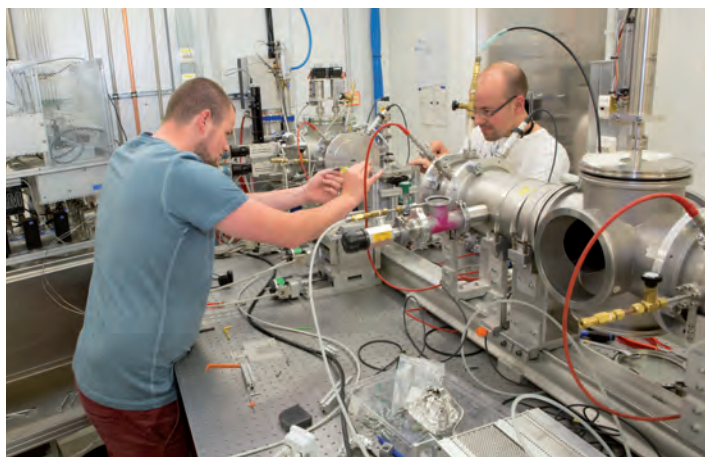
13 – 17 June: Conference on Resonant Elastic X-ray Scattering at DESY

The Conference on Resonant Elastic X-ray Scattering (REXS 2016) was the 3rd in a row after very successful events in Aussois 2011 and Oxford 2013. The conference aimed at stimulating interaction and discussion among scientists who work in the field of hard condensed matter research with synchrotron radiation and who use spectroscopy and scattering methods which utilize resonance effects occurring in the vicinity of X-ray absorption edges. The conference was attended by more than 50 participants who followed ten keynote and invited talks, as well as 23 contributed talks and a poster session.

17 June: First User Operation at a PETRA III Extension Beamline

The first undulator beamline of the newly constructed PETRA III extension took up regular user operation in June. Beamline P65, which is located in the new experimental hall 'Paul P. Ewald' and is dedicated to the X-ray absorption spectroscopy (EXAFS) technique, was opened for user experiments.

In EXAFS experiments one can identify the chemical environment of specific elements within the sample based on the absorption spectrum. This experimental method is particularly suitable for *in situ* testing of catalysts at work. Classical materials research like the observation of the phase transition between amorphous and crystalline states in metallic glasses can also be performed at P65. The beamline design allows investigating almost all chemical elements which are above calcium in the periodic table. The first users of P65 came from Karlsruhe Institute of Technology and University of Paderborn. With the help of the light of PETRA III they investigated how their catalyst samples age during operation.



Two users at the new PETRA III beamline P65 prepare an experiment to study aging of catalysts during operation.

July

22 July: DESY Summer Student Programme 2016

This year more than 550 students of natural sciences from all over the world applied for participation in the DESY Summer Student Programme. More than 200 of these applicants expressed their interest to participate in the field of Photon Science. Finally 104 students from 33 countries were selected from which 28 attended the part related to research with photons. For seven weeks the young scientists took part in the work of DESY research groups, carried out their own small projects, and attended a series of lectures. All participants appreciated the scientific programme, as well as the opportunity to get in contact with many people from various scientific and cultural background.



The DESY summer students 2016 working in Photon Science.



All students attending the 2016 summer students programme at the DESY campus in Hamburg.

August

4 August: Helmholtz International Fellow Award for Linda Young

Linda Young, one of the pioneers of X-ray laser science, was elected to receive an International Fellow Award from the Helmholtz Association. The physicist, currently at the Argonne National Laboratory in the United States, is one of the leading international experimental researchers looking into the fundamental interaction between matter and light, in particular X-rays. Young performed the first scientific experiments at the LCLS, thereby starting the routine experimental operation of the facility. One of the surprising discoveries made during these first experiments was the finding that shorter, intense X-ray pulses may produce less radiation damage than longer, less intense X-ray pulses carrying the same amount of energy. Nowadays, numerous experiments make use of this fact.



Linda Young, professor at Argonne National Laboratory.

September

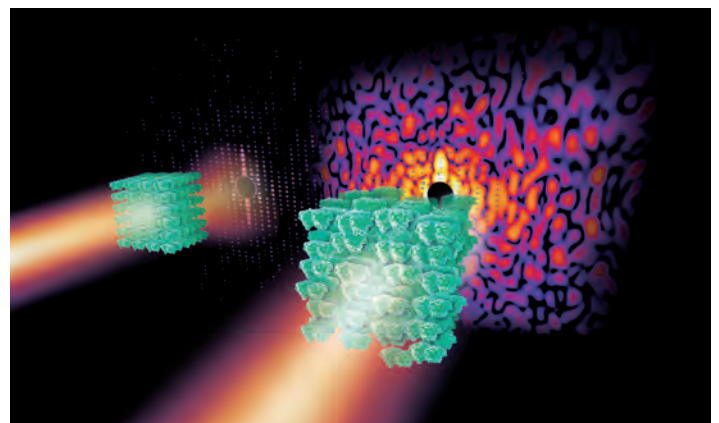
7 September: FEL Science and Applications Award for Kartik Ayyer

DESY physicist Kartik Ayyer was awarded the 'FEL Science and Applications Award of the international 'Science@FELs 2016' conference which was held in Trieste, Italy from 5 to 7 September. He works as a postdoctoral researcher in the team of Henry Chapman at CFEL.



Kartik Ayyer.

The award given to young researchers comprises of 1500 Euro. This year's prize acknowledges Kartik Ayyer's contributions to the research field of free-electron lasers and its applications. He did his PhD work on X-ray imaging in cases where the signal is very low, as expected for single biomolecule imaging at XFELs. He was also part of the team which recently showed that one can perform diffractive imaging with protein crystals which are not perfectly ordered but show a certain kind of disorder. This novel technique will allow researchers to resolve the structure of molecules which are of great relevance to medicine and biology but which were practically inaccessible by methods existing up to now. Furthermore, the structural information can be achieved at higher resolution compared to conventional crystallography.



Slightly disordered crystals of complex biomolecules produce a complex continuous X-ray diffraction pattern (right) which contains far more information than the so-called Bragg peaks of a strongly ordered crystal alone (left).

September

14 – 16 September: Joint Workshop on High Pressure, Planetary and Plasma Physics

It was the 5th instalment of the successful workshop series which was initiated in 2012 in Hamburg and is coordinated by a collaboration of DESY, European XFEL, DLR Berlin, the University of Rostock, and Bayerisches Geoinstitut in Bayreuth. Its aim is to foster interdisciplinary discussions of scientific questions related to matter under extreme conditions in terms of high pressure (HP) and high temperature (HT). These conditions are prevalent in the deep and not-so-deep interiors of solar system planets, their satellites as well as in massive solid and gas giant extrasolar planets. Studying matter under these extreme conditions is not yet fully accessible by conventional experimental and theoretical methods. However, new enabling techniques creating HP/HT regimes such as high energy laser compression or pulsed and laser heated diamond anvil cells taking benefit of intense pulsed X-ray sources now make it possible to investigate matter under these extreme conditions. In addition, new *ab initio* simulations for matter under extreme conditions provide more and more predictive data sets for planetary interiors in this HP/HT regime.

This year a total of 70 participants from seven countries joined the workshop for exciting discussions on topics ranging from compression of helium and hydrogen relevant to gas giants, to the study of rocky solids encountered in earth and super earth like planets. Contrasting this information to theoretical prediction of phase stabilities and other physical properties as well as space craft observation complemented the presented experimental data. The next workshop will take place in 2017 in Göttingen at the Max Planck Institute for Solar System Research.



Participants of the joint workshop on high pressure, planetary and plasma physics at DESY.

14 – 16 September: Scientists and engineers of the four largest high energy synchrotron radiation sources meet at DESY

The '16th Three-way Meeting' brought together more than 100 scientists and engineers from the high-energy synchrotron radiation sources APS, ESRF, PETRA III, and SPring-8. The title of the meeting reflects the three continents, America, Asia, and Europe, hosting high energy third generation sources. This meeting takes place about every 18 months and it was held at DESY for the first time.

It offers the opportunity for the staff of the four X-ray facilities to discuss, compare, and co-ordinate research and development between the four synchrotron radiation sources.

In specialized sessions the challenges and opportunities concerning data policy, big data, and fast data evaluation, the need for complementary laboratory infrastructure and special sample environments, the increasing demands for nano positioning and stability, and the machine developments towards diffraction limited storage rings were discussed.

A satellite workshop on optics addressed current and future optics requirements and latest developments.



Attendees of the '16th Three-way Meeting'.

14 September: Inauguration of two new experimental halls for PETRA III

With the PETRA III extension project two new experimental halls were created. Each hall can accommodate up to five additional PETRA III beamlines. A special inaugural ceremony was held to celebrate the naming of the two new experimental halls of the PETRA III extension: The halls were baptized to the names of the Israeli Nobel laureate Ada Yonath and the German theoretical physicist Paul P. Ewald.

In the experimental hall 'Paul P. Ewald', which is located north of the initial experimental hall 'Max-von-Laue', two new beamlines dedicated to X-ray absorption spectroscopy already went into operation for research. In the experimental hall 'Ada Yonath' several experiments are currently under construction in collaboration with international partners from Sweden, Russia, and India.



The experimental hall 'Paul P. Ewald' is one of the two new buildings of the PETRA III extension.

In front of a large audience the ceremony was attended by Ada Yonath herself, Olaf Scholz, the First Mayor of Hamburg, Harsh Vardhan, India's Minister of Research, Edelgard Bulmahn, Vice-President of Germany's Bundestag, Georg Schütte, State Secretary at the Federal Ministry for Education and Research, and Eva Gümbel from Hamburg's Department of Science, Research and Equal Opportunities, as well as by members of Ewald's family and high-ranking visitors from India, Sweden and Russia.



Nobel laureate Ada Yonath in front of the new PETRA III experimental hall which was named after her. (credit: G.Born/DESY)

Both, Ada Yonath and Paul P. Ewald play a very special role for PETRA III. At the beginning of the 20th century, Paul P. Ewald developed his theory on the interaction between X-rays and crystals, the so-called Dynamical Theory of X-ray Diffraction. This created the foundations for the subsequent development of X-ray crystallography which has become essential for many experiments done at PETRA III. Ada Yonath received the Nobel Prize in Chemistry in 2009, together with Venkatraman Ramakrishnan and Thomas A. Steitz, for deciphering the structure and function of the ribosome. From 1986 until 2004, she was head of the Max Planck Research Unit for Ribosomal Structure at DESY in Hamburg. Her work at DESY's light sources contributed to the decryption of the extremely complex structure of ribosomes. Both researchers symbolise the tremendous progress that has been made in X-ray structural analysis, which researchers at the PETRA III measuring stations can now benefit from.



At the naming ceremony: In a panel discussion representatives from the partner countries India, Russian Federation and Sweden chat about the engagement of their counties in experiments at PETRA III.

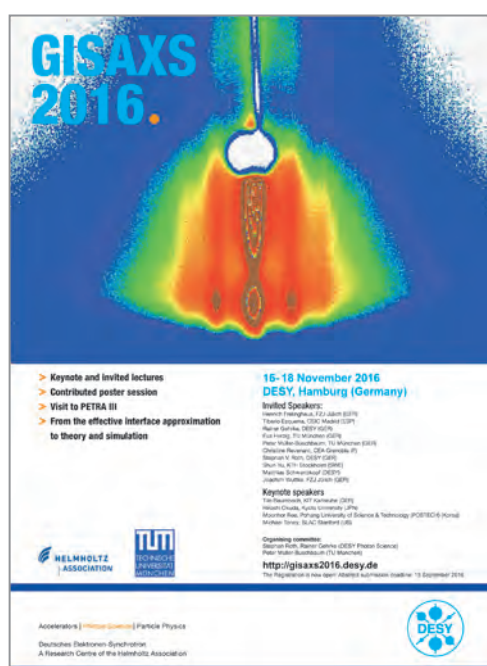
November

16 – 18 November: International Workshop on Grazing Incidence Small Angle Scattering

The GISAXS2016 International Workshop on Grazing Incidence Small Angle Scattering was a continuation of a series of workshops organised at DESY and started in 2005 with the intention to bring together the different research communities working in the fields of thin films, nanostructures, surfaces and interfaces to get insights into this powerful surface sensitive scattering technique. This year the workshop attracted more than 120 participants. Present activities and trends in this field were presented by four keynote lectures and ten invited talks as well as in a poster session with lively discussions. Special attention was paid to fast real time investigations and new developments in data analysis. An important part of all the workshops of this series was practical training. Therefore, besides visiting the micro- and nano-focus X-ray scattering beamline P03 at PETRA III with a detailed insight into its GISAXS possibilities, the participants again had the opportunity to participate in hands-on training with online treatment and simulation of GISAXS data.



Participants of the GISAXS2016 workshop held at DESY.



Poster of the GISAXS2016 workshop.

December

2 December: PhD Thesis prize for Cornelius Gati

The 2016 PhD thesis prize of the Association of the Friends and Sponsors of DESY was awarded to Cornelius Gati who worked on his doctoral thesis in the group of Henry Chapman at DESY (CFEL) and University of Hamburg. His thesis is entitled 'Data Processing and Analysis in Serial Crystallography at Advanced X-ray Sources' and the award was presented on the occasion of the DESY Science Day.

Gati studied biology at the Eberhard Karls University in Tübingen and was awarded a Bachelor of Science in Biology in 2010. After studying at the Technical University in Munich and working at Roche Diagnostics GmbH, he received a Master of Science at the Paul Scherrer Institute in Switzerland in 2012. He then started working on his PhD at DESY at the Center for Free-Electron Laser Science, CFEL. In his work he investigated methods for structure determination of biomolecules using X-ray free-electron lasers. With X-ray free-electron lasers images of e.g. biomolecules can be acquired so quickly that these images are not affected by radiation damage. In other words, the complete image is obtained before the molecule explodes in the extremely intense light pulse. The technique called 'Serial Femtosecond Crystallography (SFX)' repeats this measurement for a large number of individual samples and reconstructs the three-dimensional structure of the crystal by combining all these results. In his dissertation, Gati describes various examples of how this technique can be applied: The smallest protein crystals from which structure information with atomic resolution has been obtained, the first structure determination of a human membrane protein at room temperature, and the first completely unknown protein structure that was solved using SFX. In the latter case, important insights were obtained about a receptor that is of huge pharmacological significance and plays a key role in high blood pressure. Another part of Gati's dissertation describes in detail how the SFX technique can be adapted to modern microfocus beamlines at conventional synchrotron radiation sources. This opens the opportunity of examining micrometer sized protein crystals to a broader community of structural biologists.



Cornelius Gati giving a presentation at the award ceremony.

December

14 – 16 December:

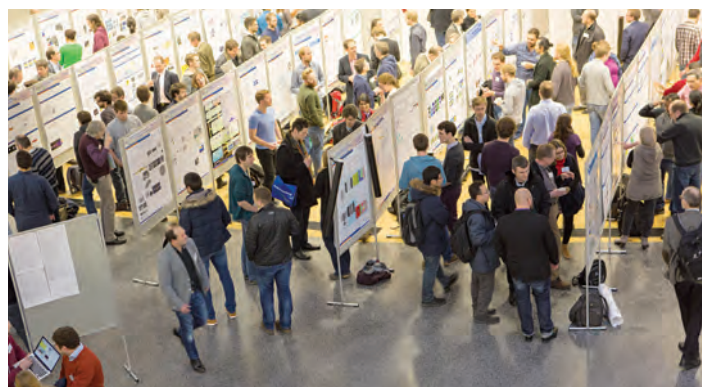
Workshop on science of the Helmholtz Programme 'From Matter to Materials and Life'

The DESY in-house research activities in the field of photon science are part of the programme 'From Matter to Materials and Life (MML)' within the research field 'Matter' of the Helmholtz Association. This programme is devoted to analyzing and modifying the structure, dynamics, and function of matter and materials by the use of large-scale facilities in close collaboration with users from academic science and industry. All research is closely connected to the use and operation of a wide range of research infrastructures including photon-, neutron-, and ion-sources, high-magnetic field facilities, and high power lasers. Currently in-house research at MML focuses on five themes:

Extreme states of matter in the range from cold ions to hot plasmas, quantum condensed matter involving magnetism, superconductivity and more, materials and processes for energy and transport technologies, nanoscience and materials for information technologies, and soft matter, health and life sciences.

The workshop on science within the MML programme took place at DESY and attracted more than 300 participants from all involved Helmholtz Centres. They presented and

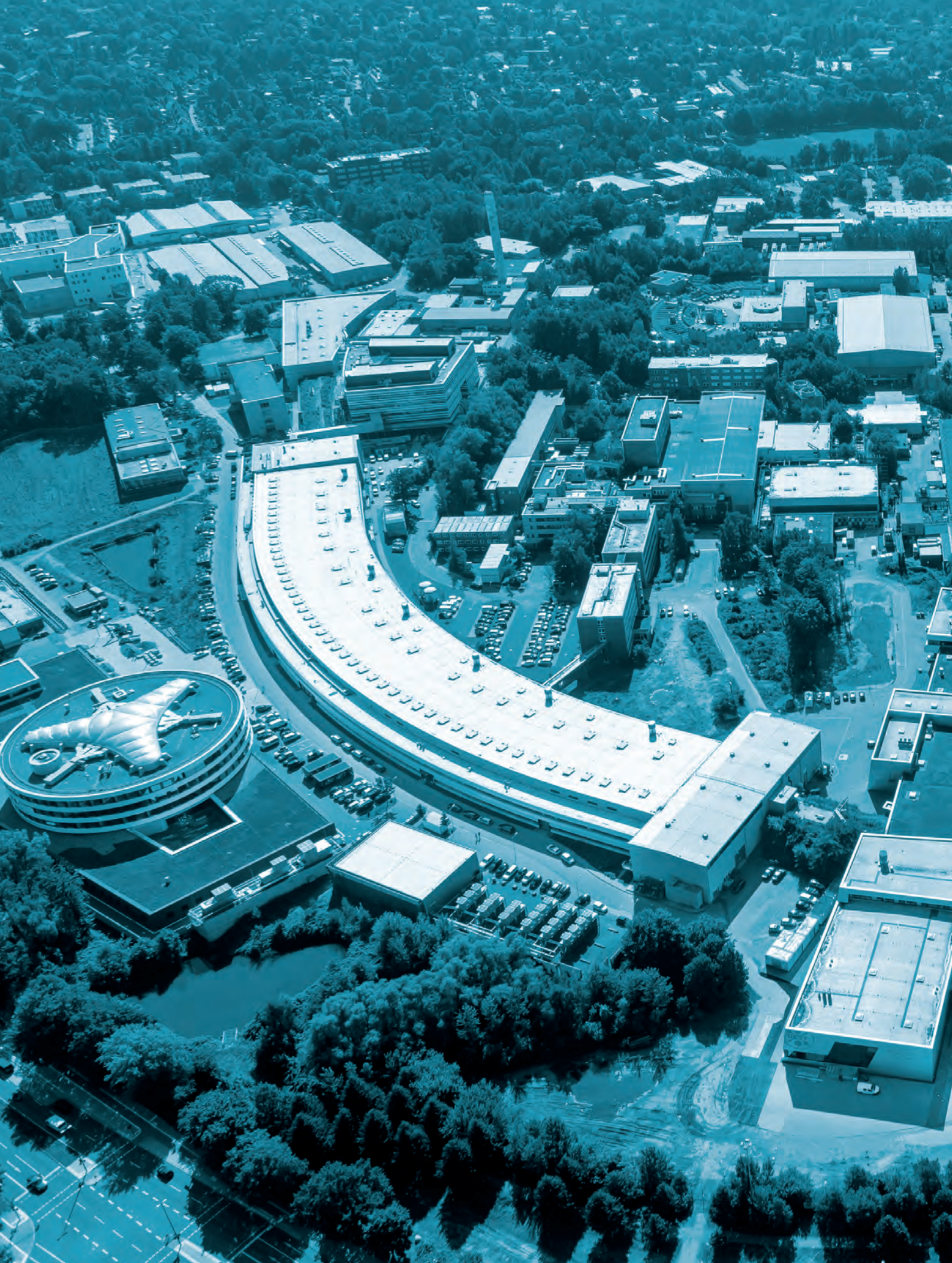
discussed their current research activities, the development of the large scale facilities, and the related instrumentation. Particular emphasis was given to new ideas and potential new topics for in-house research in the frame of MML. The scientific programme of the workshop featured review talks covering the most recent achievements and highlights, contributed talks in parallel sessions dedicated to the five in-house research topics, and a poster session.



Poster session during the MML workshop at DESY.



Group photo with the participants of the MML workshop.



Science Highlights.

Cultural and natural history

- The 'wilting' of Van Gogh's Sunflowers 22
- The early amber caught the worm 24

Surfaces, thin films and interfaces

- Watching degradation in polymeric solar cells 26
- Capturing nanoscale fireworks 28
- Matter and light, unite 30
- Live-view of catalyst degradation at the nanometre-scale 32

Electronic and magnetic structure

- Negative piezoelectricity of poly(vinylidene-fluoride) 34
- Ironing out the mystery of Earth's magnetic field 36
- Magnetic field controlled charge density wave coupling in underdoped $\text{YBa}_2\text{Cu}_3\text{O}_{6+x}$ 38
- Magnetic sensors custom-made 40
- Strongly correlated electrons meet topology 42

Structure and structural dynamics

- Direct insights into phase transformations in nano-scaled microstructures 44
- Coherent X-rays spotlight on a colloidal crystal 46
- Earth's mantle may produce oxygen 48
- Accessing nanoscale dynamics at SACLA 50
- A nanoparticle supercrystal with exceptional mechanical properties 52
- A deep view inside intact biological cells 54

Life Sciences

- Exploiting crystal disorder to improve resolution 56
- Crystal structure of Zika virus protease 58
- The inhibition mechanism of human 20S proteasomes 60
- Proteins in action 62
- Building with DNA 64
- In cellulo serial crystallography of alcohol oxidase crystals 66
- How arsenic toxicity affects plants on the subcellular level 68
- Structure based pro-drug discovery 70

Atomic and molecular dynamics

- FLASH uncovers intricate nanoplasma heating 72
- Molecular dynamics made visible through mathematics 74

Science of X-ray sources - methods and developments

- Fast local reactions of proteins 76
- Ultrashort FLASHes 78
- Creating spiraling FLASHes 80
- Synchronous laser-microwave networks 82
- Lightwave electronics on a chip 84
- Polarization on demand 86

The 'wilting' of Van Gogh's Sunflowers.

Evidence for degradation of the chrome yellow pigments

The darkening of yellow colours in Van Gogh's *Sunflowers* in the Van Gogh Museum in Amsterdam has been suspected but also frequently debated over the last decades. Our work presents firm evidence for the chemical alteration of chrome yellows, with indication of the areas of the painting where the risk of darkening is higher due to pigment's degradation. Non-invasive *in situ* spectroscopic analysis on the surface of the painting combined with synchrotron radiation-based X-ray examinations of two micro-samples revealed the presence of different types of chrome yellows, including the lightfast PbCrO_4 and the sulphur-rich $\text{PbCr}_{1-x}\text{S}_x\text{O}_4$ ($x \sim 0.5$). This variety of the pigment is known for its high tendency to degrade via a photo-reduction mechanism. Cr^{III} -compounds were found at the varnish/paint interface as products of alteration.

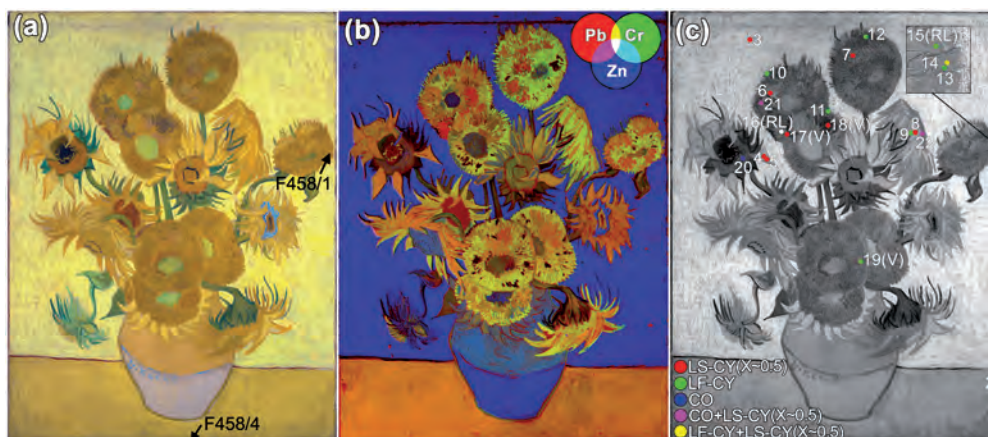


Figure 1

(a) Photograph of Van Gogh's *Sunflowers* (Van Gogh Museum, Amsterdam). Arrows and labels show the sampling spots (cf. Figs. 2a and 3a). (b) RGB composite map of Pb/Cr/Zn obtained by MA-XRF. (c) Raman distribution of different CY types [LS-CY: light sensitive chrome yellow- $\text{PbCr}_{1-x}\text{S}_x\text{O}_4$ ($x \sim 0.5$); LF-CY: lightfast chrome yellow- PbCrO_4 ; CO: chrome orange- $(1-x)\text{PbCrO}_4 \cdot x\text{PbO}$]. 'V' and 'RL' indicate spots containing also vermillion and red lead, while the white circle shows the location where only red lead was identified.

The fourth version of *Sunflowers*, painted by the famous Dutch artist Vincent van Gogh in Arles in 1888-1889, comprises three similar paintings that are currently exhibited at the museums in London, Tokyo and Amsterdam respectively. The vibrancy and brightness of these masterpieces was made possible by the use of chrome yellows (CYs), an early 19th C. class of pigments with hues ranging from lemon-yellow to orange-yellow. In spite of similarities, different yellow tones with tiny variations characterize the sunflower petals, the background and the table in the three paintings. The extent to which the current appearance of various yellow shades are ascribable to Van Gogh's stylistic choices, over the use of pigment mixtures and/or to unintended colour changes, are the result of the degradation of original materials, has been questioned.

Our earlier studies, on artificially aged paint models and micro-samples obtained from a series of Van Gogh paintings, established that the darkening of different CY pigments $\text{PbCr}_{1-x}\text{S}_x\text{O}_4$ (with $0 \leq x \leq 0.8$) is due to a reduction of the original chromate ions to Cr^{III} -compounds. This transformation

occurs via Cr^{V} -intermediates that are thermally formed as result of the interaction of Cr^{VI} with the oil binder [1-6]. The degradation process is more favoured for the lemon-yellow, orthorhombic sulphur-rich $\text{PbCr}_{1-x}\text{S}_x\text{O}_4$ varieties of the pigment (with $x > 0.4$) than for the orange-yellow, monoclinic PbCrO_4 , that is the most lightfast of these compounds [1,2].

In this work, non-invasive *in situ* spectroscopic analyses and synchrotron radiation-based X-ray investigations on micro-samples were performed to assess the following: the extent to which the *Sunflowers* version of the Van Gogh Museum (Fig. 1a) contains lightfast PbCrO_4 (denoted as LF-CY) and light sensitive sulphur-rich $\text{PbCr}_{1-x}\text{S}_x\text{O}_4$ ($x > 0.4$) (LS-CY) and, in addition, to determine whether or not these pigments have been subject to a reduction process.

Non-invasive *in situ* macro X-ray fluorescence (MA-XRF) scanning analysis combined with vibrational spectroscopic investigations (Fig. 1b-c) allowed different CYs to be identified, including the LF-CY and the LS-CY ($x \sim 0.5$).

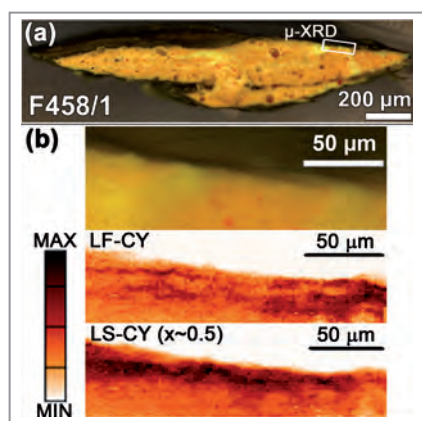


Figure 2

(a) Photomicrograph of sample F458/1 and LF-CY and LS-CY ($x \sim 0.5$) distribution maps obtained by (b) SR μ -XRD [map size: $190 \times 51 \mu\text{m}^2$; pixel size ($h \times v$): $2 \times 1 \mu\text{m}^2$] at the micro-probe endstation of the PETRA III beamline P06. In (a) the white rectangle and label indicates the position where data of (b) were acquired.

Synchrotron radiation-based μ -XRD mapping analysis of a region of interesting of sample F458/1 (from an ochre-yellow petal; Fig. 2a) were performed at the micro-probe endstation of the PETRA III beamline P06, confirming not only the non-invasive findings but also providing further insights into the spatial distribution of the two CY types: LF-CY is the chief constituent of the orange-yellow shades, while LS-CY ($x \sim 0.5$) is the main phase in the lighter yellow hues (Fig. 2b).

Since chrome yellows were often found in mixture with other pigments (e.g. vermilion, zinc white, emerald green, red lead) as well as alone, the visual assessment of any colour change due to chromate photo-reduction is not straightforward. Thus, the degradation state of the CY paint was evaluated by determining the Cr-oxidation state via Cr K-edge μ -XANES/ μ -XRF analysis of the two micro-samples at the ESRF beamline ID21 in Grenoble, France.

Clear indications for the presence of reduced Cr were found inside the varnish layer and at the varnish/paint interface of both the analyzed samples. At one location of the sample F458/4 (from the light yellow table; Fig. 3a-b), Cr^{III} -species are observable both as Cr_2O_3 particles or widespread inside the varnish, reaching a relative abundance up to 100 % (Figure 3d:

$01_{4-I}, 02_{4-I}$). In another region (Fig. 3a,c), Cr^{III} -compounds are present as a thin layer (2-3 μm thickness) at the varnish/paint interface, while only Cr^{VI} -species have been identified in the yellow paint underneath (Fig. 3d: pts $01_{4-II}, 02_{4-II}$). This pattern resembles to that we have earlier observed in photochemically aged LS-CY ($x > 0.4$) paint models, [2] suggesting that the observed colour change arises from the CY reduction.

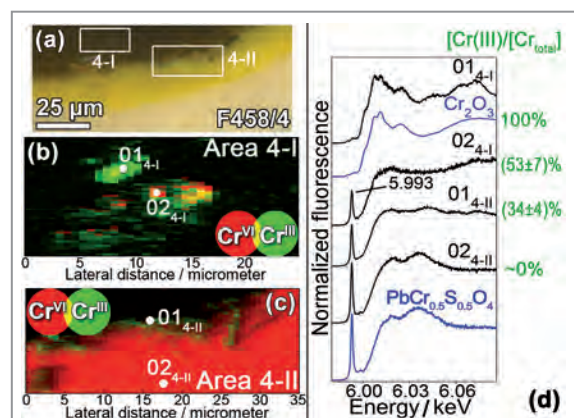


Figure 3

(a) Photomicrograph detail of sample F458/4 and corresponding (b-c) RG composite $\text{Cr}^{\text{VI}}/\text{Cr}^{\text{III}}$ chemical state maps. (d) Cr K-edge μ -XANES spectra acquired from points shown in (b-c) (data obtained at ID21 beamline of ESRF). Green labels show the relative abundance of reduced chromium obtained by linear combination fitting analysis.

The obtained results provide evidence of the chemical alteration of chrome yellows in Van Gogh's *Sunflowers*. Selected areas of the painting with the highest probability of colour change due to Cr^{VI} -reduction have been identified, thus calling for careful monitoring in the future. The findings of this study, supported by those of our previous research [1,2], open up the way to the development of strategies for the safer illumination of the extraordinary paintings.

Contact: Letizia Monico, letizia.monico@cnr.istm.it

Authors

Letizia Monico^{1,2}, Koen Janssens², Ella Hendriks³, Frederik Vanmeert², Geert Van der Snickt², Marine Cotte⁴, Gerald Falkenberg⁵, Brunetto Giovanni Brunetti¹ and Costanza Miliani¹

1. Department of Chemistry, Biology and Biotechnologies/SMAArt Centre, University of Perugia and CNR-ISTM, Perugia, Italy.
2. Department of Chemistry, University of Antwerp, Antwerp, Belgium
3. Van Gogh Museum, Amsterdam, The Netherlands
4. ESRF, Grenoble, France
5. Deutsches Elektronen-Synchrotron DESY, Photon Science, Hamburg, Germany

Original publication

'Evidence for Degradation of the Chrome Yellows in Van Gogh's Sunflowers: A Study Using Noninvasive In Situ Methods and Synchrotron-Radiation-Based X-ray Techniques', *Angew. Chem.* 127, 14129–14133 (2015), DOI:10.1002/ange.201505840.

References

1. L. Monico, G. Van der Snickt, K. Janssens, W. De Nolf, C. Miliani, J. Verbeeck, H. Tian, H. Tan, J. Dik, M. Radepon and M. Cotte, 'Degradation process of lead chromate in paintings by Vincent van Gogh studied by means of synchrotron X-ray spectromicroscopy and related methods. Part 1: Artificially aged model samples', *Analytical Chemistry* 83, 1214-1223 (2011).

2. L. Monico, K. Janssens, C. Miliani, G. Van der Snickt, B.G. Brunetti, M. Cestelli Guidi, M. Radepon and M. Cotte, (...) Part 4: 'Artificial aging of model samples of co-precipitates of lead chromate and lead sulfate', *Analytical Chemistry* 85, 860-867 (2013).
3. L. Monico, K. Janssens, F. Vanmeert, M. Cotte, B. G. Brunetti, G. Van der Snickt, M. Leeuwestein, J. Salvant Plisson, M. Menu and C. Miliani, (...) Part 5. 'Effects of non original surface coatings into the nature and distribution of chromium and sulfur species in chrome yellow paints', *Analytical Chemistry* 86, 10804–10811 (2014).
4. L. Monico, K. Janssens, M. Cotte, A. Romani, L. Sorace, C. Grazia, B. G. Brunetti and C. Miliani, 'Synchrotron-based X-ray spectromicroscopy and electron paramagnetic resonance spectroscopy to investigate the redox properties of lead chromate pigments under the effect of visible light', *Journal of Analytical Atomic Spectrometry* 30, 1500-1510 (2015).
5. L. Monico, K. Janssens, M. Alfeld, M. Cotte, F. Vanmeert, C. G. Ryan, G. Falkenberg, D. L. Howard, B. G. Brunetti and C. Miliani, 'Full spectral XANES imaging using the Maia detector array as a new tool for the study of the alteration process of chrome yellow pigments in paintings by Vincent van Gogh', *Journal of Analytical Atomic Spectrometry* 30, 613-626 (2015).
6. L. Monico, K. Janssens, M. Cotte, L. Sorace, F. Vanmeert, B. G. Brunetti and C. Miliani, 'Chromium speciation methods and infrared spectroscopy for studying the chemical reactivity of lead chromate-based pigments in oil medium', *Microchemical Journal* 124, 272-282 (2016).

The early amber caught the worm.

A 100 million-year-old onychophoran reveals past migrations

The split of the supercontinent Pangaea into southern Gondwana and northern Laurasia divided the fauna of these two regions. Therefore, the present-day occurrence of supposedly Gondwanan organisms in Laurasian-derived regions remains a puzzle of palaeobiogeographical history. We studied the oldest amber-embedded species of velvet worms (Onychophora) in order to illuminate the colonisation of Southeast Asia by Gondwanan lineages of these animals. Our results indicate that an early Eurogondwanan migration is the most likely scenario for Onychophora, while an ‘Out-of-India’ colonisation of Southeast Asia would instead be incompatible with the age of the amber fossil studied. This suggests a recent colonisation of India by onychophorans and refutes their Gondwanan relict status in this region.

Burmese amber from Myanmar is known not only for its physical beauty but also for preserving one of the richest palaeobiota in the world, being arguably the most relevant fossil resin for studying terrestrial diversity during the mid-Cretaceous period, approximately 100 million years ago [1]. Among the most consequential organisms found in Burmese amber is the oldest amber-embedded representative of Onychophora — a small group of soft-bodied, terrestrial invertebrates pivotal for understanding animal evolution and biogeography. Onychophorans are extremely rare in fossiliferous amber, with the Burmese †*Cretoperipatus burmiticus* being only the third species ever discovered [2]. Indeed, this species is crucial for clarifying the question of how onychophorans colonised Southeast Asia, one of the most enigmatic and controversially discussed biogeographical issues relating to this group.

Representatives of Peripatidae, an onychophoran subgroup to which †*C. burmiticus* was suggested to belong, show a disjointed distribution pattern across three distinct geographical regions — the Neotropic zone, Tropical Africa, and Southeast Asia — each home to a monophyletic group. Molecular data suggest that these clades diverged during the time of the supercontinent Pangaea, approximately 286–244 million years ago [3]. Hence, it is commonly assumed that their current discontinuous distribution resulted from past tectonic shifts and/or climatic events. While continental drift could explain the split between the Neotropical and Tropical African Peripatidae, the major question is how peripatids reached Southeast Asia, as this area has never been in direct contact with the other two landmasses.

It has previously been suggested that peripatids from Gondwana arrived in Southeast Asia prior to the split of continents (= continental drift) via a land bridge formed by Europe, a

hypothesis recently named the Eurogondwana model [4]. Alternatively, since onychophorans are poor dispersers, it was proposed that the Indian subcontinent acted as a raft during its northward drift and brought Gondwanan species of Peripatidae to Southeast Asia after the so-called ‘India–Asia collision’, a biogeographical model commonly called ‘Out-of-India’ [5]. Accordingly, the only onychophoran species reported from India, *Typhloperipatus williamsoni* [6], is putatively described as being a Gondwanan relict that survived

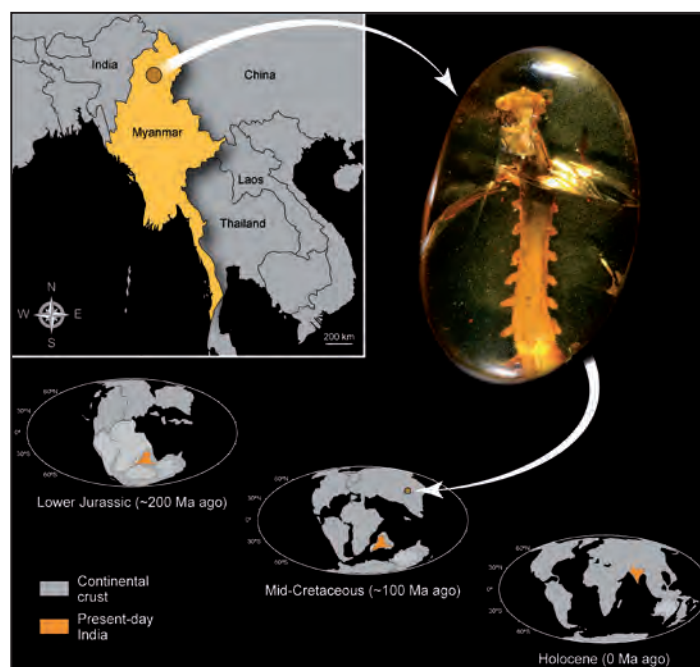


Figure 1

The geographic position of the Hukawng Valley amber deposit in Myanmar (brown circle), where the exceptionally well-preserved material of †*Cretoperipatus burmiticus* (photograph) was found. Bottom row shows the drift of India through time. Notice that the fossil species inhabited Southeast Asia during a period when India was still an island.

the ~100-million-year isolation of the Indian subcontinent as it moved towards Southeast Asia. Depending on which scenario is considered, extinction has been invoked for explaining the current lack of present-day peripatids in Europe (Eurogondwana model), or in the great part of India ('Out-of-India' hypothesis). It is important to note, however, that these two hypotheses are not mutually exclusive, as onychophorans may have found their way to Southeast Asia via both routes simultaneously. In any case, hypotheses on vicariance, dispersion and extinction require fossil data to be tested empirically.

Recently, additional material of †*C. burmiticus*, including an exceptionally well-preserved amber-embedded specimen, was discovered at the species type locality in Myanmar (Fig. 1). This fossil dates to the mid-Cretaceous, a period in time after the continental drift but before the 'India-Asia collision', i.e., sometime between the two suggested scenarios accounting for the colonisation of Southeast Asia by peripatids. Thus, its relevance for clarifying these biogeographical and evolutionary issues should not be understated. Using the imaging beamline P05 at PETRA III, we performed a full micro-CT scan of this specimen in amber and used these data to reconstruct hitherto unknown anatomical details of †*C. burmiticus* (Fig. 2). By performing a morphological analysis of this animal and comparing it to extant taxa, we confirmed †*C. burmiticus* to be a member of the Peripatidae and resolved the Indian species *T. williamsoni* as its closest relative.

These findings support an early migration of Peripatidae to Southeast Asia, i.e. the Eurogondwana hypothesis, followed by a posterior colonisation of India by onychophorans from Southeast Asia. In other words, the fact that †*C. burmiticus* roamed Southeast Asia long before there was a terrestrial connection with India excludes this species as originating from India, while its sister-group relationship to *T. williamsoni* refutes the putative Gondwanan relict status of the latter. Furthermore, this suggests that the migration of onychophorans into India happened not earlier than ~25 million years ago, i.e., after the 'India-Asia collision' and much later than what was previously thought.

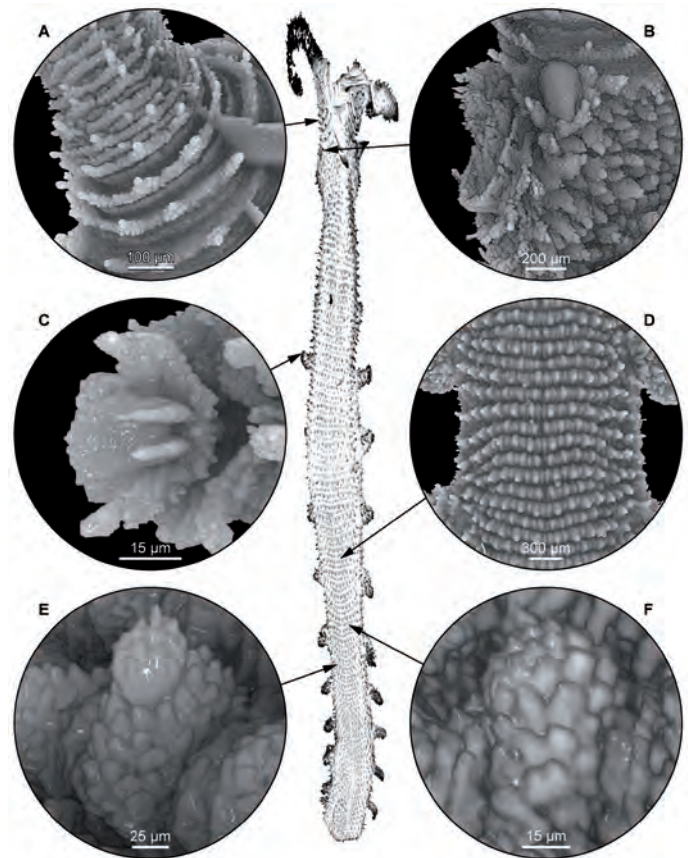


Figure 2

Novel morphological features of †*Cretoperipatus burmiticus* revealed by synchrotron radiation micro-computed tomography (= SRμCT). (a) Detail of the antenna. (b) Eye and slime papilla. (c) Foot. (d) Overview of the dorsal integument. (e) A dorsal primary papilla. (f) A dorsal accessory papilla.

This study demonstrates the utility of X-ray microtomography for accessing morphological characters that were previously unavailable to traditional techniques due to the nature of fossilisation. Thus, it opens the door to generating a wealth of new data from fossil specimens that have been kept for years in museums or private collections and using these data to address long-standing issues.

Contact: Ivo de Sena Oliveira, ivo.oliveira@uni-kassel.de

Authors

Ivo de Sena Oliveira^{1,2*}, Ming Bai^{1*}, Henry Jahn², Vladimir Gross², Christine Martin², Jörg U. Hammel³, Weiwei Zhang¹ and Georg Mayer²

1. Key Laboratory of Zoological Systematics and Evolution, Institute of Zoology, Chinese Academy of Sciences, Beijing, China

2. Department of Zoology, Institute of Biology, University of Kassel, Kassel, Germany

3. Institute of Materials Research, Helmholtz-Zentrum Geesthacht, Geesthacht, Germany

* Co-first author

Original publication

'Earliest Onychophoran in Amber Reveals Gondwanan Migration Patterns', *Current Biology* 26, 2594–2601 (2016). DOI: 10.1016/j.cub.2016.07.023

References

1. A. Ross, C. Mellish, P. York and B. Crighton, 'Burmese Amber', *Biodiversity of Fossils in Amber from the Major World Deposits*, 208–235 (Siri Scientific Press, Manchester, UK, 2010).
2. D.A. Grimaldi, M.S. Engel and P.C. Nascimbene, 'Fossiliferous cretaceous amber from Myanmar (Burma): its rediscovery, biotic diversity, and paleontological significance', *Am. Mus. Novit.* 3361, 3–72 (2002).
3. J. Murienne, S.R. Daniels, T.R. Buckley, G. Mayer and G. Giribet, 'A living fossil tale of Pangean biogeography', *Proc. R. Soc. B.* 281, 20132648 (2014).
4. M.D. Ezcurra and F.L. Agnolín, 'A new global palaeobiogeographical model for the late Mesozoic and early Tertiary', *Syst. Biol.* 61, 553–566 (2012).
5. K.P. Karanth, 'Out-of-India Gondwanan origin of some tropical Asian biota', *Curr. Sci. (Bangalore)* 90, 789–792 (2006).
6. S. Kemp, 'Onychophora', *Rec. Indian Mus.* 8, 471–492 (1914).

Watching degradation in polymeric solar cells.

The crux of unstable morphologies

Organic photovoltaics render a novel approach converting sunlight to electricity. This is conventionally done using silicon-based semiconductors which rely on energy-demanding and expensive manufacturing. In contrast, organic solar cells offer the chance of a low-cost processability on a large scale, e.g. by roll-to-roll printing technologies and using flexible and transparent substrates. In that way, cheap and versatile solar cells with low weight and even optical (semi)transparency are meanwhile feasible and allow for expansion of solar power production into yet remote fields of application. Although ever increasing power conversion efficiencies have been obtained during the last decade, organic solar cells still suffer from shorter lifetimes as compared to state-of-the-art silicon-based photovoltaics. To gain deeper understanding on device degradation we present an *in operando* investigation of the nanometre-scaled morphology. The morphology and the photovoltaic characteristics are simultaneously probed via combined grazing incidence small angle X-ray scattering and current-voltage tracking during the first hours of operation.

In the present work we illuminate the role of nanometre-scaled changes of the internal solar cell structure on the degradation behaviour of organic solar cells (Organic Photovoltaics, OPV) which are enhanced with processing additives. Here, a PCPDTBT:PC₇₁BM solar cell prepared with 1,8-octanedithiol (ODT) as a processing additive (PA) is used. An operational solar cell is simultaneously probed for its internal nanometre-scaled structure and its photovoltaic performance. For this purpose, a cell is mounted in a specialised chamber which allows for illumination with visible and X-ray light. During illumination with simulated sunlight, the photovoltaic characteristics are perpetually recorded. While this characterisation is ongoing, micro-focused grazing incidence small angle X-ray scattering (μ GISAXS) patterns are recorded at beamline P03 of DESY's synchrotron radiation source PETRA III. By using this technique a complete data set on the nanometre-scaled active layer of the solar cell and its electric characteristics after different operation times is obtained. In previous investigations, we were able to draw first evidence for morphological degradation in polymer-based solar cells [1].

The active layer in polymer-fullerene solar cells, in which light is converted to electricity, is applied from a mutual solution containing a fullerene derivative and a semiconducting polymer. During film fabrication, the two materials phase separate into an interpenetrating network of both, polymer and fullerene domains. For an efficient power conversion, this phase separation must occur on a nanometre scale. In case the domain structure is too coarse, the generation of separated charge carriers in the active layer is low. It relies on a large interfacial area of the two domains. In case of too fine domain structures, charge carriers are efficiently generated while recombination

processes during charge carrier transport deteriorate the overall efficiency. Using processing additives, the domain network morphology can be tuned such that optimum charge carrier generation and transport towards the solar cell electrodes is achieved. Device degradation, a manifestation of morphological changes, occurs as a consequence of device operation. It is called morphological degradation and has been first evidenced in our earlier work [1].

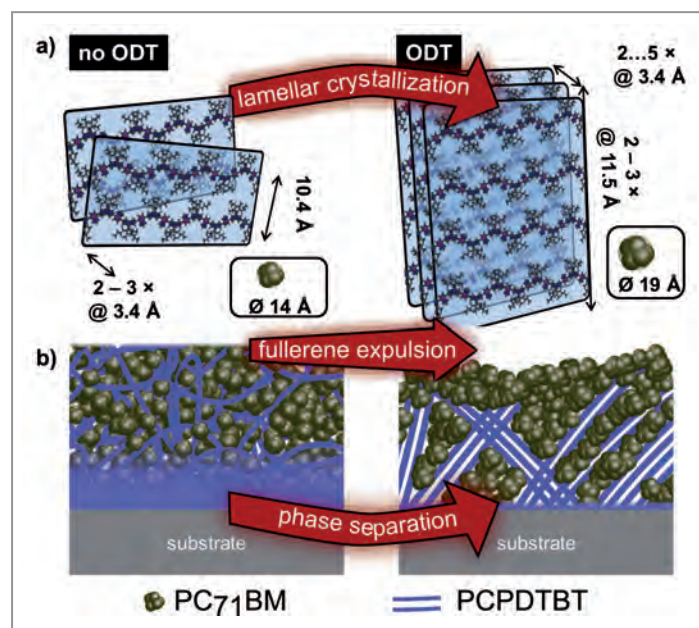


Figure 1
The use of 1,8-octanedithiol (ODT) as processing additive in a PCPDTBT:PC₇₁BM solution leads to enhanced crystallization and phase separation on the nanometre scale. Image from the original publication in ACS Applied Materials & Interfaces [2].

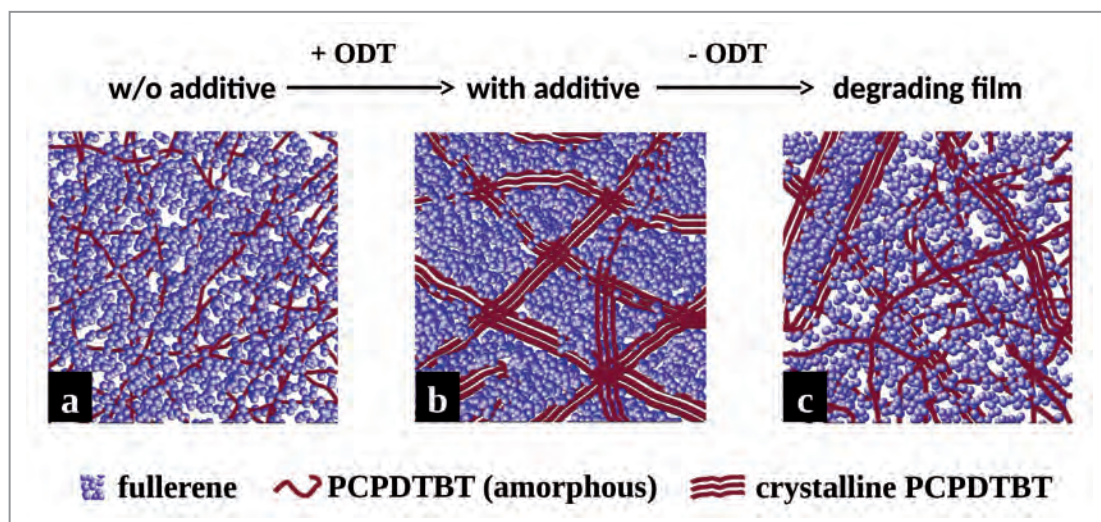


Figure 2

Morphological degradation in PCPDTBT:PC₇₁BM solar cells. (a) Without solvent additive the domain morphology is too fine. (b) The use of 1,8-octanedithiol as processing additive leads to enhanced phase separation on the nanometre scale. (c) When ODT is expelled from the film during operation, the morphology changes towards the one without ODT and leads to enhanced charge carrier recombination processes: The overall efficiency deteriorates.

In case of the investigated PCPDTBT:PC₇₁BM solar cell system, a too fine morphology is produced during cell fabrication. However, the use of a low amount of processing additive ODT in the mutual solution leads to an enhanced phase separation on the nanometre-scale, which was shown in our previous work [2] (Figure 1). The observed enhancements allow for well improved photovoltaic performance in several material systems [3], however, the influence of processing additives on device stability was not yet clear.

In the present study we use *in situ* μ GISAXS on an organic solar cell in operation to investigate the influence of a processing additive on the morphological degradation behaviour. We find that the solar cell deteriorates strongly during the first hours of operation. Hereby, the loss of performance is mainly governed by a rapid loss of the fill factor, which implicitly describes the efficiency of charge carrier collection.

At the same time, very small domains on a length scale of 10 nm are found to shrink to half of their original size,

accompanied by a loss of the overall scattering intensity. The scattering data also indicates a loss of residual ODT in the film. We conclude that – under operation – residual processing additive is expelled from the film, causing the film morphology to approach the state where no ODT is available (see Figure 2). Here, the charge carrier transport is deteriorated, which leads to overall device degradation.

Altogether, this study shows that processing additives provide not only an easy way to enhance the performance of organic photovoltaics but also introduce an additional pathway towards device degradation. After having identified the mechanism, the development of proper encapsulation or other ways of morphological stabilization, such as the use of block-copolymers or chemical cross-linking, are suggested. These insights will enable a future production of stable organic photovoltaics.

Contact: Peter Müller-Buschbaum, muellerb@ph.tum.de

Authors

Christoph J. Schaffer¹, Claudia M. Palumbiny¹, Martin A. Niedermeier¹, Christian Burger¹, Gonzalo Santoro², Stephan V. Roth² and Peter Müller-Buschbaum¹

1. Technische Universität München, Physik-Department, Lehrstuhl für Funktionelle Materialien, Garching, Germany
2. Deutsches Elektronen-Synchrotron DESY, Photon Science, Hamburg, Germany

Original publication

'Morphological Degradation in Low Bandgap Polymer Solar Cells – An In Operando Study', *Advanced Energy Materials* 6, 1600712 (2016), DOI:10.1002/aenm.201600712

References

1. C. J. Schaffer, C. M. Palumbiny, M. A. Niedermeier, C. Jendrzewski, G. Santoro, S. V. Roth, P. Müller-Buschbaum, 'A Direct Evidence of Morphological Degradation on a Nanometer Scale in Polymer Solar Cells', *Adv. Mater.* 25, 6760–6764 (2013).
2. C. J. Schaffer, J. Schlipf, E. D. Indari, B. Su, S. Bernstorff, P. Müller-Buschbaum, 'Effect of Blend Composition and Additives on the Morphology of PCPDTBT:PC₇₁BM Thin Films for Organic Photovoltaics', *ACS Appl. Mater. Interfaces* 7 (2015).
3. J. Peet, J. Y. Kim, N. E. Coates, W. Ma, D. Moses, A. J. Heeger, G. C. Bazan, 'Efficiency enhancement in low-bandgap polymer solar cells by processing with alkane dithiols', *Nature Materials*, 6, 397–500 (2007).

Capturing nanoscale fireworks.

Imaging single nanoparticle explosions with femtosecond temporal and nanometre spatial resolution

Many ultrafast non-equilibrium phenomena such as chemical reactions, phase transitions and light-matter interactions, remain uncharted due to the lack of imaging methods combining high spatial and temporal resolutions. X-ray free-electron lasers (FELs) with intense, femtosecond flashes open up unprecedented opportunities to resolve complex ultrafast dynamics even in isolated nanosized samples. We superheated single xenon nanoclusters using an intense infrared pulse and imaged the following expansion with single X-ray FEL pulses. Thereby, we resolved nanometre-scale surface softening within 100 fs of the heating pulse. Our study is the first time-resolved visualisation of irreversible femtosecond processes in free, individual nanometre-sized samples.

Conventional imaging methods such as electron or optical microscopy provide either high spatial or high temporal resolution, but fail to incorporate both. X-ray FELs open new opportunities to capture phenomena with a single exposure on a femtosecond timescale and with nanometre spatial resolution. Following the demonstration of the diffractive single-particle imaging approach at the FEL FLASH at DESY [1,2], subsequent studies on non-equilibrium dynamics provided unique insights into shock waves in materials [3] and protein quakes [4]. Studies at FLASH indicated that diffraction images provide indirect information about transient nanoplasma states [5]. However, most experiments to date were static or limited to picosecond temporal resolutions, while measurements on particle ensembles often lack the desired precision due to averaging effects. In the present study, we captured structural dynamics on the femtosecond timescale in free, single nanoparticles. Our study paves the way towards high-resolution femtosecond imaging of individual nanoparticles without the interaction with surroundings and under well-defined conditions.

In our experiment, individual xenon clusters with radii around 20 nm were exposed to a single near-infrared (NIR) laser pump and a subsequent X-ray laser probe pulse at the Linac Coherent Light Source (LCLS). The heating NIR laser pulse, with a wavelength of 800 nm and pulse duration of 70 fs, ionised and transformed single xenon clusters into a non-equilibrium nanoplasma evolving on the femtosecond timescale. We imaged the following cluster expansion by recording the diffraction from the nanosamples with delayed X-ray FEL pulses with 0.8 nm wavelength.

The X-ray diffraction from pristine and superheated clusters is shown in Fig. 1. The top panel demonstrates patterns recorded from a spherical xenon cluster similar to far-field

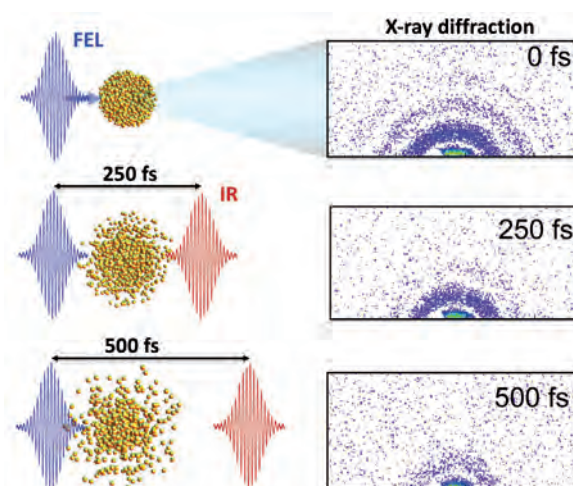


Figure 1

X-ray diffraction patterns of pristine and pre-heated xenon clusters. The top panel shows diffraction from a pristine spherical cluster. Shown below are the diffraction patterns produced 250 fs (middle) and 500 fs (bottom) after the exciting NIR pulse.

diffraction from a pinhole. The diffraction image changes dramatically within hundreds of femtoseconds after the heating NIR pulse excited the cluster. The loss of higher order information can be identified already after 250 fs and becomes apparent 500 fs after the heating pulse.

At first glance, one would expect very different diffraction patterns based on the assumption that the NIR pulse causes an explosion of the cluster. This model is reasonable as the NIR pulse ionises and heats the electrons trapped inside the cluster. These confined hot electrons initiate the cluster expansion as they transfer their kinetic energy to the ions. In the first order approximation, the cluster explosion can be compared to a constantly increasing pinhole leading to a finer spacing in the far-field diffraction.

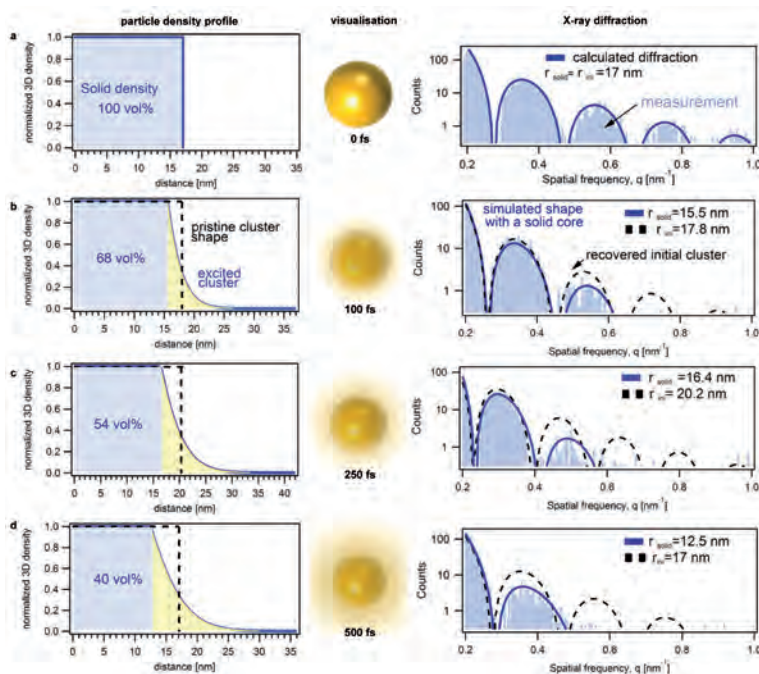


Figure 2

Evolution of the superheated nanoclusters at simultaneous NIR-FEL excitation (a), and 100 fs (b), 250 fs (c) and 500 fs (d) after the NIR pulse. Right panels: Measured diffraction integrated radially (histogram bars), fitted diffraction patterns (solid blue lines) and recovered diffraction from the pristine cluster (dashed lines). The experimental data indicate an inhomogeneous density distribution of the sample in b–d. The decrease in higher-order diffraction signal intensity suggests that the outer parts of the sample dilute due to expansion of the sample. Using the Guinier approximation, we fitted the observed diffraction patterns (solid line) with density profiles (shown on the left). Left panels: Comparison of fitted electron density profiles of the excited clusters (solid blue lines) and the recovered pristine shapes (dashed lines).

However, this aspect is not observed in the present experiment. The changes in the diffraction patterns can be correlated to the structural dynamics analytically in the limit of small scattering angles using the Guinier approximation [6]. The overall shape of the patterns suggests that the expansion first dilutes the outer shells close to the cluster surface, while leaving a core with a uniform electron density. Using the dilute shell – solid core model, the electron density profiles of the clusters can be reconstructed, as exhibited in Fig. 2.

In the right column of Fig. 2, the calculated scattering profiles of the undamaged and the reconstructed core–shell structure are compared to the recorded data. Panel A demonstrates that the pristine cluster can be perfectly fitted assuming a hard sphere with a uniform electron density profile. In panel B, the higher orders disappear rapidly already 100 fs after NIR excitation, but the peaks also broaden towards higher scattering angles, as best observed for the 500 fs data. Moreover, the minima of the heated particles are located at larger scattering angles than the minima of the simulated undamaged particles, as the small-angle information is dominated by the solid density core. This leads to the counter-intuitive situation that the larger expanding particles appear smaller than the unheated particles. This fingerprint can be used to identify potential sample damage in single-particle imaging with X-ray laser pulses.

Our study shows that imaging with X-ray lasers can gain unique insights into dynamics in matter under extreme conditions. The temporal resolution of our method can be significantly improved towards sub-10 fs using improved synchronisation techniques. In the hard X-ray regime, the spatial resolution could be pushed towards atomic resolution. The combination of both could allow one to follow structural changes with atomic resolution on the timescale of electron motion, for example, conformational changes in aerosols, shock fronts in

dense plasmas and plasmon oscillations. These goals could be achieved at upcoming high repetition-rate facilities such as the European XFEL.

Contact: Tais Gorkhover, taisgork@slac.stanford.edu
 Christoph Bostedt, cbostedt@anl.gov
 Jochen Küpper, jochen.kuepper@cfel.de

Authors

Tais Gorkhover, Sebastian Schorb, Ryan Coffee, Marcus Adolph, Lutz Foucar, Daniela Rupp, Andrew Aquila, John D. Bozek, Sascha W. Epp, Benjamin Erk, Lars Gumprecht, Lotte Holmegaard, Andreas Hartmann, Robert Hartmann, Günter Hauser, Peter Holl, Andre Hömke, Per Johnsson, Nils Kimmel, Kai-Uwe Kühnel, Marc Messerschmidt, Christian Reich, Arnaud Rouzée, Benedikt Rudek, Carlo Schmidt, Joachim Schulz, Heike Soltau, Stephan Stern, Georg Weidenspointner, Bill White, Jochen Küpper, Lothar Strüder, Ilme Schlichting, Joachim Ullrich, Daniel Rolles, Artem Rudenko, Thomas Möller and Christoph Bostedt

Affiliation details at:

<http://www.nature.com/nphoton/journal/v10/n2/full/nphoton.2015.264.html>

Original publication

'Femtosecond and nanometre visualization of structural dynamics in superheated nanoparticles', *Nature Photon.* 10, 93–97, (2016), DOI: 10.1038/nphoton.2015.264

References

1. A. Barty et al., 'Ultrafast single-shot diffraction imaging of nanoscale dynamics', *Nature Photon.* 2, 415–419 (2008).
2. H.N. Chapman et al., 'Femtosecond time-delay X-ray holography', *Nature* 448, 676–679 (2007).
3. D. Milathianaki et al., 'Femtosecond visualization of lattice dynamics in shock-compressed matter', *Science* 342, 220–223 (2013).
4. D. Amlund et al., 'Visualizing a protein quake with time-resolved X-ray scattering at a free-electron laser', *Nature Methods* 11, 923–926 (2014).
5. C. Bostedt et al. 'Ultrafast x-ray scattering of xenon nanoparticles: imaging transient states of matter', *Phys. Rev. Lett.* 108, 093401 (2012).
6. A. Guinier and G. Fournet, 'Small-Angle Scattering of X-Rays', *Structure of Matter series*, Wiley, (1955).

Matter and light, unite.

Collective strong coupling of X-rays and matter

One of the central tenets of quantum optics is the demonstration of the so-called strong coupling regime, whereby an excitation of matter and a mode of the electromagnetic field exchange a photon periodically in time. This regime is a precondition for many future applications in quantum optics, both applied and for basic research. It might, for example, be used to observe nonlinearities even at relatively low intensities [1]. Strong coupling has been achieved for a variety of systems and energy ranges, but until now not with X-rays. We have, for the first time, obtained unambiguous evidence for the strong coupling of hard X-rays and the nuclear resonance of ^{57}Fe in a so-called nuclear optical lattice.

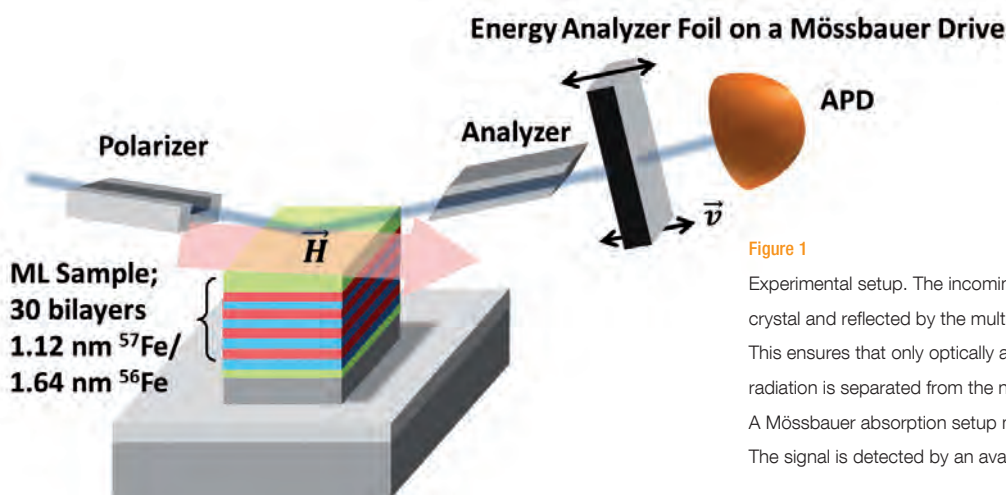


Figure 1

Experimental setup. The incoming radiation is polarised by a silicon channel cut crystal and reflected by the multilayer, which is subject to an external magnetic field. This ensures that only optically active transitions are excited. The resonantly scattered radiation is separated from the non-resonantly scattered by the analyser crystal. A Mössbauer absorption setup moved with velocity v is used for energy discrimination. The signal is detected by an avalanche photodiode (APD).

The usual route to strong coupling is to insert the matter to be excited resonantly into a cavity, which usually consists of two mirrors [1]. A good cavity restricts the interaction with the light to the one mode allowed by the cavity; furthermore, the intensity of the light within the cavity is large, leading to an enhanced interaction. The strong interaction leads to the coupling of two degrees of freedom; two normal modes form, which are superpositions of the uncoupled components of the system. If the cavity is probed, for instance by monitoring its reflectivity or transmissivity, its spectral signature shows two dips, which are detuned from the sample resonance and the cavity mode. Upon varying the detuning between cavity mode and resonance, it turns out that the dips undergo a very well-known anti-crossing dispersion; the minimal distance between the branches of the dispersion relation is given by the interaction strength.

X-ray cavities usually consist of thin-film multilayers sputter-deposited on a silicon wafer [2-5]. Two outer layers called the cladding layers sandwich a core layer into which an ultrathin

(~ 1 nm) layer of the resonant material is embedded. Cladding layers are chosen from high-Z materials such as platinum or palladium, while the core is almost always carbon. The standard resonant material is ^{57}Fe , which has a nuclear resonance at 14.41 keV with a linewidth of 4.7 neV.

Unfortunately, fabricating a cavity of sufficient quality to reach the strong coupling regime is not possible yet in the X-ray range. Even in the angular range of grazing incidence, where the thin-film multilayer sketched above displays cavity-like behaviour, the reflectivity of the cladding mirrors is ~ 95 % only. Compared to the reflectivity achieved for microwave and visible light cavities of > 99.999 % this is not sufficient. The problem is rooted in the fact that the spectral width of the cavity is much larger than the coupling strength. Essentially, the two dispersive dips mentioned above cannot be resolved [2, 4].

The solution lies in pioneering a new kind of nanostructure, a so-called nuclear optical lattice. An optical lattice is a system

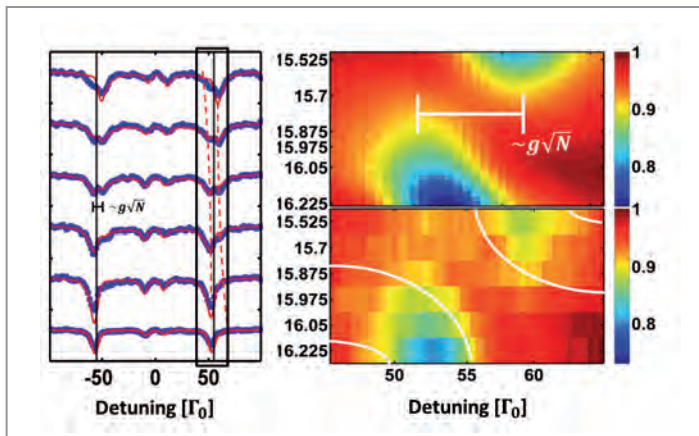


Figure 2

Experimental data. On the left, the spectra for six different angles are shown. There are four optically active transitions, each of which undergoes an anti-crossing, as indicated by the red-dashed lines, which form a guide to the eye. Blue dots are the data, red lines simulation. The spectra are vertically displaced for better visibility. The range indicated by the black box is plotted on the right hand side, with the intensity given in the colourmap; the background baseline is normalised to one. The upper right panel shows simulations, the lower shows the data. The white bar in the upper panel indicates the dip distance which gives the collective coupling strength. The white lines in the lower bar indicate the edges of the photonic band gaps.

well-known to laser physicists [6]. A laser beam reflected from a mirror will form a standing wave. In the nodes of this standing wave atoms can be trapped, forming a crystal-like regular array, which can be used as an artificial, tunable solid-state system. We implement this sort of device by sputter-depositing alternating layers of ^{57}Fe and ^{56}Fe on a substrate. As explained above, ^{57}Fe has a strong electromagnetic nuclear resonance at 14.41 keV, while the ^{56}Fe isotope has not. Thus, the multilayer's electronic index of refraction is homogeneously that of a solid block of iron. Since for X-rays the index of refraction is almost identical to one, this renders the material equivalent to an array of resonant atoms without any non-resonant contributions to the scattering contrast.

Our interest in this nuclear optical lattice lies in its unique spectroscopic properties. Like all periodic materials, the

multilayer shows a photonic band gap. This band gap leads to the reflection of incident light whose energy is within the band gap. Unlike non-resonant materials with a photonic band gap, the nuclear optical lattice's band gap exhibits peculiar spectroscopic signatures. The dispersion of the band gap mimics the polaritonic anti-crossing which is the tell-tale sign of strong coupling between light and matter.

The present study was performed at the Nuclear Resonance Beamline ID18 of the European Synchrotron Radiation Facility (ESRF). To observe the resonant dispersion relation, we measured the energy-dependent reflectivity of a sample consisting of 30 periods of 1.6 nm ^{56}Fe / 1.1 nm ^{57}Fe . The energy discrimination was performed with a resonant stainless steel absorption foil mounted on a Mössbauer drive, a device which Doppler detunes the energy of the single Mössbauer absorption line of the foil. A centrepiece of the experiment was a high-purity polarimetry setup [7], fashioned by collaborators from the Friedrich-Schiller-Universität Jena, which almost perfectly suppressed the unwanted but ubiquitous electronic scattering. The setup is shown in Fig. 1 and the results are shown in Fig. 2. A quantum theoretical model reveals that indeed the anti-crossing can be traced back to the strong coupling of the collective array of nuclei and the incoming and outgoing light modes. The physics behind the system is almost identical to that of an ensemble of atoms strongly coupled to a cavity mode.

The experiment is the latest in a series of recent successes of X-ray quantum optics [2-5]. For the first time an artificial crystal was used and the obtained results encourage the future use of similar systems to advance the coherent control of X-rays via quantum optics. As an example, Bragg reflections of a natural crystal that includes atoms with electronic resonances might be examined for evidence of strong light-matter coupling. Also, the effect of strong coupling on the quantum statistics of the reflected light might be observed.

Contact: Ralf Röhlsberger, ralf.roehlsberger@desy.de

Authors

Johann Haber¹, Kai S. Schulze^{2,3}, Kai Schlage¹, Robert Loetzsch^{2,3}, Lars Bocklage¹, Tatiana Gurieva¹, Hendrik Bernhardt^{2,3}, Hans-Christian Wille¹, Rudolf Ruffer⁴, Ingo Uschmann^{2,3}, Gerhard G. Paulus^{2,3} and Ralf Röhlsberger¹

1. Deutsches Elektronen-Synchrotron DESY, Hamburg, Germany
2. Helmholtz-Institut Jena, Jena, Germany
3. Institut für Optik und Quantenelektronik, Friedrich-Schiller-Universität Jena, Jena, Germany
4. European Synchrotron Radiation Facility ESRF, Grenoble, France

Original publication

'Collective Strong coupling of X-rays and nuclei in a nuclear optical lattice', *Nature Photonics* 10, 445 (2016). DOI:10.1038/nphoton.2016.77

References

1. M.G. Raizen, L.A. Orozco, M. Xiao, T.L. Boyd and H.J. Kimble, 'Squeezed-state generation by the normal modes of a coupled system', *Phys. Rev. Lett.* 59, 198 (1987).
2. R. Röhlsberger, K. Schlage, B. Sahoo, S. Couet and R. Ruffer, 'Collective Lamb shift in single-photon superradiance', *Science* 328, 5983 (2010).
3. R. Röhlsberger, H.-C. Wille, K. Schlage and B. Sahoo, 'Electromagnetically induced transparency with resonant nuclei in a cavity', *Nature* 482, 199 (2012).
4. K.P. Heeg, C. Ott, D. Schumacher, H.-C. Wille, R. Röhlsberger, T. Pfeifer and J. Evers, 'Interferometric phase detection at x-ray energies via Fano resonance control', *Phys. Rev. Lett.* 114, 207401 (2015).
5. K.P. Heeg, J. Haber, D. Schumacher, L. Bocklage, H.-C. Wille, K.S. Schulze, R. Loetzsch, I. Uschmann, G.G. Paulus, R. Ruffer, R. Röhlsberger and J. Evers, 'Tunable Subluminal Propagation of Narrow-band X-Ray Pulses', *Phys. Rev. Lett.* 114, 203601 (2015).
6. G. Birkel, M. Gatzke, I.H. Deutsch, S.L. Rolston and W.D. Phillips, 'Bragg Scattering from Atoms in Optical Lattices', *Phys. Rev. Lett.* 75, 2823 (1995).
7. B. Marx, K.S. Schulze, I. Uschmann, T. Kämpfer, R. Löttsch, O. Wehrhan, W. Wagner, C. Dettlefs, T. Roth, J. Härtwig, E. Förster, T. Stöhlker and G.G. Paulus, 'High-Precision X-Ray Polarimetry', *Phys. Rev. Lett.* 110, 254801 (2013).

Live-view of catalyst degradation at the nanometre-scale.

Tracking the sintering of nanoparticles under reaction conditions

Catalysts consist of noble metal nanoparticles dispersed on oxide carriers. The harsh reaction conditions tend to gradually alter the catalyst's original texture, leading to a reduction of its efficiency. Sintering, the coalescence of nanoparticles into larger ones, is a major cause of catalyst deactivation. Here, we combined high energy grazing incidence X-ray diffraction, X-ray reflectivity and *in situ* mass spectrometry to study the composition-dependent sintering of platinum-rhodium alloy nanoparticles on aluminium oxide during CO oxidation at near-ambient pressures. We conclude that the initial particle shape, which we found to be a function of platinum-rhodium composition, has an essential impact on the particles' sinter resistance.

Catalysts are materials which accelerate the rate of a desired chemical reaction without being consumed. They are employed in chemical industry for the production of fine chemicals and find wide applications in gas sensors, fuel cells and automotive exhaust control.

The oxidation of carbon monoxide into less harmful carbon dioxide ($2\text{CO} + \text{O}_2 \rightarrow 2\text{CO}_2$) represents a major catalytic reaction performed in car catalysts. To increase the effective surface area for the reaction to take place, the catalyst materials (platinum (Pt), rhodium (Rh), palladium (Pd): Monometals and alloys) are dispersed in the form of nanoparticles on highly branched oxides, mainly on Al_2O_3 . The exposure to various gases at ambient pressures and to elevated temperatures (typically 800 – 1000 K) under reaction conditions usually leads to a gradual merging of the nanoparticles [1]. This so-called sintering leads to a loss of the catalyst surface area and accordingly to a gradual catalyst deactivation, which is a major economic concern.

To improve catalyst efficiency and lifetime a detailed understanding of the atomic-scale processes that take place under realistic reaction conditions is required. A comprehension of the sintering mechanisms, which would pave the way towards sintering reduction, is lacking so far. Much attention has in recent years been paid to the investigation of alloy nanoparticles, as they constitute promising systems for tailoring catalyst selectivity, activity and stability [2-5].

The present study combined grazing incidence X-ray diffraction and X-ray reflectivity at a high photon energy ($E = 78.7\text{ keV}$) along with *in situ* mass spectrometry to unravel the composition- and hence shape-dependent sintering behaviour of $\alpha\text{-Al}_2\text{O}_3(0001)$ -supported Pt-Rh alloy nanoparticles during CO oxidation at near-ambient pressures ($p_{\text{tot}} = 200\text{ mbar}$, $T = 550\text{ K}$). The measurements were carried out at beamline

ID15A at the ESRF using a dedicated *in situ* catalysis chamber [6].

The experimental strategy is depicted in Fig. 1: The sample was mounted inside the chamber's beryllium dome which constitutes a flow reactor for catalysis. Leaking to a residual gas analyser yielded immediate information on its gas composition including the reaction product CO_2 . The sample contained stripes of particles with different Pt-Rh compositions

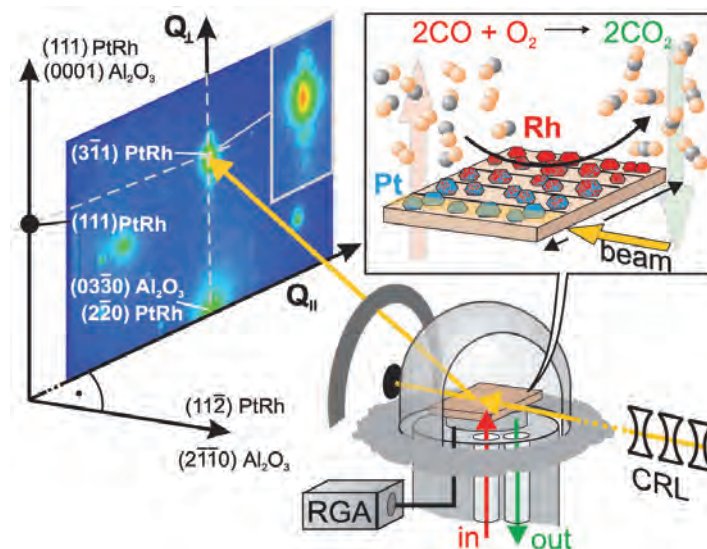
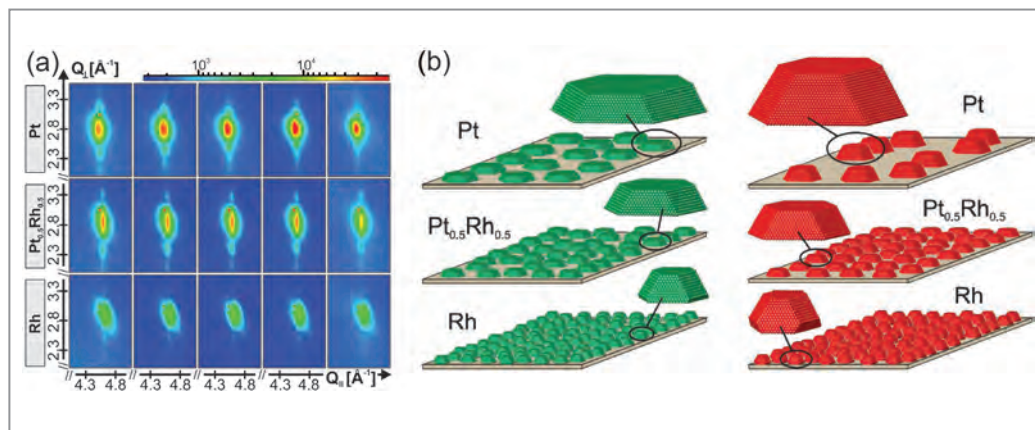


Figure 1

Experimental strategy: The chamber's beryllium dome acts as catalysis flow reactor, its gas composition, including reaction products, is monitored by a residual gas analyser (RGA). An X-ray beam collimated by compound refractive lenses (CRL) probes the individual particle stripes of varying Pt-Rh composition while large area snapshots of reciprocal space are taken with a 2D detector. They include the particle $(3\bar{1}1)$ Bragg peak and its Laue oscillations (see map and its inset for the case of pure Pt) containing quantitative information on the respective particle structure. This figure is licensed under a Creative Commons Attribution 4.0 International License.

Figure 2

(a) Series of 2D close-ups on the particle (3 $\bar{1}$ 1) Bragg peaks shown for selected Pt-Rh compositions taken in the transition to increasingly higher catalytic activity conditions (from left to right). (b) Quantitative particle shapes as deduced from the 2D maps for the respective compositions before (green) and after (red) sintering. The particle coverage on the substrate surface obtained from the X-ray reflectivity data is also indicated. This figure is licensed under a Creative Commons Attribution 4.0 International License.



which were probed individually using a highly collimated X-ray beam. For all Pt-Rh compositions the as-prepared particles featured a height of 20 Å but differed greatly in diameter with values ranging from 125 Å (pure Pt) down to 50 Å (pure Rh). The scattered X-ray signals were detected with a 2D detector, which probed a large area in reciprocal space with a single snapshot due to the high photon energy. The maps contained the respective particle (3 $\bar{1}$ 1) Bragg peaks along with distinct Laue oscillations. As was shown in the framework of our study, these intensity modulations contain information on the quantitative particle shape and were used as *in situ* probe for tracking the particle shape changes during sintering.

In the course of the experiment, the O₂ flow was stepwise increased while the CO flow was kept constant, which resulted in a stepwise rise in CO₂ productivity. Figure 2a reveals close-ups on the particle (3 $\bar{1}$ 1) Bragg peaks for selected Pt-Rh compositions measured in this transition. In the case of the pure Pt particles, the Laue oscillations moved progressively closer towards the Bragg peak, indicating tremendous vertical sintering. The quantitative map analysis revealed that the Pt particles almost doubled in height while their diameter remained relatively constant. Hence, the initially flat-shaped Pt particles adopted a more 3-dimensional shape. Our X-ray reflectivity data showed that this vertical particle growth came along with a decrease in particle

coverage from 60 % to 35 %, implying that the material needed for the vertical growth was rendered from surrounding particles.

A key result of our investigation is that a suppression of the Laue oscillation movement and hence of vertical sintering scales with the Rh content inside the alloy particles. Figure 2a reveals that in the case of Pt_{0.5}Rh_{0.5} and pure Rh particles the Laue oscillation signals almost retained their positions. Also their particle diameter stayed constant throughout the experiment, suggesting that their 3-dimensional particle shape features a high sinter-resistance. In line with these findings, the particle coverage of the Rh-rich particles was concluded to remain constant. The scenarios of the interplay between the particle of the interplay between the particle shape and coverage changes for different Pt-Rh compositions are summarised in Fig. 2b.

In conclusion, our data suggest a novel non-classical Ostwald ripening mechanism. Therein, Pt-rich particles overcome their initial flat shapes in which they are kinetically trapped after growth by the energy released in the CO oxidation reaction and adopt more stable 3-dimensional equilibrium shapes. Adding Rh as alloy constituent in the first place results in particles growing with a 3-dimensional equilibrium shape and constitutes a promising route towards sintering reduction.

Contact: Uta Hejral, uta.hejral@sljus.lu.se

Andreas Stierle, andreas.stierle@desy.de

Authors

Uta Hejral^{1,2,3}, Patrick Müller^{1,2,3}, Olivier Balmes^{4,5}, Diego Pontoni⁵ and Andreas Stierle^{1,2,3}

1. Deutsches Elektronen-Synchrotron DESY, NanoLab, Hamburg, Germany
2. Universität Hamburg, Fachbereich Physik, Hamburg, Germany
3. Universität Siegen, Fachbereich Physik, Siegen, Germany
4. MAX IV Laboratory, Lund, Sweden
5. ESRF - The European Synchrotron, Grenoble, France

Original publication

'Tracking the shape-dependent sintering of platinum-rhodium model catalysts under operando conditions', *Nature Communications* 7, 10964 (2016). DOI: 10.1038/ncomms10964

References

1. C. H. Bartholomew, 'Mechanisms of catalyst deactivation', *Appl. Catal. A Gen.* 212, 17-60 (2001).
2. J. Y. Park, Y. Zhang, M. Grass, T. Zhang and G. A. Somorjai, 'Tuning of Catalytic CO Oxidation by Changing Composition of Rh-Pt Bimetallic Nanoparticles', *Nano Lett.* 8, 673-677 (2008).
3. A. Cao and G. Veszteg, 'Exceptional high-temperature stability through distillation-like self-stabilization in bimetallic nanoparticles', *Nat. Mater.* 9, 75-81 (2010).
4. J. Greeley and M. Mavrikakis, 'Alloy catalysts designed from first principles', *Nat. Mater.* 3, 810-815 (2004).
5. F. Tao, S. Zhang, L. Nguyen and X. Zhang, 'Action of bimetallic nanocatalysts under reaction conditions and during catalysis: evolution of chemistry from high vacuum conditions to reaction conditions', *Chem. Soc. Rev.* 41, 7980-7993 (2012).

Negative piezoelectricity of poly(vinylidene-fluoride).

Revealing the role of microstructure

Piezoelectricity describes interconversion between electrical charge and mechanical strain. The proportionality constant is positive for all piezoelectric materials, with the exception of the ferroelectric polymer PVDF. Reported explanations of this negative coefficient consider exclusively the crystalline or the amorphous part of the semi-crystalline polymer. To distinguish between these conflicting interpretations, we performed *in situ* dynamic X-ray diffraction measurements on P(VDF-TrFE) capacitors. According to our quantitative analysis an additional contribution, due to electromechanical coupling between the intermixed crystalline and amorphous regions, is operative. Our findings tie the counter-intuitive negative piezoelectric response of PVDF and its copolymers to the dynamics of their composite microstructure.

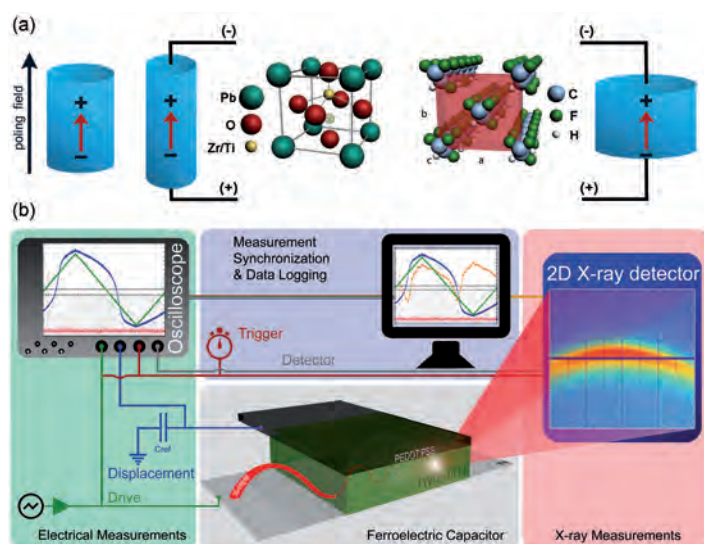


Figure 1

(a) Piezoelectricity. Schematic illustration of the counter-intuitive piezoelectric behaviour of PVDF and its copolymers. Upon application of an electric field these materials contract, exhibiting a negative piezoelectric coefficient (right). Common piezoelectric materials, such as PZT, have a positive piezoelectric coefficient and expand (left).
(b) Dynamic *in situ* XRD measurement. An AC voltage is applied over a P(VDF-TrFE) capacitor, triggering the measurement of the 2D X-ray diffraction pattern under grazing incidence synchrotron X-ray irradiation. The electrical response of the capacitor as well as the detector timing data are recorded by the oscilloscope of the Sawyer-Tower setup.

The direct piezoelectric effect is observed as a change in surface charge density of a material in response to an external mechanical stress. The thermodynamically equivalent inverse effect is a change in dimension upon applying an electric field. Typically, the electro-mechanical coupling constants are positive; piezoelectric materials expand when an applied electric field is aligned with the poling direction. The only exceptions are the ferroelectric polymer PVDF and its copolymers with trifluoroethylene P(VDF-TrFE), which show an

unusual negative piezoelectric effect. Counterintuitively, these polymers contract in the direction of the applied electric field, as depicted in Fig.1a. Two contradicting microscopic models have been proposed. The reported explanations consider exclusively contraction of either the crystalline or the amorphous part of these semi-crystalline polymers [1,2]. Curiously, each appears to fully account for the experimentally observed piezoelectric response.

To reveal the microscopic origin of the negative piezoelectric effect and resolve the controversy, the change in lattice constant has to be measured as a function of electric field. To selectively address the contribution of the crystalline part, we performed *in situ* X-ray diffraction measurements on P(VDF-TrFE) capacitors, a severe experimental challenge. The minute changes can only be determined dynamically, by measuring the diffracted X-ray intensity as a function of a time-varying electric field. For a quantitative description of the piezoelectric effect the changes in lattice constant must be measured simultaneously with the ferroelectric polarization, yielding constraints on data acquisition and synchronisation. The relatively short range order and small atomic form factors of the polymer's constituent atoms make high intensity X-rays from a synchrotron a prerequisite for a decent signal to noise ratio.

Grazing incidence X-ray diffraction measurements were thus performed on P(VDF-TrFE) capacitors aligned in the high precision 6-circle diffractometer at the High Resolution Diffraction Beamline P08 at PETRA III. The experiment is schematically described in Fig.1b. An AC voltage was applied over the capacitor and the electric displacement was measured as a function of time using an oscilloscope. Crucially, the X-ray diffractogram was measured as a function of time, too, using a time resolved 2D X-ray detector [3]. Thousands of recorded grazing incidence scattering images were azimuthally

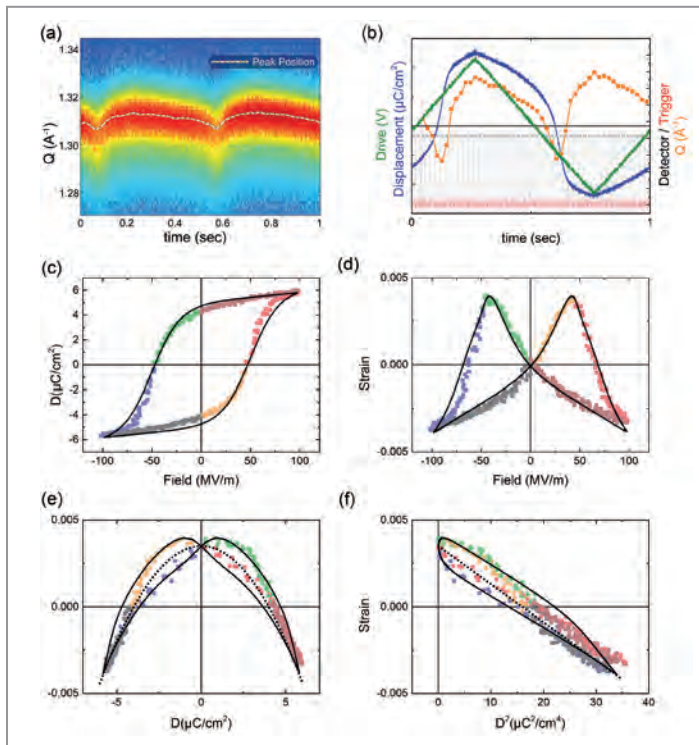


Figure 2

Data acquisition and analysis. (a) An example of a processed X-ray signal, showing the scattering vector, Q , from a capacitor driven with a 1 Hz triangular waveform. A clear oscillation around 1.3 \AA^{-1} , the characteristic for the combined (110)/(200) diffraction of the monoclinic low temperature phase of P(VDF-TrFE), is observed. (b) Recorded data from the oscilloscope, showing the drive signal (green) and the displacement current of the ferroelectric capacitor (blue). The trigger signal (red) starts the X-ray exposures, mirrored by the grey lines. The synchronised diffraction data are presented in orange. (c) Ferroelectric displacement as a function of applied electric field, fitted with an empirical model [5]. (d,e) Strain as a function of field and displacement. (f) Strain as a function of displacement squared. The dotted lines are fits when the strain is a function of the displacement squared [1]. The black fully drawn lines are our fit, including the additional field-dependent contribution to the piezoelectric strain.

integrated and exposures pertaining to the same time-bin relative to the driving frequency were averaged. An example of the signal after integration/binning and the simultaneously collected electrical data are shown in Fig. 2a,b.

Following data synchronisation, the electric displacement and the strain, calculated as the relative change in lattice constant, were plotted as a function of electric field (Fig. 2c,d). The strain measurement shows the negative longitudinal piezoelectric effect; the unit cell contracts when an electric field is applied in the direction of the polarization. The strain as a function of electric field shows a typical butterfly shape.

To understand the origin of the negative piezoelectric effect the strain measurements have to be quantitatively interpreted. The previously widely used formalism, in which the strain is a function of the displacement squared, could only describe data in a limited field range [4]. The strain as a function of displacement and displacement squared should then be a hysteresis-free parabola and straight line, respectively, as indicated in Fig. 2e,f

by the dotted lines. The experimental data, however, do show hysteresis; the piezoelectric effect is dominated by the change in lattice constant but, surprisingly, it cannot be accounted for by the response of the crystalline part alone. For the analysis of the lattice strain measurements a linear field contribution to the strain has to be included. This additional term becomes increasingly important with increasing electric field and introduces the experimentally observed hysteresis. The full reported data set can then unambiguously and quantitatively be described (solid lines in Fig. 2e,f). The extracted total piezoelectric coefficient is -31 pm/V , similar to previously reported values [1].

Our quantitative analysis shows that the major contribution to the piezoelectric response is a previously overseen electromechanical coupling between the intermixed crystalline lamellae and amorphous regions; changes in lattice constant are coupled to volume changes in the amorphous regions and vice versa. We support our analysis by showing that the effect depends on the microstructure of the polymer by varying the crystallinity. These findings connect the counterintuitive negative piezoelectric response in ferroelectric polymers to the dynamics of their intricate microstructure and thus have technological implications for organic transducers and actuators. The methodology used can also be transferred to the inorganic counterparts.

Contact: Ilias Katsouras, ilias.katsouras@tno.nl
 Martin M. Nielsen, mmee@fysik.dtu.dk
 Dago M. de Leeuw, deleeuw@mpip-mainz.mpg.de

Authors

Ilias Katsouras^{1,2}, Kamal Asadi¹, Mengyuan Li^{3,4}, Tim B. van Driel⁵, Kasper S. Kjær⁵, Dong Zhao¹, Thomas Lenz¹, Yun Gu⁵, Paul W.M. Blom¹, Dragan Damjanovic⁶, Martin M. Nielsen⁵ and Dago M. de Leeuw^{1,7}

1. Max-Planck Institute for Polymer Research, Mainz, Germany
2. Holst Centre, High Tech Campus 31, Eindhoven, The Netherlands
3. Zernike Institute for Advanced Materials, University of Groningen, Groningen, The Netherlands
4. Electronic Information Industry, CCID Thinktank, China Center for Information Industry Development No. 27 Wanshou Road, Beijing, China
5. Department of Physics, Technical University of Denmark, Copenhagen, Denmark
6. Ceramics Laboratory, Swiss Federal Institute of Technology – EPFL, Lausanne, Switzerland
7. King Abdulaziz University, Abdullah Sulayman, Jeddah, Saudi Arabia

Original publication

'The negative piezoelectric effect of the ferroelectric polymer poly(vinylidene-fluoride)', *Nature Materials* 15, 78–84 (2016). DOI:10.1038/nmat4423

References

1. V. S. Bystrov et al., 'Molecular modeling of the piezoelectric effect in the ferroelectric polymer poly(vinylidene fluoride) (PVDF)', *J. Mol. Model.* 19, 3591–3602 (2013)
2. Y. Wada and R. Hayakawa, 'A model theory of piezo- and pyroelectricity of poly(vinylidene fluoride) electret', *Ferroelectrics* 32, 115–118 (1981).
3. T. Ejdrup et al., 'Picosecond time-resolved laser pump/X-ray probe experiments using a gated single-photon-counting area detector', *J. Synchrotron Radiat.* 16, 387–390 (2009).
4. T. Furukawa and N. Seo, 'Electrostriction as the origin of piezoelectricity in ferroelectric polymers', *Jpn. J. Appl. Phys.* 29, 675–680 (1990).
5. J. J. Brondijk, K. Asadi, P. B. W. Blom and D. M. de Leeuw, 'Physics of organic ferroelectric field-effect transistors', *J. Polym. Sci. B*, 50, 47–54 (2012).

Ironing out the mystery of Earth's magnetic field.

Direct measurements of thermal conductivity in solid iron at planetary core conditions

Knowledge of transport properties of minerals and melts inside Earth holds a key to answering important questions about its interior, regarding energy balance of the core, geodynamo, thermal structure of the outer core, or age of the inner core. Attempts to describe thermal transport in Earth's core have been problematic, with predictions of high thermal conductivity at odds with traditional geophysical models and direct evidence for a primordial magnetic field in the rock record. We combined laser-heated diamond anvil cell technique with finite element modelling of transient heat transfer to directly measure the thermal conductivity of iron up to core-mantle boundary conditions, yielding conductivity values much lower than previously calculated.

Iron, as a main constituent of the terrestrial cores, has become a frequent subject of high pressure-temperature studies. In the Earth's core, thermal conductivity of iron is closely related to the heat flux conducted down the adiabatic gradient, and hence the energy available to support the geodynamo. However, recently, the heat transport in the Earth's core has been revisited in light of new high thermal conductivity values for iron derived from theoretical calculations [1,2]. The conductivity values found in theory (> 150 W/m/K) are raising questions over how the geodynamo evolved - a problem that has been called the 'new core paradox' [3]. The conventional view is that the convection in the liquid outer core has provided most of the energy for the geodynamo for at least 3.4 billion years [4]. Even before the nucleation of the inner core, thermal convection was solely sufficient to drive the magnetic field. With high thermal conductivity values, however, the numerical simulations have problems to explain a working dynamo throughout the entire Earth's history.

There is a demand to investigate the transport properties of iron at high pressures and temperatures with alternative methods. We adopted a flash heating method, which is a technique being used for thermal conductivity measurements. In such flash heating measurements, one side of a thin opaque sample is heated by laser pulses, whereas a detector measures the temperature response of the sample from the other side. In a diamond anvil cell (DAC), this has been realized by preheating an iron foil by continuous wave near-infrared laser beams from both sides. An additional pulsed laser beam heats one side of the sample in order to create a thermal disturbance. The evolution of this disturbance was characterized by nano-second-resolved radiative temperature measurements using a streak camera coupled to a grating spectrograph which records the thermal incandescent history from both sides of the foil [5].

Temperature variations across the foil are modelled using time dependent finite element simulations of the laser-heated

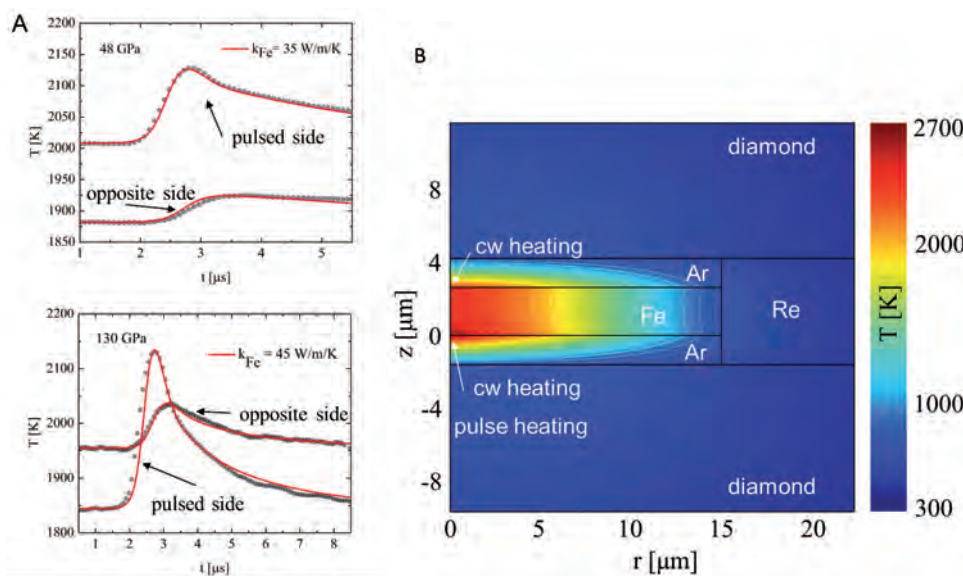


Figure 1
A) Measured temperature histories (grey) on the pulsed and opposite sides of the foil together with finite-element models (red) for best-fit thermal conductivity k of Fe, at 48 GPa and 130 GPa. B) Instantaneous temperature map of the modelled sample area at initiation of flash heating at 112 GPa, as a function of radial (r) and axial (z) position. Contour lines are isotherms.

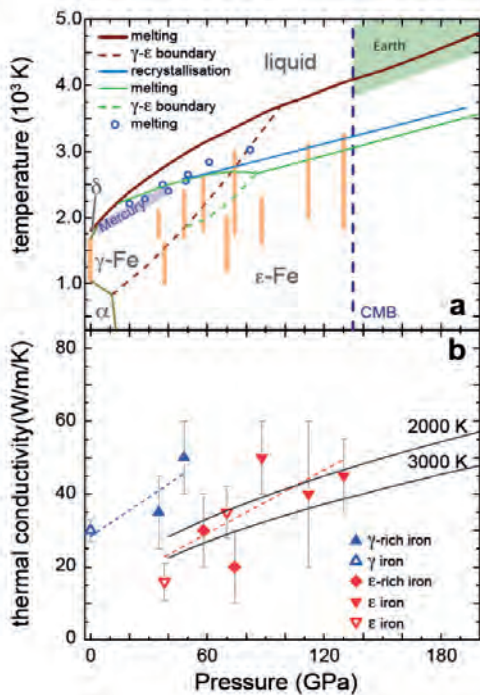


Figure 2

a) Phase diagram of Fe with conditions of the thermal conductivity measurements (orange) falling in the domain of the γ and ϵ phases. The shaded areas depict conditions of Earth's core and Mercury's core, with the vertical dashed line marking the pressure at Earth's core–mantle boundary (CMB).
 b) Thermal conductivity results from this study are shown as solid symbols. Prior direct thermal conductivity measurements on the γ phase and the ϵ phase are shown as open symbols. The dashed lines are linear fits to the results from the γ and ϵ domains, whereas solid lines are model values. Error bars include uncertainty (one standard deviation) and range of measurements.

DAC to determine the thermal conductivity of Fe samples (Fig. 1). Simulations were performed in several iterative steps in search of the best value for the thermal conductivity. Several datasets at different temperatures were analysed at pressures up to 130 GPa. A sample of platinum was also used at the same conditions for comparison [5]. Heat wave propagation across the Pt was much faster than for Fe, corresponding to a lower thermal diffusivity for Fe. Fe samples were also observed to sustain larger axial temperature gradients than the Pt samples, which is a direct manifestation of iron's lower thermal conductivity compared to Pt.

Platinum shows a general trend of increasing thermal conductivity with pressure and temperature, similar to its behaviour at ambient conditions. The thermal conductivity of Pt varies between 120 and 180 W/m/K [5]. Iron, in contrast, exhibits much more complex behaviour, strongly affected by phase transitions (Fig. 2). The γ -phase of iron (fcc structure), representative of Mercury's core, has thermal conductivity of 35 ± 10 W/m/K, similar to ambient pressure values in γ -Fe. This suggests that the thermal conductivity is not strongly dependent on the pressure at Mercury's core conditions. At pressure above 80 GPa, Fe is unambiguously in the hexagonal closed packed (hcp, ϵ) structure, as confirmed by X-ray diffraction performed at beamline P02.2 at PETRA III, and the conditions are approaching those at the Earth's core–mantle boundary. Modelling the pressure and temperature variations of the thermal conductivity values at 112 GPa, we find that the conductivity decreases with temperature and slightly increases with pressure. At the conditions of the outer core, slight extrapolation of the data yields thermal conductivity of the solid iron of 40 ± 10 W/m/K.

Addition of light-element impurities is expected to reduce conductivity by 10–40%, which yields thermal conductivity for Earth's liquid core between 18 and 45 W/m/K. In general, our

results are in agreement with the low end of previous estimates, in particular with the electrical resistivity measurements on shock compressed iron [6]. On the contrary, first principle calculations of transport properties [1, 2] and recent electrical resistivity measurements in the laser heated DAC [7] are 6–8 times larger than our values. This large discrepancy needs to be resolved in future, for example, by benchmarking the methods against simpler metals without any phase transitions.

The heat flux requirements for a convective early core are moderate for the values of thermal conductivities found in this study (2.2 – 5.5 terawatts). Later in the planet's history, after a solid inner core has formed, the core–mantle heat flux necessary to sustain a dynamo may be smaller, given that convection can be driven both compositionally and thermally. However, within our direct experimental constraints, there is no requirement that Earth's geodynamo ever existed in the absence of an inner core. Indeed, the planet's dynamo and its solid inner core may have co-existed since soon after the formation of Earth.

Contact: Zuzana Konôpková, zuzana.konopkova@xfel.eu

Authors

Zuzana Konôpková^{1*}, R. Stewart McWilliams², Natalia Gómez-Pérez³, Alexander F. Goncharov^{4,5}

1. Deutsches Elektronen-Synchrotron DESY, Hamburg, Germany.
 2. School of Physics and Astronomy and Centre for Science at Extreme Conditions, University of Edinburgh, Edinburgh, UK.
 3. Departamento de Geociencias, Universidad de Los Andes, Bogotá, Colombia.
 4. Key Laboratory of Materials Physics, Institute of Solid State Physics, Chinese Academy of Sciences, China.
 5. Geophysical Laboratory, Carnegie Institution of Washington, Washington DC, USA.
- * Present address: European XFEL GmbH, Schenefeld, Germany

Original publication

'Direct measurement of thermal conductivity in solid iron at planetary core conditions', *Nature* 534, 99–101 (2016). DOI:10.1038/nature18009

References

1. M. Pozzo, C. Davies, D. Gubbins and D. Alfe, 'Thermal and electrical conductivity of iron at Earth's core conditions', *Nature* 485, 355–358 (2012).
2. N. de Koker, G. Steinle-Neumann and V. Vlcek, 'Electrical resistivity and thermal conductivity of liquid Fe alloys at high P and T, and heat flux in Earth's core', *Proc. Natl. Acad. Sci.* 109, 4070–4073 (2012).
3. P. Olson, 'The new core paradox', *Science* 342, 431–432 (2013).
4. J. A. Tarduno, R. D. Cottrell, W. J. Davis, F. Nimmo and R. K. Bono, 'A Hadean to Paleoproterozoic geodynamo recorded by single zircon crystals', *Science* 349, 521–524 (2015).
5. R. S. McWilliams, Z. Konôpková and A. F. Goncharov, 'A flash heating method for measuring thermal conductivity at high pressure and temperature: application to Pt', *Phys. Earth Planet. Inter.* 247, 17–26 (2015).
6. Y. Bi, H. Tan and F. Jing, 'Electrical conductivity of iron under shock compression up to 200 GPa', *J. Phys. Condens. Matter* 14, 10849 (2002).
7. K. Ohta, Y. Kuwayama, K. Hirose, K. Shimizu and Y. Ohishi, 'Experimental determination of the electrical resistivity of iron at Earth's core conditions', *Nature*, 534, 95–98 (2016).

Magnetic field controlled charge density wave coupling in underdoped $\text{YBa}_2\text{Cu}_3\text{O}_{6+x}$

Interplay between superconductivity and charge order

The application of magnetic fields to layered cuprates suppresses their high-temperature superconducting behaviour and reveals competing ground states. In widely studied underdoped $\text{YBa}_2\text{Cu}_3\text{O}_{6+x}$ (YBCO), the microscopic nature of field-induced electronic and structural changes at low temperatures remains unclear. Using hard X-ray diffraction, we studied the high-field charge density wave (CDW) in YBCO. We find that a field of $B \sim 10$ T induces additional CDW correlations along the CuO chain (b -direction) only, leading to a three-dimensional ordered state along this direction at $B \sim 15$ T. The CDW signal along the a -direction is also enhanced the field, but does not develop an additional pattern of correlations. A magnetic field modifies the coupling between the CuO_2 bilayers in the YBCO structure, and causes the sudden appearance of the 3D CDW order. This observation provides an explanation to why some techniques report field-induced CDW order whereas others find charge order already in zero-field.

Charge density wave (CDW) correlations, that is, periodic modulations of the electronic charge density accompanied by a periodic distortion of the atomic lattice, have long been known to exist in underdoped La-based cuprate high-temperature superconductors [1]. More recently, it has been found that charge order is a universal property of underdoped high-temperature cuprate superconductors [2–4]. CDW correlations appear typically at temperatures well above the superconducting transition temperature T_c . Cooling through T_c suppresses the CDW and leads to a state, in which the superconducting and CDW order parameters are intertwined and competing.

The application of magnetic fields suppresses superconductivity. In the case of underdoped $\text{YBa}_2\text{Cu}_3\text{O}_{6+x}$ (YBCO), a number

of changes in electronic properties have been reported in the field range $B \sim 10 - 20$ Tesla. Here we investigated the CDW for propagation vectors along the a - and b -directions, allowing us to extend a pulsed-field measurement [7] and identify new field-induced anisotropies in the CDW. We also show that field-induced changes in the CDW can be associated with many of the anomalies observed in electronic properties, e.g. via thermal Hall and ultrasound measurements.

Our experiments used 98.5 keV hard X-ray synchrotron radiation from PETRA III. A 17 T horizontal cryomagnet was installed at the P07 beamline. Access to the $(h, 0, \ell)$ and $(0, k, \ell)$ scattering planes was obtained by aligning either the a - c axes or the b - c axes horizontally, with the c -axis approximately along the magnetic field and beam direction.

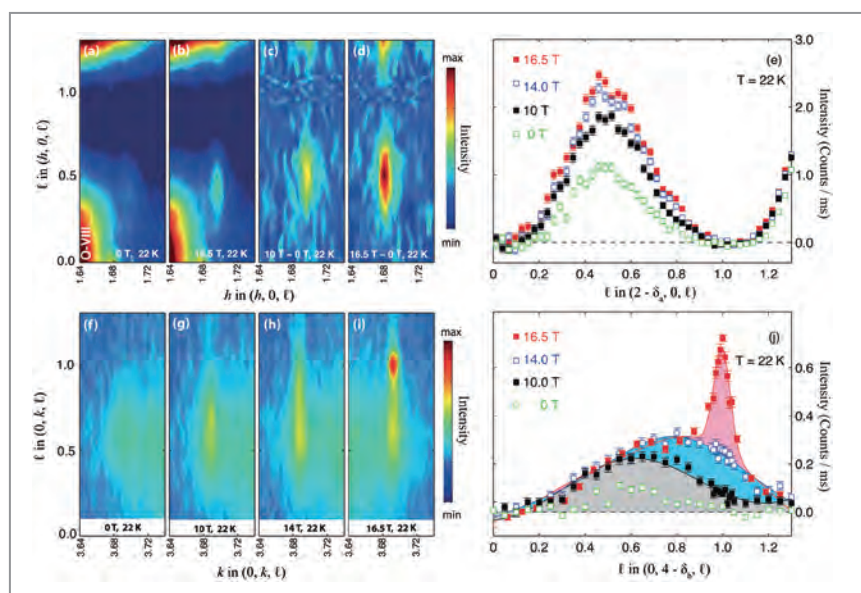


Figure 1

A magnetic field applied along the c -axis introduces new CDW correlations propagating along both CuO bond directions a and b in the CuO_2 planes. (a,b,f–i) Raw X-ray scattering intensity data for the $(h, 0, \ell)$ (a,b) and $(0, k, \ell)$ (f–i) planes for magnetic fields $0 \leq B \leq 16.5$ T. Strong features in (a,b) are due to CuO chain scattering. (c,d) Field-induced scattering for $(h, 0, \ell)$. (e,i) CDW intensity along lines $\mathbf{Q} = n\mathbf{a}^* + m\mathbf{b}^* \pm \mathbf{q}_{ab} + \ell\mathbf{c}^*$ isolated from data such as (a,b,f–i). The CDW intensity has been isolated by fitting peaks due to the CDW and other structural features to a series of h - or k -cuts through data such as (a,b,f–i). CDWs propagating along the a axis (a–e) within individual bilayers become stronger without changing phase relationship with neighbouring bilayers. Those propagating along the b axis (f–j) are enhanced by a magnetic field when neighbouring bilayers scatter in phase, which changes the profile in ℓ . The shaded areas in (j) show: weakly anti-correlated CDW (grey); 3D CDW precursor correlations (blue); and 3D CDW order (red).

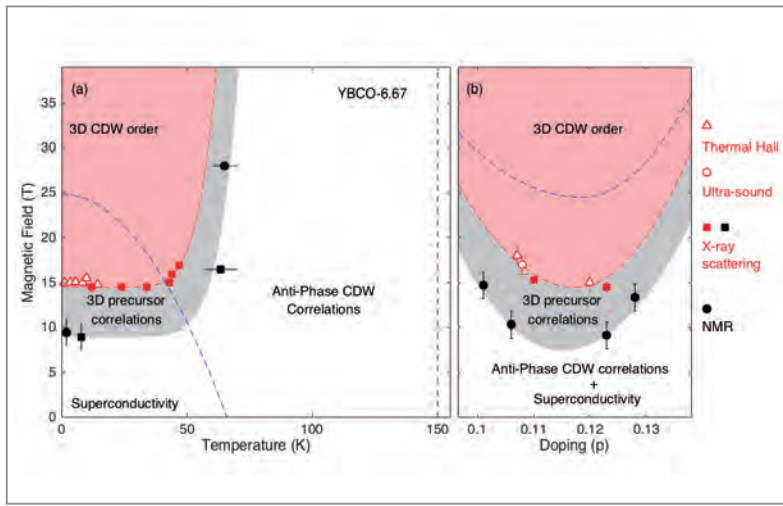


Figure 2

Magnetic field phase diagrams for YBCO. The pink shaded areas represent the regions where short-range 3D CDW order exists. Grey bands indicate the regions where growing 3D CDW precursor correlations are observed. (a) Temperature-magnetic field phase diagram. (b) Doping-magnetic field phase diagram. Solid red square points indicate the onset of a 3D CDW order with $\mathbf{q}_b = (0, \delta_b, 0)$ (see Fig. 1j). Triangles are the Fermi surface reconstruction onset determined from the thermal Hall coefficient. Solid black squares indicate the onset of growing in-plane CDW correlation lengths (3D precursor correlations). Dashed blue lines in (a,b) indicate the B_{c2} line. Solid black circles in (a,b) are derived from NMR [2]. The vertical black dashed line is the onset of weakly anti-phase CDW correlations [3,4]. Red circular and triangular points originate from ultrasound [5] and thermal Hall effect experiments, whereas the red squares are the field onset of $\mathbf{q}_b = (0, \delta_b, 0)$ found by X-ray diffraction.

YBCO shows a superposition of modulations localized near the CuO_2 bilayers, with basal plane components of their propagation vectors along both \mathbf{a} and \mathbf{b} : $\mathbf{q}_a = (\delta_a, 0, 0)$ and $\mathbf{q}_b = (0, \delta_b, 0)$ with correlation lengths up to $\xi_a \sim 70 \text{ \AA} \sim 20 a$. These give rise to scattering along lines in reciprocal space given by $\mathbf{q}_{\text{CDW}} = n\mathbf{a}^* + m\mathbf{b}^* + \ell\mathbf{c}^* \pm \mathbf{q}_{a,b}$, where n and m are integers. The distribution of the scattered intensity along ℓ depends on the relative phase of the CDW modulations in the bilayers stacked along the c -direction. In zero magnetic field, there is weak correlation of phases in neighbouring bilayers and we observe scattered intensity spread out along the \mathbf{c}^* direction, peaked at $\ell \approx 0.5 - 0.6$. This is illustrated by our X-ray measurements on $\text{YBCO}_{6.67}$ ($p = 0.123$, $T_c = 67 \text{ K}$ and ortho-VIII CuO -chain ordering), shown in Fig. 1a,f. Note that the strong scattering around $Q \sim (13/8, 0, 0)$ in Fig. 1a,b is due the CuO -chain ordering, which does not change with field, and can be subtracted, as in Fig. 1c,d. By taking cuts through the data we obtain the intensity of the CDW scattering versus ℓ for the \mathbf{q}_a and \mathbf{q}_b positions (Fig. 1e,j).

Figure 1 shows that the effect of applying a magnetic field is very different for the two components (\mathbf{q}_a and \mathbf{q}_b) of the CDW. For the \mathbf{q}_a component of the correlations (Fig. 1b), the rod of scattering becomes stronger with no discernible change in the ℓ width or position of the maximum, that is, the correlations simply become stronger. In contrast, for the \mathbf{q}_b correlations, (Fig. 1i) we see two qualitative changes. First, at $B \sim 10 \text{ T}$, the rod of diffuse scattering becomes broader in ℓ and its peak position begins to move to larger ℓ . Second, at $B \sim 15 \text{ T}$, a new peak (shaded pink and first reported in [2,4]) appears centred on $\ell = 1$, but only for the \mathbf{q}_b component. The new peak indicates that the sample has regions where the CDW modulation is in phase in neighbouring bilayers and is coherent in three spatial directions. These regions would have a typical length along the c -axis of $\xi_c \sim 47 \text{ \AA}$.

We studied this field-induced three-dimensional charge-density-wave ordering as a function of temperature and doping. This allows us to draw the B - T and doping- B phase diagrams shown in Fig. 2. In addition to the field-induced 3D CDW order we found that this effect has a precursor. The grey area in

Fig. 2 indicates the onset above which an enhanced in-plane CDW correlation length is found. These observations allowed an explanation as to why different techniques have reported different field-induced electronic reconstructions [2,5]. For future studies, a clarification as to whether this uni-directional ordering is compatible with the electronic reconstruction observed by quantum oscillations [6] would be of great interest.

Contact: Johan Chang, johan.chang@physik.uzh.ch
 Martin von Zimmermann, martin.v.zimmermann@desy.de
 Stephen Hayden, S.Hayden@bristol.ac.uk

Authors

J. Chang¹, E. Blackburn², O. Ivashko¹, A.T. Holmes³, N.B. Christensen⁴, M. Hückler⁵, Ruixing Liang^{6,7}, D.A. Bonn^{6,7}, W.N. Hardy^{6,7}, U. Rüttel⁸, M.v. Zimmermann⁹, E.M. Forgan² and S.M. Hayden⁹

1. Physik-Institut, Universität Zürich, Zürich, Switzerland.
2. School of Physics and Astronomy, University of Birmingham, Birmingham, UK.
3. European Spallation Source ERIC, Lund, Sweden.
4. Department of Physics, Technical University of Denmark, Kongens Lyngby, Denmark.
5. Condensed Matter Physics & Materials Science Department, Brookhaven National Lab, Upton, New York, USA.
6. Department of Physics & Astronomy, University of British Columbia, Vancouver, Canada.
7. Canadian Institute for Advanced Research, Toronto, Canada.
8. Deutsches Elektronen-Synchrotron DESY, Hamburg, Germany.
9. H. H. Wills Physics Laboratory, University of Bristol, Bristol, UK.

Original publication

'Magnetic field controlled charge density wave coupling in underdoped $\text{YBa}_2\text{Cu}_3\text{O}_{6+x}$ '
 Nature Communications 7, 11494 (2016). DOI:10.1038/ncomms11494

References

1. J. M. Tranquada et al., 'Evidence for stripe correlations of spins and holes in copper oxide superconductors', *Nature* 375, 561 (1995).
2. T. Wu et al., 'Magnetic-field-induced charge-stripe order in the high temperature superconductor $\text{YBa}_2\text{Cu}_3\text{O}_7$ ', *Nature* 477, 191–194 (2011).
3. G. Ghiringhelli et al., 'Long-range incommensurate charge fluctuations in $(\text{Y,Nd})\text{Ba}_2\text{Cu}_3\text{O}_{6+x}$ ', *Science* 337, 821–825 (2012).
4. J. Chang et al., 'Direct observation of competition between superconductivity and charge density wave order in $\text{YBa}_2\text{Cu}_3\text{O}_{6.67}$ ', *Nat. Phys.* 8, 871–876 (2012).
5. D. LeBoeuf et al., 'Thermodynamic phase diagram of static charge order in underdoped $\text{YBa}_2\text{Cu}_3\text{O}_7$ ', *Nat. Phys.* 9, 79–83 (2012).
6. N. Doiron-Leyraud et al., 'Quantum oscillations and the Fermi surface in an underdoped high- T_c superconductor', *Nature* 447, 565–568 (2007)
7. S. Gerber et al., 'Three-dimensional charge density wave order in $\text{YBa}_2\text{Cu}_3\text{O}_{6.67}$ at high magnetic fields', *Science* 350, 949–952 (2015).

Magnetic sensors custom-made.

Deposition procedure allows free adjustment of magneto-resistive multilayer properties

Magneto-resistive multilayer devices have revolutionized sensor and magnetic data storage technology but still they are restricted due to limitations of conventional magnetic multilayer design. We show that a new deposition procedure in oblique incidence can overcome these limitations and thus enables a free magnetic adjustment of the devices for the first time. This new approach allows us to precisely set the magnetisation axis and switching field of each individual layer in the multilayer stacks. Newly accessible, arbitrarily crossed magnetisation profiles form the basis for advanced, custom-made magneto-resistive sensor applications and allow for multiple addressable remanent states which can be advantageous for new magnetic memory applications.

Magnetic sensors – or more accurately, magneto-resistive sensors – are tiny, highly sensitive and efficient components that are all around us in our daily life. For example in cars they measure the speed of rotation of wheels and drive shafts and the angular position of steering wheels. In computers they are widely used as read heads to detect the information stored in magnetic hard drives. The magneto-resistive devices themselves can also be used as tiny magnetic data storage elements. The wide variety of applications demands that the sensors' functionalities can be tuned to fulfil the requirements of specific tasks.

The sensors are made up of microscopic stacks of alternating magnetic and non-magnetic layers, each just a few nanometres thick [1]. When an external magnetic field is applied, the magnetic orientation of the layers in the stack and thereby the electrical resistance changes. The discovery of this giant mag-

neto-resistive effect (GMR), for which Albert Fert and Peter Grünberg were awarded a Nobel Prize in 2007, has revolutionised sensor technology, but basic problems still persist: The magnetic field strength at which the sensor stack switches is largely fixed and the magnetic arrangement of the layers is restricted to axial configurations. As a consequence a flexible adjustment of the sensing functionality cannot be achieved so far.

We have developed a deposition procedure that allows to precisely adjust the field strength at which each individual magnetic layer in the sensor stack switches. The procedure which gives us full control of the magnetic properties of the layers is based on a fabrication process known as oblique incidence deposition, or OID [2]. In this way the coercive field value at which the switching of the magnetisation occurs can be accurately adjusted over a wide range by choosing the polar angle of deposition relative to the sample surface. This

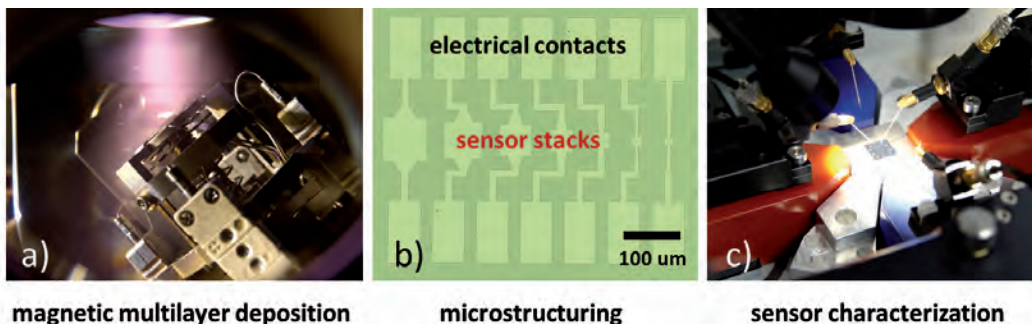


Figure 1

Fabrication and characterization of the magneto-resistive sensor stacks in three steps:

- The ultra-thin layer stacks are sputter deposited in a self-made UHV chamber optimized for oblique incidence deposition. The image shows a deposition at an angular orientation of 50° relative to the wafer surface normal which can be recognized by the purple coloured plasma of the deposition source.
- Micro and nanostructuring is performed to allow a realistic investigation of the multilayer properties for sensing applications.
- The magneto-resistive properties are measured in a custom-made setup. The image shows a vector magnet which is used to generate rotary magnetic fields and a set of metallic needles to measure the change of electrical resistance in the tiny layer stacks to determine their performance as speed sensors.

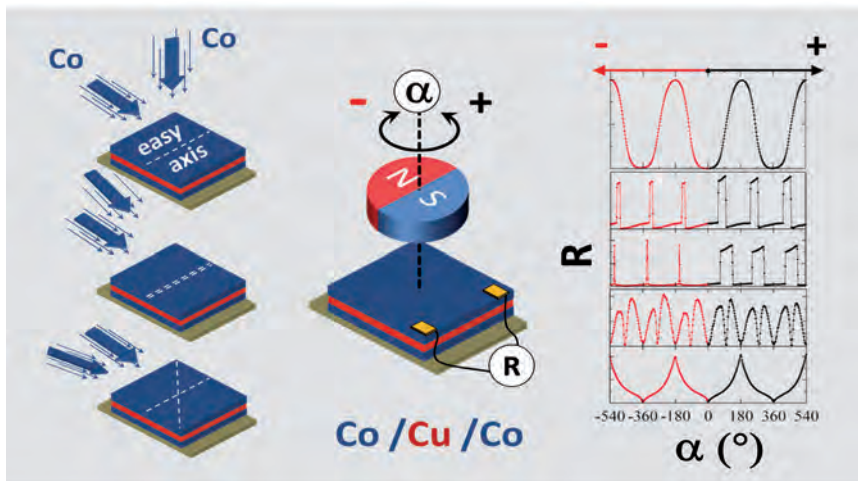


Figure 2

Example that demonstrates the potential of the OID technique for sensor applications. Depending on the OID deposition parameters of the cobalt layers (azimuthal and polar angle) different arrangements of the magnetisation axes and switching fields are realized in the tri-layer stack. They lead to a drastic difference in the GMR characteristic and are advantageous for different sensing applications. The image on the right shows GMR curves of Co/Cu/Co tri-layer structures of identical thickness which are used for detection of a rotary magnetic field.

flexibility, which is highly desirable for sensing applications, can hardly be achieved with any other technique.

In addition, the preferential direction of magnetisation of the individual layers, the so-called ‘easy axis’, can be chosen to lie in any orientation thus considerably expanding the possibilities available in conventional magnetic multilayer design as well as the functionality of the multilayer stacks. This applies for layers of any ferromagnetic material down to layer thicknesses of a few nanometres and lateral dimensions of a few 100 nm. As a result, a multitude of new sensor properties and applications can be easily achieved.

We have manufactured the multilayer stacks in a self-made vacuum deposition chamber specifically designed for this purpose (Fig. 1) and have then conducted experiments at the P01 beamline of PETRA III to precisely characterise the magnetic properties of each layer of the stacks produced. Applying nuclear resonant X-ray reflectometry [3] we were able to demonstrate that the new OID deposition routine permits arbitrarily complex and, most importantly, new magnetisation structures to be created in extended multilayer stacks with extremely high precision.

In terms of magneto-resistive sensors, this means that it is now possible to straightforwardly produce custom-made multilayer stacks having identical composition of materials and thicknesses but exhibiting very different and novel sensor characteristics. Thus a single OID deposition device is capable to produce various magneto-resistive elements for very different sensing applications, which drastically reduces the manufacturing costs.

The potential of the new deposition procedure is demonstrated by means of a GMR sensor for detection of rotary magnetic

fields (Fig. 2). The angular dependent change of electrical resistance in the simple Co/Cu/Co tri-layer structure under the influence of an external rotary magnetic field can be freely adjusted. Depending on the angular orientation of the sensor stack during deposition and thus arrangement of magnetisation axes and strength of magnetic switching fields, either a sinusoidal, peak-like or plateau-like GMR characteristic can be realised. Each of them is preferable for different sensing applications. Moreover, the tri-layer can be produced in such a way that one can detect the rotation frequency of the external magnetic field and, in contrast to existing devices, the direction of the rotation as well. These new features allow for monitoring rotational movements much more precisely than possible today, significantly improving the safety of motors, drive units and engine control systems, especially under extreme conditions.

Contact: Kai Schlage, kai.schlage@desy.de

Authors

Kai Schlage¹, Lars Bocklage^{1,2}, Denise Erb¹, Jade Comfort¹, Hans-Christian Wille¹ and Ralf Röhlsberger^{1,2}

1. Deutsches Elektronen-Synchrotron DESY, Hamburg, Germany
2. The Hamburg Centre for Ultrafast Imaging (CUI), Hamburg, Germany

Original publication

‘Spin-Structured Multilayers: A New Class of Materials for Precision Spintronics’, *Advanced Functional Materials* 26, 7423-7430 (2016), DOI: 10.1002/adfm.201603191

References

1. C. Chappert, A. Fert, F. N. Van Dau, *Nat. Mater.* 6, 813 (2007).
2. J. L. Bubendorff, S. Zabrocki, G. Garreau, S. Hajjar, R. Jaafar, D. Berling, A. Mehdaoui, C. Pirri, G. Gewinner, *Europhys. Lett.* 75, 119 (2006).
3. K. Schlage, R. Röhlsberger, *J. Electron Spectrosc. Relat. Phenom.* 189, 187 (2013).

Strongly correlated electrons meet topology.

Resonant X-ray scattering reveals 'all-in all-out' magnetic structure in $\text{Sm}_2\text{Ir}_2\text{O}_7$

Until recently, the fields of strongly correlated electrons and topology have been treated as distinct research areas. At the interface of the two subjects, a rich world of material phenomena could emerge and establish entirely new phases. However, candidate materials that exhibit both strong correlations and topological phenomena are rare, and prove to be challenging for theory and experiment. One example is the prediction of a correlated, topological Weyl semimetal state in antiferromagnetic pyrochlore iridates. To realize this state, the microscopic magnetic structure has to obey certain symmetries. Using resonant X-ray scattering, we studied the magnetic order and excitations of the pyrochlore iridate $\text{Sm}_2\text{Ir}_2\text{O}_7$ and confirmed that the conditions for a Weyl semimetal state are met.

The recently proposed, and shortly thereafter discovered, topological Weyl semimetal state in materials has attracted much interest from both theory and experiment [1-4]. In a Weyl semimetal, the low-energy physics close to the Fermi level is governed by the Weyl equation, a special case of the Dirac equation, which describes massless fermions with definite handedness [5]. While no elementary particles that behave as Weyl fermions have yet been observed, the low-energy quasi-particles emerging in a Weyl semimetal can mathematically closely resemble Weyl fermions.

Inside materials, the occurrence of Weyl fermions as quasi-particles hinges on stringent symmetry constraints. The key requirement is that there are non-degenerate, touching valence and conduction bands at the Fermi level, which implies that either time-reversal or inversion symmetry must be broken [6]. So far, all Weyl fermions have been found in materials with broken inversion symmetry, where electronic correlations are negligible. When electronic correlations become significant, magnetic order can be stabilised, which offers the possibility of a time-reversal symmetry breaking Weyl semimetal. The most promising candidate material is the family of pyrochlore iridates, $R_2\text{Ir}_2\text{O}_7$, where R is a rare-earth element. To realise a correlated Weyl semimetal state in pyrochlore iridates, the microscopic magnetic order has to preserve inversion symmetry. Theoretical studies have identified that the antiferromagnetic 'all-in all-out' structure would fulfil the required symmetries. In this all-in all-out magnetic structure, the magnetic moments either point all towards or away from the centre of the tetrahedra formed by the iridium ions (Fig. 1).

However, despite substantial experimental effort, the microscopic magnetic order of pyrochlore iridates has remained

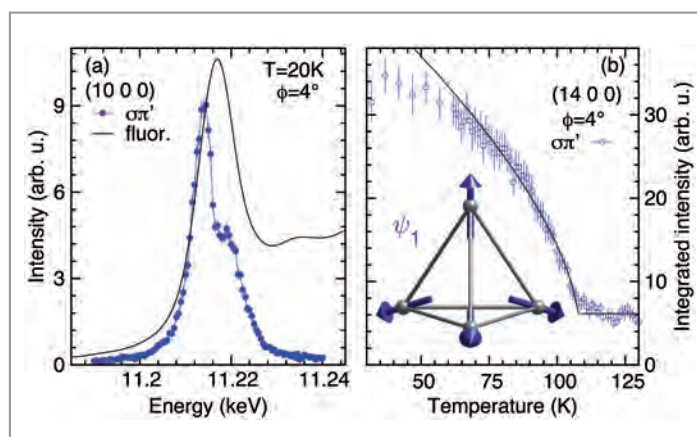


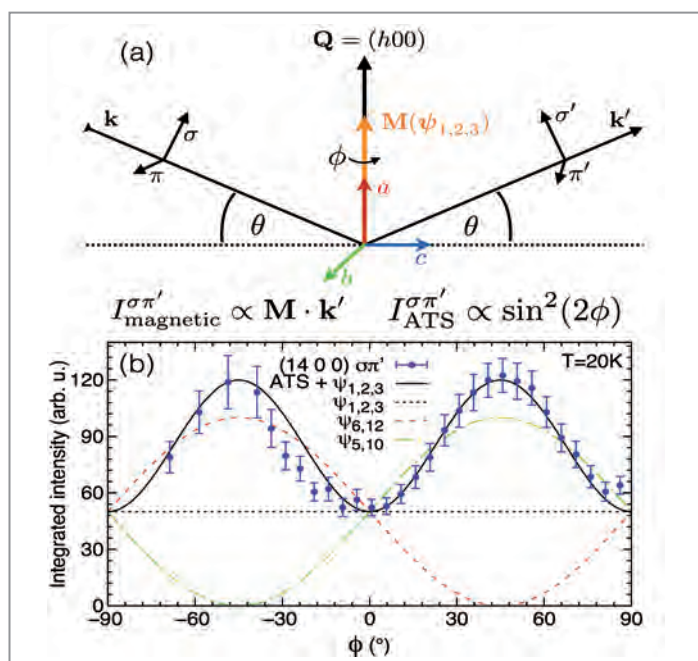
Figure 1

(a) Energy dependence of the intensity of the charge-forbidden (10 0 0) reflection (blue) at the Ir L_3 edge resonance (black). (b) Temperature dependence of the charge-forbidden (14 0 0) reflection, which confirms a substantial contribution from magnetic scattering. The inset shows the proposed 'all-in all-out' magnetic structure (ψ_1) for pyrochlore iridates.

elusive. While neutron scattering is the natural choice for solving magnetic structures, it is generally not feasible in pyrochlore iridates, due to small sample sizes (200 μm), small magnetic moments (0.2 μ_B), and highly neutron-absorbing elements (Ir). Resonant magnetic X-ray scattering is not affected by these limitations.

A team of researchers from the London Centre for Nanotechnology and the University of Oxford, working with collaborators at large scale facilities, have discovered that the magnetic moments in pyrochlore iridates indeed order in the 'all-in all-out' structure. Using resonant elastic and

Figure 2
 (a) Scattering geometry used on beamline P09, PETRA III to infer the orientation of the magnetic structure factor, \mathbf{M} . (b) Collected resonant X-ray scattering data as a function of azimuthal rotation ϕ (around the scattering vector \mathbf{Q}). The data can be explained by contributions from ATS (anisotropic tensor susceptibility) plus magnetic scattering of magnetic structures $\psi_{1,2,3}$. As the magnetic contribution stays constant as a function of ϕ , one can deduce that the magnetic structure factor lies parallel to the scattering vector \mathbf{Q} . This is fully consistent with the ‘all-in all-out’ magnetic structure (ψ_1).



inelastic X-ray scattering at the Ir L_3 edge, the magnetic order and excitations were comprehensively characterised in the prototypical pyrochlore iridate $\text{Sm}_2\text{Ir}_2\text{O}_7$. The experiments were performed at beamline P09 at PETRA III and beamline ID20, ESRF.

On beamline P09, we found a strong resonant enhancement of charge-forbidden reflections (Fig. 1). The temperature dependence of these reflections suggests that they originate from long-range antiferromagnetic order. However, when tuning to an absorption edge, the nominal selection rules for diffraction no longer apply, and ATS (anisotropic tensor susceptibility) scattering can also contribute to forbidden reflections. Microscopically, ATS scattering originates from the sensitivity of the absorbing ion to its local environment. When crystal fields remove the spherical symmetry of a free ion, the scattering amplitude can be described by an anisotropic tensor, which results in additional reflections that show a non-trivial polarization dependence. Through a comprehensive study of forbidden reflections as a function of polarization, momentum and azimuthal angle we could disentangle magnetic and ATS scattering contributions, and hence analyse the magnetic structure (Fig. 2).

This constrained the type of magnetic order to just two possibilities, one of which is the theoretically proposed ‘all-in all-out’ structure. Following the experiment on P09, we measured the magnetic excitation spectrum using resonant inelastic X-ray scattering on beamline ID20. The main result is that the magnetic excitations show an energy gap throughout the Brillouin zone, which is only compatible with the ‘all-in all-out’ magnetic structure. Furthermore, it was possible to deduce the effective Hamiltonian describing this class of material for the first time.

While the discovery confirms that pyrochlore iridates adopt the required type of magnetic order to host Weyl fermions, the magnetic excitations indicate that electronic correlations could be too strong to achieve a Weyl semimetal state. In order to observe topological phenomena in pyrochlore iridates, it may be necessary to fine-tune the electronic groundstate by applying internal or external perturbations.

Contact: Des McMorrow, d.mcmorrow@ucl.ac.uk

Authors

C. Donnerer¹, M. C. Rahn², M. Moretti Sala³, J. G. Vale¹, D. Pincini¹, J. Stremper⁴, M. Krisch³, D. Prabhakaran², A. T. Boothroyd² and D. F. McMorrow¹

1. London Centre for Nanotechnology and Department of Physics and Astronomy, University College London, UK
2. Department of Physics, University of Oxford, UK
3. European Synchrotron Radiation Facility ESRF, Grenoble, France
4. Deutsches Elektronen-Synchrotron DESY, Hamburg, Germany

Original publication

‘All-in–all-Out Magnetic Order and Propagating Spin Waves in $\text{Sm}_2\text{Ir}_2\text{O}_7$ ’, *Physical Review Letters* 117, 037201 (2016); DOI: 10.1103/PhysRevLett.117.037201

References

1. X. Wan, A. M. Turner, A. Vishwanath and S. Y. Savrasov, ‘Topological semimetal and Fermi-arc surface states in the electronic structure of pyrochlore iridates’, *Phys. Rev. B* 83, 205101 (2011).
2. S.-Y. Xu et al., ‘Discovery of a Weyl fermion semimetal and topological Fermi arcs’, *Science* 349.6248, 613–617 (2015).
3. B. Q. Lv et al., ‘Experimental discovery of Weyl semimetal TaAs’, *Phys. Rev. X* 5, 031013 (2015).
4. L. X. Yang et al., ‘Weyl semimetal phase in the non-centrosymmetric compound TaAs’, *Nature Physics* 11.9, 728–732 (2015).
5. H. Weyl, ‘Elektron und gravitation. I’, *Z. Phys.* 56, 330 (1929).
6. C. Herring, ‘Accidental degeneracy in the energy bands of crystals’, *Phys. Rev.* 52, 365–373 (1937).

Direct insights into phase transformations in nano-scaled microstructures.

Observation of orthorhombic phase formation in an advanced γ -TiAl alloy

Intermetallic titanium aluminide alloys, based on the ordered γ -TiAl phase, were recently introduced into civilian aero engines as a structural blade material. Nevertheless, their attractive property profile, light-weight combined with high-temperature strength has room for improvements, as for example, their room-temperature ductility remains low. Advanced γ -TiAl alloys with nano-scale modulated microstructures show significantly enhanced ductility behaviour. The microstructural modulation consists of several phases and at least one orthorhombic phase. Using *in situ* high-energy X-ray diffraction experiments we studied orthorhombic phase formation and have elucidated the formation path and the crystallographic structure of the phase that is formed.

The demand to reduce fuel consumption and greenhouse gas emissions of gas turbines requires the development of novel light-weight materials for high-temperature applications. Most recently, γ -TiAl based alloys were successfully introduced into civil aero engines. In contrast to the presently used heavy nickel-base alloys ($\sim 8 \text{ g/cm}^3$), TiAl alloys combine a high specific strength, good creep properties and oxidation resistance at service temperatures of $750 \text{ }^\circ\text{C}$, with a low density of about $\sim 4.2 \text{ g/cm}^3$ [1]. Nevertheless, their low room temperature ductility is still a serious drawback. To overcome this problem Appel et al. [2] introduced a new high-niobium containing TiAl alloy with a nominal composition of Ti-42Al-8.5Nb (in at. %), that shows improved mechanical properties at room and elevated temperatures. The alloy exhibits a near fully lamellar microstructure with γ lamellae and another type of modulated lamellae (Fig. 1). It is assumed, that the alloy shows its good balance of mechanical properties due to the presence of a nano-scaled modulation within one type of the lamellae present.

Transmission electron microscopy (TEM) studies indicated an orthorhombic phase as one constituent of the nano-scaled modulation [2]. However, an unambiguous identification of the crystal structure and formation path of the orthorhombic phase that forms was challenging. TEM investigations reached their limits due to the crystallographic similarity of possible orthorhombic phases to the various existing phases (hexagonal α/α_2 and cubic β/β_0 phase) in the Nb-rich TiAl alloy system investigated. Differing views of the structure and formation path of orthorhombic phases in titanium aluminide alloys were discussed in the literature [3, 4]. In addition, the available phase diagrams for ternary Ti-Al-Nb alloys [5] do not include the formation of an orthorhombic phase within the investigated composition range.

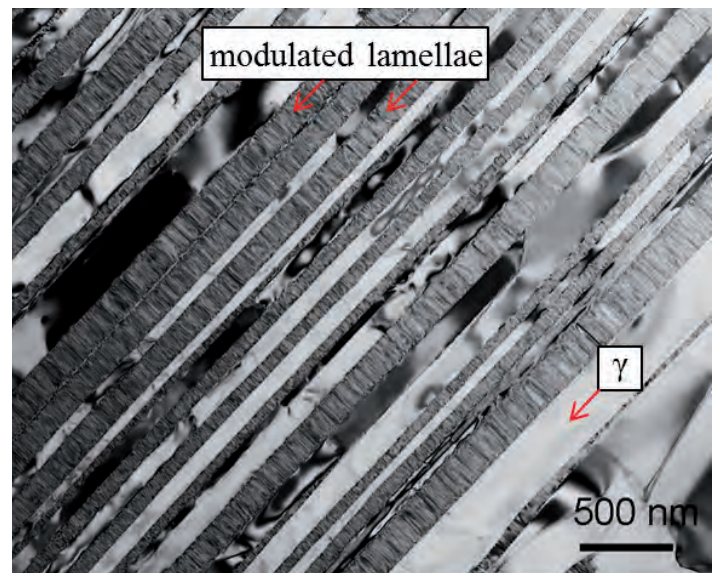


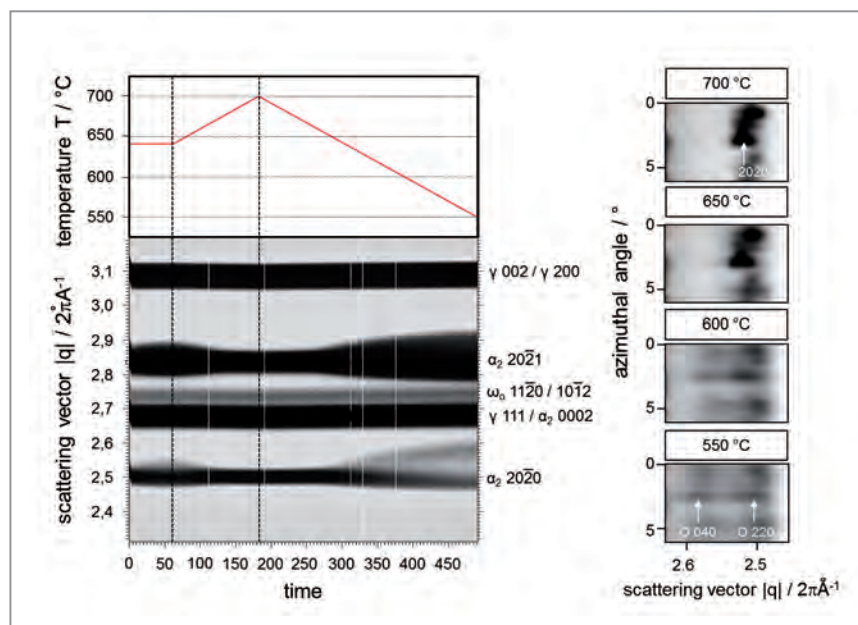
Figure 1

TEM micrograph of the modulated lamellar microstructure in a cut perpendicular to the lamellae. The modulation is located in one type of lamellae (modulated lamellae) and visible as varying shades of grey. The ordered γ -TiAl lamellae are without modulation.

To start with a chemically and microstructural homogenous material, a metallurgically produced and hot isostatically pressed Ti-42Al-8.5Nb powder alloy was used for this study. High-energy X-ray diffraction (HEXRD) experiments were performed at the Helmholtz-Zentrum Geesthacht (HZG) running the high-energy materials science beamline HEMS P07 at PETRA III using photon energies of 87.1 keV ($\lambda = 0.14235 \text{ \AA}$) and 100 keV ($\lambda = 0.1240 \text{ \AA}$). During heating and cooling of specimens, employing a modified deformation and quenching dilatometer DIL805A/D [6], the diffraction rings were continuously recorded with a flat panel detector.

Figure 2

(Left) Reversible transformation of orthorhombic O phase to hexagonal α_2 phase during an *in situ* heating and cooling experiment. The scattering vector is plotted versus the temperature which is indicated in the upper part of the figure. The measured intensity is plotted using a logarithmic grey scale. The formation of the O phase is clearly visible as a widening of former α_2 ($20\bar{2}0$) and α_2 ($20\bar{2}1$) peaks at temperatures below 660 °C. (Right) Sections of the Debye-Scherrer diffraction rings taken during cooling from 700 °C to 550 °C. They show the evolution of the 220 and 040 diffraction peaks of the O phase from α_2 ($20\bar{2}0$) diffraction spots. The high resolution of the HEXRD experiments allows the observation of O phase formation from a single α_2 grain (marked with arrow). The figures are based on figures from the original publication.



The subsequent data analysis was performed using the Fit2D software tool and a Rietveld refinement program.

Figure 2 shows an experiment performed over the temperature range 550 – 700 °C. During this *in situ* HEXRD experiment we used a very slow heating and cooling rate of 0.5 K/min to achieve a thermodynamically more stable condition. Starting at 640 °C a slight broadening of the α_2 ($20\bar{2}0$) and α_2 ($20\bar{2}1$) peak is visible. This peak broadening indicates an orthorhombic distortion of the crystallographic lattice of the hexagonal α_2 phase. With increasing temperature the broadening decreases and at 700 °C only sharp α_2 ($20\bar{2}0$) and α_2 ($20\bar{2}1$) reflections are present. During cooling an orthorhombic distortion again occurs, which becomes more pronounced with decreasing temperature. Simulations and Rietveld refinements of the diffraction data showed that the structure of the orthorhombic phase formed is comparable to the O phase, known from α_2 based alloys. The lattice parameters of the O phase were determined as $a = 5.918 \text{ \AA}$, $b = 9.801 \text{ \AA}$, $c = 4.673 \text{ \AA}$. At temperatures below 700 °C the reversible formation of the O phase from α_2 phase takes place. The high

brilliance of the PETRA III storage ring allowed the direct observation of O phase formation out of the hexagonal α_2 -Ti₃Al phase in individual α_2 grains (Fig. 2 right).

For the first time orthorhombic phase formation in a high-niobium containing γ -TiAl based alloy was studied *in situ* with HEXRD experiments. We were able to determine the structure, the formation path and the range of thermal stability of the orthorhombic phase that formed. The findings provide paths to selectively adjust the O phase for further microstructure optimisation. Additionally, the results can be used to create more accurate phase diagrams for complex ternary γ -TiAl based alloys.

Contact: Marcus Willi Rackel, marcus.rackel@hzg.de

Authors

Marcus Willi Rackel¹, Andreas Stark¹, Heike Gabrisch¹, Norbert Schell¹, Andreas Schreyer^{1,2} and Florian Pyczak¹

1. Institute of Materials Research, Helmholtz-Zentrum Geesthacht Centre for Materials and Coastal Research, Geesthacht, Germany
2. European Spallation Source ERIC, Lund, Sweden

Original publication

'Orthorhombic phase formation in a Nb-rich γ -TiAl based alloy – An *in situ* synchrotron radiation investigation', *Acta Materialia* 121 (2016) 343-351.
DOI: <http://dx.doi.org/10.1016/j.actamat.2016.09.030>

References

1. F. Appel, J. D. H. Paul and M. Oehring, 'Gamma Titanium Aluminide Alloys', Wiley-VCH (2011).
2. F. Appel, M. Oehring and J. D. H. Paul, 'Nano-Scale Design of TiAl Alloys Based on β -Phase Decomposition', *Advanced Engineering Materials* 8 (2006) 371-376.
3. K. Muraleedharan, D. Banerjee, S. Banerjee, and S. Lele, 'The α_2 -to-O transformation in Ti-Al-Nb alloys', *Philosophical Magazine A* 71 (1995) 1011-1036.
4. E. Abe, T. Kumagai and M. Nakamura, 'New ordered structure of TiAl studied by high resolution electron microscopy', *Intermetallics* 4 (1996) 327-333.
5. V. T. Witusiewicz, A. A. Bondar, U. Hecht and T. Y. Velikhanova, 'The Al-B-Nb-Ti system', *Journal of Alloys and Compounds* 472 (2009) 133-161.
6. N. Schell, A. King, F. Beckmann, T. Fischer, M. Müller and A. Schreyer, 'The High Energy Materials Science Beamline (HEMS) at PETRA III', *Materials Science Forum* 772 (2014) 57-61.

Coherent X-rays spotlight on a colloidal crystal.

Periodic structure and defects revealed in 3D

Colloidal crystals are attractive novel materials with unique optical properties such as the full photonic band gap, 'slow' photons and negative refraction. They can also find unique applications in catalysis, biomaterials, and sensorics. Understanding the real structure of colloidal crystals and its disorder is an important aspect from both fundamental and practical points of view. For applications such as photonic crystals, most of the growth-induced defects can deteriorate the optical properties. Monitoring an internal 3D structure of colloidal crystals including defects in real time remains a challenge. Utilizing the coherent X-ray diffractive imaging approach we visualised the internal 3D structure of an individual colloidal crystal grain with high resolution.

Colloidal crystals nowadays are actively exploited as an important model system to study nucleation phenomena in freezing, melting, and solid-solid phase transitions, jamming and glass formation (for recent examples see [1, 2]). Colloidal crystals grown by self-organisation provide a low cost large-scale alternative to lithographic techniques. Even at equilibrium, colloidal crystals can have a finite density of defects, which can be anomalously large for certain colloidal lattices. The opposite can also happen as defects can play a decisive role in the choice of the crystal structure. At the same time, controlled incorporation of certain defects can be desirable to enhance the functionality such as creating wave-guides, trapping photons, and developing optical chips.

High-resolution X-ray microscopy, small-angle X-ray scattering and coherent X-ray diffraction imaging (CXDI) are extraordinary tools for non-destructive studies of the real three-dimensional structure of colloidal systems [2-4]. In this work, we present

the first successful realisation of a detailed reconstruction from CXDI measurements, visualising 3D positions of individual particles in a single colloidal crystal grain.

The experiment was performed at the coherence beamline P10 at the PETRA III storage ring, utilising a monochromatic coherent X-ray beam of 8 keV photon energy focused at the sample (see Fig. 1). The sample was mounted on a goniometer, which allows azimuthal rotation around the vertical axis. The diffraction data were recorded using a pixel detector positioned in transmission geometry downstream from the sample. Samples were prepared from dried sediments of colloidal crystals and mounted to the tip of a carbon fibre. They consisted of sterically stabilised silica spheres with a diameter of 230 nm. The colloidal crystal grain used in this study had dimensions of about $2 \times 3 \times 4 \mu\text{m}^3$.

The full data set consisted of a rotation series of 360 diffraction patterns with 0.5° angular increment covering the entire reciprocal space information. In Figure 1 (top left inset) an example of the measured diffraction pattern is shown. The full 3D reciprocal space map is shown in Fig. 2a. It contains several Bragg peaks surrounded by the interference speckles in between. Remarkable features observed in this map are a

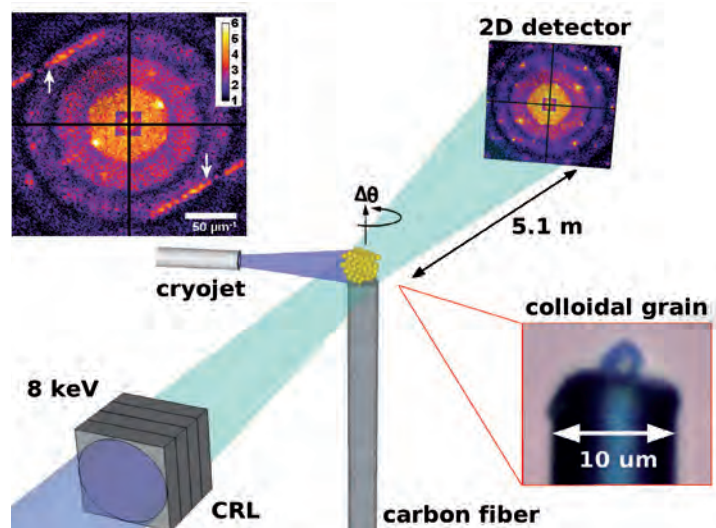


Figure 1

Schematic layout of the experimental setup. Compound refractive lenses (CRL) focus the coherent X-ray beam at the crystal grain mounted on the top of the carbon fibre. A light microscope image of the sample and tip is shown in the lower right inset. The sample was constantly cooled by a flow of nitrogen using a cryojet. The diffraction data were recorded by a 2D detector positioned in the far field. The top left inset shows a typical diffraction pattern, the intensity scale is logarithmic. Two elongated rods visible in this image (indicated by arrows) originate from the presence of a planar defect in the crystal grain.

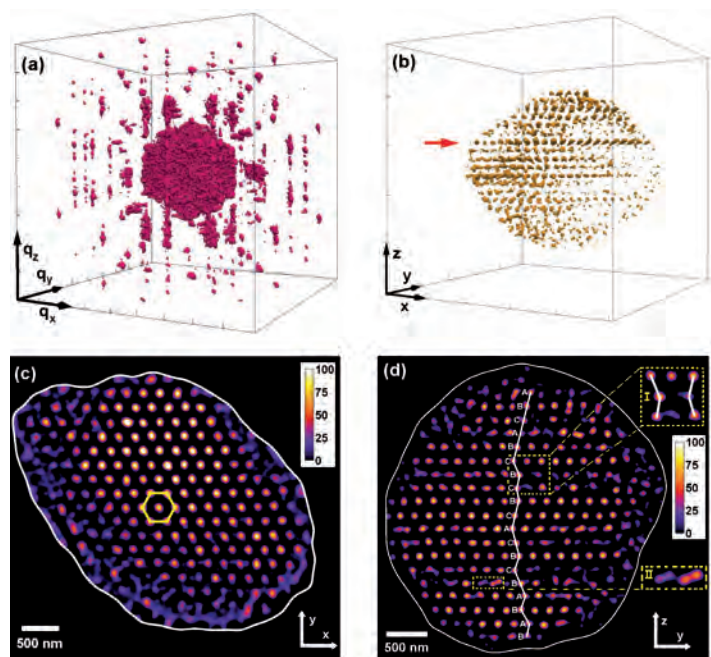


Figure 2

(a) Measured 3D scattered intensity in reciprocal space, represented by volume rendering. (b) Reconstructed 3D electron density distribution in real space. The red arrow marks the crystalline plane shown as a 2D slice in Fig. 2c. Length of the coordinate arrows correspond to $50 \mu\text{m}^{-1}$ in (a) and $1 \mu\text{m}$ in (b). (c) Slice through one of the packing planes. The well-pronounced hexagonal symmetry is outlined by a yellow hexagon. (d) Projection of the density map on the [100] crystallographic direction of the hexagonal lattice. Each layer is marked by the corresponding letter, the insets (I and II) show examples of in-plane defects.

number of streaks, which connect some of the Bragg peaks (see Fig. 2a and diffraction pattern in Fig. 1 (top left inset)). These streaks (Bragg rods) indicate the presence of plane defects in the crystalline lattice and the intensity modulations along them are directly related to the exact stacking sequence.

The 3D reciprocal space maps were inverted to real space images by using phase retrieval algorithms [5]. The reconstructed 3D electron density is shown in Fig. 2b. It reveals periodic behaviour that corresponds to positions of colloidal particles in the crystal grain. In Figure 2c a slice through one of the packing planes is presented. Remarkably, positions of individual colloidal spheres are clearly resolved and show perfect hexagonal symmetry. We found that the position of each individual colloidal sphere in the lattice is determined with an accuracy of about 4% (or 9 nm) due to the fact that several orders of Bragg peaks were measured simultaneously.

To determine the stacking sequence, we analysed the projection of the 3D density map along the [100] crystallographic direction of the hexagonal lattice (see Fig. 2d). Since the vector of lateral displacement is perpendicular to the direction of the projection plane, the lateral position of each layer can be directly determined. Starting from the layer on

the top, we identified 19 layers in the colloidal crystal (see Fig. 2d). One of the possible sequences of elementary stacking order may be ABC ABCB CBCA CB CBAB AB (from top to bottom) that reveals three structures: fcc, hcp, and double hexagonal close-packed (dhcp) structures. In addition to regular structures revealed by our analysis, we have observed a number of linear defects in the projection of the 3D colloidal crystal grain (see insets in Fig. 2d). Thus, our reconstruction visualizes the exact stacking sequence of layers and in-plane defects in the colloidal crystal grain.

Our results constitute a breakthrough in applications of coherent X-ray diffraction for visualisation of the inner three-dimensional structure of different mesoscopic materials, such as photonic crystals. The outcome of this work is of significant importance for further progress and developments of CXDI methods with an aim to resolve the 3D structure of colloidal crystals with smaller particle size and nanocrystals with atomic resolution [6]. Our achievements pave the way to atomic resolution imaging of nanocrystals at the next generation diffraction-limited storage rings, which are expected to provide two orders of magnitude higher brilliance and coherent flux.

Contact: Ivan Vartanyants, Ivan.Vartanyants@desy.de

Authors

A. G. Shabalin^{1,2}, J.-M. Meijer³, R. Dronyak¹, O. M. Yefanov¹, A. Singer¹, R. P. Kurta¹, U. Lorenz¹, O. Y. Gorobtsov^{1,4}, D. Dzhigaev^{1,5}, S. Kalbfleisch⁶, J. Gulden¹, A. V. Zozulya¹, M. Sprung¹, A. V. Petukhov^{3,7} and I. A. Vartanyants^{1,5}

1. Deutsches Elektronen-Synchrotron DESY, Hamburg, Germany
2. FSRC 'Crystallography and Photonics' RAS, Moscow, Russia
3. Van 't Hoff Laboratory for Physical and Colloid Chemistry, Debye Institute for Nanomaterials Science, Utrecht University, Utrecht, Netherlands
4. NRC Kurchatov Institute, Moscow, Russia
5. National Research Nuclear University MEPhI (Moscow Engineering Physics Institute), Moscow, Russia
6. Institute for X-Ray Physics, University of Göttingen, Göttingen, Germany
7. Laboratory of Physical Chemistry, Department of Chemical Engineering and Chemistry, Eindhoven University of Technology, Eindhoven, Netherlands

Original publication

'Revealing Three-Dimensional Structure of an Individual Colloidal Crystal Grain by Coherent X-Ray Diffractive Imaging', *Physical Review Letters* 117, 138002 (2016). DOI: 10.1103/PhysRevLett.117.138002

References

1. Y. Peng, F. Wang, Z. Wang, A. M. Alsayed, Z. Zhang, A. G. Yodh, and Y. Han, 'Two-step nucleation mechanism in solid–solid phase transitions', *Nat. Mater.* 14, 101–108 (2015).
2. B. Cabane, J. Li, F. Artzner, R. Botet, C. Labbez, G. Bareigts, M. Sztucki, and L. Goehring, 'Hiding in Plain View: Colloidal Self-Assembly from Polydisperse Populations', *Phys. Rev. Lett.* 116, 208001 (2016).
3. A. Bosak, I. Snigireva, K. S. Napolskii, and A. Snigirev, 'High-Resolution Transmission X-ray Microscopy: A New Tool for Mesoscopic Materials', *Adv. Mater.* 22, 3256–3259 (2010).
4. J. Gulden, O. M. Yefanov, A. P. Mancuso, V. V. Abramova, J. Hilhorst, D. Byelov, I. Snigireva, A. Snigirev, A. V. Petukhov, and I. A. Vartanyants, 'Coherent x-ray imaging of defects in colloidal crystals', *Phys. Rev. B* 81, 224105 (2010).
5. J. R. Fienup, 'Phase retrieval algorithms: a comparison', *Appl. Opt.* 21, 2758–2769 (1982).
6. J. Gulden, O. M. Yefanov, E. Weckert, and I. A. Vartanyants, 'Imaging of Nanocrystals with Atomic Resolution Using High-Energy Coherent X-rays', *AIP Conf. Proc.* 1365, 42–45 (2011).

Earth's mantle may produce oxygen.

Iron oxides under extreme conditions

Information about geochemical processes in deep Earth's interior may be acquired only by experiments on relevant materials at conditions simulating those in the depth of the Earth. Iron oxides are involved in many geochemical cycles and are known to undergo a series of structural, electronic and magnetic transformations at high pressures and high temperatures. To correctly describe and understand them, one needs accurate structural data. We conducted a systematic investigation of the behaviour of iron oxides at pressures over 100 GPa and temperatures above 2500 K using single crystal X-ray diffraction (XRD) and synchrotron Mössbauer spectroscopy, which suggests that mixed-valence iron oxides may play a significant role in oxygen cycling between Earth reservoirs.

Banded iron formations (BIFs) are one of the most enigmatic geological objects on our planet. These huge sedimentary rock formations with thicknesses up to several hundred metres and lateral expansions of hundreds of kilometres occur on all continents. The main iron-bearing minerals in BIFs are hematite, α - Fe_2O_3 , and magnetite, Fe_3O_4 , constituting up to 85 wt% of the formations. Deposited in the world's oceans, BIFs as part of the ocean floor are recycled into the Earth's interior by subduction to depths extending possibly to the core-mantle boundary region. Dobson et al. suggested

that relics of BIFs subducted between 2.8 and 1.8 billion years ago may be a source of anomalous zones with ultra-low velocity as seen in seismic tomography [1]. However, the behaviour of iron oxides at high pressure-temperature conditions of the interior of the deep Earth is largely unknown. Despite wide interest and intense decades-long investigations of Fe_2O_3 and Fe_3O_4 at extreme conditions using various methods, particularly powder XRD and in-house Mössbauer spectroscopy, the crystal chemistry and the phase diagram of iron oxides remain highly controversial.

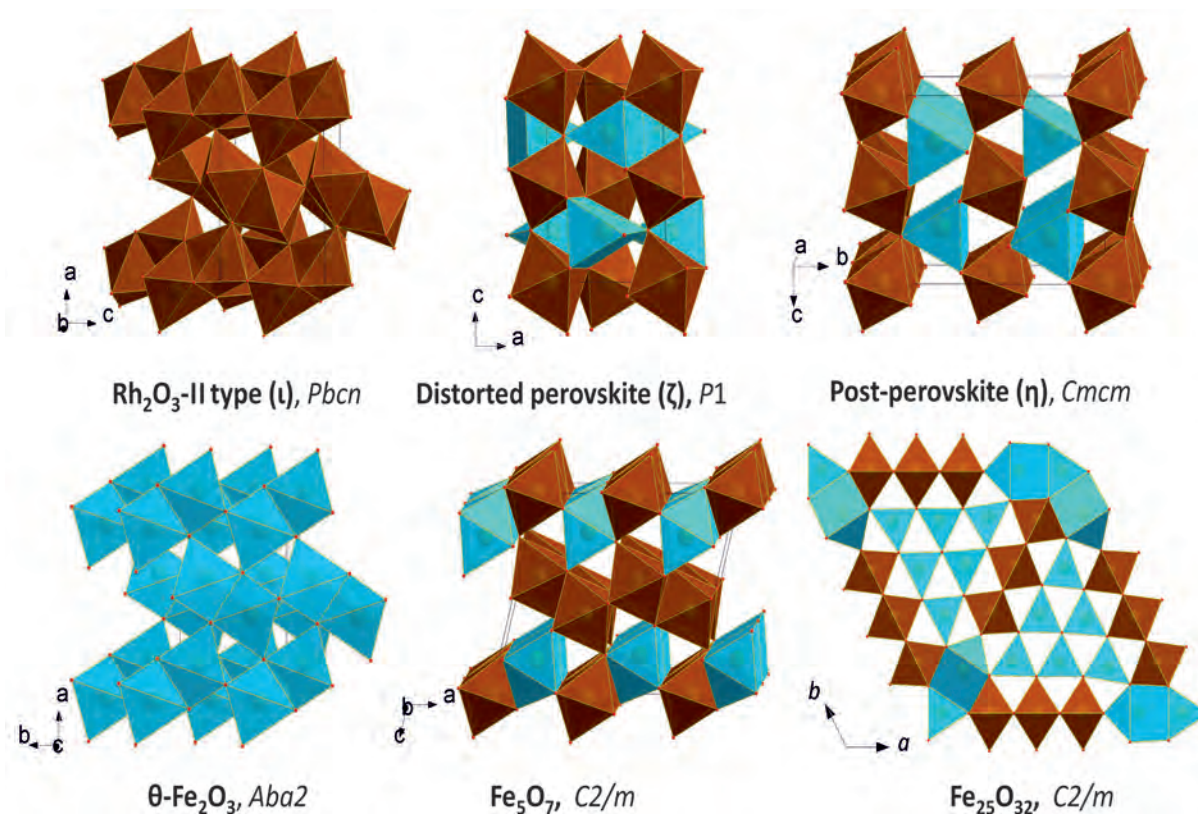


Figure 1
Structures of some Fe-O compounds studied *in situ* at high pressures by means of single-crystal XRD. Building blocks are octahedra (brown) and trigonal prisms (blue). The θ - Fe_2O_3 , Fe_5O_7 , and $\text{Fe}_{25}\text{O}_{32}$ polymorphs were for the first time described in our original publication.

To clarify the fate of iron oxides in deep Earth interior and their role in geochemical processes in Earth's mantle, we conducted a series of simultaneous high-pressure high-temperature experiments on single-crystal samples of hematite and magnetite using the diamond anvil cell technique combined with laser heating [2,3]. We used single-crystal XRD to characterise the crystal structures and phase compositions of the revealed phases. The single-crystal X-ray diffraction experiments were conducted at 3rd generation synchrotrons, in particular, at PETRA III at the Extreme Conditions Beamline P02.2. The experiments on Fe₂O₃ additionally employed synchrotron Mössbauer spectroscopy to track changes in the electronic and magnetic states of Fe³⁺ ions.

In the course of our investigations we uncovered a sequence of phase transitions in Fe₃O₄ and Fe₂O₃. Accurate crystallographic information was obtained for all high pressure Fe-O polymorphs reported in literature and synthesised by us. We observed two transformational paths in Fe₂O₃ depending on the type of external stimuli applied. During room-temperature compression Fe₂O₃ undergoes two phase transitions (to ζ-Fe₂O₃ at 54 GPa and θ-Fe₂O₃ at 67 GPa) accompanied with an iron spin crossover and a related abrupt change of the unit cell volume. The highest-pressure phase θ-Fe₂O₃, having Fe³⁺ in only low spin state, can be observed to at least 100 GPa, but it is not quenchable. Moderate laser heating provokes transformation to the η-Fe₂O₃ phase exhibiting a post-perovskite structure, which is stable down to at least 50 GPa; at this pressure further laser heating results in transformations of η-Fe₂O₃ first into ζ-Fe₂O₃ and then ι-Fe₂O₃. Fig. 1 demonstrates that the crystal structures of these phases are composed of similar building blocks, namely octahedra and trigonal prisms.

Our most intriguing finding is the observation that at conditions of the Earth's lower mantle (Fig. 2), high-pressure polymorphs of Fe₂O₃ and Fe₃O₄ become chemically unstable. When we applied a pressure of more than 67 GPa to the Fe₂O₃ samples and heated them to more than 2700 K, they decomposed and formed Fe₅O₇, an iron oxide that has not been reported before (Fig. 1). These conditions correspond to roughly 1500 kilometres below the surface of the Earth. At an even

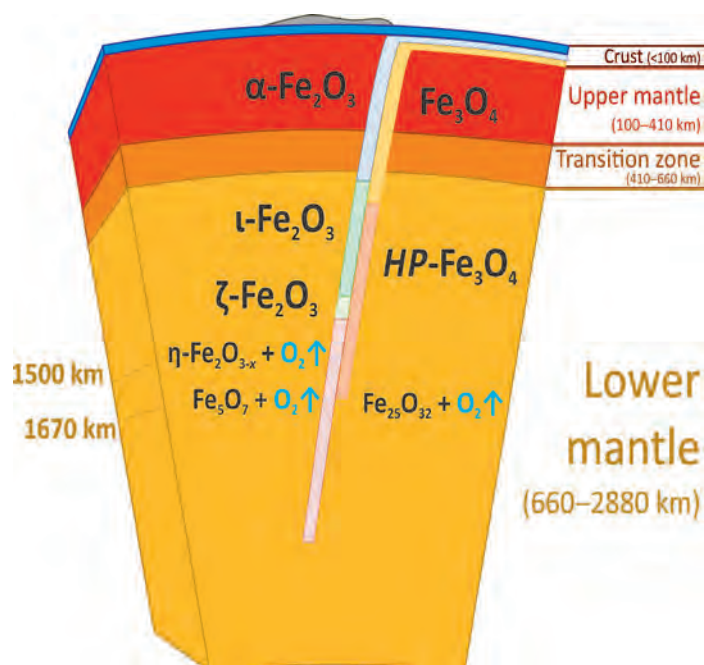


Figure 2

Possible sequence of phase transitions of Fe₂O₃ and Fe₃O₄ in a banded iron formation subducted to the lower mantle. At conditions corresponding to depths below 1500–1700 km Fe₂O₃ and Fe₃O₄ start to decompose producing new iron oxides (Fe₅O₇ and Fe₂₅O₃₂) and oxygen.

higher pressure of 70 GPa, corresponding to about 1670 kilometres below the surface, Fe₃O₄ decomposes and another new iron oxide forms, Fe₂₅O₃₂. The formation of both so far unknown compounds leads to the release of oxygen (Fig. 2).

The quantities of oxygen released are significant: Based on the estimated rate at which BIFs are subducted, the decomposition of hematite alone could have produced 8 to 10 times the mass of oxygen in the modern atmosphere over the about 2 billion years. Thus, the subducted BIFs may supply the deep Earth's interior with a substantial amount of oxygen which may lead to heterogeneities in the oxygen fugacity in different parts of the mantle. This can significantly affect geochemical processes by changing oxidation states and mobilising trace elements.

Contact: Elena Bykova, elena.bykova@uni-bayreuth.de

Authors

Elena Bykova^{1,2}, Leonid Dubrovinsky¹, Natalia Dubrovinskaia², Maxim Bykov^{1,2}, Catherine McCammon¹, Sergey V. Ovsyannikov¹, Hanns-Peter Liermann³, Ilya Kupenko^{1,4}, Aleksandr I. Chumakov⁴, Rudolf Rüffer⁴, Michael Hanfland⁴ and Vitali Prakapenka⁵

1. Bayerisches Geoinstitut, University of Bayreuth, Bayreuth, Germany.
2. Laboratory of Crystallography, University of Bayreuth, Bayreuth, Germany.
3. Deutsches Elektronen-Synchrotron DESY, Photon Science, Hamburg, Germany.
4. European Synchrotron Radiation Facility, Grenoble, France.
5. Center for Advanced Radiation Sources, University of Chicago, Chicago, Illinois, USA.

Original publication

'Structural Complexity of Simple Fe₂O₃ at High Pressures and Temperatures', *Nature Commun.* 7, 10661 (2016). DOI: 10.1038/ncomms10661

References

1. D. P. Dobson and J. P. Brodholt, 'Subducted banded iron formations as a source of ultralow-velocity zones at the core-mantle boundary', *Nature* 434, 371–374 (2005).
2. L. Dubrovinsky, T. Boffa-Ballaran, K. Glazyrin, A. Kurmosov, D. Frost, M. Merlini, M. Hanfland, V. B. Prakapenka, P. Schouwink, T. Pippinger and N. Dubrovinskaia 'Single-crystal X-ray diffraction at megabar pressures and temperatures of thousands of degrees', *High Pressure Res.* 30, 620–633 (2010).
3. I. Kupenko, L. Dubrovinsky, N. Dubrovinskaia, C. McCammon, K. Glazyrin, E. Bykova, T. Boffa Ballaran, R. Sinmyo, A. I. Chumakov, V. Potapkin, I. Kantor, R. Rüffer, M. Hanfland, W. Crichton, and M. Merlini, 'Portable double-sided laser-heating system for Mössbauer spectroscopy and X-ray diffraction experiments at synchrotron facilities with diamond anvil cells', *Rev. Sci. Instrum.* 83, 124501 (2012).

Accessing nanoscale dynamics at SACLA.

X-ray photon correlation spectroscopy at free-electron lasers

Studying dynamics of complex materials is one of the key applications of hard X-ray free-electron laser (FEL) facilities. Due to the high degree of coherence of the individual X-ray pulses and the high time-averaged flux, matter can be studied at length and time scales simultaneously that are unreachable at conventional X-ray sources. However, shot-to-shot fluctuations of the FEL radiation and sample damage challenge the use of well-established techniques. Here, we demonstrate the application of X-ray photon correlation spectroscopy (XPCS) at a hard X-ray FEL studying dynamics in soft matter using sequential shots well below the radiation damage threshold.

In the last decades XPCS has become a widely used technique to study dynamics of soft and hard matter materials [1]. It relies on the (partial) transverse coherence of the X-ray beam at 3rd generation storage rings or FEL sources, giving rise to

grainy diffraction (speckle) patterns. The actual structure of the sample is hereby encoded in the intensity distribution of the speckle pattern $I(q, \tau)$ for wave vector transfers $q = \frac{4\pi}{\lambda} \sin(\frac{\theta}{2})$, at scattering angle θ and wavelength λ , and time τ . In conventional XPCS experiments, the temporal evolution of the sample is tracked by monitoring changes of the speckle patterns over time. At storage ring sources timescales from a few thousand seconds down to milliseconds and length scales between micro- and nanometre are routinely accessed with state-of-the-art 2D detectors.

The accessible timescale in XPCS experiments can in principle be reduced to femtoseconds at FEL facilities using split-pulse techniques [2]. Conventional sequential pulse XPCS at FELs provides various advantages compared to storage ring experiments. For instance, the higher averaged flux and superior degree of coherence of FELs allow to access larger wave vector transfers q . It is limited by the repetition rate of the FEL pulses, i.e. about $\tau_{\text{rep}} = 8$ to 50 ms at the currently existing hard X-ray sources LCLS (USA) and SACLA (Japan). With the start of the European XFEL, this will be routinely reduced to the sub- μs regime, not accessible at any FEL or synchrotron X-ray source up to now. However, due to shot-to-shot fluctuations of transverse coherence, intensity and pointing stability originating from the stochastic nature of the underlying self-amplified spontaneous emission (SASE) process the application of XPCS at FELs has been a challenge.

In order to quantify the impact of SASE fluctuations on XPCS, we studied diffusion dynamics of colloidal samples at the SACLA free-electron laser. The beam was focused to $1.8 \times 1.5 \mu\text{m}^2$ at 8 keV photon energy. The repetition rate was 20 Hz, resulting in a minimum accessible time of $\tau_{\text{rep}} = 50$ ms. We chose well-defined and characterized model systems, i.e. (1) static hard spheres and (2) Brownian motion of several 100 nm large particles to elucidate the effect of fluctuating FEL pulse properties on XPCS. A sketch of the experimental

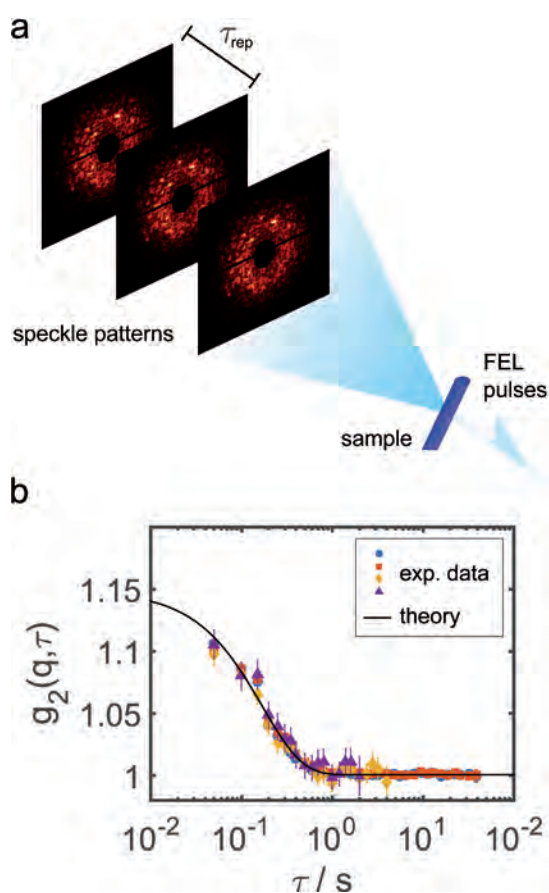


Figure 1
(a) Sketch of the experimental set-up. FEL pulses from SACLA are scattered by the sample resulting in speckle patterns measured with the repetition rate of $\tau_{\text{rep}} = 50$ ms by a 2D detector. (b) Intensity-intensity correlation function $g_2(q, \tau)$ for different runs expressed by different symbols and colours for $q = 0.031 \text{ nm}^{-1}$. The solid line represents the theoretical results for spheres undergoing Brownian motion.

set-up is given in Fig. 1a. The intensity-intensity correlation functions from series of speckle patterns are derived from $g_2(q, \tau) = \langle I(q, t)I(q, t + \tau) \rangle / \langle I(q, t) \rangle^2$. Sample dynamics are accessed by modelling the correlation function according to $g_2(q, \tau) = 1 + \beta^2 \exp(-2\Gamma(q)\tau)$, where the contrast β is a measure of the degree of coherence and the relaxation rate is given by $\Gamma(q) = Dq^2$ for Brownian motion with the diffusion coefficient D . The correlation functions for different series of speckle patterns are shown in Fig. 1b. The relaxation rate and contrast are obtained as function of q and are shown in Fig. 2a and Fig. 2b. Here, the q -dependence of the relaxation rate is well-modelled using the diffusion coefficient in so-called Stokes-Einstein representation. Most importantly, the result is reproduced in different runs of sequential shots, suggesting that there is no significant influence from beam-induced heating or radiation damage. On the other hand, the contrast obtained from the correlation function is about a factor of 2 below the expected value of 0.79 that was found for single speckle patterns [3] and is a consequence of the shot-to-shot average of the transverse coherence. The reduced contrast observed in the present experiments may be connected to either dynamic processes that are faster than the accessible time scale, e.g., β -relaxation close to glass transition and crystallization [4], or determined by small instabilities of the FEL in terms of coherence, pointing, beam size and shape. Since the model systems are far away from any phase transition we found that weak fluctuations of less than $0.4 \mu\text{m}$ can explain the experimental results for both static and dynamic samples.

Our results demonstrate that conventional sequential XPCS can be performed routinely at FELs, in particular below the radiation damage threshold for soft matter materials. The

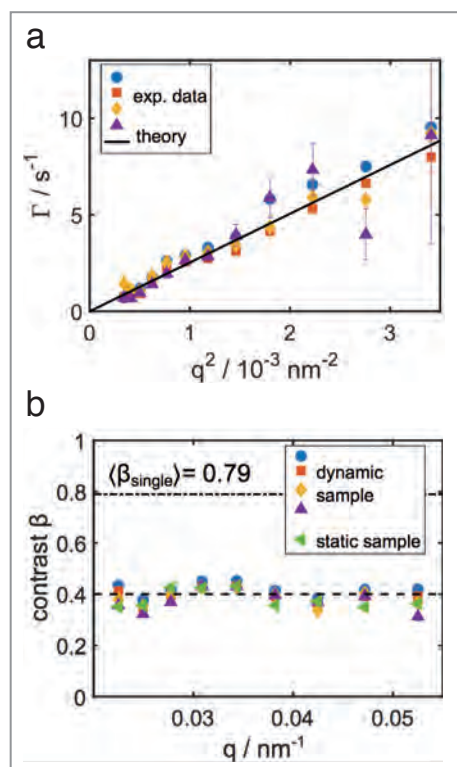


Figure 2
XPCS results. (a) Relaxation rate Γ for different experimental runs compared with theory for Brownian motion. (b) Contrast β obtained from the correlation function $g_2(q, \tau)$ for different runs of the dynamic sample and the static sample. The expected single shot contrast of 0.79 is indicated by the upper line and the average contrast of 0.4 is given by the lower one.

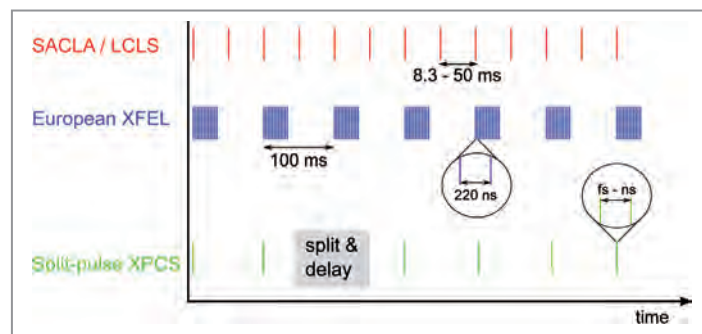


Figure 3
Schematic time structure for sequential and split-pulse XPCS at FEL facilities.

results pave the way to XPCS experiments with so far unreached access to timescales between femto- and micro-seconds at upcoming FEL facilities; see the schematics in Fig. 3. The pulse structure of the European XFEL will enable sequential mode XPCS with repetition rates of up to 4.5 MHz corresponding to an accessible timescale of 220 ns. The application of split-pulse techniques allows for further reduction down to the duration of single pulses, i.e. a few femto-seconds. The first of such devices has been installed at the LCLS demonstrating the feasibility of ultrafast XPCS [2]. Thus, nanoscale dynamics will become routinely accessible by XPCS, studying for example molecular liquids and glasses, protein folding, spin transitions and magnetic domain dynamics [5] over timescales from femtoseconds to several 1000 s.

Contact: Felix Lehmkuhler, felix.lehmkuehler@desy.de

Authors

Felix Lehmkuhler^{1,2}, Pawel Kwasniewski¹, Wojciech Roseker¹, Birgit Fischer^{1,2,3}, Martin A. Schroer^{1,2}, Kensuke Tono⁴, Tetsuo Katayama⁴, Michael Sprung¹, Marcin Sikorski⁵, Sanghoon Song⁵, James Glownia⁵, Matthieu Chollet⁵, Silke Nelson⁵, Aymeric Robert⁵, Christian Gutt⁶, Makina Yabashi⁷, Tetsuya Ishikawa⁷ and Gerhard Grübel^{1,2}

1. Deutsches Elektronen-Synchrotron DESY, Photon Science, Hamburg, Germany
2. The Hamburg Centre for Ultrafast Imaging, Hamburg, Germany
3. Institut für Physikalische Chemie, Universität Hamburg, Hamburg, Germany
4. Japan Synchrotron Radiation Research Institute, Hyogo, Japan
5. Linac Coherent Light Source, SLAC National Accelerator Laboratory, Menlo Park, USA
6. Universität Siegen, Siegen, Germany
7. RIKEN Spring-8 Center, Hyogo, Japan

Original publication

'Sequential Single Shot X-ray Photon Correlation Spectroscopy at the SACLA Free Electron Laser', *Scientific Reports* 5, 17193 (2015). DOI: 10.1038/srep17193

References

1. G. Grübel and F. Zontone, 'Correlation Spectroscopy with Coherent X-rays', *J. Alloys Compd.* 362, 3-11 (2004).
2. W. Roseker et al., 'Performance of a picosecond x-ray delay line unit at 8.39 keV', *Opt. Lett.* 34, 1768-1770 (2009).
3. F. Lehmkuhler et al., 'Single Shot Coherence Properties of the Free-Electron Laser SACLA in the Hard X-ray Regime', *Sci. Rep.* 4, 5234 (2014).
4. V. M. Girodano and B. Ruta, 'Unveiling the structural arrangements responsible for the atomic dynamics in metallic glasses during physical aging', *Nature Comm.* 7, 10344 (2016).
5. G. Grübel et al., 'XPCS at the European X-ray free electron laser facility', *Nucl. Instrum. Meth. Phys. B* 262, 357-367 (2007).

A nanoparticle supercrystal with exceptional mechanical properties.

The role of organic linkers for strength and hardness of supercrystals

It is commonly accepted that the combination of the anisotropic shape and nanoscale dimensions of the mineral constituents of natural biological composites underlies their superior mechanical properties when compared to those of their rather weak mineral and organic constituents. We demonstrated that the self-assembly of nearly spherical iron oxide nanoparticles (NPs) in supercrystals combined with a thermally induced coupling reaction of oleic acid molecules leads to a nanocomposite carrying an exceptional bending modulus of 114 GPa and strength up to 630 MPa. It is the covalent backbone of the linked organic molecules that dominates the mechanical properties leading to a nanohardness of up to 4 GPa. This is in contrast to the common hypothesis that only a shear load transfer enables ceramic/polymer-composites to reach high strength and stiffness.

One of the main challenges in materials science is to produce hard, stiff and strong as well as damage tolerant materials at ambient temperatures with a minimum of energy consumption. Polymers, metals, ceramics and plastics have excellent mechanical properties within their specific application areas, but usually cover only one aspect in the desired property spectrum. Therefore, developing new materials that combine several properties is highly interesting to overcome the weakness of one material class and achieve multifunctionality. We developed a nanocomposite with several mechanical properties and thus open up new applications in medical technology and product manufacture.

The structure of the new material is a building block of iron oxide nanoparticles (NPs) surrounded by a shell of organic oleic acid. The connection between the oleic acid molecules and iron oxide NPs is much stronger than the van der Waals bonds because of a sequence of drying, hot pressing and a controlled heat treatment that connects the oleic acid molecules in a network. This important information is the basis for the successful modeling of the mechanical properties of this new material. The main difference to approaches used up to now is the adjusted size of the nanoparticles in a closed packed supercrystal, so that monolayers of oleic acid molecules on the surface of the NPs bridge the tetrahedral and octahedral sites. This requirement is fulfilled for particle diameters smaller than 16 nm. With this geometrical confinement the linker molecules are closely packed and their mechanical response is very stiff and strong. The cross-linking bonds between the oleic acid molecules are controlled by a moderate heat treatment at temperatures up to 350 °C, which determine the stiffness of the molecular bridges between the NPs (Fig. 1). A detailed chemical view of the processes in the organic phase was also carried out by XPS and ultra-high vacuum infrared reflection absorption spectroscopy (UHV-IRRAS) during thermal treatment at DESY Nanolab (Fig. 1). The UHV-IRRAS of thermally treated sample at 350 °C shows the bands at 1377 cm⁻¹ and 1603 cm⁻¹, characteristic for symmetric and asymmetric carboxylate OCO-stretching modes, indicating oleic acid bonding with iron atoms via its oxygen atoms. The XPS measurements of the Fe 2p, O 1s and C 1s regions provide further evidence for thermally induced chemical changes in the iron oxide/oleic acid system. The magnetite phase is indicated after annealing at 300 °C by two

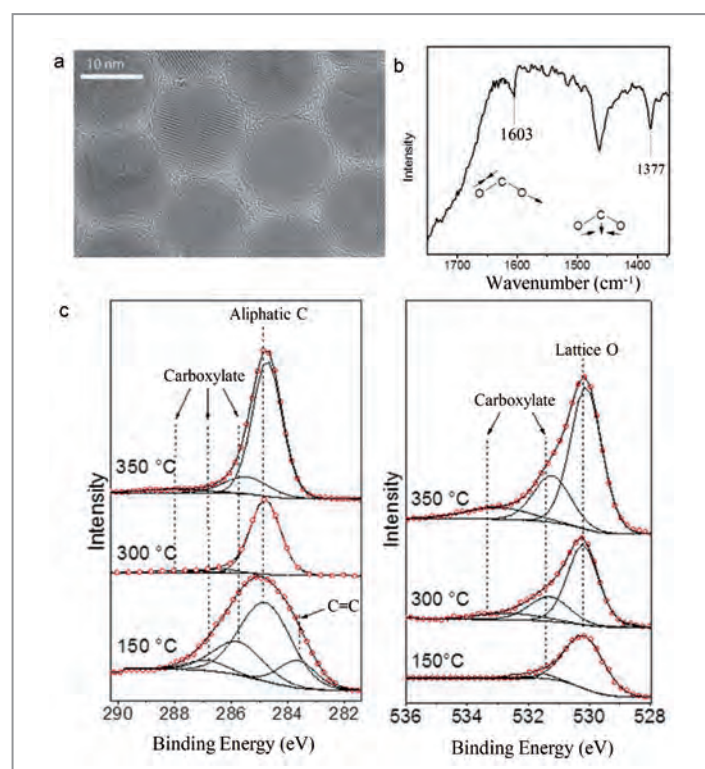


Figure 1

(a) TEM image of iron oxide NPs in a network of oleic acid. (b) UHV-IRRAS spectra of oleic acid on iron oxide particles at 350 °C. (c) XPS spectra of oleic acid on iron oxide particles during annealing and deconvoluted for the C 1s and O 1s regions.

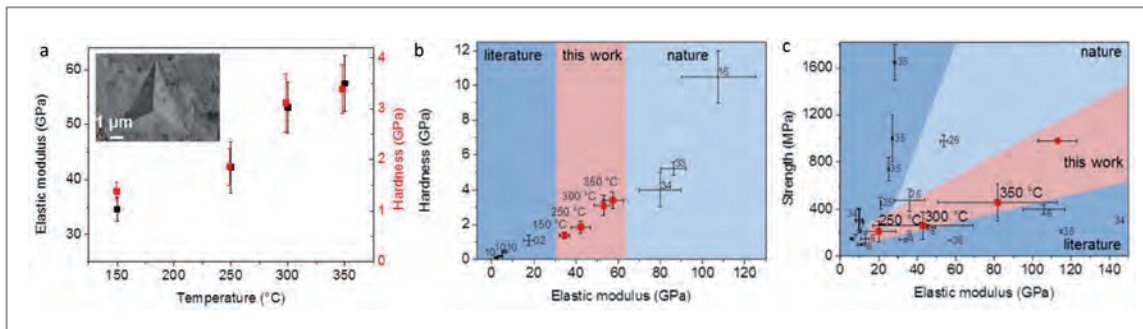


Figure 2

(a) Nanoindentation (inset) in the iron oxide / oleic acid nanocomposite shows an increase of the elastic modulus and hardness with increasing annealing temperature. (b,c) Comparison of our results with literature values and those of naturally occurring materials.

peaks at 710.6 eV and 724.1 eV, corresponding to Fe $2p_{3/2}$ and Fe $2p_{1/2}$, respectively. In the O 1s regions the iron oxide lattice oxygen and carboxylate groups (OCO) in oleic acid were detected at 530.0 eV and 533.2 eV. In the C 1s region the C sp^2 peak was observed at 283.9 eV at 150 °C and disappeared completely at higher temperatures, as shown in the IRRAS spectrum by the absence of C=C-stretching mode at 1640 cm^{-1} , showing the removal of oleic acid C=C double bonds during cross-linking reactions.

The main features of the tensile mechanical behaviour of the nanocomposites were explained using a nanomechanical model consisting of 15 nm thick magnetite layers bridged by 1 nm long cross-linked oleic acid molecules with an area density ρ_{cl} . From atomic force microscopy (AFM) and quantum chemistry calculations the elastic force (F)–strain (ϵ) relation for single alkane chains under tension and small strains is known to be $F = \gamma_1 \epsilon$ ($\gamma_1 = 28.7\text{ nN}$) [1]. With an area density ρ_{cl} of the nanoparticles bridging alkane chains, which represent the area density of cross-links, we get the stress–strain relation of cross-linked chains $\sigma = \rho_{cl} \gamma_1 \epsilon = E_{cl} \epsilon$ and hence their elastic modulus $E_{cl} = \rho_{cl} \gamma_1$. E_{cl} is identified with the experimentally determined elastic modulus E_{OA} of the oleic acid layer calculated from the measured modulus E_{comp} of our nanocomposite and the known magnetite elastic modulus, $E_{magnetite} = 163\text{ GPa}$ [2] applying a model of parallel oriented layers perpendicular to the loading direction. With the experimentally determined area density of the oleic acid ρ_{ol} the fraction of cross-links $f = \rho_{cl} / \rho_{OA}$ can be determined. Heat treatment increases the fraction of cross-links from 5 % to 46 %. The average breaking force F_{cl} of a bridging chain can be determined from the

measured strength of the nanocomposite as $F_{cl} = \sigma_c / \rho_{cl}$. This model is also able to predict the elastic behaviour as well as the strength of the nanocomposite.

The mechanical properties of the heat treated nanocomposites measured by micro-cantilever beams and micro-pillars, fabricated by a focused ion beam, display an increase of the nano-hardness from 1.39 to 3.39 GPa and the elastic modulus from 34.6 to 57.5 GPa with increasing temperature up to 350 °C. The bending strength of the samples treated at 350 °C reaches up to 630 MPa and 1074 MPa. To our knowledge these are the highest combined values of elastic modulus, strength and nanohardness ever reported for a synthetic bioinspired organic/inorganic nanocomposite, comparable to micro-cantilever beam and micro-pillar strengths and moduli values of enamel (Fig. 2) [3,4].

In this contribution, we have demonstrated an easy concept to link inorganic NPs in a well-ordered superstructure by soft organic molecules during a thermal process. As oleic acid is one of the most often used linker molecules for NPs this cross-linking process can be applied to a variety of nanoparticle systems. The nanostructure of our material resembles that of some types of biological hard tissue. As in nature, the wide range of possibilities to modify organic molecules will allow one to influence the macroscopic mechanical behaviour. This toolbox can render unprecedented mechanical properties possible, tailor-made for specific applications.

Contact: Heshmat Noei, Heshmat.noei@desy.de

Authors

Axel Dreyer¹, Artur Feld², Andreas Kornowski², Ezgi D. Yilmaz¹, Heshmat Noei³, Andreas Meyer², Tobias Krekeler⁴, Chengge Jiao⁵, Andreas Stierle^{3,6}, Volker Abetz^{2,7}, Horst Weller^{2,8,9} and Gerold A. Schneider¹

- Institute of Advanced Ceramics, Hamburg University of Technology, Hamburg, Germany
- Institute of Physical Chemistry, Hamburg University, Hamburg, Germany
- Deutsches Elektronen-Synchrotron DESY, NanoLab, Hamburg, Germany
- Electron Microscopy Unit, Hamburg University of Technology, Hamburg, Germany
- FEI Company, Eindhoven, The Netherlands
- Physics Department, Hamburg University, Hamburg, Germany
- Institute of Polymer Research, Helmholtz-Zentrum Geesthacht, Geesthacht, Germany
- Center for Applied Nanotechnology, Hamburg, Germany
- Department of Chemistry, Faculty of Science, King Abdulaziz University, Jeddah, Saudi Arabia

Original publication

'Organically linked iron oxide nanoparticle supercrystals with exceptional isotropic mechanical properties', Nature Materials 15, 522–528 (2016). DOI: 10.1038/nmat4553

References

- T. Hugel, M. Rief, M. Seitz, M. Gaub, H. E. Gaub, R. Netz, 'Highly Stretched Single Polymers. Atomic-Force-Microscope Experiments Versus Ab-Initio Theory', Phys. Rev. Lett. 94, 48301 (2005).
- H. J. Reichmann, S. D. Jacobsen, 'High pressure elasticity of natural magnetite crystal', Am. Min. 89, 1061 (2004).
- Z. Tang, N. A. Kotov, S. Magonov, B. Ozturk, 'Nanostructured artificial nacre', Nat. Mat. 2, 413 (2003).
- P. Podsiadlo, A. K. Kaushik, E.M. Arruda, A. M. Waas, B.S. Shim, J. Xu, H. Nandivada, B.G. Pumplin, J. Lahann, A. Ramamoorthy, N.A. Kotov, 'Ultrastrong and Stiff Layered Polymer Nanocomposites', Science, 318, 80–83 (2007).

A deep view inside intact biological cells.

Structural analysis by scanning X-ray nanodiffraction and ptychography

Biological cells contain highly ordered nanoscale structures. The typical thickness of whole cells of several micrometres makes it challenging to image and analyse these structures without sectioning or slicing the sample. Hard X-ray imaging provides a suitable approach to this problem due to the high penetration depth. We use a combination of ptychography and scanning X-ray nanodiffraction to quantitatively resolve cellular structures at the nanoscale. Employed sequentially, these techniques provide high-resolution real space and reciprocal space images while exposing the cells to a comparatively small radiation dose. The structural arrangement and diameter of keratin protein bundles inside epithelial cells was revealed and filament diameters and distances could be derived.

High resolution imaging of biological cells and their components is a crucial prerequisite for understanding cellular processes and function. Clearly, fluorescence-based techniques, including novel super-resolution methods and electron microscopy are the most successful and most widely used experimental tools in this context. Additionally, hard X-ray imaging is well suited to visualize such small (nanometres) structures in comparatively large objects (micrometres) due to the small wavelength and high penetration depth [1-3]. However, while the resolution is reaching the nanometre scale, even in the hard X-ray regime, the dose is increasing concomitantly. Thus, especially for biological and other radiation sensitive specimens, it is essential to develop strategies to overcome or reduce radiation damage.

We approached this intrinsic problem by combining two different X-ray techniques, namely ptychography and nano-diffraction. Over the last years, ptychography has been proven to be an excellent imaging technique and it is more and more applied in combination with complementary techniques such as

fluorescence imaging, Bragg diffraction or resonant scattering [4]. In ptychography, the sample is scanned through a coherent beam, recording a far-field diffraction pattern at each position of the scan. Appropriate overlap between the illuminations at adjacent scan points allows for the unambiguous reconstruction of the complex transmission function of the object by numerical phase retrieval algorithms. Here, we combined this versatile technique with scanning X-ray nanodiffraction.

The experiment was performed in a collaboration between scientists from the Institute of X-Ray Physics, University of Göttingen and DESY, Hamburg, at the nanofocus extension of beamline ID13 at the ESRF in Grenoble. The X-ray beam at a photon energy of 14.9 keV was focussed by refractive lenses. For the ptychography scans, which require a slightly increased beam size to reduce the number of required overlapping scan points, the sample was positioned 1 mm out of focus. By contrast, for the scanning X-ray nanodiffraction recordings, we moved the sample into the beam focus (see Fig. 1 for a sketch of the setup).

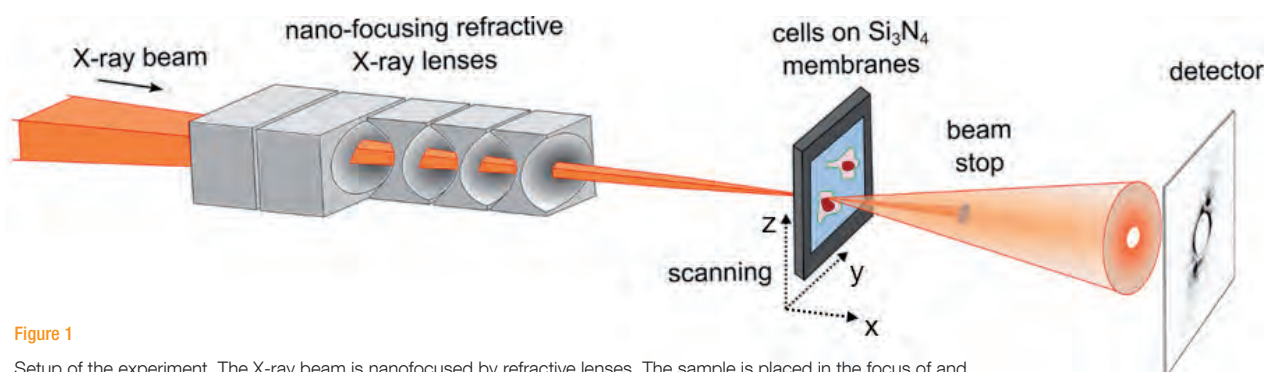


Figure 1

Setup of the experiment. The X-ray beam is nanofocused by refractive lenses. The sample is placed in the focus of and scanned through the beam to record a full diffraction pattern for each position. For the ptychography experiments the sample is moved out of focus to achieve a larger spot size on the sample.

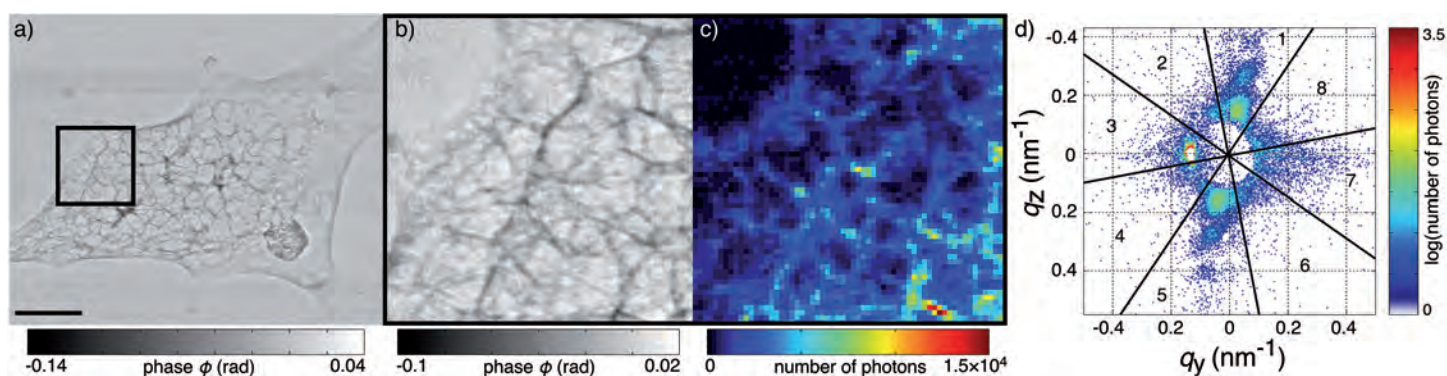


Figure 2

a) Ptychography image, scale bar 5 μm and b) detail from the region of interest shown by the black box in a). c) Dark-field image computed from scanning X-ray nanodiffraction of the same region, and d) example of one pixel from (c) showing an anisotropic diffraction signal.

Employing this combination of complementary techniques, we were able to record large fields of view at high real space resolution of 65 nm (Fig. 2a and b) utilizing a comparatively low dose of 10^3 Gy, avoiding radiation damage on the samples. Subsequently, we chose a region of interest and performed nanodiffraction scans for a more detailed structural analysis of these regions. Here, the reciprocal space resolution was considerably increased, allowing us to resolve structures as small as 10 nm, albeit at the expense of imposing considerably higher dose 10^8 Gy on the sample. The intensity values in the individual scattering patterns were integrated in order to derive dark-field-images (Fig. 2c) at an intermediate resolution, which corresponds to a beam size in the order of 100 nm. Further analysis of each individual pattern revealed a local scattering signal (Fig. 2d) which could be assigned to the specific position in the cell.

As a sample system we studied highly ordered, hierarchical protein bundle structures in biological cells. The mechanical properties of biological cells are to a greater part governed by the so-called cytoskeleton, a composite network of fibrous proteins. This present study focuses on keratin bundles, which in epithelial cells constitute one of the filament types. By fitting a hexagonally packed bundle model [5] to the data, the radius of individual filaments ($r = 5.5 \pm 0.7$ nm), the inter-filament distance ($a = 15.2 \pm 1.4$ nm) and the bundle diameter ($D = 72.0 \pm 5.5$ nm) could be derived. These values are in agreement with results from electron microscopy [6], but were obtained without slicing or staining the cell and are thus at a reduced risk of artefacts.

This study demonstrates the advantage of combining ptychography and scanning X-ray nanodiffraction in biological imaging since it provides nanometre resolution imaging of

specific cellular structures while avoiding pronounced radiation damage of the samples.

Contact: Sarah Köster, sarah.koester@phys.uni-goettingen.de
Christian Schroer, christian.schroer@desy.de

Authors

Clément Y. J. Hémonnot¹, Juliane Reinhardt², Oliva Saldanha¹, Jens Patommel³, Rita Graceffa¹, Britta Weinhausen⁴, Manfred Burghammer^{4,5}, Christian G. Schroer^{2,6} and Sarah Köster¹

1. Institute for X-Ray Physics, University of Göttingen, Göttingen, Germany
2. Deutsches Elektronen-Synchrotron DESY, Hamburg, Germany
3. Institute of Structural Physics, Technische Universität Dresden, Dresden, Germany
4. European Synchrotron Radiation Facility, Grenoble, France
5. Department of Analytical Chemistry, Ghent University, Ghent, Belgium
6. Institute for Nanostructure and Solid State Physics, Department of Physics, University of Hamburg, Hamburg, Germany

Original publication

'X-rays Reveal the Internal Structure of Keratin Bundles in Whole Cells', *ACS Nano* 10, 3553–3561 (2016), DOI: 10.1021/acsnano.5b07871

References

1. B. Weinhausen, J.-F. Nolting, C. Olendrowitz, J. Langfahl-Klabes, M. Reynolds, T. Salditt and S. Köster, 'X-Ray Nano-Diffraction on Cytoskeletal Networks', *New J. Phys.* 14, 085013 (2012).
2. B. Weinhausen, O. Saldanha, R. N. Wilke, C. Dammann, M. Priebe, M. Burghammer, M. Sprung and S. Köster, 'Scanning X-ray Nano-Diffraction on Living Eukaryotic Cells in Microfluidic Environments', *Phys. Rev. Lett.* 112, 088102 (2014).
3. V. Piazza, B. Weinhausen, A. Diaz, C. Dammann, C. Maurer, M. Reynolds, M. Burghammer and S. Köster, 'Revealing the Structure of Stereociliary Actin by X-Ray Nano-Imaging', *ACS Nano* 8, 12228–12237 (2014).
4. R. Hoppe, J. Reinhardt, G. Hofmann, J. Patommel, J.-D. Grunwaldt, C. D. Damsgaard, G. Wellenreuther, G. Falkenberg and C. G. Schroer, 'High-Resolution Chemical Imaging of Gold Nanoparticles Using Hard X-Ray Ptychography', *Appl. Phys. Lett.*, 102(20), 203104, (2013)
5. M. P. Priebe, S. Kalbfleisch, M. Tolkiehn, S. Köster, B. Abel, R. Davis and T. Salditt, 'Orientation of Biomolecular Assemblies in a Microfluidic Jet', *Biophys. J.* 107, 2662–2673 (2014).
6. J.-F. Nolting, W. Möbius and S. Köster, 'Mechanics of Individual Keratin Bundles in Living Cells', *Biophys. J.* 107, 2693–2699 (2014).

Exploiting crystal disorder to improve resolution.

New approach triggers paradigm shift in crystallography

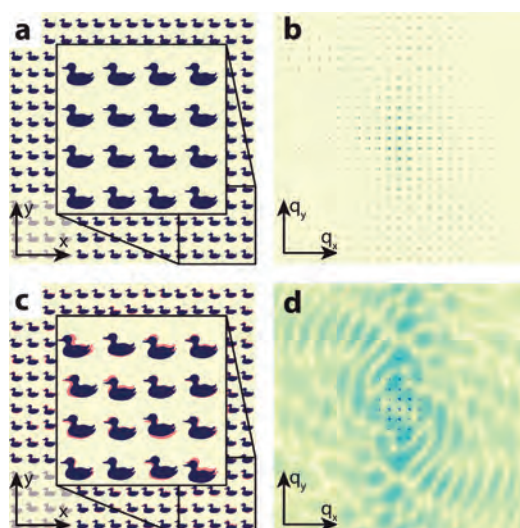
Translational disorder in crystals of biomolecules illuminated by coherent X-rays reveals a diffraction pattern of the continuous molecular transform that contains more structural information than obtainable using perfectly ordered crystals. We demonstrate this new 'diffractive imaging' approach using imperfect crystals of the macromolecular complex photosystem II.

The majority of protein structures are, in practice, elucidated by X-ray crystallography. Often the most difficult step in obtaining high-quality structures is production of high-quality crystals required for X-ray structure determination. High-quality crystals are necessary to ensure X-ray diffraction in the form of Bragg peaks extending to sufficiently large scattering angles and hence yielding information of sufficiently high resolution with which to solve the crystal structure. High-resolution Bragg diffraction from a crystal requires a high degree of regularity, which is often not obtained in practice. Indeed, crystals with reduced unit-cell volumes and tighter macromolecular packing often produce higher-resolution Bragg peaks, suggesting that crystallographic resolution for some macromolecules may be limited not by their heterogeneity, but by a deviation of strict positional ordering of the crystalline lattice. Various perturbations to perfect crystalline order limit the number of detectable peaks and therefore the resolution of the molecular image that can be obtained from Bragg peaks alone.

A perfectly ordered crystal would produce nothing but Bragg peaks. However, when individual molecules within the crystal

lattice are displaced with respect to a perfect lattice, their scattering no longer adds perfectly in phase. The resulting decoherence between scattered molecular transforms means that the scattered intensity from each molecule adds up in the detector plane rather than interfering with each other to produce Bragg peaks. The resulting signal is like accumulating signal from thousands of individual molecules each aligned with respect to each other, overcoming the weak signal problem of measuring diffraction from single (uncrystallised) molecules [1]. The crystal is essentially used as a way to get a lot of molecules into the beam that are aligned in a common orientation (Fig. 1).

We used the X-ray laser LCLS to measure imperfect micro-crystals of the membrane protein complex photosystem II (PSII) that is part of the photosynthesis machinery in plants. The diffraction patterns revealed a mixture of Bragg diffraction and continuous diffraction signals (Fig. 2). The continuous diffraction of the crystals stems from molecules in the crystal lattice that are located away from their ideal positions by as little as the width of a single atom. This continuous diffraction can be phased by adapting techniques from coherent diffraction imaging (Fig. 3) [2].



New analysis techniques had to be developed in order to analyse this data. A particularly robust method was to treat the Bragg and continuous diffraction as two distinct sources of data of the same structure, the first arising from a coherent interference of molecules in the unit cell, and the second due to the incoherent addition of aligned single-molecule diffraction.

Figure 1

The continuous molecular transform is revealed by introduction of translational disorder into the crystal lattice. Diffraction from an arrangement of objects in a perfect lattice (a) results in regularly spaced Bragg peaks (b) as a result of constructive interference. Translational disorder of the objects (c) disrupts Bragg interference beyond a certain reciprocal-lattice resolution length (d). The loss of correlation instead gives rise to the incoherent sum of the Fraunhofer diffraction patterns of individual objects, which increases with photon momentum transfer q in balance with the diminishing Bragg intensities.

Starting with a known search model for PSII, we first produced an electron density map of the PSII dimer by molecular replacement phasing to a resolution of 4.5 Å, limited by the angular extent of the Bragg peaks. This map was then used to generate a low-resolution binary mask of the smoothed molecular envelope of a single PSII dimer, forming the real-space constraint used to generate a 3D image of the electron density of the PSII dimer by iterative phasing of the continuous diffraction using the ‘difference-map’ algorithm [2] over the resolution range of 4.5 – 3.3 Å. After convergence, Fourier amplitudes and phases over the entire resolution range were combined to synthesize a 3.3-Å resolution structure.

Averaging solutions obtained over multiple random starts to eliminate phase bias produced a self-consistent electron density to a resolution of 3.5 Å. Regions of the final electron density map are noticeably superior to the same regions generated using the Bragg peaks alone. In particular, helices show better definition in side-chains, and the model better follows the electron density as seen in Fig. 3. The improvement in resolution is quantified by metrics such as the R_{free} factor at low resolution.

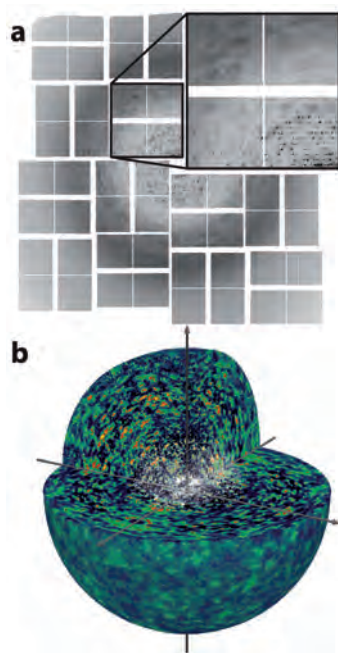


Figure 2

Molecular coherent diffraction revealed from crystals of photosystem II with translational disorder. (a) An XFEL snapshot ‘still’ diffraction pattern of a PSII microcrystal shows a weak speckle structure beyond the extent of Bragg peaks, which is enhanced in this figure by limiting the displayed pixel values. (b) A rendering of the entire 3D diffraction volume assembled from 2,848 still patterns. Speckles are clearly observed beyond the 4.5-Å extent of Bragg diffraction (visualised by the white dots). This continuous speckle can be phased using iterative algorithms from the field of coherent diffractive imaging to recover the molecular structure.

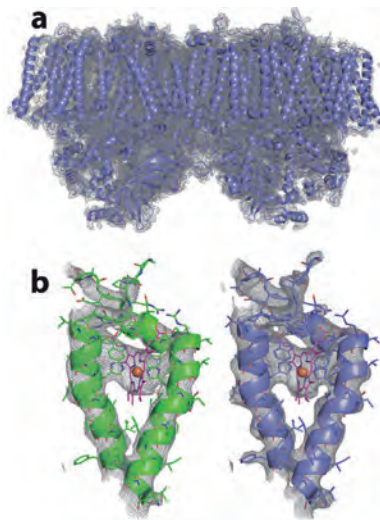


Figure 3

Improvement in resolution and quality of electron density obtained by phasing the continuous transform using coherent diffractive imaging methods. (a) Electron density map obtained to 3.5 Å resolution by iterative phase retrieval on the continuous diffraction data using support constraint (molecular envelope). The map is contoured at 1σ . (b) Electron density maps of a region of the PSII dimer, using only the Bragg diffraction (models shaded green), and the Bragg and continuous diffraction (models shaded blue), showing the haem group of PsbE/F, contoured at 1.25σ .

It is interesting to note that similar continuous diffraction has actually been seen for a long time from many different poorly diffracting crystals. It simply wasn’t appreciated that you can get static structural information from it and so analysis techniques suppressed it. In principle, as well as improving the resolution, this additional information is sufficient to uniquely solve the phase problem without having to resort to other measurements or assumptions.

This novel concept for molecular imaging thus leads to a paradigm shift in crystallography — the most ordered crystals are not necessarily the best. Instead, looking between Bragg peaks may provide a much richer source of structural information. With imperfect, translationally-disordered crystals, the continuous diffraction fills in the gaps between and beyond the Bragg peaks, giving vastly more information than in normal crystallography. For some crystals we now have access to single molecule diffraction that has not previously been directly accessible in crystallography.

Contact: Kartik Ayyer, kartik.ayyer@cfel.de
 Anton Barty, anton.barty@cfel.de
 Henry Chapman, henry.chapman@cfel.de

Authors

Kartik Ayyer¹, Oleksandr M. Yefanov¹, Dominik Oberthür², Shatabdi Roy-Chowdhury^{3,4}, Lorenzo Galli^{1,2}, Valerio Mariani¹, Shibom Basu^{3,4}, Jesse Coe^{3,4}, Chelsie E. Conrad^{3,4}, Raimund Fromme^{3,4}, Alexander Schaffer^{3,4}, Katerina Dörner^{1,3}, Daniel James^{4,5}, Christopher Kupitz^{2,6}, Markus Metz², Garrett Nelson^{4,5}, Paulraj Lourdu Xavier^{1,2}, Kenneth R. Beyerlein¹, Marius Schmidt⁶, Iosifina Sarrou⁷, John C. H. Spence^{4,5}, Uwe Weierstall^{4,5}, Thomas A. White¹, Jay-How Yang^{3,4}, Yun Zhao^{4,5}, Mengning Liang⁸, Andrew Aquila⁸, Mark S. Hunter⁸, Joseph S. Robinson⁸, Jason E. Koglin⁸, Sébastien Boutet⁸, Petra Fromme^{3,4}, Anton Barty¹ and Henry N. Chapman^{1,2,9}

1. Center for Free-Electron Laser Science CFEL, DESY, Hamburg, Germany.
2. Department of Physics, University of Hamburg, Hamburg, Germany.
3. School of Molecular Sciences, Arizona State University, Tempe, Arizona, USA.
4. Center for Applied Structural Discovery, Biodesign Institute, Arizona State University, Tempe, Arizona, USA.

5. Department of Physics, Arizona State University, Tempe, Arizona, USA.
6. Physics Department, University of Wisconsin, Milwaukee, Wisconsin, USA.
7. Institute of Molecular Biology and Biotechnology, Foundation for Research and Technology, Hellas, Greece.
8. Linac Coherent Light Source, Stanford Linear Accelerator Center (SLAC), National Accelerator Laboratory, Menlo Park, California, USA.
9. Centre for Ultrafast Imaging, University of Hamburg, Hamburg, Germany.

Original publication

‘Macromolecular diffractive imaging using imperfect crystals’, *Nature* 530, 202–206 (2016). DOI: 10.1038/nature16949

References

1. J. M. Cowley, ‘Diffraction Physics’ (North-Holland, 1981).
2. V. Elser and R. P. Millane, ‘Reconstruction of an object from its symmetry-averaged diffraction pattern’, *Acta Cryst. A* 64, 273–279 (2008).

Crystal structure of Zika virus protease.

Complex with an inhibitor suggests routes to antiviral drug design

The present Zika virus outbreak in the Americas is associated with a dramatically increased number of neurological disorders in patients as well as fetal microcephaly. Therefore, the World Health Organization has declared this situation a 'Public Health Emergency of International Concern'. In order to provide a basis for the design of antiviral drugs, the Zika virus NS2B-NS3 protease, an enzyme essential for viral replication, was crystallised and its X-ray structure was determined using diffraction data collected at the PETRA III beamline P11. The structure reveals the active conformation of the protease, achieved by co-crystallisation with a boronic-acid inhibitor.

Discovered almost 70 years ago in the Zika Forest in Uganda [1], the Zika virus (ZIKV) was considered relatively harmless for humans in the past few decades. Up to 2007, only a total of 12 human cases of ZIKV infection were reported from Nigeria, Gabon, Malaysia, Indonesia and India. The symptoms were usually mild and included rash and medium to high fever. Already in 1947, mosquitos of the *Aedes* family had been identified as vectors for the virus. In 2007, an explosive outbreak of ZIKV occurred on the Pacific island of Yap, where up to 1/3 of the population were diagnosed as infected. This was followed by a major outbreak in French Polynesia, also in the Pacific Ocean, in 2013. However, the virus only gained broad attention when it reached the South American continent in 2014, causing the massive outbreak in Brazil and other Latin American countries that is still ongoing. Meanwhile,

ZIKV infections have been reported from over 65 countries worldwide, most recently from Singapore, Thailand, and Vietnam. It is estimated that one third of the world's population is at risk of contracting the virus. This is indeed very alarming as it has been recognized in 2015 and recently verified that ZIKV infection of pregnant women can lead to microcephaly (small head size with underdeveloped brain) of the newborn child and also that the virus directly attacks neuronal cells, causing diseases such as Guillain-Barré syndrome.

Zika virus belongs to the genus *Flavivirus*, along with other highly pathogenic, mosquito-borne viruses such as Yellow Fever Virus, Dengue Virus, West Nile Virus (WNV), and Japanese Encephalitis Virus. All these viruses feature a genome consisting of single-stranded RNA, which is directly translated into a huge polyprotein comprising about 3400 amino-acid residues. This polyprotein is cleaved by host-cell proteases and by the viral NS2B/NS3 protease into 3 structural proteins that form the capsid of the newly budding virus, and 7 non-structural (NS) proteins that constitute the replication complex responsible for copying the RNA. The viral protease, NS2B/NS3^{pro}, is thus part of this polyprotein itself and splices itself out of it, before it acts on other cleavage sites in the polyprotein. Accordingly, blocking the viral protease would prevent replication of the Zika virus; hence, NS2B/NS3^{pro} is an attractive target for antiviral drug discovery.

The NS3^{pro} component is a serine protease carrying the usual catalytic triad consisting of serine, histidine, and aspartic acid residues, but it has very little catalytic activity in the absence of its cofactor protein, NS2B. The latter is to a major part embedded in the membrane of the endoplasmic reticulum (ER) of the flavivirus-infected host cell and anchors the replication complex to this membrane. However, by identifying a stretch of about 45 hydrophilic amino-acid residues of

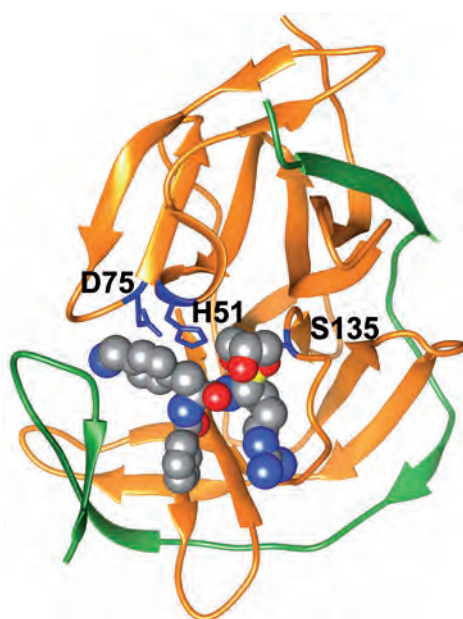


Figure 1
Three-dimensional structure of Zika virus NS2B-NS3 protease. The main chain of the NS3 protease and its NS2B cofactor are shown as orange and green ribbons, respectively. Catalytic residues Ser135, His51, and Asp75 are indicated in blue. The peptidomimetic boronate inhibitor is shown in a space-filling mode, with the boron atom in yellow, carbon in grey, nitrogen in blue, and oxygen in red.

NS2B, it was possible to nail down the region of the cofactor protein that activates NS3^{pro}. A stable construct (NS2B-NS3^{pro}) that had the cofactor region of NS2B connected via a covalent linker to NS3^{pro} proved a good model for flavivirus proteases [2]. We found that for the Zika virus enzyme, this construct, when produced in *E. coli* bacteria via genetic engineering, was hyperactive towards some standard substrates. Thus, its activity was 20-fold higher compared to that of the related WNV protease construct. A more active viral protease cannot only lead to faster replication of the virus, but also to a more efficient degradation of the innate immune response of the infected host cells, because flavivirus proteases have been shown to interfere with the production of the antiviral agents α - and β -interferon by cleaving components of the signal cascades leading to its activation [3]. Therefore, we hoped that the three-dimensional structure of ZIKV protease would reveal the molecular basis for the observed catalytic hyperactivity.

We obtained crystals of the ZIKV NS2B-NS3 protease in complex with a peptidomimetic boronic-acid inhibitor by screening thousands of conditions with the help of a crystallisation robot. Diffraction data collected at PETRA III beamline P11 corresponded to a resolution of 2.8 Å, but indicated serious merohedral twinning - superimposition of more than one lattice in the crystal. Fortunately, this problem could be handled by using advanced software that deconvoluted the lattices. The crystallographic phase problem was solved by using the method of molecular replacement and a core of the NS3^{pro} domain of the related West Nile Virus protease [4] as a search model. In successive rounds of model building and crystallographic refinement, the NS2B chain of ZIKV protease and the boronic-acid inhibitor were located in the electron density maps. The NS2B chain was found to embrace the NS3^{pro} core, making important interactions by completing the N-terminal β -barrel and the S2 substrate-binding site of the NS3^{pro} (Fig. 1). The enzyme structure thus revealed the active form of the protease, which is only observed in the presence of inhibitors (or substrate), whereas in the inactive form, NS2B is only loosely coupled to NS3^{pro}. The boronic-acid inhibitor was found to have reacted with glycerol (which was present during purification and crystallization of the protease), to yield a cyclic diester boronate. This observation alone suggested many new ideas on how to

modify the boronic acids to decrease their hydrophilicity and improve their membrane-traversing properties, so as to ensure cell permeability of these antivirals.

A strong and unique interaction between residue Asp83 of ZIKV NS2B and the positively charged P2 residue (usually lysine or arginine) of the substrate (Fig. 2) was suspected to be the cause of the enzyme's hyperactivity, and indeed, when this aspartic-acid residue was replaced by asparagine (by site-directed mutagenesis), the catalytic activity dropped by almost 30%. This observation is being confirmed with other substrates.

The new crystal structure is now used by many researchers, including ourselves, to design the first antiviral drugs targeting Zika virus.

Contact: Rolf Hilgenfeld, hilgenfeld@biochem.uni-luebeck.de

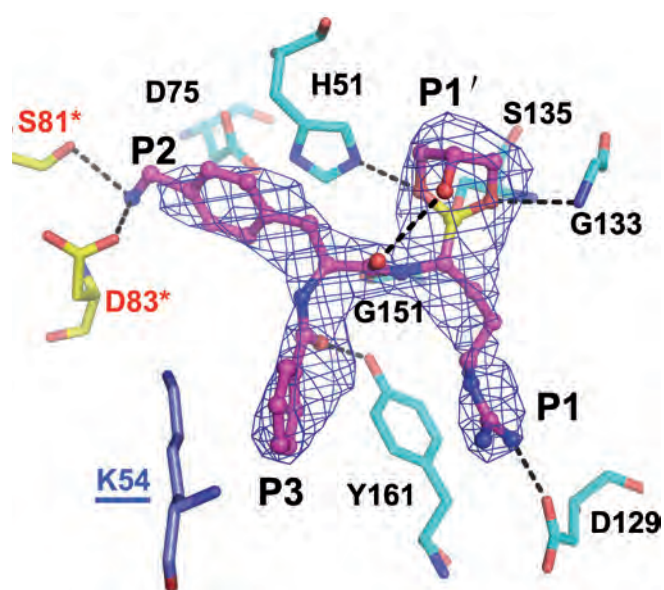


Figure 2 Details of the boronate inhibitor binding to the active site of Zika virus NS2B-NS3 protease. Carbon atoms are cyan in the NS3^{pro} chain, yellow in the NS2B cofactor, purple in the inhibitor. Other atom colours are yellow for boron, blue for nitrogen, and red for oxygen. Hydrogen bonds are indicated by dashed lines. Selected amino-acid residues interacting with the inhibitor are labeled using the single-letter code. Residues of the cofactor NS2B are labeled by an asterisk (*).

Authors

Jian Lei^{1,2}, Guido Hansen¹, Christoph Nitsche³, Christian D. Klein³, Linlin Zhang^{1,2} and Rolf Hilgenfeld^{1,2}

1. Institute of Biochemistry, Center for Structural and Cell Biology in Medicine, University of Lübeck, Lübeck, Germany
2. German Center for Infection Research (DZIF), Hamburg-Lübeck-Borstel-Riems Site, University of Lübeck, Lübeck, Germany
3. Medicinal Chemistry, Institute of Pharmacy and Molecular Biotechnology, Heidelberg University, Heidelberg, Germany

Original publication

'Crystal structure of Zika virus NS2B-NS3 protease in complex with a boronate inhibitor', *Science* 353, 503–505 (2016). DOI: 10.1126/science.aag2419

References

1. G. W. A. Dick, 'Zika virus. II. Pathogenicity and physical properties', *Trans. Roy. Soc. Trop. Med. Hyg.* 46, 521–534 (1952)
2. D. Leung, K. Schroder, H. White, N. X. Fang, M. J. Stoermer, G. Abbenante, J. L. Martin, P. R. Young, D. P. Fairlie, 'Activity of recombinant dengue 2 virus NS3 protease in the presence of a truncated NS2B co-factor, small peptide substrates, and inhibitors', *J. Biol. Chem.* 276, 45762–45771 (2001).
3. S. Aguirre, A. M. Maestre, S. Pagni, J. R. Patel, T. Savage, D. Gutman, K. Maringer, D. Bernal-Rubio, R. S. Shabman, V. Simon, J. R. Rodriguez-Madoz, L. C. Mulder, G. N. Barber, A. Fernandez-Sesma, 'DENV inhibits type I IFN production in infected cells by cleaving human STING', *PLoS Pathog.* 8, e1002934 (2012).
4. M. Z. Hammamy, C. Haase, M. Hammami, R. Hilgenfeld, T. Steinmetzer, 'Development and characterization of new peptidomimetic inhibitors of the West Nile virus NS2B-NS3 protease', *ChemMedChem* 8, 231–241 (2013).

The inhibition mechanism of human 20S proteasomes.

Human proteasome structures

The proteasome is a validated target for anti-cancer therapy and proteasome inhibition is employed in the clinic for tumor and hematological malignancy treatment. We determined crystal structures of the human 20S proteasome and its complexes with drugs that are either approved for cancer treatment or are in clinical trials. The structures - at unprecedented resolutions - allow direct observation of inhibition mechanisms that differ from earlier models determined at lower resolution. The high-resolution structures provide new insights into the catalytic mechanisms of inhibition and necessitate a revised description of the proteasome active site. This provides insights into peptide hydrolysis and can guide strategies for the development of next-generation proteasome-based cancer therapeutics.

Proteasomes play a major role in cytosolic and nuclear proteolysis and are central to cellular physiology and growth [1]. The inhibition of proteasomes is an efficient strategy for restricting cancer growth. The development of new proteasome inhibitors is currently hampered by a lack of structural knowledge of ligand binding sites and by a lack of understanding the biochemical mechanisms underlying proteasome inhibition. The proteasome is a large macromolecular complex (750 kDa), with an overall architecture that is defined by four stacked hetero-heptameric rings (Fig. 1A). Most of the current structural knowledge about the proteasome and its binding sites for inhibitors comes from studies of the yeast proteasome [2]. The first human 20S proteasome structures in complex with inhibitors were determined by X-ray crystallography and cryo-electron microscopy at 2.9 and 3.5 Å resolution recently [3, 4], albeit direct observation of the atomic details of inhibition was not possible at the attained resolutions.

To obtain structural information at higher resolution, we established an optimized and robust pipeline for the production, purification, and crystallization of human 20S proteasomes that allows hundreds of crystals to be grown which routinely diffract to high resolution. Summarized this pipeline consist in:

- 1) A chromatography-free purification procedure at constant ionic strength was introduced yielding stable complexes with 10 fold higher specific enzymatic activity than previously reported.
- 2) The protein purification buffer was optimized by the ProteoPlex method and is identical to the crystallization buffer [5].
- 3) New crystallization condition allowed growing crystals to typical dimension of 150x150x200 μm^3 within 20 hours at 18°C belonging to space group 2₁2₁2₁.
- 4) Post-crystallization treatments performed at 4°C yield complete, isotropic diffraction datasets to better than 2.0 Å resolution using 'top-hat' beam profiles defined by compound refractive lenses on beamline P14 at the PETRA III storage ring.

We first determined the crystal structure of the native human 20S proteasome at 1.8 Å resolution. Second, crystal structures of inhibitor complexes of the human 20S proteasome and clinically relevant inhibitors were elucidated in the resolution range of 1.9 - 2.1 Å giving rise to a revised view of the inhibition chemistry. The final crystallographic maps of the native structure revealed exceptionally clear electron densities. At 1.8 Å resolution, a number of functionally important differences with respect to the previously published 20S proteasome structures become visible. Notably, a solvent molecule, previously assigned as catalytic water (NUK) [6], was identified

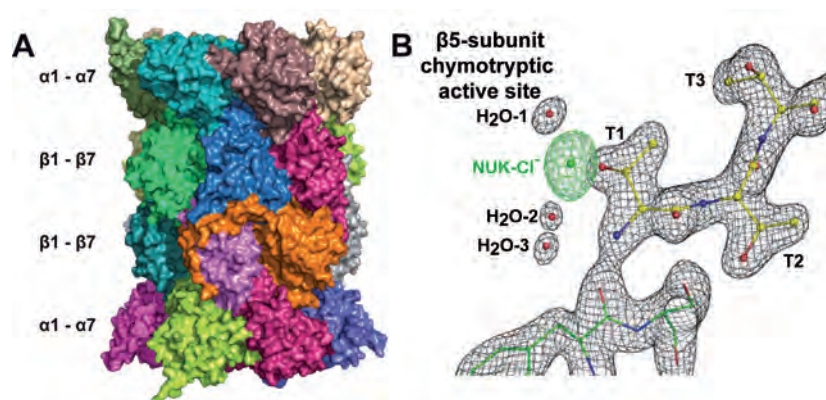


Figure 1

A) Space filling representation of the human 20S proteasome. The four coaxially stacked hetero-heptameric rings, the outer two consisting of α subunits (α 1-7) and the inner two formed by β -subunits (β 1-7) are indicated in individual colors. B) Close-up view of the chymotryptic (β 5) active site. Shown are Thr1, Thr2 and Thr3 along with three H_2O molecules and the corresponding electron density map. The NUK solvent molecule was identified to be a chloride (green sphere). From original publication, reprinted with permission from AAAS.

as a chloride ion in all active sites (Fig. 1B) and three additional, localized water molecules (H₂O-1, -2, and -3), are visualized in the proteasome active site.

The most prominent differences were observed in the β 5 active site of the 1.9 Å proteasome-Oprozomib co-crystal structure. It had been previously suggested that the proteasome active site Thr1 reacts with both the ketone moiety and the carbon atom in α position of the epoxyketone inhibitor, allegedly to form a 6-membered ring product [3, 7]. In our Oprozomib-human 20S proteasome structure (Fig. 2A) we were unable to confirm this reaction mode. The cyclic moiety could only be modelled as a 7-membered ring structure, as a consequence of Thr1's reaction with the ketone and the carbon atom in β position of the epoxyketone inhibitor. To explore the structural implications of a 6-ring linkage, we determined the structure of the human 20S proteasome inhibited by Z-LLY-Ketoaldehyde at 2.1 Å resolution (Fig. 2B). In this case, the electron density can indeed be interpreted by a 6-membered ring, albeit without the abstraction of water from the carbinolamine moiety as previously reported [8].

In order to better understand the proteasome inhibition mechanism, we performed cluster quantum chemical calculations (Fig. 2C). Our results indicate that the 7-ring pathway is kinetically favored. Thermodynamically, the 6-ring is more stable, but the strain of the transition state results in a preferential 7-ring formation. This was corroborated by enzymatic measurements (Fig. 2D): The first-order inhibition rate constant for the 6-ring is ~20-fold smaller than for the 7-ring.

The insights into the atomic details of the catalytic center of the human 20S proteasome, target of cancer therapeutics, provide important clues for the design of a new class of proteasome inhibitors. Our results suggest that dual-electrophile inhibitors, where both electrophiles are in a β position to each other, would exhibit kinetically enhanced inhibition rates.

Contact: Ashwin Chari, ashwin.chari@mpibpc.mpg.de
Gleb Bourenkov, gleb@embl-hamburg.de

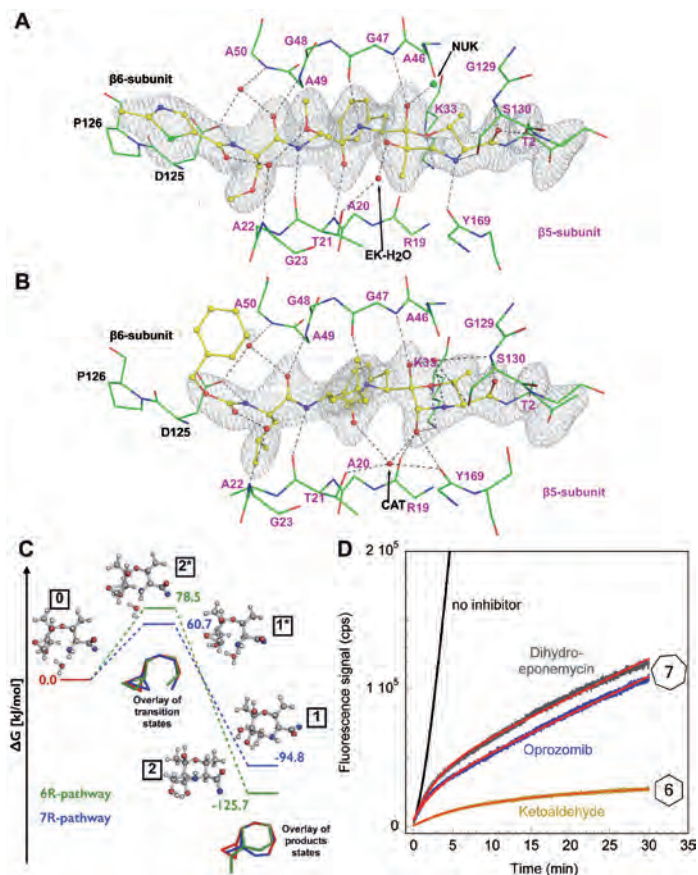


Figure 2

A) Illustrated is the Oprozomib inhibited β 5 active site, along with an omit map contoured for the inhibitor, the cyclic linkage and β 5Thr2. The main chain segments of β 5 residues are indicated along with the β 5 and β 6 side chains as sticks (green carbon). The respective inhibitors covalently attached to Thr1 are depicted in ball-and-stick representation (yellow carbon, red oxygen, blue nitrogen and green sulfur). The NUK chloride is shown as a green dot. Dashed lines signify hydrogen bonds (≤ 3.2 Å distance). Note the clear density for a 7-ring linkage. B) Illustrated is the Ketoaldehyde inhibited β 5 active site. The notation is the same as in A). Note the clear density for a 6-ring linkage. C) Computed reaction pathways including a schematic overlay of the starting state structure (red) and the stationary points. The 7-ring reaction pathway proceeds from '0' through '1*' to '1', whereas the 6-ring reaction pathway proceeds from '0' through '2*' to '2'. D) Kinetic analyses of the first-order inactivation rate constants for the 6-ring forming ketoaldehyde, and for the 7-ring forming Dihydro-eponemycin and Oprozomib indicates that 7-ring formation occurs kinetically faster (fits shown in red). From original publication, reprinted with permission from AAAS.

Authors

Jil Schrader^{1,†}, Fabian Henneberg^{1,†}, Ricardo Mata², Kai Tittmann³, Thomas R. Schneider⁴, Holger Stark¹, Gleb Bourenkov¹ and Ashwin Chari¹

1. Department of Structural Dynamics, Max Planck Institut für Biophysikalische Chemie, Göttingen, Germany.
 2. Computational Chemistry and Biochemistry Group, Institut für Physikalische Chemie, Georg-August-Universität, Germany.
 3. Göttinger Zentrum für Molekulare Biowissenschaften & Schwann-Schleiden-Forschungszentrum, Georg-August-Universität Göttingen, Göttingen, Germany.
 4. EMBL Hamburg, c/o Deutsches Elektronen-Synchrotron (DESY), Hamburg, Germany.
- [†] These authors contributed equally to this work

Original publication

'The inhibition mechanism of human 20S proteasomes enables next-generation inhibitor design', *Science* 353, 594-598 (2016). DOI:10.1126/science.aaf8993

References

1. A. Ciechanover, 'The ubiquitin-proteasome proteolytic pathway', *Cell* 79, 13-21 (1994).
2. E. Kish-Trier and C. P. Hill, 'Structural biology of the proteasome', *Annu. Rev. Biophys.* 42, 29-49 (2013).
3. W. Harshbarger, C. Miller, C. Diedrich and J. Sacchettini, 'Crystal structure of the human 20S proteasome in complex with carfilzomib', *Structure* 23, 418-424 (2015).
4. P. C. da Fonseca and E. P. Morris, 'Cryo-EM reveals the conformation of a substrate analogue in the human 20S proteasome core', *Nat. Commun.* 6, 7573 (2015).
5. A. Chari et al., 'ProteoPlex: stability optimization of macromolecular complexes by sparse-matrix screening of chemical space', *Nat. Methods* 12, 859-865 (2015).
6. M. Groll et al., 'Structure of 20S proteasome from yeast at 2.4 Å resolution', *Nature* 386, 463-471 (1997).
7. M. Groll, K. B. Kim, N. Kairies, R. Huber and C. M. Crews, 'Crystal structure of epoxomicin: 20S proteasome reveals a molecular basis for selectivity of α' , β' -epoxyketone proteasome inhibitors', *J. Am. Chem. Soc.* 122, 1237-1238 (2000).
8. M. A. Grawert et al., 'Elucidation of the α -keto-aldehyde binding mechanism: a lead structure motif for proteasome inhibition', *Angew. Chem. Int. Ed. Engl.* 50, 542-544 (2011).

Proteins in action.

Femtosecond structural dynamics in photoactive yellow protein

Serial femtosecond crystallography using intense femtosecond-duration pulses from an X-ray free-electron laser enables studies of light-triggered dynamics in photosensitive proteins.

The majority of macromolecular structures are obtained using the method of X-ray crystallography and the majority of those structures are static, representing just one state of the molecule. However, most proteins are dynamic, changing their structure as they carry out their biochemical function. The visualisation of these changes is required to understand biological function – obtaining movies of molecules in action.

Photoactive yellow protein (PYP) undergoes structural and conformational changes on femtosecond timescales in response to light. Its chromophore, p-coumaric acid (pCA), can be photoexcited by absorbing a photon, which initiates a reversible photocycle involving numerous reaction intermediates (Fig. 1a). The primary event that controls entry into the photocycle is the isomerisation of pCA about its C₂=C₃ bond (Fig. 1b). Although structural changes on timescales longer than 100 ps have been investigated by time-resolved Laue crystallography at synchrotrons [1], elucidating faster structural dynamics requires the use of shorter duration X-ray pulses to probe the structure. Previous experiments at the Linac Coherent Light Source (LCLS) [2] established that the structure of reaction intermediates for PYP could be obtained from time-resolved difference electron density (DED) maps to

near-atomic resolution, by using free-electron laser (FEL) X-ray pulses, and diffraction from microcrystals to maximize the extent of reaction initiation. The challenge was to extend this to femtosecond timescales.

Acquiring diffraction data from a stream of nanocrystals with highly brilliant femtosecond pulses delivered by X-ray FELs overcomes many of the limitations of previous large-crystal studies. Serial femtosecond crystallography (SFX), as it has come to be known, avoids conventional radiation damage by using X-ray pulses that are shorter than the timescale of most damage processes, while each crystal is exposed to the beam only once before being discarded, meaning that radiation damage does not accumulate [3, 4]. Furthermore, the high peak power of FEL pulses enables the study of micron-sized crystals, which can be more uniformly excited by the laser. And of course, the 40-femtosecond duration X-ray pulses available from FELs enable measurements on much shorter timescales than are accessible at synchrotron sources.

To achieve femtosecond time resolution, electronic excitation in PYP microcrystals was initiated by femtosecond laser pulses of 450 nm wavelength and 140 fs duration, and the light induced structural changes probed with 40 fs X-ray FEL pulses at 9 keV (1.36 Å wavelength) using the Coherent X-ray Imaging (CXI) instrument of the LCLS. The arrival times of the optical and X-ray laser pulses had to be synchronized on the femtosecond timescale in order to achieve femtosecond time resolution. In practice, the X-rays and optical laser jitter with respect to each other on timescales of about 280 fs. To beat this limit, the relative arrival time of pump laser and X-ray pulses was measured for every pulse and was combined with

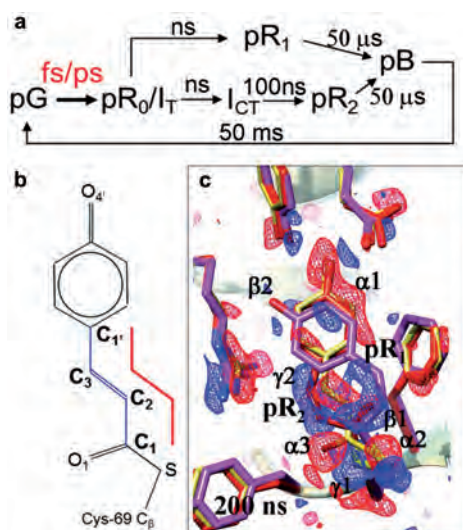


Figure 1

Structural dynamics of PYP. (a) Simplified photocycle of PYP. Ground state pG is activated by absorption of a blue photon to a transient state pR₀ that begins the photocycle on sub-picosecond timescales. Longer lived intermediates are well characterized by pump-probe Laue diffraction. (b) The chemical structure of the pCA chromophore. (c) Weighted DED map at 200 ns time delay showing positive (blue) and negative (red) features. The structure is a mixture of pR₁ (red) and pR₂ (magenta) intermediates.

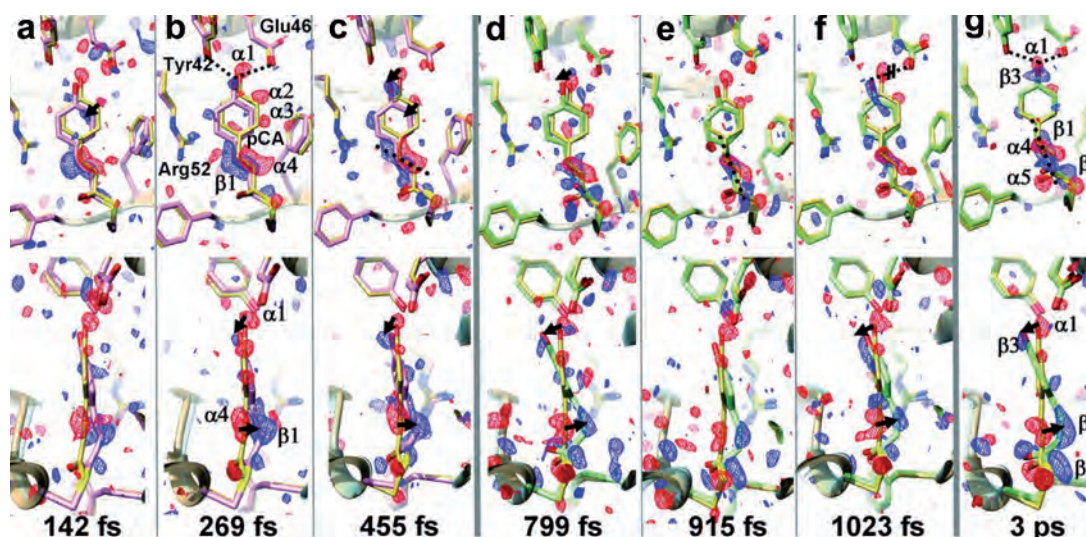


Figure 2

Trans-to-cis isomerisation in PYP. Weighted DED maps with positive (blue, $+3\sigma$) and negative (red, -3σ) features shown in front (upper) and side (lower) views. Time delays and chromophore configurations (a)-(c) are before trans-to-cis isomerisation and (d)-(g) after the transition. The $C_2=C_3$ bond is shown by a dashed line in the twisted trans state in (c), and the cis state in (e) and (g).

adjustments to account for experimental drifts, thus associating a definite ‘time-stamp’ with every diffraction pattern. In this way the data could be post-sorted into diffraction pattern ‘time bins’, with time delays ranging from 100 fs to 1000 fs, obtained using nominal time delays of only 300 fs and 600 fs. Since the quality of calculated DED maps depends on the number of snapshots, we chose to divide the data into eight pump-probe delays, each with about 40,000 snapshots. Reaction initiation by the pump laser was verified by a positive control experiment with a 200 ns pump-probe time delay, showing well characterized positive and negative DED features between the reference (dark) and excited (light) states (Fig. 1c), which match previous synchrotron studies at similar time resolution.

Difference structure factor amplitudes and weighted DED maps were calculated from SFX amplitudes for the different delays using a ‘dark’ reference, measured by setting the optical pulse to arrive 1 ps after the X-rays. Upon visual inspection of DED maps it was found that the features in all maps at delays less than 500 fs were similar (Fig. 2a-c), and those at delays more than 700 fs were similar (Fig. 2d-f), but different from those in maps at less than 500 fs delay, thus suggesting that the trans-to-cis isomerisation takes place between 500 fs and 700 fs. To characterize the transition and

involved timescales in more detail, the data were binned into narrower time bins, containing about 20,000 snapshots each, and the resultant DED maps subjected to singular value decomposition [5], which separates the time and space components. This analysis showed that the fastest evolution of the structure starts less than 200 fs after excitation, and the trans-to-cis isomerisation takes place around 550 fs. This transition was further confirmed by iterative refinement of the phases associated with the observed difference structure factor amplitudes, using initial structural constraints derived from quantum mechanics/molecular mechanics (QM/MM) calculations.

These results for PYP demonstrate that time resolved SFX at FELs has great potential to elucidate elementary reaction mechanisms and structural dynamics in biomolecules on timescales ranging from milliseconds to tens of femtoseconds. Efforts are already underway to explore ultrafast kinetics and dynamics of chemically triggered reactions in a wide range of biologically and pharmaceutically important proteins.

Contact: Kanupriya Pande, kanupriya.pande@cfel.de
 Anton Barty, anton.barty@cfel.de
 Henry Chapman, henry.chapman@cfel.de
 Marius Schmidt, smarius@uwm.edu

Authors

Kanupriya Pande, Christopher D. M. Hutchison, Gerrit Groenhof, Andy Aquila, Josef S. Robinson, Jason Tenboer, Shibom Basu, Sébastien Boutet, Daniel P. DePonte, Mengning Liang, Thomas A. White, Nadia A. Zatsepin, Oleksandr Yefanov, Dmitry Morozov, Dominik Oberthuer, Cornelius Gati, Ganesh Subramanian, Daniel James, Yun Zhao, Jake Koralek, Jennifer Brayshaw, Christopher Kupitz, Chelsie Conrad, Shatabdi Roy-Chowdhury, Jesse D. Coe, Markus Metz, Paulraj Lourdu Xavier, Thomas D. Grant, Jason E. Koglin, Gihan Ketawala, Raimund Fromme, Vukica Šrajer, Robert Henning, John C. H. Spence, Abbas Ourmazd, Peter Schwander, Uwe Weierstall, Matthias Frank, Petra Fromme, Anton Barty, Henry N. Chapman, Keith Moffat, Jasper J. van Thor and Marius Schmidt

Affiliation details at:

<http://science.sciencemag.org/content/352/6286/725>

Original publication

‘Femtosecond structural dynamics drives trans/cis isomerization in photoactive yellow protein’, *Science* 352, 725–729 (2016). DOI:10.1126/science.aad5081

References

1. Y. O. Jung et al., ‘Volume-conserving trans-cis isomerization pathways in photoactive yellow protein visualized by picosecond X-ray crystallography’, *Nat. Chem.* 5, 212–220 (2013).
2. J. Tenboer et al., ‘Time-resolved crystallography captures high-resolution intermediates of photoactive yellow protein’, *Science* 346, 1242–1246 (2014).
3. R. Neutze et al., ‘Potential for biomolecular imaging with femtosecond X-ray pulses’, *Nature* 406, 752–757 (2000).
4. H. N. Chapman et al., ‘Femtosecond X-ray protein nanocrystallography’, *Nature* 470, 73–77 (2011).
5. M. Schmidt et al., ‘Application of singular value decomposition to the analysis of time-resolved macromolecular x-ray data’, *Biophys. J.* 84, 2112–2129 (2003).

Building with DNA.

Shape and inner structure of DNA origami objects in harsh conditions

Scaffolded DNA origami nanostructures enable the rational design of nearly arbitrarily shaped objects. Yet, varying physiological conditions such as temperature or ionic strength can induce structural changes in the nanoscale architecture. Here, we report on high precision measurements of overall shape and interhelical distance of DNA origami structures in solution using synchrotron small-angle X-ray scattering. Sheet-, brick-, and cylinder-shaped DNA constructs were determined with angstrom resolution from fits to the scattering profiles. With decreasing divalent salt concentration, electrostatic swelling of both shape cross section and interhelical DNA spacing of the DNA origami structures is observed. With increasing temperature, the cylinder-shaped structures show no thermal expansion in a wide temperature window before they abruptly melt above 50 °C.

Programmed self-assembly is an efficient approach to take control on the nanoscale. Many objects can be assembled in one go without the need to manufacture every single object on its own. Due to its programmability, DNA is one of the most suitable materials for bottom-up self-assembly [1,2]. Self-assembled DNA structures can position other nanoscale components such as nanoparticles, quantum dots or proteins with nanoscale precision [2,4]. Those objects have a wide range of potential applications for example for protein crystallization to enable structural analysis, drug delivery, single molecule sensing or creation of metamaterials [1,2,4]. One of the techniques used in the DNA nanotechnology community is DNA origami where a ~8k bases long single-stranded scaffold strand is folded by annealing into complex shapes by short single-stranded DNA oligonucleotides, so called 'staple strands', due to the base pairing rules [3]. With the DNA origami technique 2D or 3D objects are usually shaped as bundles of interconnected DNA double helices,

with the helices being arranged in a square- or a honeycomb-lattice [2].

The assembly of the structures is accomplished by subjecting the DNA to divalent or monovalent salts to screen the negative charge of the DNA during annealing ramps [3]. This imposes constraints on the stability of the resulting structures concerning buffer conditions and temperature [5]. The established methods for characterisation of these structures such as transmission electron microscopy (TEM) operate in vacuum and in contact with a substrate. Small-angle X-ray scattering (SAXS) can provide exclusive information about the structures of DNA origami objects in their natural environment in order to probe structural integrity. SAXS data with high statistics were obtained at beamline P08 at PETRA III and ID1 at ESRF. We tested three simple geometric DNA origami objects: Sheet-, brick- and cylinder-shaped structures. These structures show scattering curves in a textbook-like manner (grey line in Fig. 1).

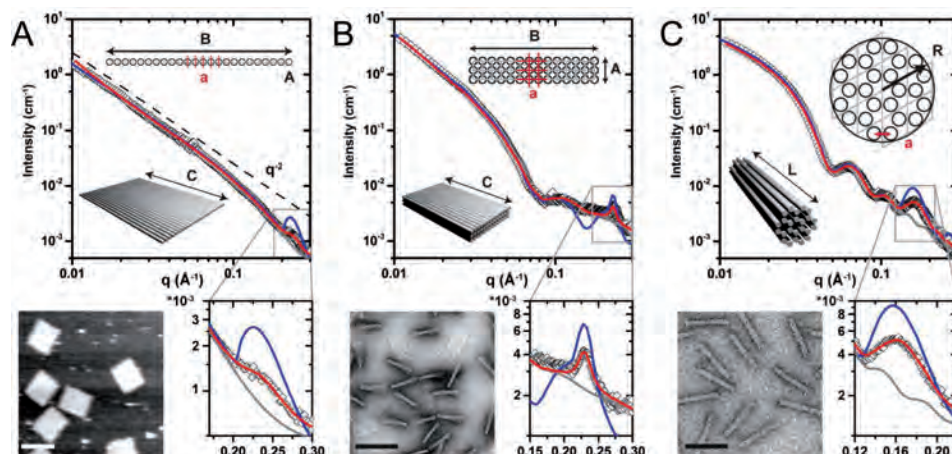


Figure 1

Small-angle scattering intensity and simulated intensities of three DNA origami structures with corresponding model and AFM or TEM image: (a) sheet, (b) three-layer block and (c) 24-helix bundle. The geometric model takes only the overall shape into account (grey lines). Treating the double helices as rigid cylinders predicts the existence and position of a peak corresponding to interhelical distance but overestimates the peak's intensity (blue lines). The geometric model with a Lorentzian peak attributed to the interhelical arrangement reproduces the scattering intensity with high accuracy (red lines). Scale bars: 100 nm. From Nano Lett., 2016, 16 (7), pp 4282–4287. Copyright 2016 American Chemical Society.

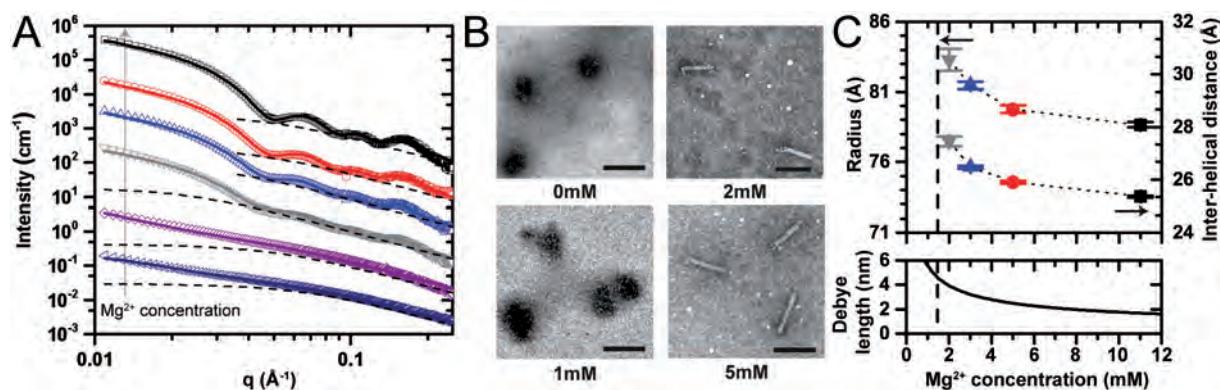


Figure 2

(a) Scattering curves of 24-helix bundles at varying MgCl_2 concentrations (11 mM, 5 mM, 3 mM, 2 mM, 1 mM, and 0 mM from top to bottom) with background of excess oligonucleotides (dashed lines). (b) TEM images of DNA structures exposed to 0 mM, 1 mM, 2 mM, and 5 mM MgCl_2 . Scale bars: 100 nm. (c) Radii of the overall cylinder-shaped structure and interhelical distances extracted from (a) and Debye length for the corresponding MgCl_2 concentrations. Reprinted with permission from *Nano Lett.*, 2016, 16 (7), pp 4282–4287.

Copyright 2016 American Chemical Society.

Furthermore, an additional peak appears which cannot be explained with this simple geometric form factor (inset of Fig. 1). We can attribute this peak to the characteristic repeat distance of the interconnected DNA double helices. Therefore, the position of this peak provides a precise way of determining the mean interhelical distance in DNA origami structures.

We exposed the cylinder-shaped structure to varying salt conditions, from 11 mM MgCl_2 to 0 mM MgCl_2 . For high salt concentration we observed the typical form factor of the cylinder with the additional peak related to the inner structure. For decreasing salt concentrations, the features of the structure became less pronounced (Fig. 2a) until the typical features of the scattering curve of a cylinder vanished, which is the case for buffer of less than 2 mM MgCl_2 . This observation is in agreement with TEM images (Fig. 2b). Importantly, it is possible to extract the overall radius of the structure and the interhelical distance (Fig. 2c) from the SAXS data with high precision. Here, we observed swelling of the whole structure and an increase of the interhelical distance with decreasing salt concentration, which suggests electrostatic repulsion of the negatively charged DNA to be the cause. This argument is supported by similar behaviour of the Debye length calculated for the given salt concentrations. The maximum swelling is about 10 % before the structure disassembles, which is interestingly close to the Lindemann criterion for the melting of solids.

In a second part of the study, we tested the robustness of our DNA origami structure to high temperatures. We followed the structure's behaviour during an increase of temperature and observed a strong decrease of the scattering signal starting at 50 °C. At the same temperature, the structural peak also started to disappear. Interestingly, no significant change of the scattering signal is observable below this temperature,

which implies that the structure stays intact until it finally disassembles in a narrow temperature window.

We showed that SAXS is able to provide structural information of the overall shape of DNA origami nanoobjects and furthermore can give insight into its inner structure. In contrast to many other techniques like (cryo) transmission electron microscopy, we benefit especially from the fact that SAXS experiments can be performed in solution and under variation of temperature and salt conditions.

Contact: Bert Nickel, nickel@lmu.de

Tim Liedl, tim.liedl@lmu.de

Authors

Stefan Fischer¹, Caroline Hartl¹, Kilian Frank¹, Joachim O. Rädler¹, Tim Liedl¹ and Bert Nickel¹

¹. Fakultät für Physik and Center for NanoScience, Ludwig-Maximilians-Universität, München, Germany

Original publication

'Shape and Interhelical Spacing of DNA Origami Nanostructures Studied by Small-Angle X-ray Scattering', *Nano Letters* 16, 4282-4287 (2016). DOI: 10.1021/acs.nanolett.6b01335

References

1. N. C. Seeman, 'Nanomaterials based on DNA', *Annu. Rev. Biochem.* 79, 65–87 (2010).
2. A. V. Pinheiro, D. Han, W. M. Shih and H. Yan, 'Challenges and opportunities for structural DNA nanotechnology', *Nature Nanotechnology* 6, 763-772 (2011).
3. P. W. K. Rothemund, 'Folding DNA to create nanoscale shapes and patterns', *Nature* 440, 297-302 (2006).
4. A. Kuzyk, R. Schreiber, Z. Y. Fan, G. Pardatscher, E. M. Roller, A. Högele, F. C. Simmel, A. O. Govorov and T. Liedl, 'DNA-based self-assembly of chiral plasmonic nanostructures with tailored optical response', *Nature* 483, 311-314 (2012).
5. J. Hahn, S. F. J. Wickham, W. M. Shih and S. D. Perrault, 'Addressing the instability of DNA nanostructures in tissue culture', *ACS Nano* 8, 8765-8775 (2014).

In cellulo serial crystallography of alcohol oxidase crystals.

A crystal factory inside yeast cells.

Developments in X-ray free-electron laser technologies and serial crystallography techniques have opened up new opportunities for studying challenging protein systems and complexes. Cell organelles known as peroxisomes naturally produce protein crystals in their interior. We show that it is possible to study crystals *in situ* in their native cell environment with advanced X-ray sources and see potential for harnessing this natural process for investigating proteins that are difficult to study with traditional methods.

Crystallography is an effective method for producing detailed atomic 3D models of proteins. But while crystallography is one of the most powerful methods in the structural biologist's toolbox, producing protein crystals in preparation for crystallographic experiments remains a bottleneck. There is no patent protocol for the crystallisation of proteins, and especially larger proteins, protein complexes and membrane proteins are notoriously difficult to crystallise – a process that can be extremely time and resource intensive. Large protein complexes will often produce minute crystals that are too fragile to be handled in the traditional way at the beamline. Radiation produced at X-ray free-electron lasers (XFELs) with brilliant X-ray pulses lasting only a few femtoseconds offers new opportunities for probing the 3D structures of protein species that as yet have been difficult to study at the synchrotron. For such samples, serial data collection strategies [1,2] have recently been developed to aid the data collection from many thousands of small crystals that are often easier to obtain than the large crystals needed for conventional crystallography experiments. These recent advances in XFEL technologies have sparked an interest in exploring other techniques producing large numbers of small crystals of biological macromolecules.

We explored the observation that protein crystals sometimes spontaneously form within cells and organelles [3]. Cell organelles known as peroxisomes are membrane bound organelles found in eukaryotic cells. Through our work with peroxisomes we knew they produce crystals in their interior, which are used to isolate and pack the toxic processes of fatty acid degradation. In the yeast *Hansenula polymorpha* (Hp), alcohol oxidase (AO) enzymes break down methanol into useful byproducts. These proteins are produced in such high numbers in peroxisomes that, to use the limited space most efficiently, they assemble into a tightly packed crystalline arrangement. We wondered whether this natural process could be harnessed to produce protein crystals of our own choice that could then be measured *in situ*, thereby circumventing the need for crystallisation trials and adding an additional tool

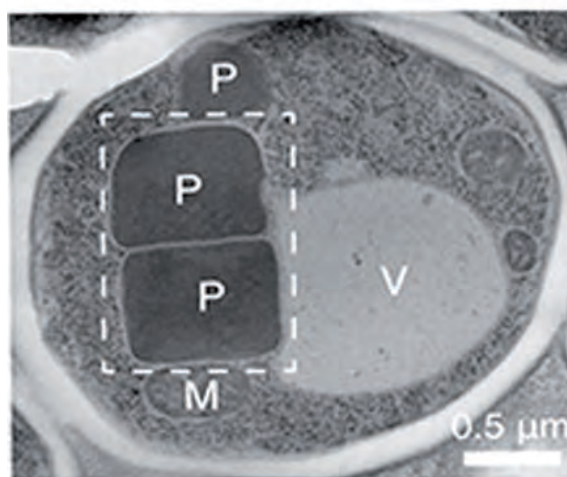


Figure 1 Electron micrograph of a wild type *Hansenula polymorpha* cell containing crystalline alcohol oxidase in electron-dense peroxisomes (P) seen next to mitochondria (M) and a vacuole (V).

to the structural biologist's toolbox. But first we needed to test whether this system can actually be used for crystallography experiments. Diffraction data of the Hp AO complex have only been observed to very low resolution to date. The small dimensions of the Hp peroxisomes make it an ideal candidate for testing the possibilities of XFELs for this purpose.

In order for this cellular process to be suitable for diffraction experiments, a uniform size and number of peroxisome crystals per cell is necessary, i.e. one large crystal per cell. Naturally occurring crystals are variable in size and number, however colleagues at the University of Groningen (NL) identified a mutant strain of Hp that only produces a single crystal filling out the entirety of the cell space. Yeast cultures were then grown on a methanol rich medium to induce the growth of AO crystals. Cell suspensions of the wild type and mutant Hp strains were tested at the EMBL operated macromolecular crystallography beamline P14 at PETRA III. Powder patterns



a

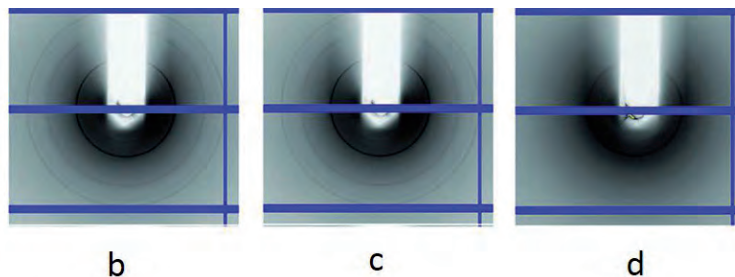


Figure 2

(a) Setup for powder diffraction experiments with cell and peroxisome suspensions on the P14 beamline at PETRA III showing from left to right the nozzle of the cooling device, the capillary with the sample and the pinhole of the X-ray beam. X-ray powder diffraction patterns are shown for (b) wild-type, (c) peroxisome and (d) cell suspensions.

were collected, visualised and analysed suggesting that the peroxisomes contained protein crystals.

In a next step at the Coherent X-ray Imaging (CXI) experiment at the Linac Coherent Light Source (LCLS), we tested the diffraction properties of the AO crystals *in situ* within intact cells, and within the peroxisomes which were extracted from the yeast cells. Being such a novel experiment, in collaboration with colleagues from the Chapman group at the Center for Free-Electron Laser Science (CFEL) and the University of Hamburg, we first had to optimise the conditions and methods for introducing the peroxisome and cell suspensions into the X-ray beam. We worked with a gas dynamic virtual nozzle (GDVN) to deliver the samples as a thin liquid jet into the X-ray beam. During initial test runs while using purified peroxisomes stored in sucrose buffers, we found that the sticky sucrose solutions rapidly clogged the nozzle resulting in instable jets. We therefore switched to using a sorbitol solution which worked well with the GDVN.

Diffraction patterns were obtained by exposing a fully hydrated stream of cells to X-ray pulses of 30 femtoseconds and energy of 7.925 keV. We collected data sets for suspensions both of intact cells and isolated peroxisomes. Although occasional

diffraction patterns were found for the peroxisome suspensions, the very low resolution and the poor overall quality of the data meant we could not process these data sets any further. The data collected from the cell suspensions were more encouraging. While the majority of the diffraction patterns were restricted to 30 Å, resolutions of 6 Å were also seen.

We have been able to show that it is possible to obtain diffraction patterns from a large protein complex that has been crystallised in its native environment. HpAO is a challenging project for structure determination. Based on estimates from previous studies we believe the size of the crystals within the peroxisomes to be significantly smaller than grown in the traditional way in the laboratory. Hence we feel obtaining 6 Å resolution data from sub-µm sized crystals is a significant achievement for such a challenging sample using this novel method. Long term, we hope to be able to harness the natural ability of the peroxisome to also produce crystals from other proteins. Once developed, we see potential for the use of *in cellulo* serial crystallography as an additional complementary method for studying the atomic structure of difficult to crystallise proteins.

Contact: Matthias Wilmanns
matthias.wilmanns@embl-hamburg.de

Authors

Arjen Jakobi^{1,2}, Daniel M. Passon¹, Kévin Knoops³, Francesco Stellato⁴, Mengning Liang⁴, Thomas A. White⁴, Thomas Seine^{1,4}, Marc Messerschmidt⁵, Henry N. Chapman^{4,6,7} and Matthias Wilmanns^{1,8}

- EMBL c/o DESY, European Molecular Biology Laboratory (EMBL), Hamburg, Germany
- Structural and Computational Biology Unit, European Molecular Biology Laboratory (EMBL), Heidelberg, Germany
- Molecular Cell Biology, Groningen Biomolecular Sciences and Biotechnology Institute, University of Groningen, Groningen, The Netherlands
- Center for Free-Electron Laser Science, Deutsches Elektronen-Synchrotron DESY, Hamburg, Germany
- Linac Coherent Light Source, SLAC National Accelerator Laboratory, California, USA
- Department of Physics, University of Hamburg, Hamburg, Germany
- Center for Ultrafast Imaging, Hamburg, Germany
- University Medical Center Hamburg-Eppendorf, Hamburg, Germany

Original publication

'In cellulo serial crystallography of alcohol oxidase crystals inside yeast cells', IUCrJ 3 (Part 2), 88-95 (2016). DOI:10.1107/s2052252515022927

References

- C. Gati, G. Bourenkov, M. Klinge, D. Rehders, F. Stellato, D. Oberthür, O. Yefanov, B. P. Sommer, S. Mogk, M. Duszhenko, C. Betzel, T.R. Schneider, H. N. Chapman and L. Redecke, 'Serial crystallography on *in vivo* grown microcrystals using synchrotron radiation', IUCrJ 1, 87-94 (2014).
- F. Stellato, D. Oberthür, M. Liang, R. Bean, C. Gati, O. Yefanov, A. Barty, A. Burkhardt, P. Fischer, L. Galli, R. A. Kirian, J. Meyer, S. Panneerselvam, C. H. Yoon, F. Chervinskii, E. Speller, T. A. White, C. Betzel, A. Meents and H. N. Chapman, 'Room-temperature macromolecular serial crystallography using synchrotron radiation', IUCrJ 1, 204-212 (2014).
- J. Doye and W. Poon. 'Protein crystallization in vivo', Curr. Opin. Colloid Interface Sci. 11, 40-46 (2006).

How arsenic toxicity affects plants on the subcellular level.

Insights from X-ray emission (μ XRF) and absorption (μ XANES) microanalysis in *Ceratophyllum demersum*

Arsenic (As) toxicity to plants is a severe problem for agricultural productivity and food safety. We investigated As toxicity under environmentally relevant conditions using the aquatic shoot model plant *Ceratophyllum demersum*. X-ray microanalysis showed profound differences between subcellular As localisation and speciation at sublethal vs. lethal conditions. At sublethal concentrations the nucleus of the cells in the leaf epidermis ('skin') was identified as main accumulation site of As, indicating DNA damage as one of the primary toxicity mechanisms. At lethal concentrations As accumulated also in other parts of the cell, leading to additional damages. Biosynthesis of chlorophyll became already inhibited by the small quantity of As that entered the photosynthetic tissue.

Arsenic is a toxic element with no known beneficial physiological role. It has become a problem for agriculture because it occurs in elevated concentrations in soil and water due to both anthropogenic influence and natural geological factors. In India and Bangladesh, millions of people are affected by As toxicity because of contaminated drinking water and food, and indirectly because As hampers the growth and yield of crops. In order to alleviate those problems, breeding of more As-tolerant plants that furthermore accumulate less As in their edible parts is essential. As a prerequisite, the mechanisms how As affects plant physiology need to be understood. *Ceratophyllum demersum* (rigid hornwort, also called coontail) shares all relevant biochemical pathways with crops and is very sensitive to toxicity. As *Ceratophyllum* is rootless, it has the advantage that effects on the green parts are similar to those in shoots of terrestrial plants but can be analysed without interaction of the roots and soil that often make interpretations of nutrition/toxicity studies in terrestrial plants difficult. Therefore, we used it as a model organism in several earlier studies [1-5].

Among the methods for analysing metal/metalloid distribution in tissues, scanning micro X-ray fluorescence (μ XRF) in imaging

tomography mode has the advantages of detecting multiple elements simultaneously with very high spatial resolution and high sensitivity as compared to conventional methods. In precursor studies [1-5] data have been obtained at tissue level, e.g. X-ray absorption spectroscopy (μ XANES) at PETRA III beamline P06 with confocal optics was used to determine the chemical speciation of As [1]. The current study combined the microprobe at P06 with a MAIA detector [6] which allowed for the analysis of As distribution at the subcellular level, and the comparison of functionally different parts such as nucleus, chloroplasts and vacuoles. Furthermore, we have also shown that from the ratio of absorption to Compton scattering signal important tissue structural information can be obtained which is useful for the interpretation of the tomographic results of frozen-hydrated samples (Fig.1). For all measurements, the samples were shock-frozen and were kept frozen during the measurement with the help of a cryostream to avoid beam damage and artefacts of element re-distribution occurring during measurements in non-frozen state.

Most importantly, the measurements on subcellular level revealed that at sublethally toxic concentrations As

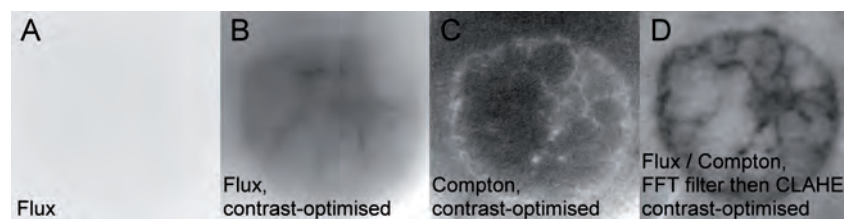


Figure 1
Resolution of leaf tissue structures. (a) Raw tomogram of sample absorption represented by the photon flux after the sample. (b) Tomogram after contrast stretching and background correction. Some structures become visible. (c) Tomogram of Compton scattering after contrast stretching and background correction. Structure of the epidermis is revealed. (d) Flux/Compton ratio tomogram after application of an FFT filter, CLAHE algorithm and linear contrast stretching. All structures are clearly visible. Source: Figure 1 of the original article, published under CC-BY-3.0.

predominantly accumulates in a single large organelle, i.e. the nucleus, identified from its size and position (Fig. 2a). This is an important result because one proposed mode of As toxicity is the replacement of P by As in the DNA. Our results indicate that this may occur at physiologically relevant concentrations. This is also in agreement with μ XANES measurements on the same samples [1] showing that a large proportion of the As was surrounded by oxygen ligands as it is the case for P in DNA. At this sublethal concentration, small amount of As that entered the chloroplasts already caused a strong inhibition of tetrapyrrole (= building block of chlorophyll) biosynthesis, while other parts of the plant metabolism (i.e. photosynthetic electron transport, photosystem II reaction centre and respiration) were not yet affected [2].

At lethal concentrations, the large central storage compartment of plant cells, the vacuole, becomes the primary storage site for As (Fig. 2b). Binding with thiol containing ligands (GS = glutathione, PC = phytochelatin) after reduction to arsenite and sequestration of As-thiols in vacuoles is considered as the primary mechanism of As detoxification in plants. Thus, correlating the element localisation data obtained with μ XRF with data on the chemical state of As measured by confocal μ XANES allows for judgement how As is metabolised in the cells and how plants try to defend themselves against toxicity (Fig. 3). In young leaves, at sublethal concentration, As was mostly accumulated in the epidermis, while at lethal concentrations a significant amount was also accumulated in mesophylls [1]. At the same lethal concentration, epidermis of mature leaves exhibited a large proportion of As-thiols, while young leaves exhibited a large proportion of weakly bound As indicating a high As toxicity in young leaves. The change in chemical state of As in growing tissues caused the transition from sublethal to lethal toxicity. Measurements of the speciation of thiol bound As in fresh plant extract by means of chromatography coupled to mass spectroscopy were in good agreement with the data shown here [1] and confirm our findings.

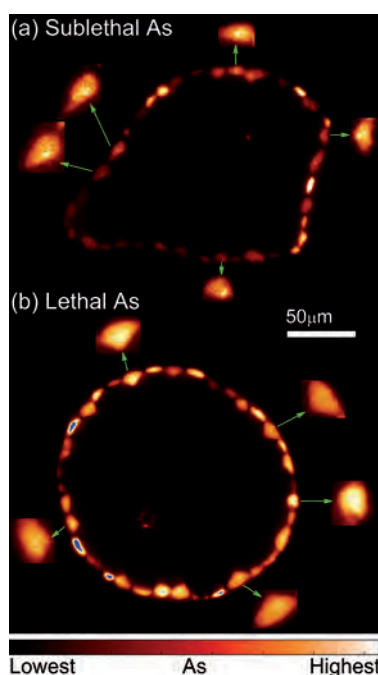


Figure 2

X-ray fluorescence microtomograms showing intra-cellular details of As distribution after 2 weeks of As treatment.

(a) Young mature leaf at 1 μ M As showing predominant accumulation of As in the nuclei.

(b) Mature leaf at 5 μ M As showing As storage in the large central vacuoles.

Enlarged views of selected cells show intra-cellular details of As distribution.

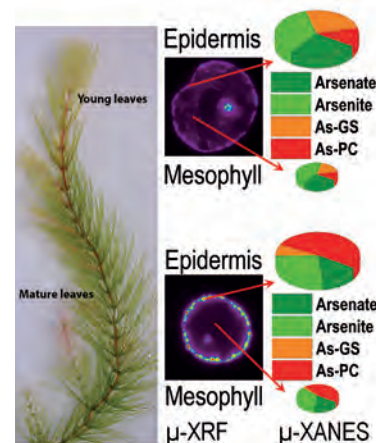
Source: Figure 3 of the original article, published under

CC-BY-3.0.

Figure 3

Scheme showing the As distribution (analysed by μ XRF tomography) and speciation (analysed by confocal μ XANES) in the epidermis and the mesophyll of young (top) and mature (bottom) leaves of *Ceratophyllum demersum*, respectively, at 5 μ M As.

Source: The data shown were published in the original article (μ XRF) published under CC-BY-3.0 and [1] (μ XANES). This figure is a modified version of figure 8 shown in [1].



This study shows that at a concentration that can be easily attained in shoots of crop plants, As is already toxic to plants and accumulates in the nuclei of the leaf epidermis. Small amounts reaching the chloroplasts already strongly and specifically inhibit chlorophyll biosynthesis. This knowledge can be a starting point for targeted breeding of more resistant plants.

Contact: Seema Mishra, seema_mishra2003@yahoo.co.in
Hendrik Küpper, hendrik.kuepper@umbr.cas.cz

Authors

Seema Mishra^{1,2}, Matthias Alfeld³, Roman Sobotka^{4,6}, Elisa Andresen^{2,5}, Gerald Falkenberg³, Hendrik Küpper^{2,5,6}

1. CSIR-NBRI, Plant Ecology & Environmental Science Division, Lucknow (U.P.), India
2. Universität Konstanz, Math.-Naturwiss. Sektion, FB Biologie, Konstanz, Germany
3. Deutsches Elektronen-Synchrotron DESY, Hamburg, Germany
4. Centre Algatech, Institute of Microbiology AS CR, Třeboň, Czech Republic
5. Institute of Plant Molecular Biology, Department of Biophysics and Biochemistry of Plants, Biology Centre of the CAS, České Budějovice, Czech Republic
6. University of South Bohemia, Faculty of Science, České Budějovice, Czech Republic

Original publication

'Analysis of sub-lethal arsenic toxicity to *Ceratophyllum demersum*: Subcellular distribution of arsenic and inhibition of chlorophyll biosynthesis.

Journal of Experimental Botany 67, 4639-4646 (2016). DOI: 10.1093/jxb/erw238

References

1. S. Mishra, G. Wellenreuther, J. Mattusch, H.-J. Stärk, H. Küpper, 'Speciation and Distribution of Arsenic in the non-hyperaccumulator Macrophyte *Ceratophyllum demersum*', Plant Physiology 163, 1396 (2013).
2. S. Mishra, H.-J. Stärk, H. Küpper, 'A different sequence of events than previously reported leads to arsenic-induced damage in *Ceratophyllum demersum* L.'

Structure based pro-drug discovery.

A new method to combat MRSA

Infections caused by *Staphylococcus aureus* (MRSA) are proven to be affecting global health, which is even more pronounced by emerging multi-drug resistance. Therefore new drug targets and the discovery of novel strategies to treat bacterial infections are urgently required. By following this demand the research collaboration focused on the biosynthesis of vitamin B1 (thiamin), which is not present in humans. Thiamin pyrophosphate is an essential co-factor for all organisms. Thiamin analogous compounds, when introduced into the vitamin B1 biosynthetic pathway can be converted into non-functional co-factors, which will subsequently poison vitamin B1 dependent enzymes of the pathogen. We structurally characterized one of the *S. aureus* vitamin B1 biosynthetic key enzymes in complexes with two selected pro-drugs using high resolution diffraction data collected at the EMBL beamline P14 at PETRA III.

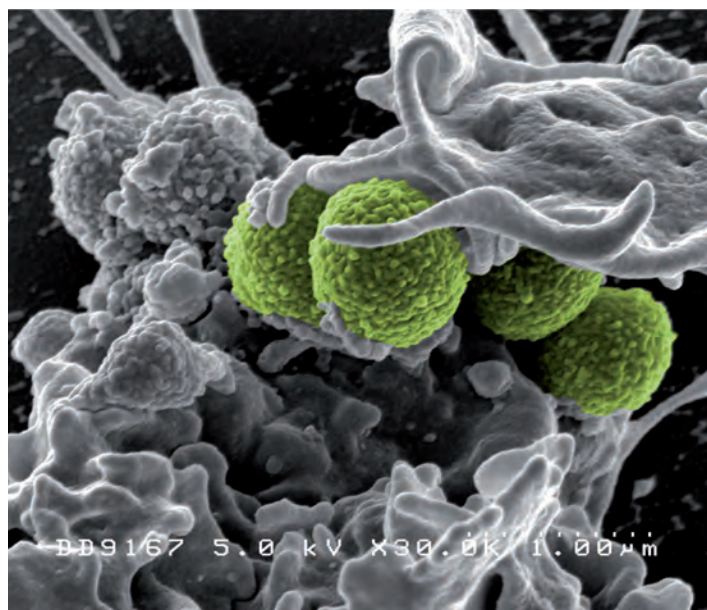


Figure 1
Hospital-associated Methicillin-resistant *S. aureus* (MRSA) (taken from NIAID/NIH).

In terms of drug discovery, a major goal is to identify differences between bacteria and the respective host organism, which is exploited for the proliferation of the pathogen. Therefore, ideal drug targets are significantly different or even absent in the human host when compared to the pathogenic bacteria. Structure based approaches were developed to identify potential drug targets and subsequently the deriving potential inhibitors were screened. As mentioned above, the idea of drugs targeting co-factor metabolisms in bacteria is today most promising. Due to the short reproduction time and the capability of horizontal gene transfer, bacteria like *S. aureus*, (Fig. 1) are highly adaptable to any kind of environ-

mental changes. This will consequently lead to the occurrence of drug resistance, especially if only one target (enzymatic step) will be attacked. In order to circumvent this problem, an innovative option is to target a variety of different enzymes and / or metabolic pathways with only a single drug application. By following this strategy, the design of so-called 'suicide drugs' is today highly favoured, because these special compounds mimic the natural substrate with only minor but essential chemical modifications. Consequently, these special compounds, named pro-drugs, will be metabolized by the pathogenic enzymes and thereby channelled into the respective product pool (Fig. 2). Applying this methodology on vitamin B biosynthetic pathways, the product pool will harbour besides the endogenous co-factors also the non-functional suicide co-factors which will subsequently poison vitamin B-dependent enzymes and result in bacteria's death [1].

By utilizing the pro-drug discovery approach we focussed on the vitamin B1 biosynthesis pathway in MRSA, which is consisting of six enzymes, ThiM, ThiD, ThiE, a nonspecific GTPase, TenA and TPK [2]. We had solved already the first structure of this metabolic pathway, the 3D structure of the thiaminase TenA [3]. And as main target in terms of pro-drug design we have analysed the structure-function relationship of the 5-(hydroxyethyl)-4-methylthiazole (THZ) kinase ThiM, which phosphorylates THZ in one of the first steps within vitamin B1 biosynthetic pathway. The native structure of SaThiM (Fig. 3) revealed a conserved ribokinase-like fold and a trimeric assembly, which was confirmed by complementary SAXS experiments, also performed at PETRA III. Three active sites have been identified, each located within the interface regions of two monomers, respectively. Structural data of THZ bound in the active sites of SaThiM allowed *in silico*

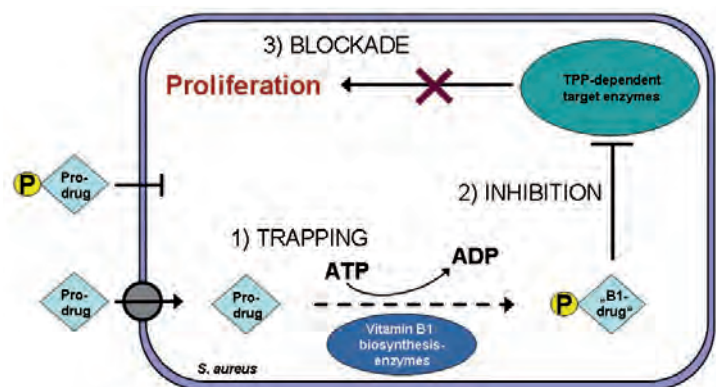


Figure 2

Schematic illustration of the exploitation of the vitamin B1 biosynthetic pathway in *S. aureus*. Uptake of compounds occurs via a pathogen transport system. (1) Vitamin B1 biosynthetic enzymes activate compounds upon phosphorylation, which leads to an accumulation of the compounds in the cell. (2) 'Activated' compounds compete with thiamin pyrophosphate (TPP) for binding in the active site of TPP-dependent enzymes. (3) Inhibition of crucial TPP-dependent enzymes results in proliferation inhibition.

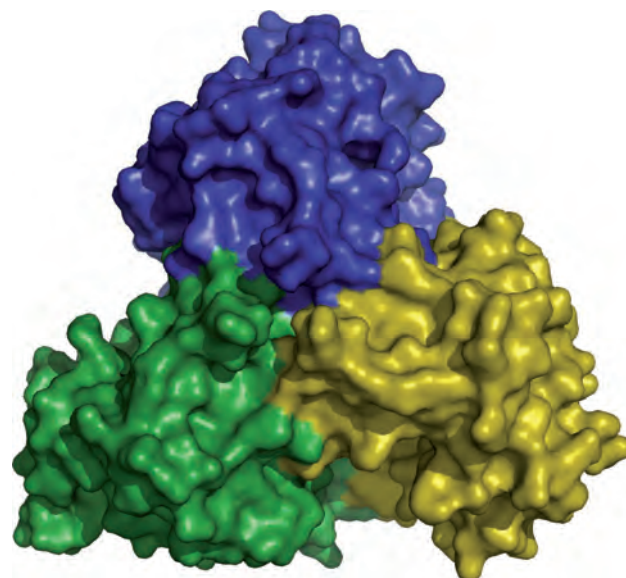


Figure 3

Trimetric 3D structure of SaThiM.

screening and the identification of two initial lead compounds. These compounds were biochemically analysed and their kinetic data confirmed that the selected compounds were accepted as substrates. Comparing the specific activities of ThiM in presence of the two compounds revealed a similar turnover as found for the natural substrate THZ. These results clearly validate the approach to combine complementary biochemical and biophysical methods for pro-drug discovery, in order to identify and improve lead compounds.

Based on these data complexes of SaThiM with compounds assigned to cpd 1 and cpd 2 were prepared and crystallized in a rather complicate approach. High resolution diffraction data were collected at PETRA III. The structures of these complexes were refined to 1.87 Å and 1.62 Å resolutions with R and R_{free} values of 16.86 % and 19.90 % for the cpd 1 complex and R and R_{free} values of 18.24 % and 20.28 % for the cpd 2 complex [4, 5]. Interestingly, cpd 2 has an additional nitrogen atom in the heterocycle and can, like cpd 1, undergo a TPP imino tautomerization, after fusion with HMP. As a result this substance can be channelled via thiaminase (TenA) into the bacterial thiamin pool, where it can act as a thiamin antagonist.

The obtained data allow developing a thiamin like pro-drug, that can be selectively converted into the active drug solely by the bacterial pathogen and subsequently inhibit various essential vitamin B1 dependent enzymes in MRSA. This innovative approach will open a new route for the development of new antimicrobial substances to treat MRSA infections.

Contact: Christian Betzel, christian.betzel@uni-hamburg.de
Carsten Wrenger, cwrenger@icb.usp.br

Authors

Julia Drebes^{1,2,#}, Madeleine Künz^{1,#}, Björn Windhügel³, Alexey G. Kikhney⁴, Ingrid B. Müller², Raphael J. Eberle^{1,4}, Dominik Oberthür^{1,§}, Huaixing Cang⁵, Dmitri I. Svergun⁴, Markus Perbandt^{1,7}, Christian Betzel^{1,7} and Carsten Wrenger⁶.

1. University Hamburg, c/o DESY, Laboratory for Structural Biology of Infection and Inflammation, Hamburg, Germany
 2. Department of Biochemistry, Bernhard Nocht Institute for Tropical Medicine, Hamburg, Germany
 3. Fraunhofer Institute for Molecular Biology and Applied Ecology IME, Hamburg, Germany
 4. EMBL Hamburg, c/o DESY, Hamburg, Germany
 5. School of Life Sciences North Western Polytechnical University, Xi'an, Shaanxi, China
 6. Unit for Drug Discovery, Department of Parasitology, Institute of Biomedical Sciences, University of São Paulo, São Paulo, Brazil
 7. The Hamburg Centre for Ultrafast Imaging (CUI), Hamburg, Germany
- ‡ Present address: Multiuser Center for Biomolecular Innovation, Department of Physics, Universidade Estadual Paulista (UNESP), São Jose do Rio Preto, Brazil
§ Present address: Center for Free-Electron Laser Science, Deutsches Elektronen Synchrotron-DESY, Hamburg, Germany
These authors contributed equally to this work

Original publication

'Structure of ThiM from Vitamin B1 biosynthetic pathway of *Staphylococcus aureus* - Insights into a novel pro-drug approach addressing MRSA infections', Sci Rep (2016). 6:22871. DOI: 10.1038/srep22871

References

1. J. Drebes, M. Künz, C. A. Pereira, C. Betzel and C. Wrenger, 'MRSA infections: from classical treatment to suicide drugs', *Curr Med Chem* 21, 1809-1819 (2014).
2. I. B. Müller, B. Bergmann, M. R. Groves, I. Couto, L. Amaral, T. P. Begley, R. D. Walter and C. Wrenger, 'The vitamin B1 metabolism of *Staphylococcus aureus* is controlled at enzymatic and transcriptional levels', *PLoS One* 4:e7656 (2009).
3. A. Begum, J. Drebes, A. Kikhney, I. B. Müller, M. Perbandt, D. Svergun, C. Wrenger and C. Betzel, '*Staphylococcus aureus* thiaminase II: oligomerization warrants proteolytic protection against serine proteases', *Acta Crystallogr D Biol Crystallogr.* 69, 2320-2329 (2013).
4. J. Drebes, M. Perbandt, C. Wrenger and C. Betzel, 'Purification, crystallization and preliminary X-ray diffraction analysis of ThiM from *Staphylococcus aureus*', *Acta Crystallogr Sect F Struct Biol Cryst Commun.* 67, 479-481 (2011).
5. J. Drebes, M. Künz, B. Windhügel, A. G. Kikhney, I. B. Müller, R. J. Eberle, D. Oberthür, H. Cang, D. I. Svergun, M. Perbandt, C. Betzel and C. Wrenger, 'Structure of ThiM from Vitamin B1 biosynthetic pathway of *Staphylococcus aureus* - Insights into a novel pro-drug approach addressing MRSA infections', *Sci Rep.* 6, 22871(2016).

FLASH uncovers intricate nanoplasma heating.

A combined scattering and spectroscopic approach on single clusters demonstrates ultrafast heat release from recombination

Atomic clusters in the gas phase are versatile nanoscale laboratories for studying laser-matter interactions across all wavelength regimes. So far, the interpretation of spectroscopic features in laser-cluster experiments has been complicated by the unavoidable averaging over both the cluster size distribution and the laser intensity profile. A new quality of analysis is achieved when intense short-wavelength pulses from extreme ultraviolet (XUV) and X-ray free-electron lasers permit a combined analysis of single clusters: In parallel to the spectroscopic analysis of interaction residuals, a ‘photograph’ of the cluster is taken by simultaneously recording the elastically scattered light. This single-shot technique was exploited to analyze ionic residuals of xenon clusters under intense XUV pulses from FLASH, leading to the observation of a so far unnoticed heating mechanism in the cluster nanoplasma.

Ultra-intense pulses from short-wavelength free-electron lasers (FEL) can turn condensed matter into highly excited plasmas in only a few femtoseconds. While this plasma formation is a troublesome artifact termed ‘ultrafast radiation damage’ [1] for coherent diffractive imaging (CDI) applications, it promises unparalleled opportunities in warm dense matter science to prepare and study extreme plasma states in a well-controlled way [2]. A precise understanding of ultrafast

light-matter interactions under intense XUV and X-ray pulses and the subsequent complex relaxation dynamics is therefore a major focus of FEL research.

Since the first operation of FLASH [3], short-wavelength laser-cluster experiments have uncovered several new non-linear effects and led to a vibrant subfield of research in FEL science. Gas-phase clusters are particularly interesting as they can be used to rigorously study ultrafast ionization dynamics and plasma formation processes in finite many-particle systems [4] and may lead to new directions in ultrafast diffractive imaging [5]. From the CDI perspective, knowledge of the plasma dynamics can be used to define the optimal experimental scenario or to support the reconstruction of the target structure. Turning this idea around, the analysis of plasma dynamics via reaction fragments can be improved substantially by simultaneously recorded diffraction images. In particular, as both target size and local laser intensity are encoded in the shape and brightness of the diffraction image [6], this approach solves the size and intensity averaging problem of gas-phase cluster experiments [7].

In our experiment, single-shot diffraction images have been measured in parallel to ion time-of-flight data to study nanoplasma dynamics induced in single xenon clusters by intense XUV pulses (sketched in Fig. 1). The cluster size and FEL intensity were inferred for each shot from the single-cluster scattering patterns. From the corresponding size-tagged single-cluster ion spectra we could extract the kinetic energy distribution for each charge state separately (see Fig. 2). One particularly striking observation is the rather narrow kinetic energy distribution of the residual ions (Fig. 2). The average kinetic energy per average charge state is more than one order of magnitude higher than expected from basic theoretical

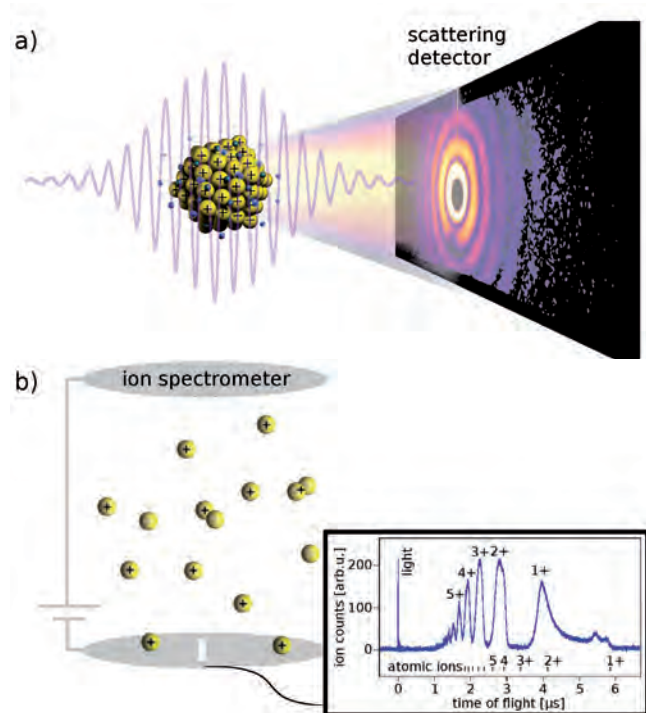


Figure 1
Combined diffractive imaging and spectroscopic approach. (a) The elastically scattered XUV light from the cluster is recorded on a large area scattering detector. (b) The residual ions of the FEL-cluster interaction are measured with a time-of-flight spectrometer.

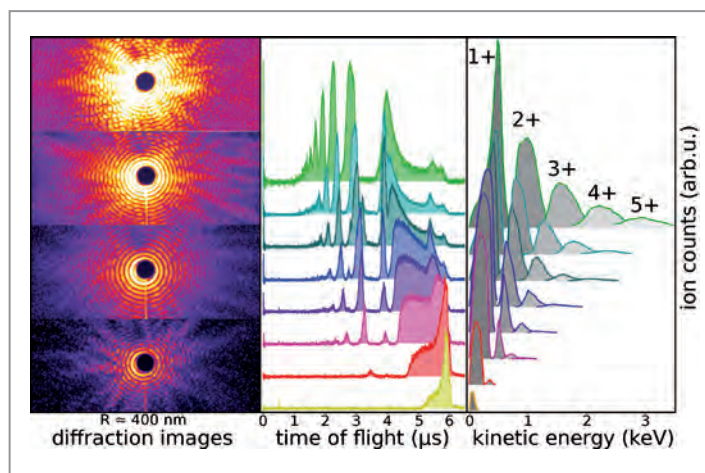


Figure 2

Single-cluster measurements allow for a novel quality in laser-cluster interaction studies. The diffraction images (left) are used to select cluster size and FEL intensity of the events. From the single-cluster ion spectra (middle) charge state resolved kinetic energy spectra (right) can be extracted.

modelling [8]. Further, slow ions are virtually absent although they were expected to dominate the signal for our scenario.

The physical picture that explains these discrepancies is connected to energy redistribution processes accompanying the massive electron-ion recombination in the dense nanoplasma. Due to the hydrodynamic pressure from hot nanoplasma electrons, the surface ions of the cluster are quickly expelled and the temperature of the nanoplasma electrons is reduced due to expansion cooling – similar to the adiabatic expansion of a gas. According to this picture, the kinetic energy of the nanoplasma electrons is transferred predominantly to ions at the cluster surface, with expected ion energies per charge state of roughly the initial electron temperature. At the same time, ions in the inner core are screened by the plasma electrons and are thus less efficiently accelerated.

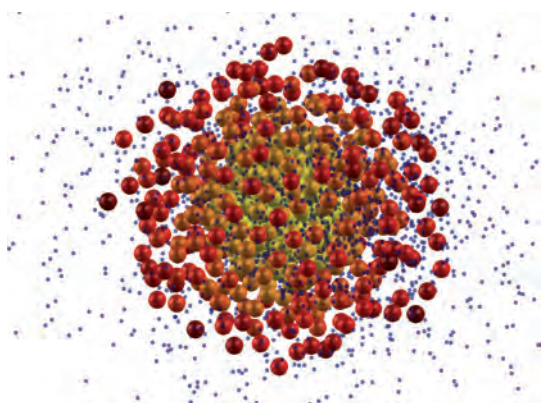


Figure 3

Typical snapshot of semiclassical molecular dynamics simulations showing the cloud of hot electrons (small blue dots) driving the cluster expansion predominantly at the cluster surface (ion colours vary from yellow for low kinetic energies to red for high kinetic energies). The correlated description of classical nanoplasma dynamics accounts for recombination and reproduces the main experimental features.

As a result, inner ions have much more time to recombine – eventually to neutral xenon atoms. Each electron recombining with an ion via three-body-recombination releases its residual kinetic energy plus its binding energy to the remaining nanoplasma electrons. In consequence, the plasma temperature increases (or decreases less rapidly), providing additional energy that is released to the emitted surface ions. This redistribution of energy can be seen as ‘recombination heating’.

When accounting for recombination processes in theoretical modelling of the dynamics, the observed characteristic features of the ‘recombination heating’ can be explained, i.e. (i) the peaked ion energies, (ii) the absence of slow ions, and (iii) an increased average ion kinetic energy. A snapshot of the dynamics as modelled with our semiclassical atomistic molecular dynamics simulations is displayed in Fig. 3, illustrating the surface expansion in the hot nanoplasma. Fundamental understanding of energy transfer processes in laser-induced nanoplasmas has implications for many fields ranging from matter under extreme conditions to biophysics, aerosol science, and X-ray imaging of nanoparticles.

Contact: Daniela Rupp, daniela.rupp@physik.tu-berlin.de
Thomas Fennel, thomas.fennel@uni-rostock.de

Authors

D. Rupp¹, L. Flückiger^{1,2}, M. Adolph¹, T. Gorkhover^{1,3}, M. Krikunova¹, J. P. Müller¹, M. Müller¹, T. Oelze¹, Y. Ovcharenko¹, B. Röben¹, M. Sauppe¹, S. Schorb^{1,3}, D. Wolter¹, R. Mitzner⁴, M. Wöstmann⁵, S. Roling⁶, M. Harmand⁶, R. Treusch⁶, M. Arbeiter⁷, T. Fennel⁷, C. Bostedt^{3,8,9} and T. Möller¹

1. IOAP, Technische Universität Berlin, Berlin, Germany
2. ARC Centre of Excellence for Advanced Molecular Imaging, La Trobe University, Bundoora, Victoria, Australia
3. LCLS, SLAC, Menlo Park, California, USA
4. Helmholtz-Zentrum Berlin, Berlin, Germany
5. Universität Münster, Münster, Germany
6. Deutsches Elektronen-Synchrotron DESY, Hamburg, Germany
7. Institut für Physik, Universität Rostock, Rostock, Germany
8. Argonne National Laboratory, Illinois, USA
9. Department of Physics and Astronomy, Northwestern University, Evanston, Illinois, USA

Original publication

‘Recombination-enhanced surface expansion of clusters in intense soft X-ray laser pulses’, *Phys. Rev. Lett.* 117, 153401 (2016); <https://doi.org/10.1103/PhysRevLett.117.153401>

References

1. K. Nass et al., ‘Indications of radiation damage in ferredoxin microcrystals using high-intensity X-FEL beams’, *J. Sync. Rad.* 22, 225–238 (2015).
2. L. Fletcher et al., ‘Ultrabright X-ray laser scattering for dynamic warm dense matter physics’, *Nat. Phot.* 9, 274–279 (2015).
3. H. Wabnitz et al., ‘Multiple ionization of atom clusters by intense soft X-rays from a free-electron laser’, *Nature* 420, 6915 (2002).
4. C. Bostedt et al., ‘Ultrafast X-Ray Scattering of Xenon Nanoparticles: Imaging Transient States of Matter’, *Phys. Rev. Lett.* 108, 093401 (2012).
5. I. Barke et al., ‘The 3D-architecture of individual free silver nanoparticles captured by X-ray scattering’, *Nat. Comm.* 6, 6187 (2015).
6. T. Gorkhover et al., ‘Nanoplasma Dynamics of Single Large Xenon Clusters Irradiated with Superintense X-Ray Pulses from the Linac Coherent Light Source Free-Electron Laser’, *Phys. Rev. Lett.*, 108, 245005 (2012).
7. M. R. Islam, U. Saalmann and J.-M. Rost, ‘Kinetic energy of ions after Coulomb explosion of clusters induced by an intense laser pulse’, *Phys. Rev. A* 73, 041201 (2006).
8. K. Ishikawa and T. Blenski, ‘Explosion dynamics of rare-gas clusters in an intense laser field’, *Phys. Rev. A* 62, 063204 (2000).

Molecular dynamics made visible through mathematics.

New algorithm improves temporal resolution of X-ray free-electron laser experiments by a factor of 300

Timing uncertainty of a series of events that are recorded sequentially can blur and reduce our ability to extract meaningful dynamical information. Applying a new data-analytical approach based on singular value decomposition and non-linear Laplacian spectral analysis to experimental pump-probe data from an X-ray free-electron laser, we demonstrate a dramatic reduction of the timing uncertainty and, hence, are able to extract from the data information on dynamical properties such as ultrafast molecular vibrations. We verify the accuracy of the extracted molecular information by quantum-mechanical simulations.

In pump-probe experiments using pulses of different wavelength, timing uncertainty – the so-called timing jitter – between the pump and the probe pulses is one of the most challenging problems. The resulting shot-to-shot data, then, inherently contain inaccurate time stamps. In a recent X-ray / optical pump-probe experiment on N_2 the timing uncertainty was about 300 fs [1]. Thus, ultrafast dynamical processes, which in N_2 mostly take place on time scales below 100 fs, cannot be resolved.

To reduce this timing uncertainty and hence extract information on ultrafast dynamical processes, in this work, we use the data-analytical approach of non-linear Laplacian spectral analysis (NLSA), which is the singular value decomposition (SVD) on curved manifolds. The extracted dynamical information is then compared to results obtained by theoretical simulations based on the multiconfiguration time-dependent Hartree (MCTDH) method. By implementing this data-analytical method, we are able to reduce the timing uncertainty by a factor of 300.

To test our method, we use data collected from the first time-resolved X-ray / optical pump-probe experiments at the X-ray free-electron laser Linac Coherent Light Source (LCLS) [1]. In our data analysis, each snapshot of this dataset is represented as a vector. A series of supervectors are formed by concatenating the vectors within a certain window that is moved over the inaccurate dataset. If the concatenation window is comparable to or longer than the timing uncertainty, then some time-evolutionary information is contained in this supervector. The matrix of supervectors is then analysed using the NLSA method. In this way, we obtain a series of statistically significant modes consisting of characteristic patterns called topograms and their time evolutions called chronograms.

Figure 1 illustrates the various physical processes that take place for the case when molecular nitrogen interacts first with

an X-ray pulse (pump pulse) followed by an infrared laser pulse (probe pulse). First, N_2 is excited from the ground electronic state to the intermediate state, which is an inner-shell-ionized N_2^+ state, followed by subsequent Auger decay to the final states, which are N_2^{2+} states. In the latter states, the molecule either breaks apart immediately, or it manages to undergo a number of vibrations before eventually breaking apart. In our quantum-mechanical calculations, we assume instantaneous photoionization by an X-ray pulse, causing the nitrogen molecules to undergo Auger decay. After a controlled time delay, the N_2^{2+} produced is exposed to an IR pulse with an 800-nm central wavelength. In describing the Auger process, we used yields and lifetimes from experimental data [2, 3].

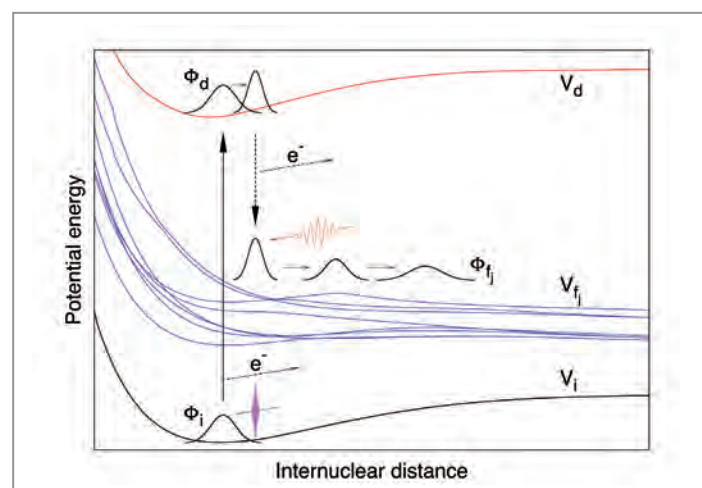


Figure 1

Illustration of various processes occurring in an X-ray / optical pump-probe experiment on molecular nitrogen. The initial wave packet Φ_i on the ground electronic state of N_2 is excited by an X-ray pulse (magenta) to an intermediate electronic state. The intermediate wave packet, Φ_d , then propagates on the intermediate electronic state and at the same time decays to the final states, Φ_{fj} , where the interaction with the optical pulse (red) takes place.

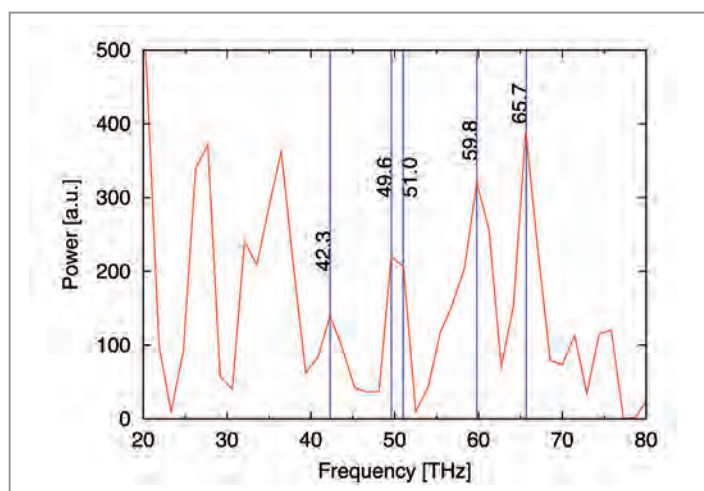


Figure 2

Oscillation frequency spectrum extracted from the data analysis. The blue lines show the extracted frequencies, which are close to well-studied molecular states [4, 5]. In addition, the new analysis technique provides information on previously unknown vibrational frequencies. The figure is taken from the original publication.

The data analysis technique reveals several modes recorded in the topograms and their corresponding chronograms. Though each mode does not represent a complete picture of the physical process in the system, key features of the processes at work can be identified in the modes since a linear combination of these modes represents the behaviour of the system during the measurement. One key feature captured in these modes is the distinct pattern of rotational motion induced by the IR pulse in the neutral molecular nitrogen when the IR pulse precedes the X-ray pulse. A second key feature is the wave-packet oscillations of the quasi-bound vibrational states of the doubly ionized nitrogen molecule when the X-ray pulse precedes the IR pulse. Further analysis of the wave-packet oscillations shows that some oscillation frequencies, shown in Fig. 2, closely coincide with some known vibrations of N_2^+ and N_2^{2+} [4, 5].

Results from the quantum-mechanical simulations using MCTDH allow us to identify some of the other detected oscillation frequencies with previously unknown vibrational frequencies in N_2^{2+} . In addition, the simulations also indicate how the vibrational wave packets oscillate in the manifolds of N_2^{2+} states, shown in Fig. 3, under the influence of the IR pulse. The wave packets decaying from the intermediate state to the final states are oscillating within the quasi-bound potential energy curves. The incoming IR pulse at varying time delay then further dissociates the doubly ionized nitrogen molecules. Since the efficiency of dissociation depends on the interatomic distance and, thus, on the molecular vibrational motion, the dissociation induced by the IR pulse is sensitive to the wave-packet dynamics associated with quasi-bound vibrational states of N_2^{2+} .

The new technique for analysing data will not only allow future experiments to be analysed more precisely. Existing data can also be re-examined. Furthermore, instead of resorting to complex technical solutions of the timing-jitter problem, it

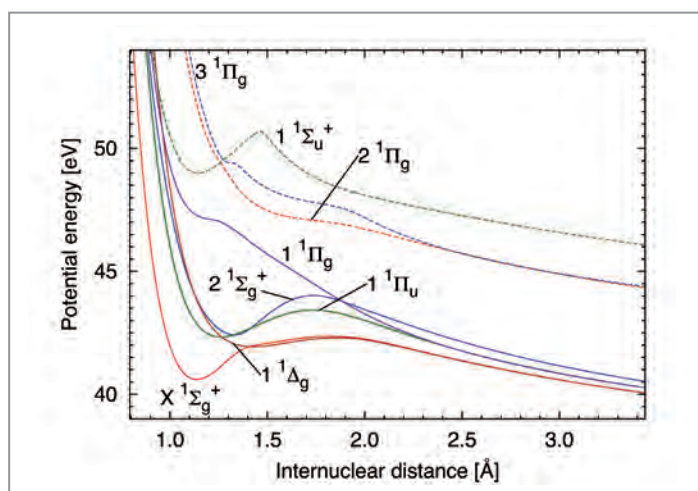


Figure 3

Potential energy curves of the N_2^{2+} final states considered in the quantum-mechanical simulations.

makes clever use of mathematical operations. Future applications could include time-resolved investigations of enzyme reactions in biology and chemistry, but also studying unusual states of matter, such as those occurring inside planets and stars. It might be even possible to use the new algorithm to more accurately calculate the timing of an even wider range of processes, such as past climatic events.

Contact: Robin Santra, robin.santra@desy.de

Authors

Russel Fung¹, Athiya M. Hanna^{2,3,4}, Oriol Vendrell^{2,3}, Sessa S. Ramakrishna⁵, Tamar Seideman⁵, Robin Santra^{2,3,4,6} and Abbas Ourmazd¹

1. Department of Physics, University of Wisconsin Milwaukee, Milwaukee, Wisconsin, USA
2. Center for Free-Electron Laser Science, DESY, Hamburg, Germany
3. The Hamburg Centre for Ultrafast Imaging, Hamburg, Germany
4. Department of Chemistry, University of Hamburg, Hamburg, Germany
5. Department of Chemistry, Northwestern University, Evanston, Illinois, USA
6. Department of Physics, University of Hamburg, Hamburg, Germany

Original publication

'Dynamics from noisy data with extreme timing uncertainty', *Nature* 532, 471 (2016). DOI:10.1038/nature17627

References

1. J.M. Glowacki et al., 'Time-resolved pump-probe experiments at the LCLS', *Opt. Express* 18, 17620-17630 (2010).
2. J.P. Cryan et al., 'Molecular frame Auger electron energy spectrum from N_2^+ ', *J. Phys. B: At., Mol. Opt. Phys.* 45, 055601 (2012).
3. B. Kempgens et al., 'A high-resolution N 1s photoionization study of the N_2 molecule in the near-threshold region', *J. Phys. B: At. Mol. Phys.* 29, 5389 (1996).
4. G. Dawber et al., 'Threshold photoelectrons coincidence spectroscopy of doubly-charged ions of nitrogen, carbon monoxide, nitric oxide and oxygen', *J. Phys. B: At. Mol. Phys.* 27, 2191 (1994).
5. S. De et al., 'Following dynamic nuclear wave packets in N_2, O_2 , and CO with few-cycle infrared pulses', *Phys. Rev. A* 84, 043410 (2011).

Fast local reactions of proteins.

Single gas-phase proteins absorb many photons simultaneously

The response of free proteins upon interaction with intense pulses of energetic photons is key for applications such as single molecule diffraction imaging. Proteins and many other biomolecules are inherently fragile species. To study their multiple photoionisation experimentally, in the first place it is necessary to gently transfer the proteins from their solvated state into the gas phase. We have combined an electrospray ionisation source with a radiofrequency ion trap to prepare a sample of multiply protonated or de-protonated ubiquitin molecules. The molecular ions were then exposed to extreme ultraviolet pulses from FLASH and photoionisation and photofragmentation were investigated by time-of-flight mass spectrometry. Simultaneous absorption of 10 or more photons from a single FLASH pulse induces the formation of small fragments. The photon-induced molecular dynamics are dominated by fast local structural responses that are independent of the initial charge state of the protein ion.

Proteins are particularly large biomolecules, consisting of long chains of amino acid residues bound together by peptide bonds. Protein structure is commonly investigated by mass spectrometry where gas-phase proteins are activated for instance by collisions or electron attachment. The excitation energy quickly equilibrates over the whole protein, raising its internal temperature. Dissociation then predominantly involves the weakest bonds. Protein activation by means of absorption of energetic photons from synchrotron sources, on the other hand, is a novel approach based on localized ionisation and excitation. Accordingly, in relatively small systems such as protonated leucine enkephalin (5 residues), small fragments containing single amino acid side chains (immonium ions)

dominate the breakup pattern [1]. These immonium ions are a fingerprint of a local activation process: The initial photoabsorption leads to fast dissociation, possibly through repulsive states, before the excitation energy has equilibrated throughout the molecule. However, when the size of the protein increases, soft X-ray absorption gets increasingly inefficient in causing immonium ion formation [2] and for protein sizes of the order of 100 amino acid residues, only little dissociation is observed [3].

Why is immonium ion formation suppressed in large proteins, even though it is considered localized and fast, occurring before the excitation energy equilibrates? Interfacing our apparatus (electrospray and ion trap) with the FLASH beamline BL3 allowed us to tackle this question from a complementary angle (see Fig. 1). Free-electron laser facilities such as FLASH deliver ultrashort pulses of energetic photons. By variation of pulse intensity, we were able to study ionisation and fragmentation of a selected gas-phase protein (ten-fold protonated ubiquitin, 76 residues) isolated in a radiofrequency (RF) ion trap as a function of the number of simultaneously absorbed extreme ultraviolet photons. The induced ionisation and fragmentation were investigated by time-of-flight mass spectrometry.

The key result for $[\text{ubi}+10\text{H}]^{10+}$ is shown in Fig. 2. In the right panel, two mass spectra obtained for low intensity (single-photon

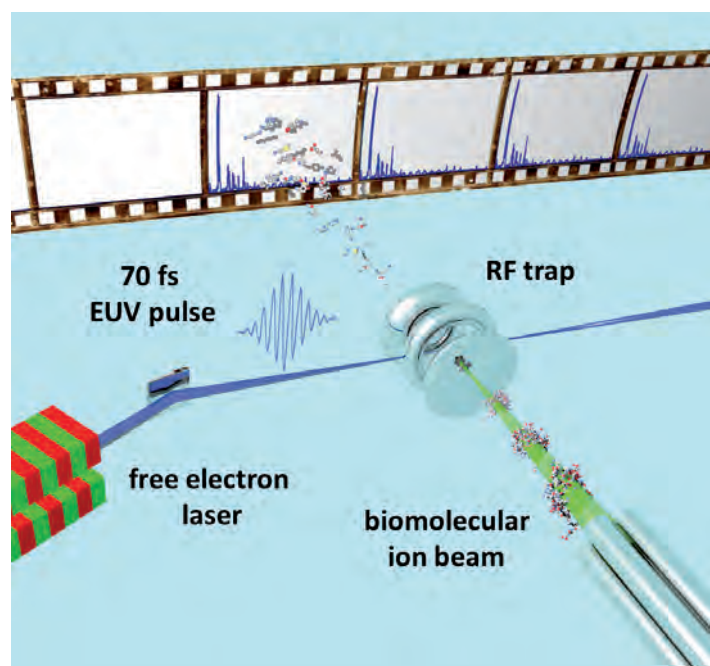


Figure 1

Sketch of the experimental arrangement. Electrosprayed protein ions arrive at the radiofrequency (RF) trap from a quadrupole mass filter. The molecular sample is exposed to FEL pulses from FLASH. The photoionisation products are extracted from the trap and analysed by mass spectrometry.

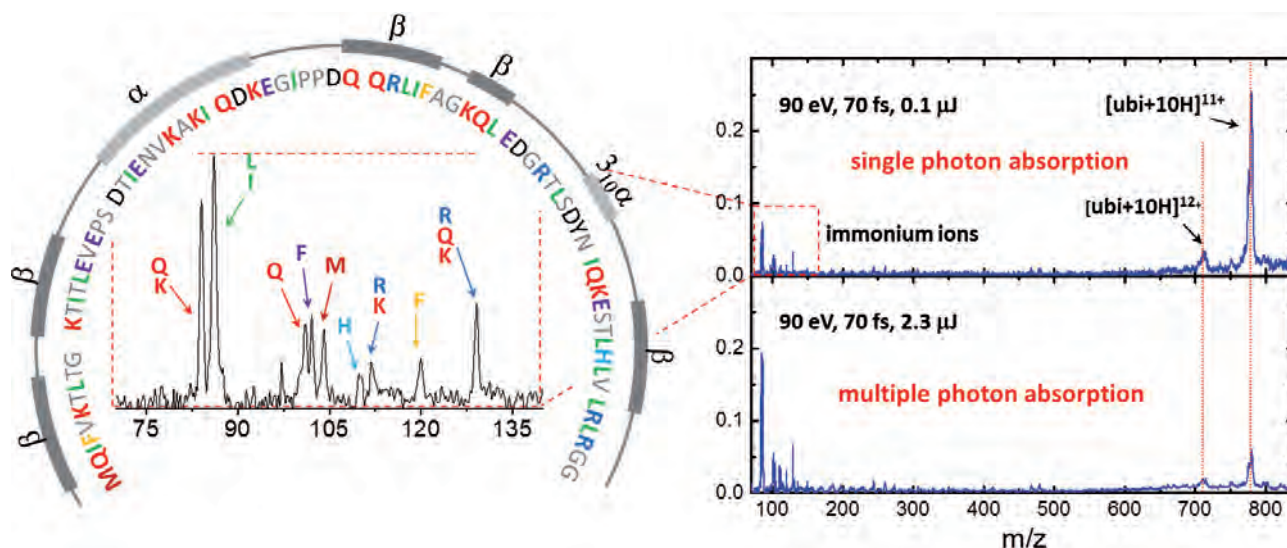


Figure 2
One-letter-code sequence of ubiquitin (coloured letters) and secondary structure (β -sheets and α -helices). The mass spectra on the right were obtained in the single (top) and multiple (bottom) ionisation regimes. The inset on the left is a zoom into the immonium ion region ($m/z = 70-140$). Reproduced with permission from the original publication. Copyright Wiley-VCH Verlag GmbH & Co. KGaA.

absorption regime) and for high intensity pulses (multiple-photon absorption regime) are displayed. For single-photon absorption, mainly non-dissociative ionisation into $[\text{ubi}+10\text{H}]^{11+}$ is observed and only a small contribution of immonium ions is observed. The inset in Fig. 2 shows a zoom into the immonium ion region, with peaks labelled with the one-letter code of the respective amino acid residue. In the multi-photon absorption regime, immonium ion formation dominates and non-dissociative ionisation is weak.

Before investigating the transition between both regimes in more detail, it is important to demonstrate that we were not merely studying the results of an increase in electrostatic repulsion that comes with the removal of an increasing number of electrons. This was accomplished by starting out from a multiply deprotonated protein instead of a multiply protonated one. We compared the photoabsorption in $[\text{ubi}-6\text{H}]^{6-}$ and in $[\text{ubi}+10\text{H}]^{10+}$. The initial difference in positive charge amounts to 16 unit charges and in the single-photon absorption regime entirely different mass spectra were observed. However, for the case of intense FLASH pulses and multi-photon absorption the obtained mass spectra were very similar and in both cases mainly positive immonium ions were formed.

Going back to $[\text{ubi}+10\text{H}]^{10+}$, we found the transition between single-photon absorption and multi-photon absorption regimes to be characterized by a linear increase in immonium ion yields. Such a linear scaling is not commonly observed in multi-photon ionisation and suggests a scenario where each gas-phase ubiquitin cation undergoes simultaneous independent photoabsorption processes. Each of these processes leads to ionisation and fast local fragmentation processes in which immonium ions are produced. These processes occur before the excitation energy equilibrates throughout the entire protein.

The protein thus responds to XUV photoionisation as an ensemble of small, few amino acid peptides.

In the future, we plan to study these processes in more detail by pump-probe type of experiments and for even higher intensities and photon energies employed in hard X-ray diffraction imaging.

Contact: Thomas Schlathölder, t.a.schlatholter@rug.nl

Authors

Thomas Schlathölder¹, Geert Reitsma^{1,2}, Dmitrii Egorov¹, Olmo González-Magaña¹, Sadia Bari^{3,4}, Leon Boschman^{1,5}, Erwin Bodewits¹, Kirsten Schnorr⁶, Georg Schmid⁶, Claus Dieter Schröter⁶, Robert Moshhammer⁶ and Ronnie Hoekstra¹

1. Zernike Institute for Advanced Materials, University of Groningen, Groningen, The Netherlands
2. Max-Born-Institut, Berlin, Germany
3. European XFEL GmbH, Schenefeld, Germany
4. Deutsches Elektronen-Synchrotron DESY, Hamburg, Germany
5. Kapteyn Institute, Groningen, The Netherlands
6. Max-Planck-Institut für Kernphysik, Heidelberg, Germany

Original publication

'Multiple Ionization of Free Ubiquitin Molecular Ions in Extreme Ultraviolet Free-Electron Laser Pulses', *Angew. Chem. Int. Ed. Engl.* 55, 10741–10745 (2016). DOI: 10.1002/anie.201605335

References

1. S. Bari, O. González-Magaña, G. Reitsma, J. Werner, S. Schippers, R. Hoekstra and T. Schlathölder, 'Photodissociation of protonated leucine-enkephalin in the VUV range of 8–40 eV', *J. Phys. Chem.* 134, 024314 (2011).
2. D. Egorov, L. Schwob, M. Lalande, R. Hoekstra and T. Schlathölder, 'Near edge X-ray absorption mass spectrometry of gas-phase proteins: the influence of protein size', *Phys. Chem. Chem. Phys.* 18, 26213–26223 (2016).
3. R. Milosavljević, F. Canon, C. Nicolas, C. M. L. Nahon and A. Giuliani, 'Gas-Phase Protein Inner-Shell Spectroscopy by Coupling an Ion Trap with a Soft X-ray Beamline', *J. Phys. Chem. Lett.* 3, 1191–1196 (2012).

Ultrashort FLASHes.

Commissioning of terahertz-field driven streaking diagnostics at FLASH

A terahertz (THz)-field driven streak camera has been commissioned at FLASH providing XUV pulse duration and arrival time information with around 10 fs resolution for each single XUV free-electron laser (FEL) pulse. Pulse durations between 200 fs and <20 fs have been measured for different FEL settings. Particularly the arrival time analysis shows how precisely FLASH can be operated.

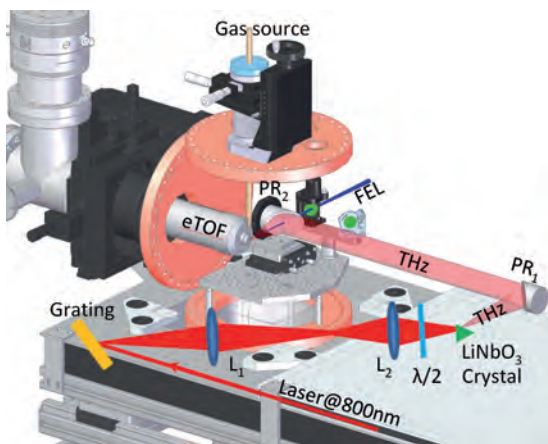


Figure 1

THz streaking setup. Lenses (L_1 and L_2) are used to image the laser pulse front tilt provided from a diffraction grating onto the Lithium niobate (LiNbO_3) crystal prism for efficient THz generation. Parabolic mirrors (PR_1 and PR_2) are guiding the THz beam to the interaction point. Here, electrons generated by the FEL pulses are interacting with the THz field and are detected in a time-of-flight detector (eTOF).

Since FLASH lases in Self-Amplified Spontaneous Emission (SASE) mode each pulse is 'unique' and has different pulse energy, XUV spectrum and pulse duration. Due to very small fluctuations in the acceleration, the arrival time of the XUV pulses jitters within several tens of femtoseconds. The focus of online diagnostics at FLASH is to measure all fluctuating properties as completely as possible. Due to the burst mode structure of FLASH with up to 800 pulses spaced by one microsecond (at a repetition rate of 10 Hz) such measurements are a challenge.

A number of methods have been developed and are in use to determine pulse energy [1], spectrum [2,3] and arrival time of the electron bunches [4], while the XUV pulse duration still lacks a suitable detector. Providing pulse length information will aid a precise analysis of measurements of nonlinear interactions as well as pump-probe experiments that make use of the short pulse length.

A THz streak camera [5,6] has the potential to deliver single-shot pulse duration information basically wavelength independent and with a high dynamic range (in pulse duration and FEL energy) and it is able to be operated with repetition rates up to several hundred kHz (potentially even MHz). In addition, it can provide arrival time information between the XUV pulse and the laser driving the THz generation for each single pulse with an accuracy well below 10 fs. Due to its wide working range the concept can not only be used for FLASH, but also for European XFEL or other X-ray FELs [7].

The measurement principle is based on a noble gas target being photo-ionized by the FEL pulse. The kinetic energy of the resulting electrons is modified by the electric field of the THz radiation when it is co-propagating through the target. If the electron wave packet is short compared to the period (>500 fs in our case), the temporal structure of the wave packet will be mapped onto the kinetic

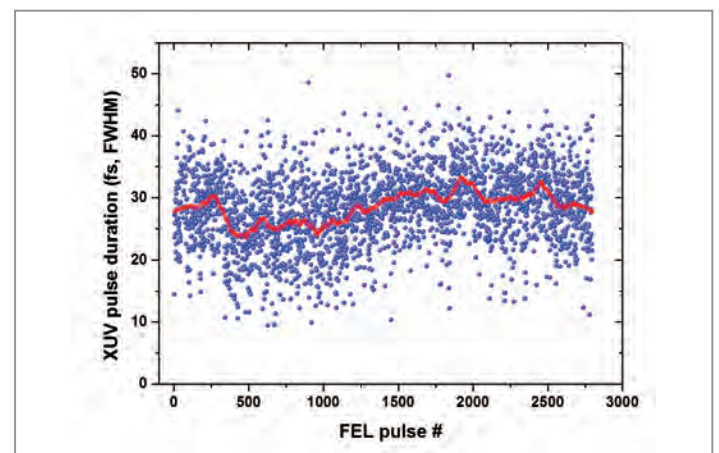


Figure 2

Single shot pulse duration for around three thousand FLASH pulses (5 min). The red line indicates the mean value of ~30 fs. Error bars (not shown) due to the fit uncertainty are on the order of $\pm 10\%$.

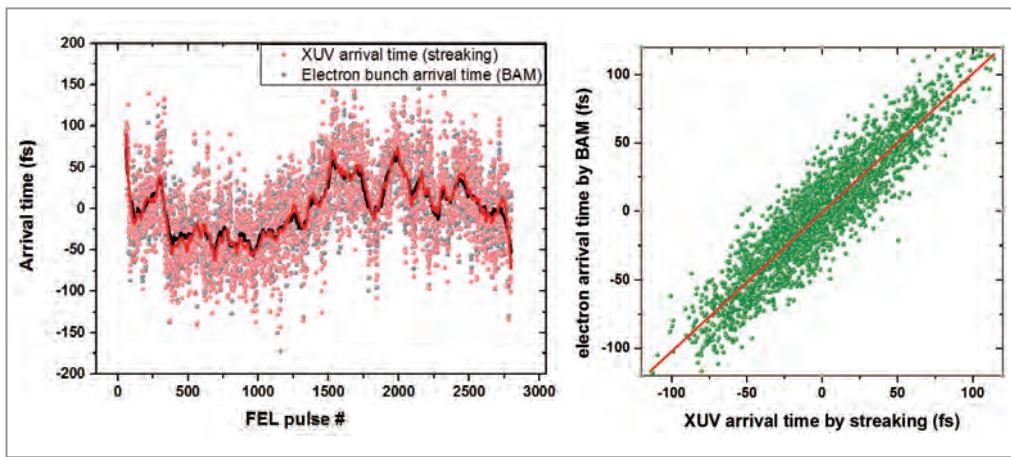


Figure 3

The arrival time is plotted (left) for the same FEL pulses as in Fig. 2. XUV (red) and electron (black) arrival times agree well on a shot-to-shot basis (dots). Averaging the arrival time (lines) still provides very good agreement and shows that besides the fast (shot-to-shot) jitter also drifts on a minute basis are only few fs. The correlation plot (right) comparing the arrival time measured for electrons in the accelerator using a BAM and the XUV pulses at the experiment (streaking) shows a correlation width of only 20 fs rms. The red line indicates the linear fit.

energy distribution of the emitted electrons [8]. The pulse duration can be extracted from the broadening of the peaks measured in the photoelectron spectrum due to the presence of the THz field. The shift of the kinetic energy peaks provides the arrival time.

The THz streak camera (Fig.1) was build and installed at FLASH at the PG0 beamline. This beamline has the capability to use the zero order FEL beam for the streaking setup while the dispersed radiation can be simultaneously used in the PG2 beamline to measure the FEL spectrum with high resolution. The THz radiation is generated by interaction of pulses delivered from the FLASH1 pump-probe laser (800 nm, 60 fs, 6 mJ) with a nonlinearly reacting crystal. In detail, the source is based on pulse front tilt optical rectification in a lithium niobate (LiNbO₃) crystal [9]. A THz field strength of ~150 kV/cm has been reached.

Several different FEL operation settings have been used to commission the technique in a wide range of pulse durations from 200 fs to less than 20 fs (FWHM). For each setting the FLASH single-shot pulse duration as well as the arrival time of the XUV pulses with respect to the THz generating optical laser was measured. As one example for the measurements, a time sequence of 5 minutes (3000 pulses) is given in Fig. 2. It shows the inherent fluctuations of the pulse duration. Thus, analysis of user experiments can be improved significantly once this information will be available online for each FEL pulse.

As a second important result of the commissioning experiments, we could verify the assumption that the electron beam arrival time monitor (BAM) measuring the arrival time of the electron bunches with high precision in the FLASH accelerator is an acceptable measure for the arrival time of the XUV photon pulses in all measured cases [10]. The arrival time of the electrons determined almost 200 metres upstream of the experimental hall in the accelerator tunnel (with respect to the FEL master timing) is in good agreement with the arrival time of the XUV pulses with respect to the pump-probe laser (generating the THz and also synchronized to the master timing) at the experiment. As presented in Fig. 3, the shot-to-shot arrival time measurement shows a correlation width of 20 fs rms or

less for most of the settings investigated so far. Thus, the time resolution of user pump-probe experiments (using the pump-probe laser) can be significantly improved by sorting their data with the arrival times measured by the BAM.

We report on the installation and commissioning of a pulse length diagnostics chamber at FLASH1 beamline PG0. Single-shot pulse duration measurements of XUV pulses covering the full range of <20 fs to 200 fs have been demonstrated. In addition, very good agreement between the electron beam arrival time monitor (BAM) data and the actual arrival time fluctuations of the XUV pulses with respect to the FLASH1 pump-probe laser at an experimental endstation was verified. Currently, the setup is used in scheduled diagnostic shifts and not yet as online diagnostics for user experiments. A dedicated laser for the THz generation is currently build by the CFEL group of F. Kärtner to overcome this limitation and the setup will be further developed to serve as an online pulse duration diagnostics for FLASH2.

Contact: *Rosen Ivanov, rosen.ivanov@desy.de*
Stefan Düsterer, stefan.duesterer@desy.de

References

1. K. Tiedtke et al., 'Gas detectors for x-ray lasers', *J. Appl. Phys.* 103, 094511 (2008).
2. G. Brenner et al., 'First results from the online variable line spacing grating spectrometer at FLASH', *Nucl. Instr. and Meth. A* 635, 99–103 (2011).
3. M. Braune et al., 'A non-invasive online photoionization spectrometer for FLASH', *Journal of Synchrotron Radiation* 23, 10–20 (2016).
4. A. Angelovski et al., 'High bandwidth pickup design for bunch arrival-time monitors for free-electron laser', *Phys. Rev. Lett. Spec. Top. – Accelerators and Beams* 15, 112803 (2012).
5. I. Grguras et al., 'Ultrafast X-ray pulse characterization at free-electron lasers', *Nature Photonics* 6, 852, (2012).
6. U. Fröhling et al., 'Single-shot terahertz-field-driven X-ray streak camera', *Nature Photonics* 3, 523 (2009).
7. P.N. Juranić et al., 'High-precision x-ray FEL pulse arrival time measurements at SACLA by a THz streak camera with Xe clusters', *Optics express* 22, 30004–30012 (2014).
8. J. Itatani et al., 'Attosecond Streak Camera', *Phys. Rev. Lett.* 88, 173903 (2002).
9. J. Hebling et al., 'Velocity matching by pulse front tilting for large-area THz-pulse generation', *Opt. Express* 10, 1161–1166 (2002).
10. S. Schulz et al., 'Femtosecond all-optical synchronization of an X-ray free-electron laser', *Nat. Commun.* 6, 5938 (2015).

Creating spiraling FLASHes.

4-mirror-polarizer at FLASH1 for ultrafast magnetism studies and other chirality-sensitive light-matter interactions

Circularly polarized radiation in the extreme ultraviolet (XUV) spectral range is a powerful tool for element specific investigations of chirality-sensitive light-matter interaction, for example in biomolecules with handedness or in magnetic materials. In particular, magnetic circular dichroism spectroscopy is a unique technique for transient absorption [1] and transient coherent imaging experiments. It gives element selective magnetic sensitivity with nanometre spatial resolution [2]. At the free-electron laser FLASH1, a device to generate circularly polarized radiation with a high degree of circular polarization reaching up to 90% and transmission values exceeding 30% was recently commissioned.

Electromagnetic radiation in free space is described as a two dimensional transverse wave with its electric field vector \mathbf{E} oscillating perpendicular to the direction of propagation. The reflection of polarized radiation at a mirror is defined by two orthogonal components of \mathbf{E} : the s-polarized component, E_s , oscillating in the plane perpendicular (s = senkrecht) to the plane of incidence and the p-polarized component E_p (p = parallel) oscillating in the plane parallel to the plane of incidence. A phase shift or retardation between the 's' and 'p' components of the electric field causes elliptical polarization; the special case of equal magnitude of the two components and a relative phase shift of exactly 90° leads to a circularly polarized light beam (compare Figs. 1a and b). While for optical wavelengths it is easy to control the state of polarization by transmission through birefringent crystals, the lack of transparent materials for extreme ultraviolet radiation requires a different approach based on reflection.

Since interaction of electromagnetic radiation with conducting materials is dominated by strong absorption, incident linearly polarized light will in general become elliptically polarized upon reflection at a metallic surface [3]. Hence, to efficiently

generate circularly polarized radiation in the XUV spectral range one has to identify an optimal metallic material and choose a reflection geometry which introduces a large phase shift between the 's' and 'p' component of the incident light field while at the same time maintaining a high degree of reflectivity [4]. By an optimization calculation we identified the metal Molybdenum (Mo) in an 4-mirror reflection geometry (Fig. 1) to yield the highest figure of merit, TP^2 (T transmission through device, P degree of circular polarization). The performance of the device is then simply determined by two adjustable parameters, the rotation angle α , which defines the ratio between the 's' and 'p' electric fields, and the grazing angle of incidence θ (Fig. 1b).

The results of the optimization calculations are summarized in Fig. 2a, where we show the transmission T (green line), the polarization P (red line), and the figure of merit TP^2 (blue line) as a function of the XUV photon energy. Importantly, the optimization algorithm yields an almost unchanged TP^2 , no matter whether we keep the parameter θ free (dashed blue line) or fix it at an angle of incidence $\theta = 12^\circ$ (solid blue line). This allows a significant simplification of the device, both with

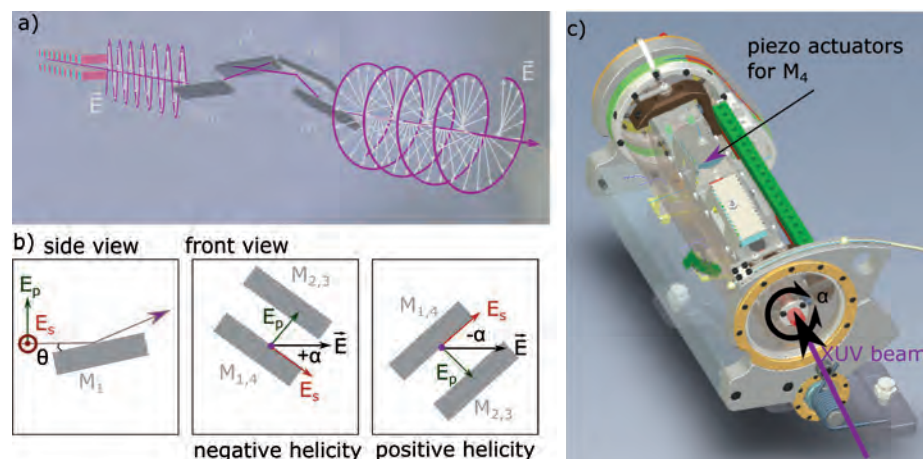


Figure 1

(a) Artistic depiction of the polarization of XUV radiation after transmission through the 4-mirror reflection polarizer. The grey arrows show the oscillating electric field vector \mathbf{E} . (b) Definition of the grazing angle of incidence θ and the angle of rotation α with respect to \mathbf{E} . The front view shows the geometry for negative and positive helicity. (c) Design model of the 4-mirror reflection polarizer. The mirror assembly can be rotated around the beam axis α ; small changes in the beam pointing are corrected by a piezo adjustable mirror.

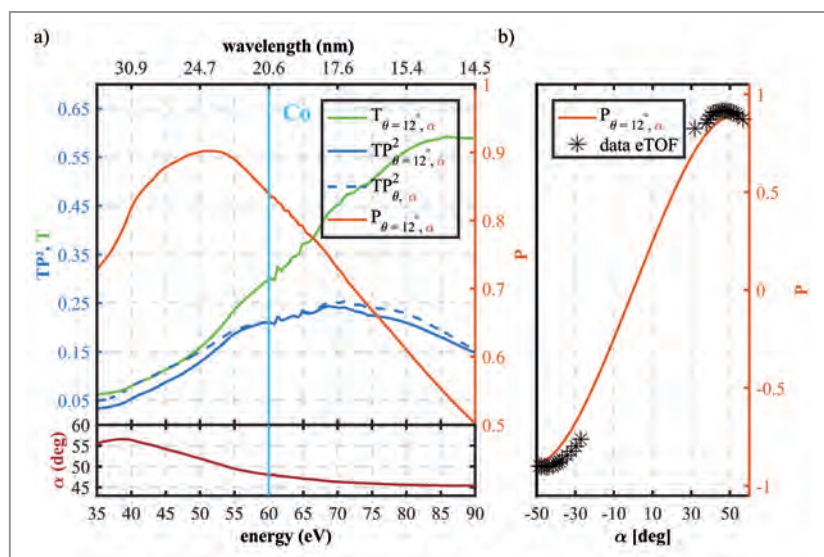


Figure 2

(a) Calculation of the transmission T , degree of circular polarization P , and figure of merit TP^2 as a function of photon energy for the 4-mirror reflection polarizer based on Molybdenum. These values are calculated for a fixed grazing angle of incidence $\theta = 12^\circ$ and maximizing TP^2 by varying the angle α . The blue dashed line shows the result for an optimization calculation of TP^2 by varying both, θ and α , clearly showing that keeping the incident angle fixed results in an almost negligible loss of performance, while greatly simplifying the mechanical design.

(b) Calculated P as a function of the rotation angle α at 60 eV (Cobalt M-edge). The preliminary analysis of the eTOF measurement yields $P = 87\%$ for $\alpha = \pm 48^\circ$ for negative and positive helicity, respectively.

regard to its mechanical design as well as to its alignment for user operation. Adjustments of the rotation angle α between $\pm 56^\circ$ and $\pm 45^\circ$ for photon energies between 35 eV and 90 eV suffice to set the polarization of the XUV radiation to positive or negative helicity, respectively. The figure of merit TP^2 is above 0.15 in the range of the most important M-edges of the magnetic transition metals Mn, Fe, Co and Ni. The degree of circular polarization reaches a maximum of 90% at 50 eV, before it drops almost linearly to 50% at 90 eV. The increasing XUV reflectivity of Mo for higher photon energies is caused by an absorption edge around 40 eV and leads to plateau of TP^2 extending all the way to 90 eV.

A design model of the 4-mirror reflection polarizer is shown in Fig. 1c: the mirror assembly can be rotated around the beam axis by a stepper motor; beam-pointing deviations of $< 30 \mu\text{rad}$ are compensated by small adjustments of the last mirror M_4 via piezo actuators. With tabulated piezo settings, determined during commissioning, the device allows rapid switching (< 10 seconds) of the XUV beam helicity without changing the beam position on the sample. The device can be quickly and reproducibly moved in and out of the FEL beam path.

The 4-mirror reflection polarizer was recently installed and commissioned at FLASH1 for user operation at any of the three BL beamlines delivering the direct and 'non-mono-chromatized' FEL beam. The degree of circular polarization was measured by a multi-channel, time-of-flight electron spectroscopy polarimeter (eTOF) [5]. Characteristic angle resolved photo-electron spectra of helium allowed to determine the plane and the degree of linear polarization of the incident radiation. The absolute degree of circular polarization can then be deduced if an unpolarised background of the light source is determined beforehand. Preliminary results of the eTOF measurements are shown in Fig. 2b as a function of the angle α , measured at the M-edge of Co at an energy of 60 eV. Agreement with the

calculated prediction is excellent with a maximum degree of circular polarization of 87%.

In summary, a polarizer for XUV radiation based on phase retardation upon reflection off a metallic mirror is now available at FLASH1 beamlines BL1-3. The simple design allows fast changes of the helicity of the incoming FEL beam with high transmission and a high degree of circular polarization reaching up to 90%. The new polarizer opens the wide field of (soft) X-ray magnetic circular dichroism (XMCD) for time-resolved experiments at FLASH. Besides studies of ultrafast magnetic phenomena, we also envision new types of polarization sensitive experiments of 'handed' or chiral materials and (bio-)molecules.

Contact: Clemens von Korff Schmising, korff@mbi-berlin.de
Rolf Treusch, rolf.treusch@desy.de

Authors

Clemens von Korff Schmising¹, Tino Noll¹, Michael Schneider¹, David Weder¹, Jens Buck², Gregor Hartmann², Jens Viehhaus², Rolf Treusch² and Stefan Eisebitt¹

1. Max-Born-Institut Berlin, Berlin, Germany

2. Deutsches Elektronen-Synchrotron DESY, Hamburg, Germany

References

1. F. Willems, C. T. L. Smeenk, N. Zhavoronkov, O. Kornilov, I. Radu, M. Schmidbauer, M. Hanke, C. von Korff Schmising, M. J. J. Vrakking, S. Eisebitt, 'Probing ultrafast spin dynamics with high-harmonic magnetic circular dichroism spectroscopy', Phys. Rev. B 92, 220405(R) (2015).
2. C. von Korff Schmising, B. Pfau, M. Schneider, C. M. Günther, M. Giovannella, J. Perron, B. Vodungbo, L. Müller, F. Capotondi, E. Pedersoli, N. Mahne, J. Lüning and S. Eisebitt, 'Imaging Ultrafast Demagnetisation Dynamics after a Spatially Localized Optical Excitation', Phys. Rev. Lett. 112, 217203 (2014).
3. Max Born and Emil Wolf, 'Principles of Optics (Sixth Edition)', Elsevier (1980).
4. R. N. Hamm, R. A. MacRae and E. T. Arakawa, 'Polarization Studies in the Vacuum Ultraviolet', J. Opt. Soc. Am. 55, 1460 (1965).
5. J. Viehhaus, F. Scholz, S. Deinert, L. Glaser, M. Iichen, J. Seltmann, P. Walter and F. Siewert, 'The Variable Polarization XUV Beamline P04 at PETRA III: Optics, Mechanics and Their Performance', Nucl. Instrum. Meth. Phys. Res. Sect. A 710, 151 (2013).

Synchronous laser-microwave networks.

Towards attosecond-resolution photon science

To observe electronic dynamics in atoms, molecules and condensed matter taking place on an attosecond time scale, next generation photon science facilities, like X-ray free-electron lasers and attoscience centres, require system-wide attosecond-level synchronization of dozens of optical and microwave signals up to kilometre distances. Here we present a timing synchronization system that can meet the strict timing requirements of such large-scale facilities. By developing new ultrafast timing detectors and suppressing optical fiber nonlinearities together with fundamental noise contributions, we realize a complete laser-microwave network incorporating two mode-locked lasers and one microwave source with a total of 950 attosecond jitter integrated from 1 μ s to 18 h.

Rapidly expanding photon science facilities like X-ray free-electron lasers (XFELs) [1,2] and attoscience centres [3] show the highest demand in synchronization, on the range of attoseconds, to generate ultrashort X-ray pulses enabling 4D-microscopy with attosecond temporal and subatomic spatial resolution. To achieve this, it is necessary to develop an attosecond-precision timing distribution system (TDS) to synchronize various microwave and optical sources across kilometre-scale facilities. Such timing stability is required for seeded XFEL operation and attosecond pump-probe measurements. So far, there has been no TDS meeting these strict requirements. Therefore, the low temporal precision

provided by current TDS remains a major obstacle for realizing attosecond hard X-ray photon science facilities. Here, we further develop the pulsed-optical TDS approach [4], which uses ultralow-noise pulses generated by a mode-locked laser as the timing signal to synchronize optical and microwave sources using balanced optical cross-correlators (BOCs) [5] and balanced optical-microwave phase detectors (BOMPdS) [6]. While this pulsed scheme has breached the 10-fs precision level [4], realization of attosecond precision requires further development of the timing detectors and a deep physical understanding of optical pulse shaping in fibre transmission.

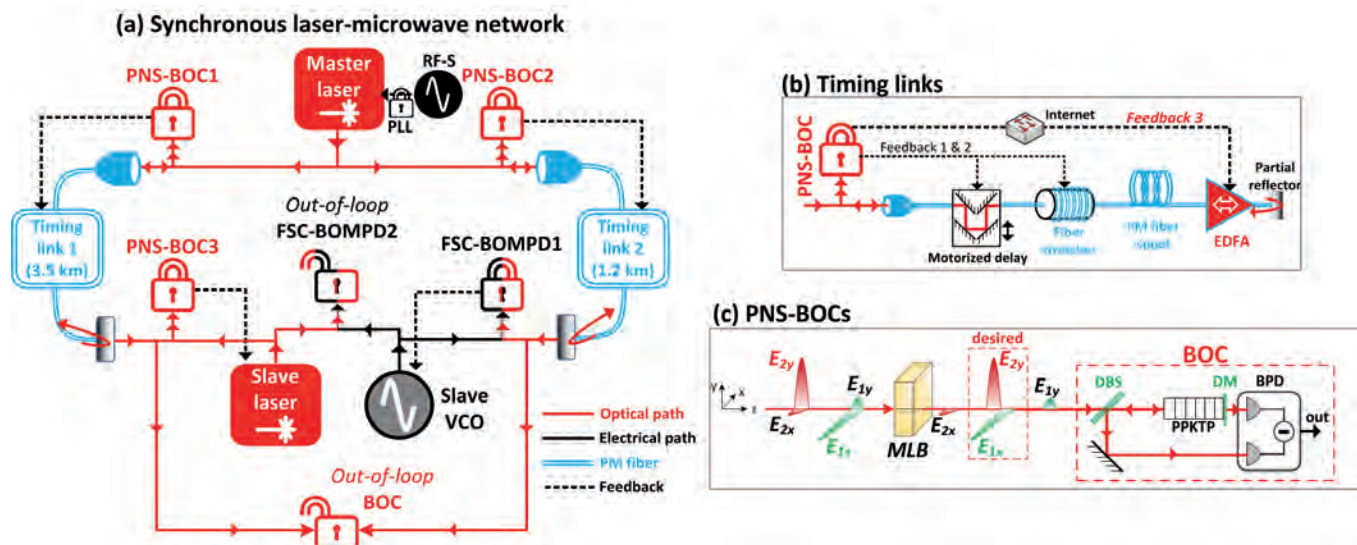


Figure 1
 (a) Schematic of the laser-microwave network. (b) Components of the timing links and their applied feedback controls. (c) Schematic of a polarization-noise suppressed BOC (PNS-BOC). It contains a single periodically poled KTP crystal (PPKTP), with appropriate dichroic beam splitter and mirror (DBS and DM). Ideally, the input pulses (E_{2y} and E_{1x}) are aligned along the two principal axes of the crystal. Due to finite polarization extinction ratios of the optical elements upstream from BOCs, there will be pulse components (E_{2x} and E_{1y}) projected along the undesired polarization axes. In a PNS-BOC a material with a large birefringence (MLB) is placed before the BOC to add a significant delay to the erroneous pulses, such that they do not overlap and interfere with the second-harmonic generation.

Theoretical analysis shows that even in the absence of environmental noise, residual link dispersion and nonlinearities add considerable excess jitter through link transmission and feedback loops. Taking the outcomes of this noise analysis into account, an attosecond precision laser-microwave network is demonstrated using the setup in Fig. 1a. The timing signal from the master laser is distributed through two independent fibre links of 1.2 km and 3.5 km length, whose outputs are used to synchronize a remote laser and a voltage-controlled oscillator (VCO) simultaneously. The dispersion of the fibre links is carefully compensated to preserve the temporal profiles of the optical pulses upon transmission, as well as to provide high peak energy for the optical cross-correlation. The time of flight fluctuations of each fibre link are detected by a BOC whose output controls a motorized delay, a fibre stretcher and an erbium-doped fibre amplifier (EDFA) to correct for the long-term temperature drift, fast jitter imposed on the link and link power fluctuations, respectively (see Fig.1b).

To improve noise performance, we realize a polarization-noise suppressed BOC (PNS-BOC) by the addition of a highly birefringent material, Fig. 1c. Since there are no time-dependent error voltages introduced by undesired pulse components, each PNS-BOC can be locked exactly at the zero amplitude-to-phase noise conversion point of its voltage response. To avoid the disadvantages of direct photodetection, free-space-coupled BOMPDS (FSC-BOMPDS) are employed as optical-to-microwave timing detectors. The free-space components at the optical input can efficiently reduce long-term drifts caused by the environment, and the delay stages can enable precise phase tuning without backlash and avoid microwave reflection and loss.

Finally, timing stability of the link network is measured with an out-of-loop BOC, whereas the performance of the complete laser-microwave network is evaluated with an out-of-loop FSC-BOMPDS as shown in Fig. 1a. Stabilization of the timing link network is operated continuously for 52 h for a test and the improvements in the timing system result in an unprecedented timing error of only 200 as RMS, measured by the out-of-loop BOC below 1 Hz (Fig. 2 a, red curve). The total integrated timing jitter of the link network from 6 μ Hz to 1 MHz is only 580 as (Fig. 2b, red curve), corresponding to a relative timing instability of 3.1×10^{-21} . After characterizing the link network performance, we activate the remote synchronization of the slave laser and VCO and observe the out-of-loop timing results with the free-running FSC-BOMPDS. The synchronous laser-microwave network shows an unprecedented long-term precision of 670 as RMS over 18 h (Fig. 2a, black curve). The relative timing stability between the two remotely synchronized devices within the full frequency range from 15 μ Hz to 1 MHz is only 950 as RMS (Fig. 2b, black curve).

This work paves the way to unfold the full potential of next-generation attosecond photon science facilities, with the ability to revolutionize many research fields from structural biology to material science and from chemistry to fundamental physics. Besides, this technique will also accelerate developments in many other fields requiring high temporal resolution such as ultrastable clocks, gravitational wave detection and coherent optical antenna arrays.

Contact: Franz Kärtner, franz.kaertner@cfel.de

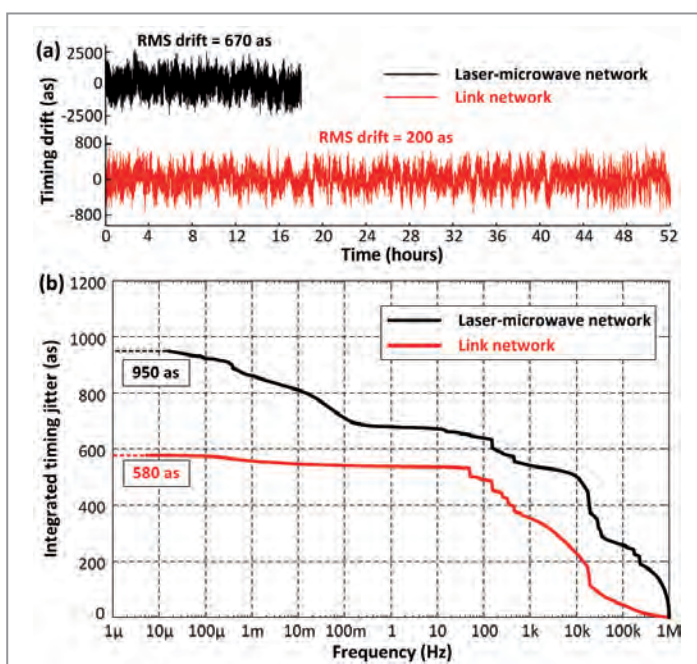


Figure 2 Out-of-loop timing measurement results. (a) Timing drift below 1 Hz and (b) integrated timing jitter from 1 MHz down to 5.3 μ Hz (i.e., 52 h) for the red curve and down to 15 μ Hz (i.e., 18 h) for the black curve.

Authors

Ming Xin¹, Kemal Şafak^{1,2}, Michael Y. Peng³, Aram Kalaydzhyan¹, Wenting Wang¹, Oliver D. Mücke^{1,4} and Franz X. Kärtner^{1,2,3,4}

1. Center for Free-Electron Laser Science CFEL, DESY, Hamburg, Germany
2. Department of Physics, University of Hamburg, Hamburg, Germany
3. Research Laboratory of Electronics, Massachusetts Institute of Technology, Cambridge, USA
4. The Hamburg Centre for Ultrafast Imaging, University of Hamburg, Hamburg, Germany

Original publication

'Attosecond precision multi-kilometer laser-microwave network',

Light: Science & Applications, 5, e16187 (2017); DOI:10.1038/lsa.2016.187

References

1. M. Altarelli et al. (ed.), 'XFEL - The European X-ray Free-Electron Laser', Technical Design Report, Report DESY-06-097 (2006).
2. P. Emma et al., 'First lasing and operation of an angstrom-wavelength free-electron laser', *Nature Photon.* 4, 641-647 (2010).
3. G. Mourou and T. Tajima, 'More intense, shorter pulses', *Science* 331, 41-42 (2011).
4. J. Kim, J. A. Cox, J. Chen and F. X. Kärtner, 'Drift-free femtosecond timing synchronization of remote optical and microwave sources', *Nature Photon.* 2, 733-736 (2008).
5. T. R. Schibli et al., 'Attosecond active synchronization of passively mode-locked lasers by balanced cross correlation', *Opt. Lett.* 28, 947-949 (2003).
6. J. Kim, F. X. Kärtner and F. Ludwig, 'Balanced optical-microwave phase detectors for optoelectronic phase-locked loops', *Opt. Lett.* 31, 3659-3661 (2006).

Lightwave electronics on a chip.

Strong-field nano-optics

In electronic devices such as field-effect or bipolar junction transistors, applied electric fields control electron motion. Conventionally, these applied fields range in frequency up to the microwave regime, i.e. up to frequencies of hundreds of gigahertz (10^9 Hz). Recently, researchers have shown that the electric fields of intense, waveform-controlled laser pulses, i.e. electric fields in the petahertz (10^{15} Hz) regime, can control electron motion around gaseous atoms and nanostructures. Requiring specialized laser systems and elaborate vacuum apparatuses however, such 'lightwave electronics' differ significantly from their microwave counterparts. In our recent work, we aimed to bridge this gap: We extended lightwave electronics to chip-scale devices based on plasmonic nanoparticles that operate out-of-vacuum and in ambient conditions.

When a light pulse interacts with electrons in matter, the comparatively slow electrons are typically pushed by changes in the envelope of the pulse. In other words, the electrons are controlled by the average behaviour of many cycles of the rapidly oscillating light wave. However, when the electric field of the incident light is sufficiently strong, individual oscillations of the light wave can control electron motion. For example, when an intense laser pulse interacts with a gas, individual cycles of the pulse's strong electric field can ionize gas atoms and steer the resulting sub-optical-cycle electrical wavepackets [1]. In this 'strong-field' regime, electrons are controlled by the instantaneous electric field of the exciting light, and just as synthesized microwave fields control electron motion in microwave electronic devices, tailored light waves can push, pull, and steer electrons in this regime of lightwave electronics [1, 2].

Motivated by the prospect of solid-state lightwave electronic devices, researchers have recently pushed strong-field

light-matter interactions from the gas-phase to solid-state nanostructures. Metallic nano-tips, illuminated with ultrafast laser pulses, have exhibited strong-field signatures in their photoemission current yields and energy spectra [3-5], and photoemission currents from these nano-tips have shown carrier-envelope phase (CEP) sensitive effects, a hallmark of lightwave electrical control [4,5]. In our recent work, we pushed a step further, and extended strong-field interactions and lightwave electronics to plasmonic nanoparticles and micro-optoelectronic devices.

We integrated arrays of plasmonic nanoparticles into micro-optoelectronic devices resembling vacuum tubes with optically driven emitters. An illustration of an example device is provided in Fig. 1a. The emitter consists of an array of plasmonic nanoparticles separated from a collector by a $\approx 5 \mu\text{m}$ wide gap. The nanoparticles are lithographically defined gold nanorods or nanotriangles with localized surface

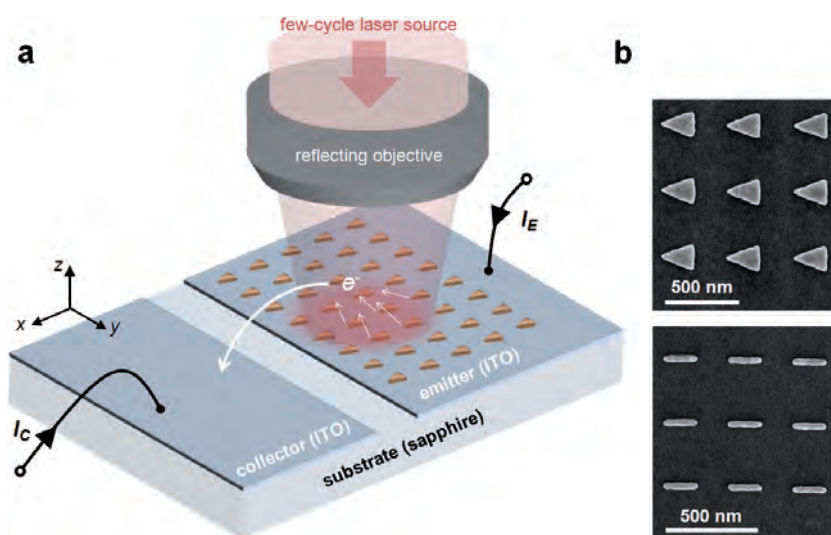


Figure 1

Basic device layout and experimental setup.

- (a) Sketch of the device and experiment: A few-cycle laser pulse is tightly focused onto an array of plasmonic nanoparticles. The nanoparticles rest on a layer of conducting, transparent indium tin oxide (ITO) and are separated from an ITO collector by a few micron wide gap. The laser pulses produce photoemission currents from the nanoparticles that jump from emitter to collector; emitter and collector currents are denoted I_E and I_C , respectively.
- (b) Scanning electron microscope images of portions of two different nanoparticle emitter arrays. The displayed nanotriangles (top) and nanorods (bottom) have resonant wavelengths of 1058 nm and 1041 nm, respectively.

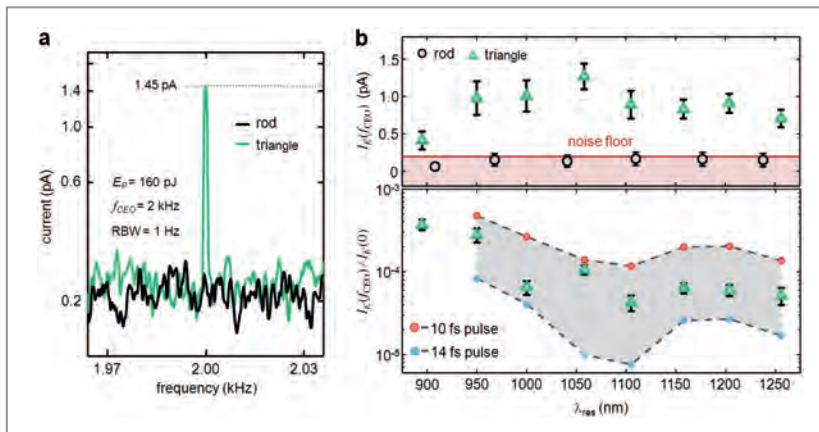


Figure 2

CEP sensitive photoemission. (a) The measured photocurrent spectra for the emitter arrays displayed in Fig. 1b. The laser pulse energy used is $E_p = 160$ pJ, and the resolution bandwidth (RBW) is 1 Hz. (b) (Top) Magnitude of the CEP sensitive current (that is I_E at f_{CEO}) for eight different nanotriangle emitter arrays and six different nanorod arrays. The current is plotted versus the resonant wavelength (λ_{res}) of each array's localized surface plasmon resonance. (Bottom) CEP sensitivity, that is the ratio of the CEP sensitive current to the total average current, for each nanotriangle emitter array. The measured CEP sensitivity of the nanotriangle emitter arrays is compared to that predicted by a simple Fowler-Nordheim tunneling model for two different pulse durations of 10 fs and 14 fs.

plasmon resonances ranging from $\approx 950 - 1250$ nm (an electron micrograph of two representative nanoparticle arrays is provided in Fig. 1b).

When the nanoparticles are illuminated by tightly focused, few-cycle laser pulses, they emit electrons, and these photoelectrons form a current from the emitter to the collector. In our experiments, we stabilize the CEP of the incident laser pulses: We set the carrier-envelope offset frequency, the rate at which the CEP circles 2π , to be $f_{\text{CEO}} = 2$ kHz. Looking at the spectrum of the photocurrent, we detect CEP modulation. Figure 2a shows the frequency spectra of the photocurrent for the two nanoparticle arrays displayed in Fig. 1b, and we see that the nanotriangles show a clear CEP dependent signature while the nanorods show no CEP sensitive behaviours.

In the strong-field regime, the photocurrents from the nanoparticles are driven by the instantaneous electric field of the exciting laser pulse. Specifically, when the strong incident field points into the nanoparticle, it collapses the particle's electrical binding potential and instantaneously drives tunneling currents out of the particle's metal surface. For a single nanotriangle we expect the incident field to be significantly enhanced only at the triangle's sharp apex. On the other hand, the nanorods will have enhanced fields at each end-cap. Therefore, in a simplified, one-dimensional model, the nanorod emission resembles that of two nanotriangles with their apices pointing in opposite directions. A simple analysis predicts that this symmetry should quench the first harmonic of the nanorods' CEP response, i.e. the nanorods should show no response at f_{CEO} , in agreement with our observation.

We repeated the measurements summarized in Fig. 2a on eight different nanotriangle arrays and six different nanorod arrays. Each array had a different surface plasmon resonance. In Fig. 2b (top), we display the measurement results. Each nanotriangle array shows a CEP sensitive current, while none of the nanorod arrays show a CEP sensitive response. In Fig. 2b (bottom) we show the CEP sensitivity, that is the ratio of the CEP sensitive current to the average current, for each nano-

triangle array. Additionally, we display the predicted CEP sensitivity derived from a simple Fowler-Nordheim tunneling model for two different model pulses that closely resemble the experimentally used pulse.

From a scientific perspective, our experiments have shown the effects that the additional geometric and resonant degrees of freedom afforded by plasmonic nanoparticles can have on their strong-field, CEP sensitive response. From a technological perspective, our compact, micro-optoelectronic devices take a first step towards pushing lightwave electronics and strong-field science from elaborate laboratory settings to compact, chip-scale devices operating in ambient conditions.

Contact: William Putnam, bputnam@mit.edu
 Franz X. Kärtner, Franz.kaertner@desy.de

Authors

William P. Putnam^{1,2}, Richard G. Hobbs^{1,2,3}, Philip D. Keathley^{1,2}, Karl K. Berggren^{1,2} and Franz X. Kärtner^{1,2,4}

1. Department of Physics and The Hamburg Centre for Ultrafast Imaging, University of Hamburg, Hamburg, Germany
2. Department of Electrical Engineering and Computer Science, Research Laboratory of Electronics, Massachusetts Institute of Technology, Cambridge, USA
3. Centre for Research on Adaptive Nanostructures and Nanodevices (CRANN), Advanced Materials Bio-Engineering Research Centre (AMBER), and School of Chemistry, Trinity College Dublin, Dublin, Ireland
4. Center for Free-Electron Laser Science (CFEL) and Deutsches Elektronen Synchrotron (DESY), Ultrafast Optics and X-rays Division, Hamburg, Germany

Original publication

'Optical-field-controlled photoemission from plasmonic nanoparticles', *Nature Physics* (2016), advance online publication, DOI: 10.1038/nphys3978

References

1. F. Krausz and M. Ivanov, 'Attosecond physics', *Rev. Mod. Phys.* **81**, 163-234 (2009).
2. E. Goulielmakis et al., 'Attosecond control and measurement: lightwave electronics', *Science* **317**, 769-775 (2007).
3. R. Bormann, M. Gulde, A. Weismann, S. V. Yalunin and C. Ropers, 'Tip-enhanced strong-field photoemission', *Phys. Rev. Lett.* **105**, 147601 (2010).
4. M. Krüger, M. Schenk and P. Hommelhoff, 'Attosecond control of electrons emitted from a nanoscale metal tip', *Nature* **475**, 78-81 (2011).
5. B. Piglosiewicz et al., 'Carrier-envelope phase effects on the strong-field photoemission of electrons from metallic nanostructures', *Nature Photon.* **8**, 37-42 (2014).

Polarization on demand.

Full polarization control in an X-ray free-electron laser

Time-resolved X-ray magnetic circular dichroism and studies of chiral dynamics in general require short pulse X-rays with circular polarization. In order to provide fully variable polarization of an X-ray free-electron laser, a so-called 'Delta'-undulator has been installed at the SLAC National Accelerator Laboratory at the end of the existing LCLS undulator section. In order to optimize the polarization properties of the X-rays online, a diagnostic unit, originally developed at DESY, helped to establish and verify a high degree of circular polarization (98%). Furthermore, a new two-colour operating mode was established and monitored by the diagnostic unit shot-by-shot. In this mode, the polarization of the second pulse and pointing, timing, intensity and wavelength of both pulses can be modified.

Free-electron lasers such as FLASH have triggered a new era of X-ray research due to their high peak brightness and short femtosecond-pulse duration. Nevertheless, they are still lacking certain flexibilities and capabilities, which are routinely available at storage ring based X-ray sources. One particular example is circular polarization, which allows investigating biologically important molecular systems having a handedness. It can also be used to probe the electronic spin, important for studies of magnetic materials. Already decades ago at the storage ring DORIS such X-ray Magnetic Circular Dichroism (XMCD) studies have been performed very successfully [1]. The availability of femtosecond pulses from a free-electron laser combined with variable polarization would allow getting insight into the associated dynamics.

The VUV free-electron laser FERMI in Trieste has already demonstrated variable polarization including a high degree of circular polarization [2] with further prospects to fully variable polarization [3]. However, X-rays of photon energies beyond what the FERMI FEL can presently offer, i.e. higher than ~300 eV, have not only the distinct advantage of elemental and orbital sensitivity, but their energy can be tuned directly

to core-valence resonances involving the *L*-edges of the magnetically relevant elements.

The goal was therefore to extend the polarization control of FELs to X-rays of higher energies. Variable polarization at the LCLS has been enabled by the recent installation of the 'Delta' undulator, built at SLAC and based on a prototype device demonstrated at Cornell University [4]. To achieve the highest degree of circular polarization and stability, the use of a reverse tapered undulator to suppress background power had to be combined with the novel technique of beam diverting to spatially separate beams of different polarization.

In order to verify the performance of these modes, a diagnostic unit was employed at the AMO end station of the LCLS to measure shot-by-shot information on the degree of linear polarization as well as the tilt angle of the plane of linear polarization in real-time. The fast processing of the data (the processing delay amounted only to a few seconds) allowed the undulator operators to optimize the relevant undulator parameters almost instantly. The whole chain of diagnostic procedures benefitted a lot from our past experiences at

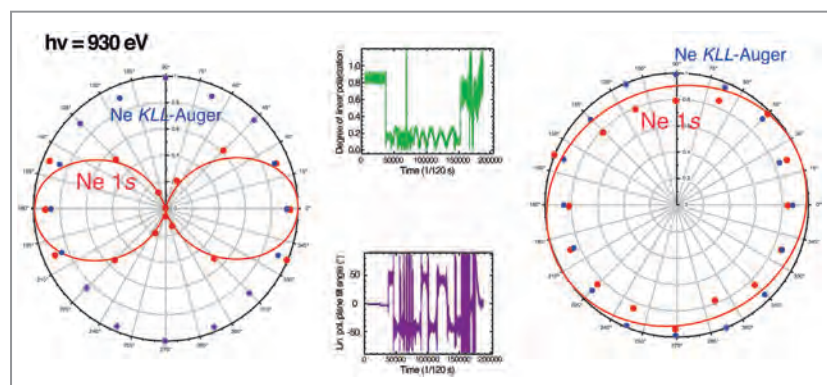


Figure 1

A screen-shot of the online data display generated by the DESY diagnostic unit for an initial 'Delta' undulator commissioning run at LCLS. (Left) Intensity of the neon *1s* photoelectron line (red) and *KLL*-Auger line (blue), respectively, in a situation where the 'Delta' undulator produced linear horizontal polarization. (Centre) Time series of the derived degree of linear polarization (top, green) and tilt of polarization plane (bottom, violet) based on the numerical calculation depicted as a red line in the polar plots. (Right) Further screen-shot while the 'Delta' undulator produced a high degree of circular polarization.

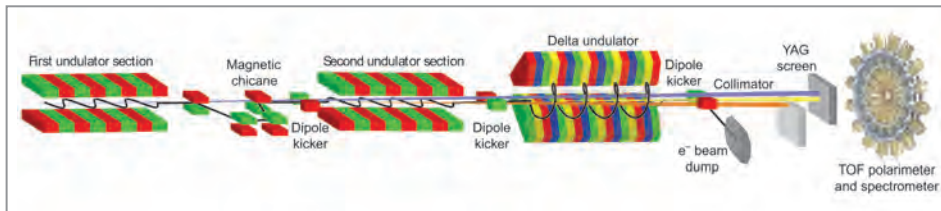


Figure 2

Schematic representation of the two-colour, two-polarization scheme realized with the 'Delta' undulator at LCLS. One half of the 'Delta' magnetic structure is omitted for clarity.

PETRA III where the device was originally developed at beamline P04 as well as from previous beam times at FLASH and FERMI [3, 4].

The basic principle of the diagnostic unit is angle-resolved electron spectroscopy using a gas phase target. A set of 16 independent time-of-flight spectrometers in a plane perpendicular to the X-ray beam enables us to acquire an angular emission pattern for each electron line. On the left hand side in Figure 1, essentially a screen-shot of the displayed information generated during one of the early 'Delta' undulator commissioning runs at the LCLS is shown. The polar plot (left) indicates the intensities of the neon 1s photoelectron line (red) compared to the sum of intensities of the neon KLL-Auger electrons (blue) for each of the 16 spectrometers. At this very moment in time, the 'Delta' undulator produced linear horizontal polarization, reflected in the '*p*-type' angular distribution of the neon 1s photoelectrons. The two plots in the middle depict the time series of the degree of linear polarization (top) and the tilt of the plane of polarization (bottom), respectively, showing the effect of systematic undulator parameter variations. Maximizing the degree of circular polarization can be simply achieved by minimizing the degree of linear polarization visualized in the top diagram. A further screen-shot indicating a high degree of circular polarization is shown on the right hand side. The degree of circular polarization was also determined in a dedicated experiment [5].

The addition of the 'Delta' undulator also allows for new two-colour operation modes (Fig. 2): The series of planar undulators is divided in two sections tuned to different undulator parameters. Consequently two X-ray pulses with different photon energies can be created. The delay between the two beams can be controlled via a magnetic chicane in between the two sections. Employing the 'Delta' undulator, the second beam can even have variable polarization. Figure 3 shows two photoelectron lines with different energies corresponding to the two different FEL beams. The angular distribution is different for the two photoelectron lines, respectively, proving that they indeed have two different polarization modes.

In summary, first variable-polarization X-ray FEL operation could be demonstrated by adding a 'Delta' undulator at the LCLS. A high degree of circular polarization (98%) was achieved. The DESY diagnostic unit has proven to be a valuable tool also for shot-to-shot characterization and optimization of FEL radiation.

Contact: Jens Viefhaus, jens.viefhaus@desy.de

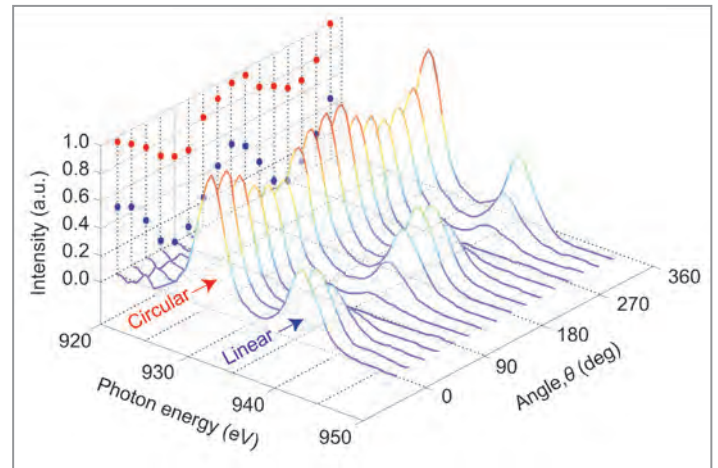


Figure 3

Pseudo-3D representation of the 16 individual electron time-of-flight neon 1s spectra obtained by the DESY diagnostic unit. The time-of-flight coordinate has been converted to kinetic energy and then to photon energy by using the known binding energy of the neon 1s photoelectron line. The angular distribution is shown for both FEL two-colour pulses as a projection for the corresponding two electron lines (red and blue), respectively.

Authors

Alberto A. Lutman¹, James P. MacArthur¹, Markus Ilichen^{1,2,3}, Anton O. Lindahl^{3,4}, Jens Buck², Ryan N. Coffee^{1,3}, Georgi L. Dakovski¹, Lars Dammann⁵, Yuantao Ding¹, Hermann A. Dürr^{1,3,6}, Leif Glaser⁵, Jan Grünert², Gregor Hartmann⁵, Nick Hartmann^{1,7}, Daniel Higley¹, Konstantin Hirsch¹, Yuri I. Levashov¹, Agostino Marinelli¹, Tim Maxwell¹, Ankush Mitra¹, Stefan Moeller¹, Timur Osipov¹, Franz Peters¹, Marc Planas², Ivan Shevchuk⁵, William F. Schlotter¹, Frank Scholz², Jörn Seltmann⁵, Jens Viefhaus⁵, Peter Walter⁵, Zachary R. Wolf¹, Zhiron Huang^{1,3} and Heinz-Dieter Nuhn¹

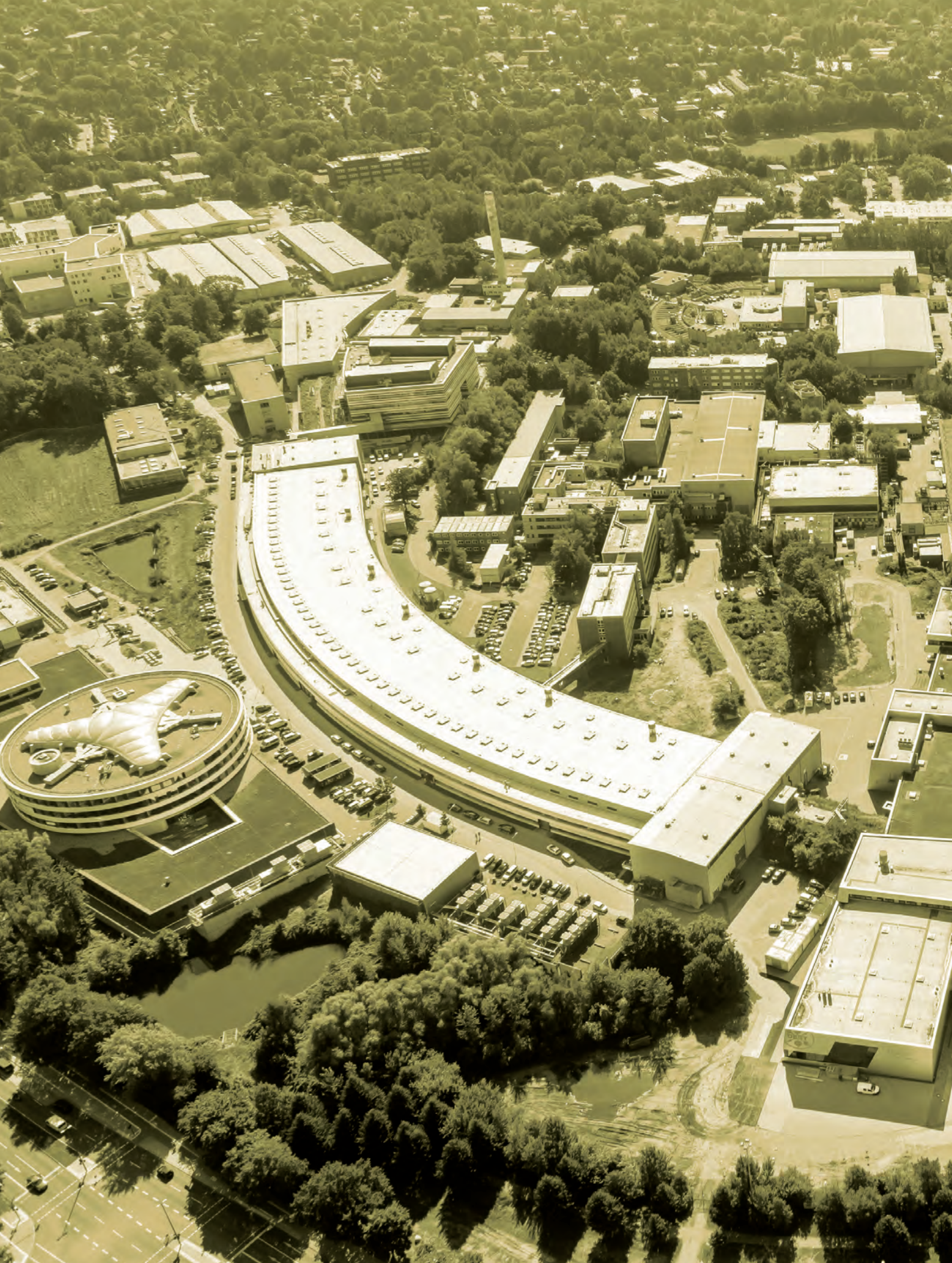
1. Stanford PULSE Institute, SLAC National Accelerator Laboratory, Menlo Park, California, USA
4. Department of Physics, University of Gothenburg, Gothenburg, Sweden
5. Deutsches Elektronen-Synchrotron DESY, Hamburg, Germany
6. Stanford Institute for Materials and Energy Sciences (SIMES), SLAC National Accelerator Laboratory, Menlo Park, California, USA
7. Institute of Applied Physics, University of Bern, Bern, Switzerland

Original publication

'Polarization control in an X-ray free-electron laser', *Nature Photonics* 10, 468–472 (2016). DOI: 10.1038/NPHOTON.2016.79

References

1. G. Schütz et al., 'Absorption of circularly polarized X rays in iron', *Phys. Rev. Lett.* 58, 737–740 (1987).
2. E. Allaria et al., 'Control of the polarization of a vacuum-ultraviolet, high-gain, free-electron laser', *Phys. Rev. X* 4, 041040 (2014).
3. E. Ferrari et al., 'Single shot polarization characterization of XUV FEL pulses from crossed polarized undulators', *Sci. Rep.* 5, 13531 (2015).
4. A. B. Temnykh, 'Delta undulator for Cornell Energy Recovery LINAC', *Phys. Rev. ST Accel. Beams* 11, 120702 (2008).
5. G. Hartmann et al., 'Circular dichroism measurements at an x-ray free-electron laser with polarization control', *Rev. Sci. Instrum.* 87, 083113 (2016).



Light Sources.

> FLASH

90

> PETRA III

94

FLASH is now FLASH1 and FLASH2.

The new generation



Figure 1
FLASH in September 2016. Both adjacent experimental halls 'Kai Siegbahn' (FLASH2, left) and 'Albert Einstein' (FLASH1, centre) are attached via the office building to the PETRA III experimental hall 'Paul P. Ewald' (bottom right corner).

In 2016 an important goal was achieved at FLASH: Since 8 April, DESY's free-electron laser is serving two user experiments in parallel operation. Two undulator lines with their respective photon beamline systems generate light pulses and guide them into the experimental hall 'Albert Einstein' (FLASH1) and the new hall 'Kai Siegbahn' (FLASH2). The first official users of the new FLASH2 beamline FL24 were researchers around Sven Toileikis and Andreas Przystawik from DESY. The FLASH2 pulses were focused with the help of a multilayer mirror onto rare gas clusters. The experimenters studied the fluorescence of the resulting nanoplasma as a function of cluster size.

Right after the very promising start, the first record for this doubled user operation was set: On 9 April, FLASH delivered 4000 pulses per second with up to 140 μJ per

pulse to an experiment at the FLASH1 beamline PG1 and in parallel 110 pulses per second with about 100 μJ each for FLASH2, making it a successful start at both ends.

FLASH is now running in regular half-year periods having two calls for proposals per year with deadlines 1 April and 1 October. The beamtime for users in 2016 was allocated in two user periods and six beamtime blocks. The 7th user period took place from January to June and the 8th from July to December. During this time, FLASH provided 310 shifts of beamtime, each shift 12 h long, to 32 user experiments. Another 4 experiments proposed for the second half of 2016 will be performed in the first half of 2017.

Along with the first user experiments, the setup of the technical infrastructure in the FLASH2 hall was ongoing and

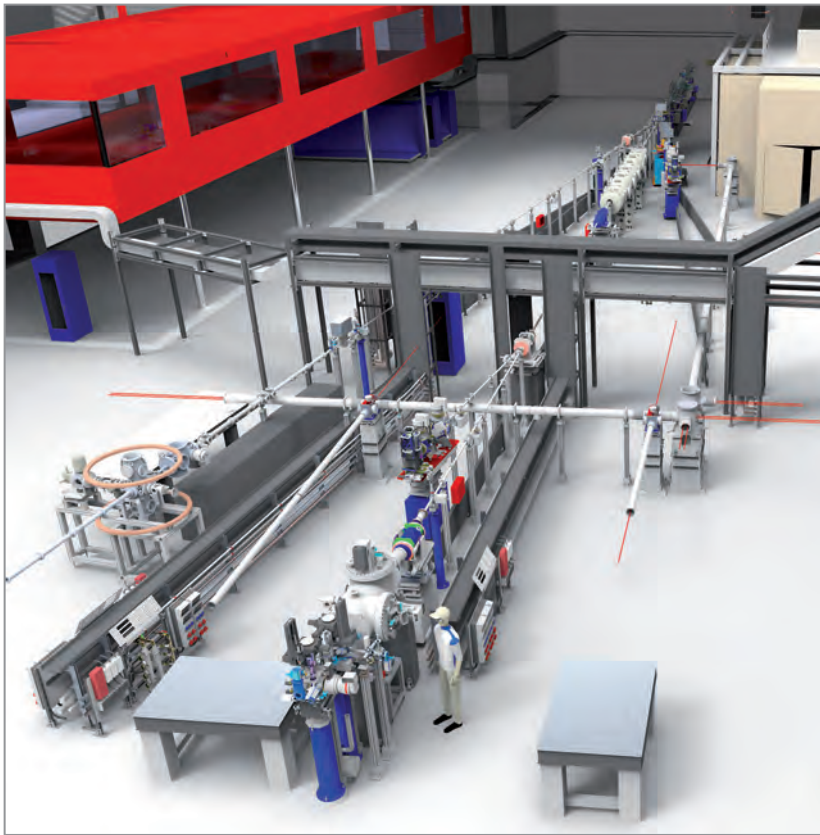


Figure 2

Sketch and view into the FLASH experimental hall 'Kai Siegbahn' (FLASH2): beamlines FL24 (right) and FL26 (REMI, left) have just taken up user operation, while the equipment is still being upgraded.

meanwhile is almost completed for the initial two beamlines, namely FL24 (open port) and FL26 (REMI – reaction microscope as a permanent endstation provided by the MPI for Nuclear Physics, Heidelberg (Fig. 3)). The installation of the Kirkpatrick-Baez focusing optics completing beamline FL24 will start in the FLASH shutdown in December 2016 and commissioning of this optics is planned for spring 2017.

In 2016, REMI at beamline FL26 has already been used for three time-resolved experiments employing different back-reflecting split multilayer mirrors. In summer 2017, a grazing incidence split and delay mirror unit will be added in front of REMI. This new unit does not exhibit the wavelength respectively bandwidth limitations of a multilayer mirror approach and hence allows to work at variable wavelengths. This way, one does not only avoid frequent multilayer mirror

changes within experiments, but can also exploit the fast wavelength tunability at FLASH2.

The installations around and in the hutch of the optical pump-probe laser for FLASH2 also made significant progress. A huge air conditioning cabinet on top of the hutch was installed over the last months and is nearing completion with the final electrical installations. The laser tables, with a size of 24 m² in total, moved into the laser hutch and are now ready for the laser installations. The laser itself is presently configured and tested in a separate laboratory and will move to the FLASH2 hall at the end of 2017.

In the FLASH experimental hall 'Albert Einstein' (FLASH1), the permanent endstation CAMP at beamline BL1 as well as the PG2 platform have been equipped with permanent

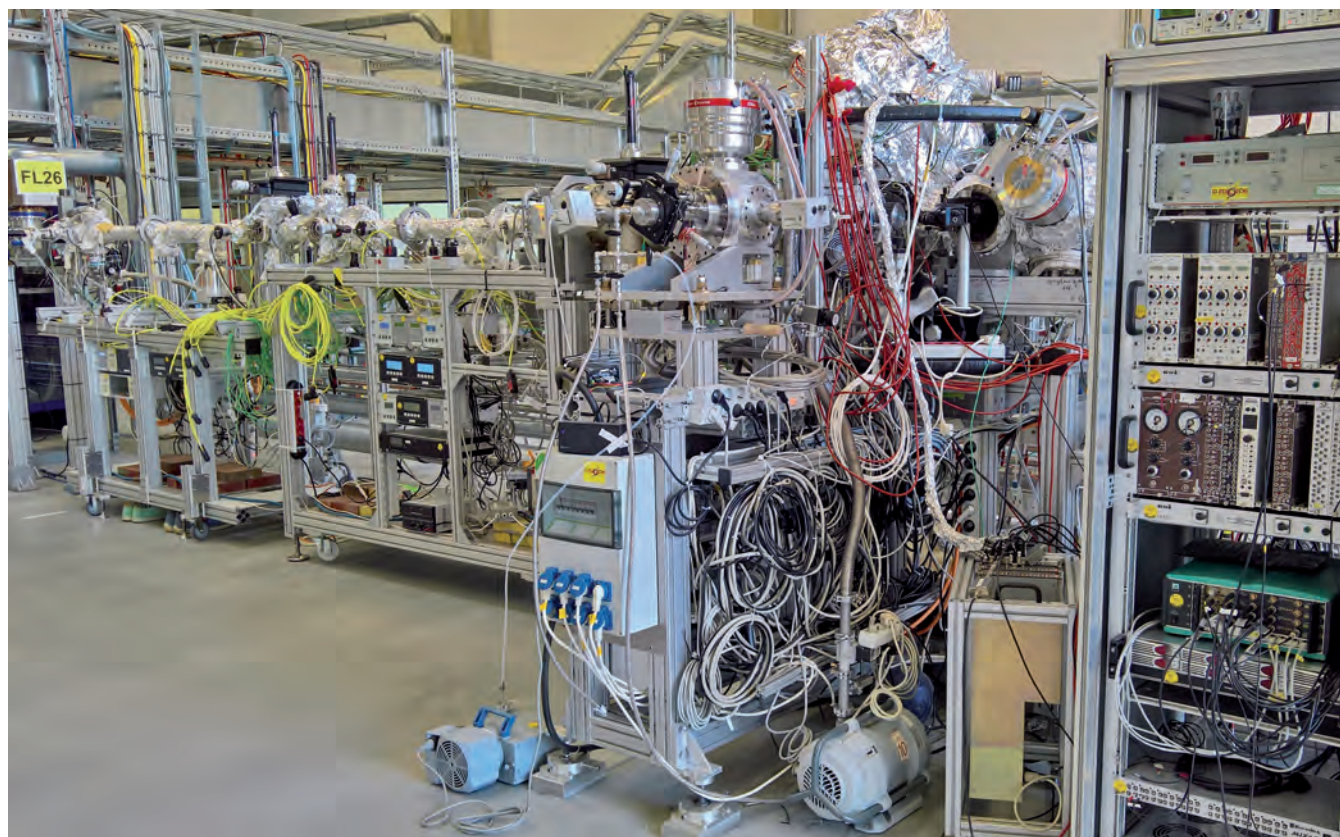


Figure 3

Setup of the reaction microscope (REM) at the end of beamline FL26 (FLASH2).

From left to right: Differential pumping stages, followed by the REM itself with the sample jet stage in the foreground, complemented by the electronics/controls rack.

laser tents (see Fig. 4). They can be partially modified in order to accommodate a large variety of different experimental setups, while allowing faster switching of the optical laser between the different experiments.

A two weeks shutdown in June provided the opportunity to install a 4-mirror-reflection-polariser in front of the three BL-beamlines at FLASH1. This shutdown was mainly required for 'FLASHForward' installations in the FLASH2 accelerator tunnel. The project FLASHForward at DESY focuses on the advancement of plasma-based particle acceleration technology (<http://vi-pwfa.desy.de/e192843/>). The new polariser allows converting the linear polarisation of the FLASH pulses into circular polarisation and opens

the wide field of (soft) X-ray magnetic circular dichroism (XMCD) for time-resolved experiments at FLASH. Besides studies of ultrafast magnetic phenomena, new types of polarisation sensitive experiments of 'handed' or chiral materials and (bio-)molecules are also envisioned. More information on this polariser is presented in a highlight in this annual report.

Given all boundary conditions of a parallel operation of FLASH1 and FLASH2, also in view of the accepted proposals, it is presently already possible to schedule about 1/3 of experiments more than in former times with FLASH1 only. With future upgrades, in particular variable gap undulators at FLASH1, it will in the long run be possible to even double

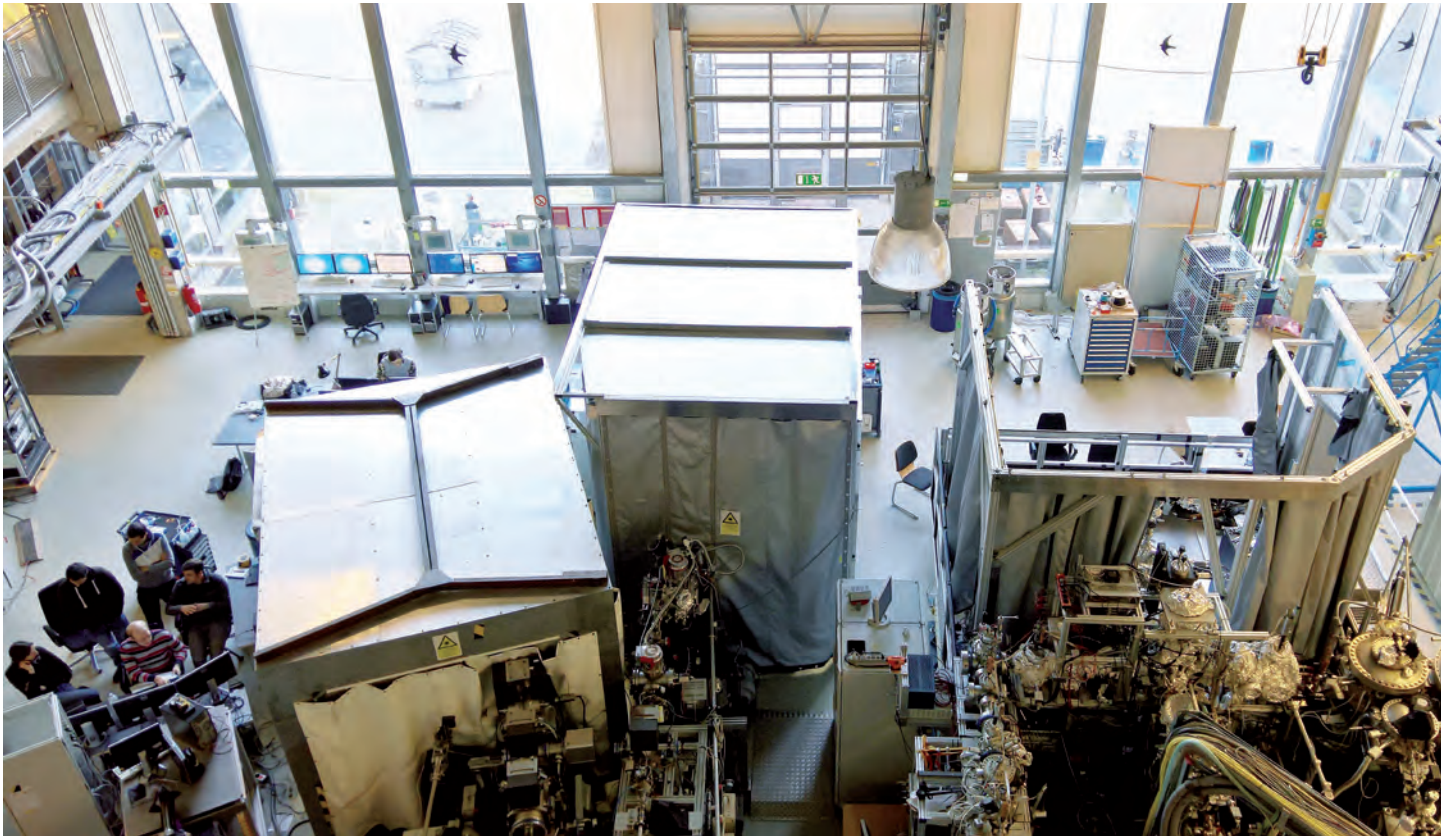


Figure 4
View into the FLASH experimental hall 'Albert Einstein' (FLASH1): New stationary laser tents at the PG2 platform (at right, roof removed), as well as at the permanent CAMP endstation (middle) along with a mobile laser tent (at left, here on top of the BL2 experiment).

the number of experiments at FLASH while substantially widening the FEL parameter space.

In addition to the regular operation for users, FLASH2 with its variable gap undulators is presently extensively used to explore a large variety of new potential schemes to generate FEL pulses with parameters tailored to users' requests. Among those schemes are, frequency doubling, a harmonic lasing self-seeded (HLSS) FEL, tests of so-called 'harmonic afterburner' undulator configurations as well as many different approaches involving tapering of the undulators. Two of the achievements within these exploratory shifts were a new short wavelength record for FLASH2 in the fundamental at 3.5 nm, and that at 13 and 20 nm wavelength a peak pulse

intensity of 1 mJ was obtained with tapering. Although these parameters are not provided in routine operation for users so far, many of the explored schemes hold great promises for the near future.

The year 2016 ended with another 4 weeks shutdown mainly for FLASHForward installations starting on 5 December. After a few weeks of FEL studies, the first block of user operation will start on February 6, 2017. For the first half of 2017, 162 shifts have been assigned to 16 user projects, while 370 shifts were requested in total by 32 user proposals.

Contact: Rolf Treusch, rolf.treusch@desy.de



Figure 1
Aerial view of the three PETRA II experimental halls 'Ada Yonath' (1; left), 'Max von Laue' (2; in the middle) and 'Paul P. Ewald' (3; right and adjacent to the FLASH halls) in September 2016.

In 2016, user operation at PETRA III resumed on 7 April after a five month shutdown, which was needed to install the frontends of the extension beamlines P22 to P24 in the ring tunnel (Fig. 2). The remaining time was split into two synchrotron radiation runs, separated by a three weeks period for machine studies and beamline commissioning in the summer. Out of a total beamtime of 4198 hours delivered until 12 December 2016, 3532 hours have been scheduled for user proposals. Beam availability was 95.1 %. In 2016, 884 proposals have been submitted for the beamlines P01-P11, P64 and P65, while additional 225 proposals have been submitted for the EMBL beamlines P12-P14 (until September 2016).

Storage ring

During the commissioning of the new X-ray absorption beamlines P64 and P65 in the PETRA III experimental hall 'Paul P. Ewald' (north) it was observed that stray fields from the canting dipole magnet between the undulators are causing orbit distortions of the electron beam when the undulator gaps are being changed. The solution to this problem is the replacement and modification of the magnet coils in all new canting dipoles, which will be accomplished in the shutdown 2016/2017. Until then a feed forward scheme using compensating fields from a corrector coil at the dipole allowed an interim operation of both beamlines in 2016 albeit with slightly reduced performance.

Due to continued settling of the 1 m thick base plate in the PETRA III experimental hall 'Ada Yonath' (east) the positions

of machine components in that area deviate from their design values. While this effect was recognised already in the 2015/16 shutdown, it was decided to re-align the machine only in the upcoming shutdown 2016/2017 to allow for complete settling of the base plate. A modified electron beam orbit was temporarily used to guarantee a smooth operation of the running beamlines until the machine will be re-aligned.

During the extended winter shutdown 2016/17 the long straight section in the east will be modified to accommodate the insertion devices for the Swedish beamline P21. At the same time, the first section of the P21 frontend will be installed, the beamline will be completed later in 2017.

In 2016, the PETRA III storage ring operation was equally split into a 'timing mode' with 40 or 60 bunches filling and a 'continuous mode' with 480 or 960 bunches. In previous years, the 'timing mode' mode had a higher share which, however, caused unwanted local activation of ring components due to high particle losses. It is expected, that the equal share of both operational modes will keep the activation at reasonable levels and will thus be chosen also in future.

In the past, some sensitive timing experiments, in particular nuclear resonance scattering, were affected by side bunches between the main bunches. These side bunches are caused by intra beam scattering or are created during top-up injection and typically amount to 10^{-5} of the main bunch. For a further reduction a bunch cleaning procedure has been tested in

2015 and was implemented in 2016. Side bunches are now regularly being stripped off in 'timing mode'. This procedure has been optimised to reliably remove side bunches with an offset larger than 2ns. The cleaning is during top-up fill and does not affect the emittance properties.

Beamlines and Experiments

All beamlines P01-P14 in the PETRA III experimental hall 'Max-von-Laue' are fully operational and have been open for user proposals since 2013. Some have since then been upgraded with additional optics, experimental setups or detectors. At the PETRA III extension, the first new beamlines became operational in the experimental hall 'Paul P. Ewald' by the end of 2015 (P65) and in spring 2016 (P64). Regular user operation at the applied XAFS beamline P65 started in June while the high-flux XAFS beamline P64 was under commissioning in 2016.

New 'Verbundforschung' projects for instrumentation upgrades at large scale facilities have been granted funding by the German Federal Ministry of Education and Research (BMBF) in 2016. Proposals for instrumentation to be used at PETRA III beamlines were very successful: 34 BMBF projects from German universities have been approved for the next three years, confirming the attractiveness of PETRA III for top level scientific research.

At the Dynamics Beamline P01 a cooperation agreement with the Max Planck Society (MPG) has been signed in January



Figure 2
Completed frontends of beamlines P22-P24 in the ring tunnel in the PETRA III experimental hall 'Ada Yonath'.

2016. A major part of this cooperation is the enhancement of the experimental possibilities of the beamline, namely the addition of a resonant inelastic scattering (RIXS) experiment working in the tender X-ray regime, 2 – 4 keV. For instance the ruthenium L-edges will become accessible for RIXS studies of ruthenates, which are correlated electron materials with intriguing physical properties. The required modification of the beamline will be finished in spring 2017 with the installation of new undulators. In addition, the X-ray Raman instrument at beamline P01 will be upgraded from currently 12 analysers to at least 160. The reconstruction work could be accomplished with only little disturbance of the user run in 2016. In the next years, a beamtime share of 40 % will be available for privileged access to P01 by MPG research groups, hence limiting the share of beamtime for public user proposals accordingly.

The Hard X-ray Diffraction Beamline P02 was split into two separate beamlines in 2016: P02 had been designed for experiments at extreme conditions in a straight branch and powder diffraction experiments at a fixed-energy side station. Both branches are successfully used by an increasing number of user groups. Therefore, it was decided to run the side station P02.1 separate from the main beamline by an independent beamline team. To strengthen the Extreme Conditions Beamline (ECB) P02.2, lab facilities for loading hydrogen under high pressures into diamond anvil cells (1200 bar) have been installed, partially funded through a BMBF project (University of Bayreuth). The same project received funds for an advanced Focused Ion Beam instrument (FEI, Scios) to be able to, for instance, prepare double stage diamond anvil cells for high pressure experiments up to 1 TPa. It has been installed at the DESY NanoLab beginning of 2016. It has since been very effectually operated jointly with the University of Bayreuth.

At the Hard X-ray Micro/Nano-Probe beamline P06 a unique method has been successfully developed to generate three-dimensional multi-element sensitive tomograms with resolution down to 100 nm. For this study an EIGER 4M area detector (*Dectris Ltd.*) and a Maia fluorescence detector (*BNL, CSIRO*) have been simultaneously used to image a catalytic particle with 50 μm diameter. Combining a moderately nano-focused X-ray beam of 300 nm \times 300 nm and the EIGER detector, ptychographic scans of 167 tomographic projections could be achieved. Subsequently, the reconstructed images of the ptychograms were used to reconstruct the full 3D-tomogram with 50 nm³ voxel size. Element sensitivity was achieved by performing a tomographic reconstruction of the Maia-detector spectra. Here, the spatial resolution matches the beam size. Merging both tomograms yields the direct correlation of structural and elemental distribution on the nanometre level (Fig. 3).

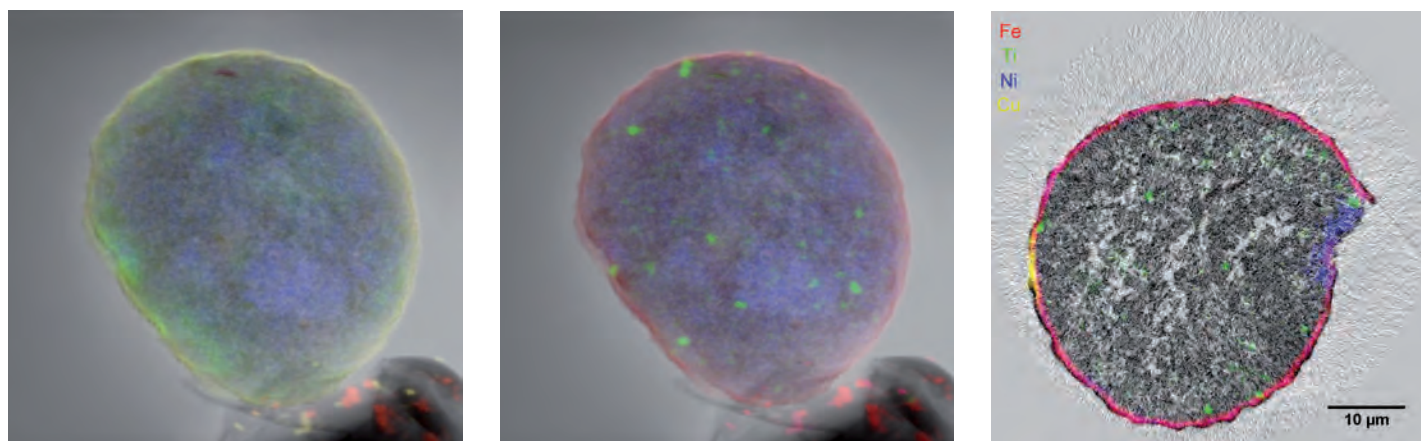
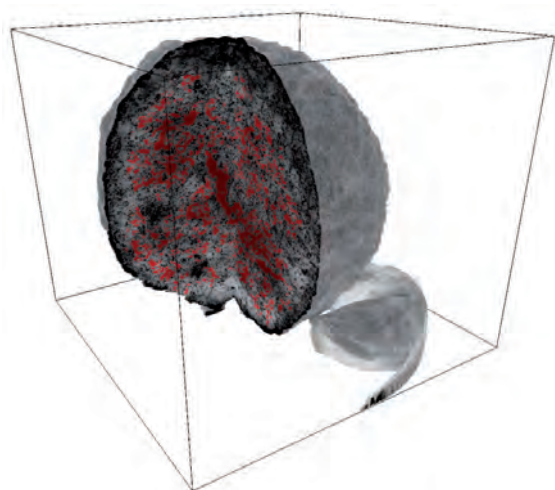


Figure 3

Measurement of a catalytic particle at PETRA III beamline P06: (at the top) Cut through an element sensitive tomogram of a 50 μm large catalytic particle. The colours in the three figures indicate the distribution of the elements (Fe, Ti, Ni, Cu) in one particle. (on the left) The red colour highlights the network of main pores.



At the extension, in the PETRA III experimental hall ‘Paul P. Ewald’ (north), the XAFS beamline P64 was commissioned with both cryo-cooled monochromators, i.e. the double crystal instrument and the fast scanning channel-cut QEXAFS monochromator, designed and built within a BMBF funded project (University of Wuppertal). Initial scientific experiments at beamline P64 could already be performed during the commissioning phase. The installation of the van-Hamos fluorescence spectrometer in the experiment hutch (University of Paderborn) is ongoing and commissioning of the full instrument is expected to begin in spring 2017. User proposals for P64 have been accepted and operation for users will be ramped up after the start of the beamline in 2017. The 100-element Ge-detector (BMBF-project, University of Paderborn) has already been used for some of the first measurements on highly diluted systems.

In the first half of 2017, the large volume press instrument at beamline P61, located in the same hall, will be operated in off-line mode for materials synthesis, while the detailed planning for the construction of the beamline will be completed. Also, the implementation of the infrastructure for the time-resolved UV luminescence beamline P66 will continue in 2017.

The upcoming beamlines P21-24 of the extension phase 2 are located in the PETRA III experimental hall ‘Ada Yonath’. Their construction is progressing as planned and the installation

of the technical infrastructure at the beamlines was the major activity in 2016 (Fig. 4).

Linked to the official hall inauguration and name giving, beamlines P21-23 which are being built in cooperation with international partners Sweden, India and the Russian Federation have been formally ‘opened’ in a ceremony on 14 September (Fig. 5).

Priority of the beamline installation has been given to the Chemical Crystallography beamline P24 as the experimental instrumentation is already available. The heavy load Kappa diffractometer, designed and funded as part of a BMBF project involving several university groups (coordinated by University of Hamburg) had been commissioned off-line and will be relocated to P24 in January 2017. The beamline optics is currently installed and the undulator is calibrated (Fig. 6). It is planned to have first X-ray beam in the experiment hutches for commissioning shortly after the machine restart in spring 2017. The rather complex frontend of the Swedish high-energy X-ray materials science beamline P21 is under construction and its first section will be installed in the ring tunnel in the shutdown beginning of 2017. The remaining section will follow in the summer shutdown of that year. The other X-ray optical components such as monochromators, the 4 m long in-vacuum undulator and the end station instruments are under construction.

The X-ray optical components of beamlines P22 (hard X-ray photoelectron spectroscopy) and P23 (nano X-ray diffraction) outside the PETRA III ring tunnel will be set up starting at the beginning of next year. The instrumentation in the experiment hutches is being installed in parallel and it is planned to have first beam for commissioning in summer 2017.



Figure 4

Experiment hutches and infrastructure for beamlines P21-24 in the PETRA III experimental hall 'Ada Yonath' (left) and for beamlines P64-P65 in the experimental hall 'Paul P. Ewald' (right).



Further installations at beamlines

A second EIGER 4M detector was acquired for PETRA III beamline P06 and the Coherence Applications beamline P10. This sophisticated detector is optimised for speckle measurements at 10 keV and will finally be able to operate at 750 Hz frame rate. The detector may also be used at other beamlines based on collaborations. A further major investment will be a PILATUS 2M detector (*Dectris Ltd.*) with a CdTe sensor for pump-probe and other time resolved applications at high photon energies up to 100 keV.

At the High Resolution Diffraction beamline P08 a mirror-based beam deflector was installed which allows tilting the X-ray beam down by a few tenth of a degree. This geometry enables the use of so-called Langmuir troughs for experiments investigating the in-plane ordering of organic monolayers on liquid surfaces. This setup will soon be further upgraded in cooperation with the Friedrich-Alexander University Erlangen-Nürnberg.

At the so-called 'physics hutch' of the High-Energy Materials Science beamline P07 one-dimensionally focusing lens structures made from silicon have been tested and commissioned. These lenses have been manufactured in cooperation with the Technical University of Dresden. They allow for focusing to $500 \mu\text{m} \times 4 \mu\text{m}$ (H \times V) at 60 keV and are therefore optimised for surface applications where a large footprint is needed to reduce the X-ray power density or for enhanced in-plane averaging as required for Langmuir experiments.

Contact: Wolfgang Drube, wolfgang.drube@desy.de,
 Oliver H. Seeck, oliver.seeck@desy.de,
 Rainer Wanzenberg, rainer.wanzenberg@desy.de



Figure 5

Beamline 'opening' ceremony for beamlines P21, P22 and P23 (see small pictures) which are being implemented in cooperation with Sweden, India and the Russian Federation in PETRA III experimental hall 'Ada Yonath.'

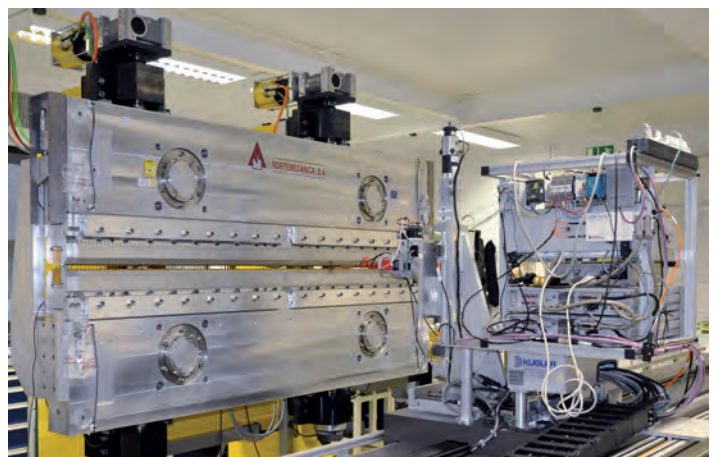
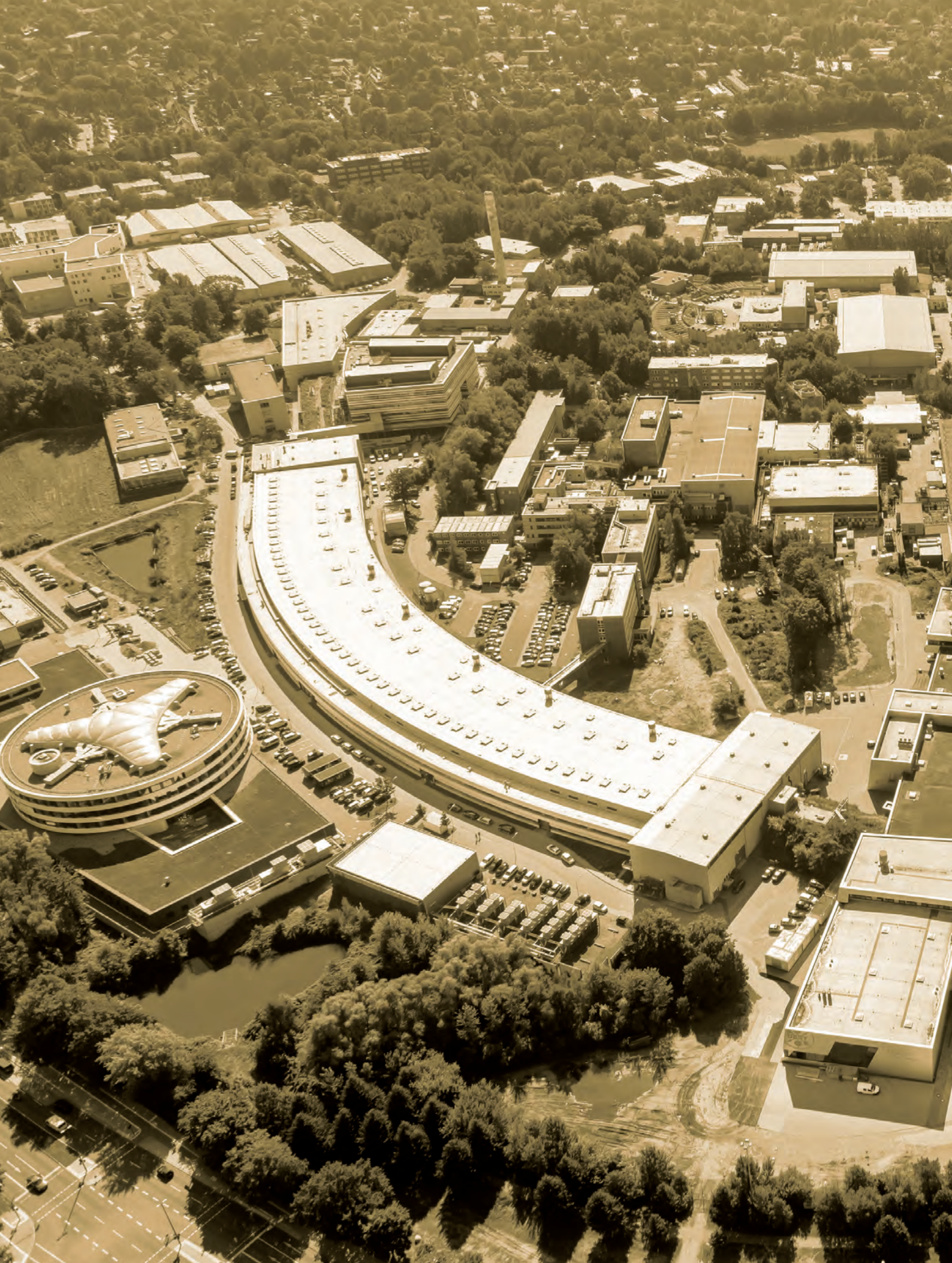
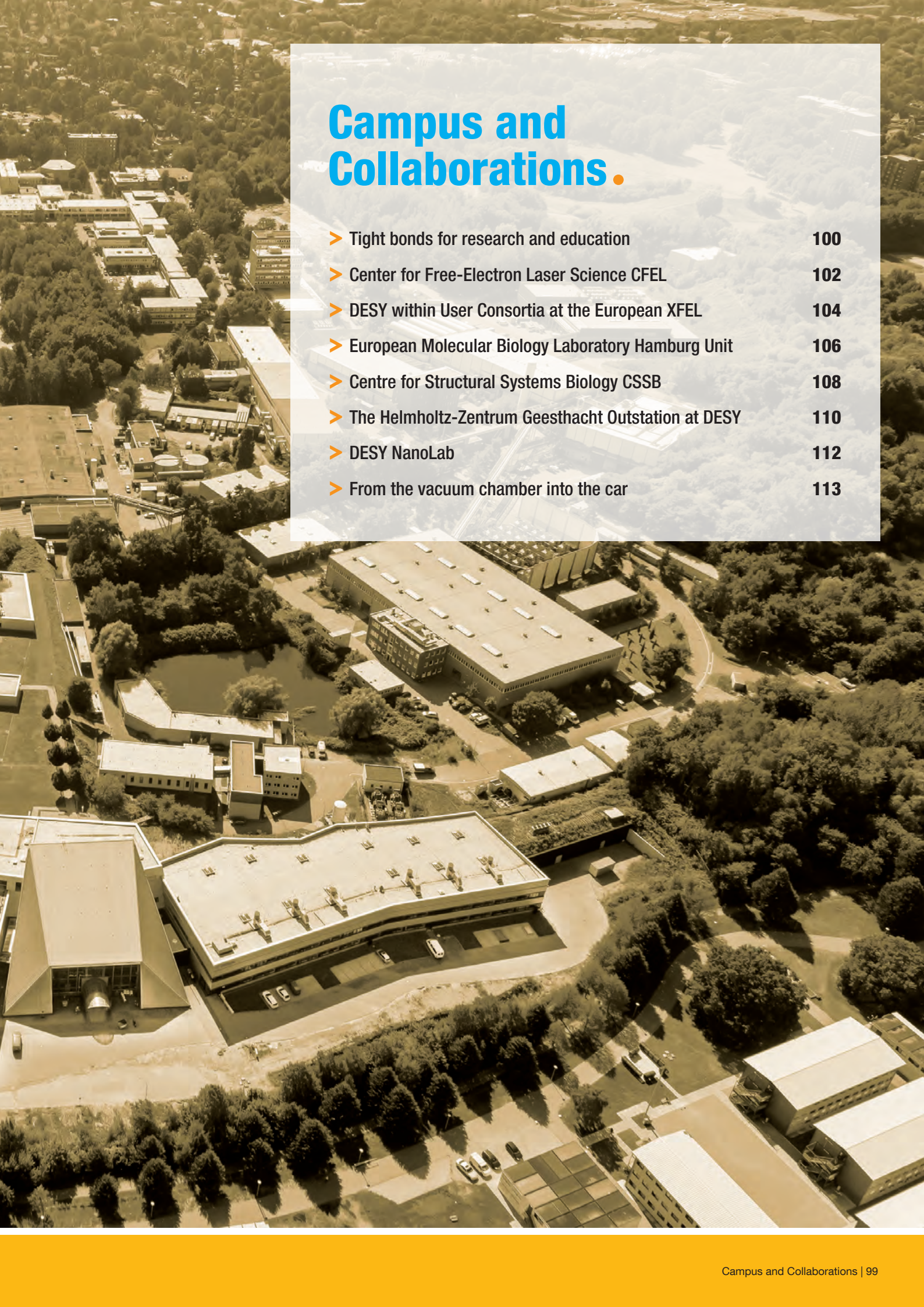


Figure 6

Measurement of the magnetic field quality of the 2m U29 undulator for beamline P24 at PETRA III.





Campus and Collaborations.

- Tight bonds for research and education 100
- Center for Free-Electron Laser Science CFEL 102
- DESY within User Consortia at the European XFEL 104
- European Molecular Biology Laboratory Hamburg Unit 106
- Centre for Structural Systems Biology CSSB 108
- The Helmholtz-Zentrum Geesthacht Outstation at DESY 110
- DESY NanoLab 112
- From the vacuum chamber into the car 113

Tight bonds for research and education.

DESY and Universities



Figure 1
Robin Santra (spokesperson of the PHGS) congratulates the first graduate within the PHGS programme, Sergio Carbajo during the PIER PhD reception in December 2015.

Close collaborations with universities are of high importance for DESY – both in research and education. Examples of current partnerships with the Universities of Hamburg, Göttingen, Kiel and Erlangen-Nürnberg are outlined in this report.

University of Hamburg

DESY and the University of Hamburg (UHH) have a long tradition of fruitful collaboration. The joint platform PIER ('Partnership for Innovation, Education and Research') continues to foster the active collaboration between both. Together with colleagues from the Max Planck Institute for the Structure and Dynamics of Matter and European XFEL, DESY and UHH run very successful common research projects in the DFG funded Cluster of Excellence CUI ('The Hamburg Centre for Ultrafast Imaging') and the collaborative research centre SFB 925 'Light induced dynamics and control of correlated quantum systems' but also collaborate in numerous joint PhD, master and bachelor projects.

Besides joint teaching activities in the physics courses for graduates and undergraduates at the university, the graduate schools embedded in CUI, in the SFB 925 and the PIER Helmholtz Graduate School (PHGS) ensure an excellent educational programme for the PhD students in Photon Science on the campus (Fig. 1). The possibilities for joint education and research will be boosted further when the Center for Hybrid Nanostructures (CHyN) will become operational next year. This centre will join forces with the DESY NanoLab. Furthermore, the Joint Science Conference (GWK) decided on 24

June 2016 to incorporate a new university centre in the 2017 funding phase: The 'Hamburg Advanced Research Centre for Bioorganic Chemistry (HARBOR)', which emerged out of the activities in CUI. This new centre will host nine university groups with up to 130 members in four divisions (Spectroscopy/Imaging, Structural Molecular Biology, Synthetic Chemistry, and Theory) and will aim to establish strong links between photon science and infection research.

In the framework of CUI, the Hamburg Prize for Theoretical Physics – a prestigious award sponsored by the Joachim Herz Stiftung – was given to Mikhail Katsnelson (Radboud University, Nijmegen) for his outstanding contributions to the quantum theory of real materials, in particular, graphene.

An important asset in the joint research and teaching activities in Photon Science between DESY and the University of Hamburg are joint appointments. In 2016 Francesca Calegari, who is working in attosecond science with an emphasis on dynamics relevant for biophysical processes, and Nina Rohringer, who has a research focus on nonlinear X-ray science, were appointed to professor positions.

Kiel University

The productive cooperation between Kiel University (CAU) and DESY has had an extremely successful year. The 'Ruprecht Haensel Laboratory' will find a home in the future Photon Science building. Melanie Schnell, who works in the field of structure and dynamics of molecules, was appointed to a joint professor position and will enhance the co-operation 'Kiel Nano, Surface and Interface Science' (KiNSIS).

BMBF funding continues to provide excellent support for new CAU science and instrumentation at DESY. A newly funded project exploiting multimodality imaging to investigate bone modelling induced by biodegradable magnesium at PETRA III beamline P05 will be led by Claus Gluer. Olaf Magnussen and Bridget Murphy were also successful in securing funding to continue of the ultrafast investigation of liquids at the X-ray diffractometer dedicated to liquid interfaces (LISA) at the

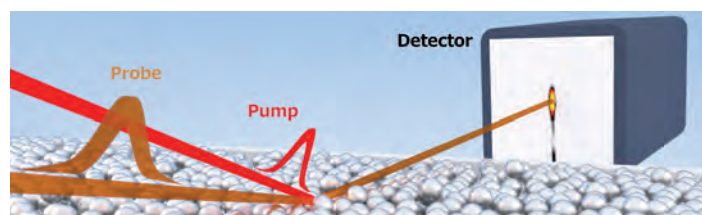


Figure 2
X-ray pump-optical probe for liquid interfaces at PETRA III beamline P08, LISA.

PETRA III P08 beamline (Fig. 2). Additionally, Kai Rossnagel will lead a joint project in collaboration with Wilfried Wurth (DESY), the University of Mainz, and the University of Duisburg-Essen. Together they develop a femtosecond time- and spin-resolved photoelectron momentum microscopy which will perform preliminary experiments at FLASH before its installation at European XFEL.

CAU continues to support and develop existing instruments at PETRA III. These include the joint CAU/Helmholtz-Zentrum Geesthacht Nanofocus Endstation at the Minax Beamline P03 (M. Müller/C. Krywka) and the spin and momentum resolved photoemission experimental station at the soft X-ray beamline P04, ASPHERE III (K. Rossnagel/L. Kipp).

Georg August University Göttingen

The collaboration between the Georg August University Göttingen (GAU) and DESY has been further strengthened in 2016 by new personnel development.

Sadia Bari has started her Helmholtz Young Investigator group



Figure 3
Sadia Bari works on an ESI setup.

in the Structural Dynamics in Chemical Systems group of Simone Techert bridging the University of Göttingen and DESY both scientifically and in teaching. She will develop new methods for examining model systems and biomolecules. The studied macromolecules will be placed in the beam of ultra-bright X-ray sources using a technique known as electrospray ionization (ESI, Fig. 3).

This novel combination will make it possible to study these systems in a defined way without any substrate or solvent allowing for answering fundamental questions in medical radiation treatment or macromolecular dynamics. As a research partner, she is also involved in the SFB 755 'Nano-scale Photonic Imaging'.

In Göttingen, at the Institute for X-Ray Physics (IRP), Markus Osterhoff has joined as a new staff scientist, supporting the collaboration with DESY. His research concentrates on the design of nanofocusing optics and the development of X-ray imaging methods. As a Principal Investigator of the SFB 755 he is also strongly involved in the developments of the 'Göttingen

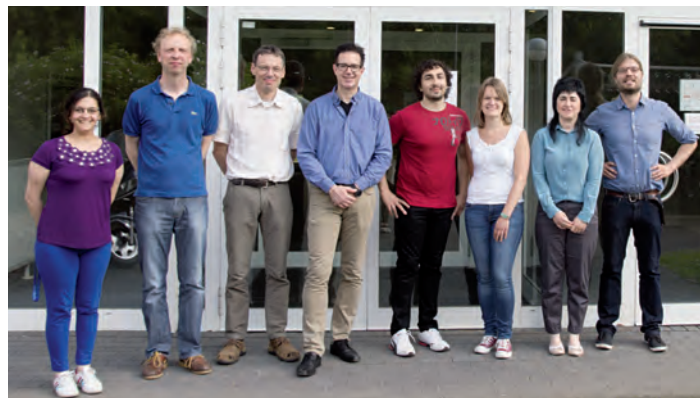


Figure 4
FAU and DESY participants from the project kick-off meeting.

gen Instrument for Nano-Imaging with X-Rays' (GINI-X) endstation at PETRA III beamline P10, built and operated by the group of Tim Salditt (GAU) in collaboration with Michael Sprung at DESY.

Friedrich Alexander University Erlangen-Nürnberg

DESY, the Helmholtz-Zentrum Geesthacht (HZG) and the Cluster of Excellence for Engineering of Advanced Materials (EAM) at the Friedrich Alexander University Erlangen-Nürnberg (FAU) agreed in 2015 to found a centre of competence ('Kompetenzanker'), which focuses on the research on catalysis, electronics, and lightweight materials. For the first two topics FAU and DESY launched pilot projects: The goal of the first project is to investigate the catalytic adsorption behaviour of hydrogen-carrying molecules, which is an important step in hydrogen storage. The adsorption of molecules on noble metal nanoparticle surfaces and the solid/liquid interface is studied in Erlangen and in the DESY NanoLab as well as at PETRA III.

The second project is related to the development of efficient electronic devices from organic thin film materials for solar cells, displays and light sources. Scientists at FAU designed a dedicated setup for *in situ* doctor blading, which is a technique for creating thin organic films on industrial levels. The beamline P08 at PETRA III will be complemented to accommodate this setup.

The projects had an excellent start with kick-off meetings (Fig. 4), the exchange of students and joint experimental campaigns at the DESY NanoLab and PETRA III. After the successful completion of the pilot projects, a long term collaboration is envisaged with a possible FAU outstation at DESY.

Contact: Wilfried Wurth, University of Hamburg and DESY, wilfried.wurth@desy.de
Bridget Murphy, University of Kiel, murphy@physik.uni-kiel.de
Simone Techert, University of Göttingen and DESY, simone.techert@desy.de
Andreas Stierle, University of Hamburg and DESY, andreas.stierle@desy.de
Oliver Seeck, DESY, oliver.seeck@desy.de

Center for Free-Electron Laser Science CFEL.

Three institutions working successfully together within CFEL

In 2016, the communicative and interdisciplinary atmosphere at CFEL has again shown to be optimal for triggering scientific meetings, great research success, and fruitful collaborations between the participating institutions (DESY, the Max Planck Institute of the Structure and Dynamics of Matter MPSD, and the University of Hamburg UHH) and external partners (Fig. 1). With over 150 publications in 2015 and even more in 2016 CFEL maintains its top position as a world leading research institution in laser and free-electron laser science as well as related fields.

CFEL hosted the International Summer School of Crystallography (ISSC16) for the third year in a row. For one week, 34 participants from 15 different countries learned the basic principles of crystallography, one of the most important tools for exploring the internal structure of materials. The school was organised by Kanupriya Pande from the group of Henry Chapman. As in the years before, Carmelo Giacovazzo, an internationally renowned expert in the field of crystallography from the University of Bari, was the main lecturer supported by local experts from CFEL, European XFEL, the cluster of excellence 'The Hamburg Centre for Ultrafast Imaging' (CUI) and the European Molecular Biology Laboratory (EMBL).

Another big success was the commitment of the Joachim Herz Stiftung to fully support the Ultrafast X-ray Summer



Figure 1

Picture taken during the Hamburg Photon Science Colloquium, which takes place at CFEL and is jointly organized by scientists from European XFEL, HZG, MPSD, UHH, and DESY.

School (UXSS) 2017. In alternation, the UXSS is taking place in Hamburg and at the PULSE Institute at Stanford University in the USA. This summer school is highly interdisciplinary, with topics ranging from accelerator physics to molecular biology. It is intended to give doctoral students and postdoctoral researchers the opportunity to familiarise themselves with the latest developments and opportunities in ultrafast X-ray science.

Oriol Vendrell from the DESY group of Robin Santra at CFEL accepted a call for an associate professorship at the Department of Physics and Astronomy at Aarhus University in Denmark. There he will continue the development and implementation of quantum dynamical approaches to theoretically describe chemical processes.

As a great success in 2016, junior research group leader Martin Eckstein of the MPSD has received a 1.5 million Euro ERC Starting Grant for his research on ultrafast dynamics in complex materials. In his research proposal 'Theory of ultra-fast dynamics in correlated multi-band systems', Martin Eckstein and his group plan to investigate how state-of-the-art laser spectroscopy can be used to manipulate solids on the femto-second timescale.

At MPSD, Michael Sentef has received one million Euro funding over five years for setting up an Emmy Noether Group of the DFG on theoretical solid state physics. The group started to work on the 'Theoretical Description of Pump-Probe Spectroscopies in Solids' on 1 September. Florian Eich has received a Marie Curie Individual Fellowship by the European Commission. The junior scientist will conduct a two-year research project on the theory of thermoelectric phenomena at the MPSD.

A large cooperation of research groups has been awarded two million Euro from the Federal Ministry of Research and Education (BMBF) for a joint research project at DESY's X-ray light source PETRA III. The PIs in this project are Arwen Pearson, Nils Huse, Thomas Schneider, Henry Chapman, Christian Betzel and Martin Trebbin. The project, 'Hadamard crystallography as a method for time-resolved investigations of the structural dynamics of biomolecules', involves research teams from CUI, UHH, EMBL and from DESY. The funding will run for three years and gives Hamburg a leading position in time-resolved structural biology.



Figure 2
Architectural vision of the MPSPD extension building with view from PETRA III towards the CFEL building in the back.

A cooperation of research groups from CFEL has been awarded 0.6 million Euro from the BMBF through the ‘Verbundforschung’-Programme for a joint research project on shortest possible pulses from FELs. The PIs in the project ‘X-Ray Pulse Compression at Free-Electron Lasers’ include Andreas Maier (coordinator, UHH), Adrian Cavalieri (MPSD) and Saša Bajt (DESY).

Additionally a research consortium around Markus Drescher (coordinator) and Jörg Rossbach from the UHH has been able to receive almost 1 million Euro from the BMBF for the project ‘Longitudinal coherence at FELs – control, analysis and application’. The project is funded for three years and is a cooperation with external partners from the universities of Freiburg and Dortmund as well as the local PIs Tim Laarmann, Winfried Decking (both DESY) and Harald Sinn (European XFEL). Among other topics, options for an X-ray FEL-oscillator (XFEL) will be investigated for the European XFEL.

Florian Grüner and Benno Zeitler from the UHH have been awarded 0.6 million Euro from the BMBF for a project aiming to demonstrate a novel concept for the linearization of the longitudinal phase space distribution of an electron bunch. It is planned to be tested in cooperation with Klaus Flöttmann (DESY) at the ‘Relativistic Electron Gun for Atomic Exploration’ REGAE, promising a reduction of the design bunch length by about one order of magnitude, resulting in electron bunches shorter than 1 fs.

Kartik Ayyer from the DESY group of Henry Chapman was honored with the ‘FEL Science and Applications award’ of the international ‘Science@FELs 2016’ conference in Trieste, Italy on 7 September 2016. He received the prize for his work on the diffractive imaging of protein crystals, which are not perfectly ordered (see highlights section of this report). Additionally Richard A. Kirian had received the Fonda-Fasella award on 11 December 2015 for his work in Henry Chapman’s group on the direct phasing of nanocrystals using coherent FEL pulses.

In recognition of his significant contributions to the chemical sciences and in particular his contributions to femtosecond electron diffraction, R. J. Dwayne Miller has been invited to become a Fellow of the Royal Society of Chemistry. In addition he was honored with the prestigious Royal Society of Chemistry Prize 2016.

Angel Rubio has received an ERC Advanced Grant of 2.5 million Euro from the EU funding for basic research in theoretical chemistry. In his project ‘Quantum Spectroscopy: exploring new states of matter out of equilibrium’ (QSpec-NewMat) he and his groups in Hamburg and Spain plan to develop novel theoretical and computational tools allowing to understand and control quantum phenomena in complex molecular systems. The project started on 1 October 2016 and runs for a period of five years. Angel Rubio also received the 2016 Medal of the ‘Real Sociedad Española de Física’ (Royal Spanish Society of Physics, RSEF) for his research work. This is the highest award among the ‘Premios de Física’ granted annually by the RSEF and the ‘Fundación BBVA’.

Following up on these successes the partners at CFEL are further expanding in personnel and infrastructure. With the upcoming extension for the MPSD and the next round within the federal excellence initiative (Bundesexzellenzinitiative) more internationally renowned colleagues will be attracted to Hamburg onto the Campus Bahrenfeld. Preparation work for the ground breaking for the new MPSD building has started. The construction start for the new building is planned for spring 2017. In the meantime the architectural design of the building was finished (Fig. 2). The three-story building will host bio- and biochemistry laboratories on the top floor while the laser and physical laboratories will be on the ground floor and basement. Offices will be sandwiched in between the functional ground and top floors. A cafeteria and garden with meeting area will be found at the roof terrace of the building.

Contact: Ralf Koehn, ralf.koehn@cfel.de

DESY within User Consortia at the European XFEL.

Approaching new frontiers in photon science with strong teams

In 2016 the European XFEL has started its commissioning phase. Besides being responsible for the construction and the operation of the European XFEL linear accelerator, DESY will also play an important role as user of the European XFEL. DESY is partner in several user consortia, which have been formed to prepare for the European XFEL's user operation in an optimal way.

The Helmholtz International Beamlines (HIB) at the European XFEL include three major instrumentations (SFX, HIBEF and hRIXS), which were substantially funded by the Helmholtz Association. In 2016, major steps have been taken regarding the design and preparation of these experiments.

SFX

The SFX consortium contributes experimental instrumentation to the European XFEL to carry out serial femtosecond crystallography and solution scattering for high-throughput determination of macromolecular structures. It aims to achieve this by enabling two experimental end-stations to be run simultaneously, by utilising the spent beam from one diffraction experiment to be used downstream in a second experiment. The consortium's contribution of the second end-

station is part of the integrated Single Particles, Clusters, and Biomolecules and Serial Femtosecond Crystallography (SPB/SFX) instrument. An automated sample delivery apparatus and a large (4 million pixel) detector will make full use of the expanded capabilities of the SPB/SFX instrument (Fig. 1). The beamline is currently under construction, led by the SPB/SFX project leader, Adrian Mancuso, with contributions from over 15 consortium-funded scientists and engineers and many in-kind contributions from the consortium partners, comprising members of the scientific communities in Germany, United Kingdom, Sweden, Slovakia, Switzerland, United States, and Australia.

HIBEF

The Helmholtz International Beamline for Extreme Fields HIBEF is an international user consortium, contributing several experimental setups and optical laser systems to the High Energy Density (HED) beamline of the European XFEL. DESY works in close collaboration with the Helmholtz-Zentrum Dresden-Rossendorf (HZDR), which leads the consortium, the UK HIBEF consortium led by the University of Oxford, and other partners. For planetary physics research at simultaneous high pressures and high temperatures a 'Diamond Anvil Cell' (DAC) setup (Fig. 2) and a Shock/Ramp

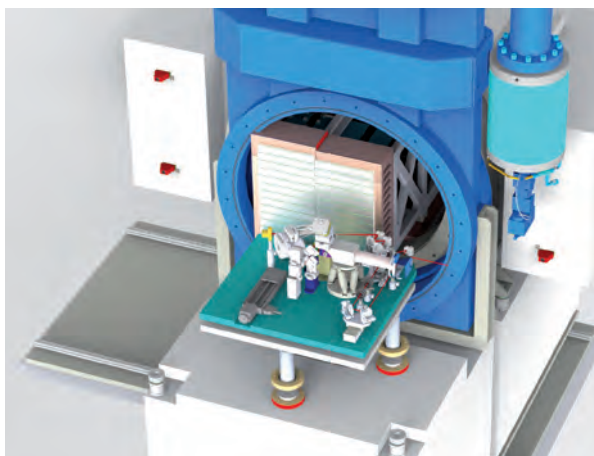


Figure 1

A conceptual design showing the AGIPD 4M detector to be used at the second end-station of the SPB/SFX instrument. One particular experiment configuration on the experimental table is shown in turquoise. The detector is over 400 mm wide and will be retractable from the in-vacuum experiment region through a gate valve. The vacuum envelope for the experiment is not shown.

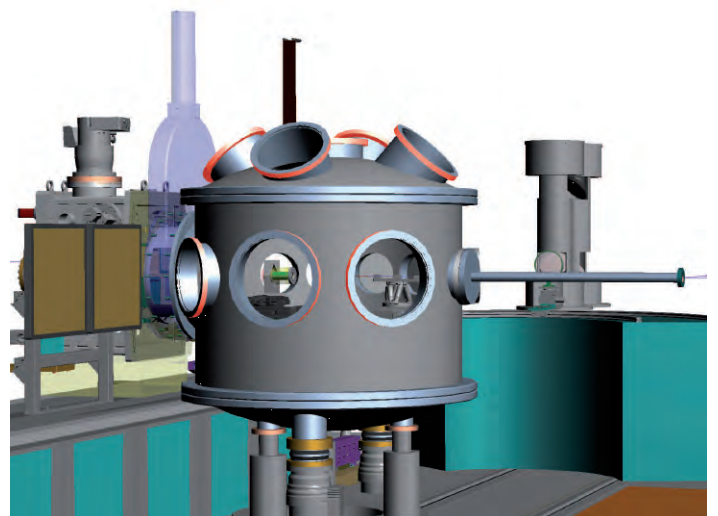
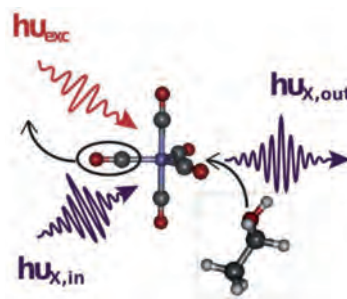


Figure 2

The image shows the planned DAC setup at the HED instrument of the European XFEL. The DAC with sample stack is located in a vacuum chamber (centre). A fully motorised detector bank (left) will be positioned downstream from the chamber while the beam of the DiPOLE laser is coupled in by periscopes from the right side.

Figure 3

hRIXS allows a novel look at the dynamics in chemistry and materials reaching the physical transform limit in energy and time. Being element specific, i.e. ultrafast metal to ligand charge transfer at an active metal atom can be directly followed. (Image adapted from [Kunnus et al., New J. Phys 18, 103011 (2016)], published under CC-BY-3.0)



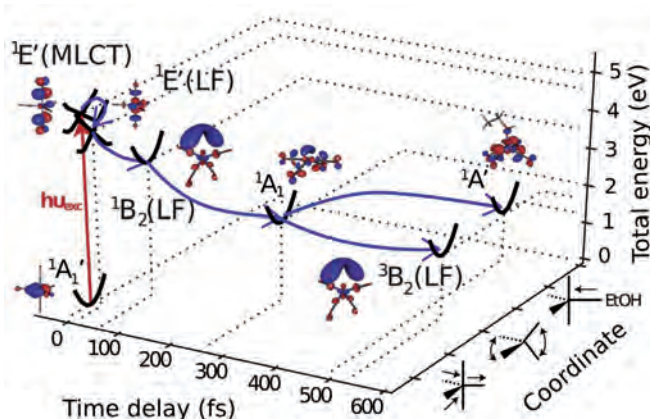
compression setup are envisaged. The corresponding Conceptual Design Reports (CDR) were composed and discussed during two workshops with the international user community. The workshop dedicated to the DAC CDR took place in January 2016 at DESY. In September the HED team organised a workshop at the European XFEL headquarter in Schenefeld to discuss the Shock/Ramp compression CDR. This CDR includes the use of the 'Diode Pumped Optical Laser for Experiments' (DiPOLE), which is contributed by the UK HIBEF consortium. Both CDRs were approved by the HIBEF management board and the different teams now enter the technical design phase that will last through 2017.

Furthermore the procurement of a Short-Pulse Laser system for the generation of strong fields has started. HIBEF will also organise workshops in 2017 for the other scientific areas of the user consortium, i.e. for physics of high energy density created by a short pulse laser and X-ray diffraction and spectroscopy experiments at high magnetic fields using pulsed power techniques.

hRIXS

The Heisenberg RIXS consortium will bring resonant inelastic soft X-ray scattering (RIXS) to the transform limit in energy and time at the European XFEL. Unique insights to chemical dynamics, driven phases as well as fundamental X-ray matter interaction opens up new science directions (Fig. 3).

The optical design of the spectrometer has recently been completed and approved, and optics have been purchased. It is based on spherical variable line-spacing gratings with the ability to achieve resolving powers ≥ 20.000 over an energy range of 250-1600 eV. hRIXS will be the world leading instrument to detect static properties and transient excitations in structure, charge, spin and orbital polarization for chemical processes as well as a wide range of energy- and bio-relevant materials. After the current mechanical construction phase the installation is planned for 2017/2018. Funding is provided by the Helmholtz Association via strategic investment in the Helmholtz-International Users consortium hRIXS. The project is partially supported by the ERC Advanced Grant 'EDAX' at Potsdam University. The hRIXS consortium includes partners from Germany, Switzerland, Finland, France, Sweden, Italy, and the UK. The project is coordinated by Potsdam University in close collaboration with DESY and European XFEL.



Two additional user consortia are led by DESY:

DataXpress

The DataXpress consortium is providing software for data analysis and real time experiment feedback for serial crystallography and single particle coherent diffraction experiments at European XFEL meeting the requirements of the high data acquisition rate of European XFEL. The data analysis pipeline provided by DataXpress will enable users to focus immediately on scientific output without having to handle the data processing and reduction challenges in each group individually. The consortium builds on research performed within CFEL/DESY, and includes partners from Germany, Sweden, and the USA. The software will be open source and available for all users. In 2016 parts of the software were tested at LCLS, PETRA III, and SACLA.

COMO

The COMO consortium is also run by DESY and will provide molecular-beam-injector setups for European XFEL instruments to enable the delivery of state-, size-, and isomer-selected samples of polar molecules and clusters. In 2016 the next scientific and technical steps were discussed and prepared, which included the definition of interfaces with the European XFEL instrumentation.

Scientific coordinators:

SFX: Henry Chapman, CFEL/DESY, henry.chapman@desy.de

HIBEF: Thomas Cowan, HZDR, t.cowan@hzdr.de

hRIXS: Alexander Föhlisch, Potsdam University and HZB, alexander.foehlich@helmholtz-berlin.de

DataXpress: Anton Barty, CFEL/DESY, anton.barty@desy.de

COMO: Jochen Küpper, CFEL/DESY and Univ. Hamburg, jochen.kuepper@desy.de

European Molecular Biology Laboratory Hamburg Unit.

Structural biology research and service provision

Thanks to recent advances in structural biology instrumentation and methodology it is now possible to study the molecular structures of large protein complexes. The Hamburg Unit of the European Molecular Biology Laboratory (EMBL) is embracing these possibilities by maintaining and developing research infrastructures operated by EMBL, as well as engaging in co-operations across the DESY campus.

Research Highlights

Members of the Schneider group together with colleagues from the Max Planck Institute for Biophysical Chemistry in Göttingen published results of structures of the cell's proteasome in complex with commercially available cancer drugs. The 2.1 Å structures revealed how the cancer drugs interact with the proteasome to inhibit its function. The results pave the way for the development of more effective therapies (see highlight section of this report) [1].

In a unique experiment, members of the Wilmanns group at EMBL in Hamburg together with members of the Chapman group (CFEL, DESY) at the Hamburg Centre for Ultrafast Imaging (CUI) were able to collect X-ray diffraction data from crystals within yeast cells at SLAC National Accelerator Laboratory in California. This in cellulo serial crystallography project is detailed in the highlight section of this report [2].

Dara, a web-server, queries over 150,000 small-angle X-ray scattering (SAXS) profiles, which were pre-computed from the high resolution models of macromolecules and biological assemblies in the Protein Data Bank, to rapidly find the most similar structure to a given experimental or theoretical SAXS pattern. Identification of the best scattering equivalents provides a straightforward and automated way of structural assessment of macromolecules based on a SAXS profile [3].

A novel quantitative measure of the resolution of *ab initio* shapes restored from small-angle scattering (SAS) data based on variability of reconstructed ensembles is validated in simulated examples and its efficiency demonstrated in applications to experimental data. It is proposed that the resolution should be reported in publications and depositions of *ab initio* SAS models [4].

Research Service Provision

EMBL's integrated facility enables academic and industrial users' access to a package of structural biology services and

expertise. It encompasses sample preparation and characterisation laboratories, beamlines for structural biology applications, as well as data processing and evaluation. Recent developments in the Sample Preparation and Characterisation (SPC) facility include two tools to determine ideal conditions for protein stability, purification and storage, which are now available for purchase from the biotech company *Molecular Dimensions*. The RUBIC Buffer Screen contains diverse and varying solutions commonly used in structural biology experiments. The RUBIC Additive Screen can be used to pinpoint ideal conditions for purification and storage. The screens can be used alone or in a two-step approach for a wide range of proteins. Moreover, in a partnership with the Centre for Structural Systems Biology (CSSB), the SPC has extended its services to include a wide range of biophysical techniques. Equipment for surface plasmon resonance, microscale thermophoresis, isothermal titration calorimetry and circular dichroism is available for use for the whole DESY campus. SPC staff can be engaged to plan experiments and train novel users. More information can be requested via spc@embl-hamburg.de.

Beamlines at PETRA III

EMBL runs three beamlines for structural biology applications for the international user community: one for Small Angle



Figure 1

The image shows the MARVIN robot placing samples in the PETRA III beamline P14 for crystallography experiments.

X-ray Scattering experiments and two for Macromolecular Crystallography. All EMBL beamlines are fully operational following the end of the PETRA III shutdown in spring 2016.

At the SAXS beamline, a multilayer monochromator now provides an increase in photon flux by a factor of fifty, to 5×10^{14} photon/sec. This high flux enables rapid kinetic experiments, whereby a scattering curve from a dilute protein solution of lysozyme can be collected in sub-millisecond time. Appropriate synchronisation is developed to study laser-triggered kinetic processes. Furthermore, an all-in-one system combining in-line sample component separation with parallel biophysical and SAXS characterisation of the separated components to counteract inherent sample polydispersity was developed. The system is coupled to an automated data analysis pipeline to provide a novel tool to study difficult samples [5].

For experiments in the field of macromolecular crystallography, MARVIN robots for mounting SPINE pins from a large capacity storage dewar (150 samples) are available on both beamlines (Fig. 1). The cycle time between two crystals is < 1 min and remote access is possible. A remotely controllable Crystal-Direct Harvester, developed by colleagues at EMBL in Grenoble together with MAATEL, was installed in November 2016. This allows the harvesting of crystals from crystallisation plates – a great advantage for handling fragile crystals. Finally, the beamline user interface mxcube has been upgraded to use a new graphics library ‘qt4’ making complex beamline features such as serial crystallography strategies easy to use.

Engagement with the external community

Coordinated by EMBL, the EU funded project BioStruct-X (www.biostruct-x.eu) supporting user access to established and key methods in structural biology has been successful in creating a single gateway to European synchrotron infrastructures. The project ended in 2016 and is succeeded by iNEXT, coordinated by the University of Utrecht (www.inext-eu.org).

In 2016 two training courses funded by the European Molecular Biology Organisation (EMBO) were held – one focussing on Solution Scattering from Biological Macromolecules, and one on Protein Expression Purification and Characterisation (PEPC). 2016 saw the 10th iteration of the PEPC course, which included an anniversary symposium celebrating the course’s history and development (Fig. 2).



Figure 2

As part of the 10th iteration of the PEPC course, organisers invited tutors and participants from the first courses to celebrate the long-standing part of the EMBL training programme.

Infrastructure projects and investments

The project SyncFELmed funded by the German Federal Ministry of Education and Research (BMBF) and the Russian Ministry of Education and Science aims to facilitate the advancement of combined synchrotron radiation and free-electron laser technologies in biomedical sciences (www.syncfelmed.org). In October in Sochi, Russia, the consortium presented recent developments in Hamburg and the field of serial crystallography. A paper presenting quantum mechanics/molecular mechanics (QM/MM) calculations to achieve maturation of antibodies in silico was published by consortium members [6].

EMBL is contributing to the establishment of an integrated biology infrastructure at the European XFEL (XBI), which will provide sample production and preparation laboratories. A senior technical officer was hired to oversee the project from EMBL’s side. The equipment is currently being purchased and expected to be delivered by the beginning of 2017.

EMBL Group Leader Thomas Schneider and Arwen Pearson from CUI were successful in securing a grant of 2 Million Euro from the BMBF to develop and build a dedicated time resolved crystallography end station at PETRA III. Its construction is planned to be completed by the end of 2017.

Contact: Matthias Wilmanns,
matthias.wilmanns@embl-hamburg.de

References

1. J. Schrader et al., *Science* 353, 6299 (2016).
2. A. J. Jakobi et al., *IUCrJ* 3, 88 (2016).
3. A. G. Kikhney et al., *Bioinformatics* 32, 616 (2016).
4. A. T. Tuukkanen A. et al., *IUCrJ* 3, 440 (2016).
5. M. A. Graewert et al., *Scientific Reports* 5, 10734 (2015).
6. I. V. Smirnov et al., *Science Advances* 2, e150169 (2016).

Centre for Structural Systems Biology CSSB.

We are taking off



Figure 1

Celebrating the Research Centre Borstel to join CSSB: Dirk Heinz, HZI Braunschweig, Chair of CSSB Council; Stefan Ehlers, FZB Director; Thomas Gutschmann, FZB Group Leader; Matthias Wilmanns, EMBL, CSSB Research Director; Chris Meier, Universität Hamburg, CSSB Deputy Director.

The mission of the Centre for Structural Systems Biology (CSSB) is to develop a fundamental understanding of infection mechanisms by investigating the molecular architecture of macromolecules from the host and pathogen as well as the functional interactions that trigger the infection process. Within the CSSB – a cooperation of ten partner institutions – scientists will use a novel approach which combines integrative structural biology with systems biology approaches to advance our understanding of the molecular mechanisms of some of the world's most widespread infections. This knowledge is fundamental for the development of new therapeutic strategies to combat infectious diseases.

This year, the Research Centre Borstel (FZB) from Schleswig-Holstein joined CSSB as an associated partner. The FZB is a Leibniz Centre for Medicine and Biosciences with focus on tuberculosis and asthma research. On 16 June, this new partnership was celebrated during a signing ceremony in Hamburg with representatives from CSSB and FZB (Fig. 1). In November, the principal investigators from FZB and CSSB held a symposium to share research ideas and to discuss collaboration opportunities and projects in more detail.

The construction of the new CSSB building on the DESY campus is soon coming to an end (Fig. 2). Upon entering the building, one is immediately struck by the bright and sweeping atmosphere created by the building's glass façade. Now, one can easily imagine the building filled with busy students and scientists discussing their current and upcoming projects. The laboratory benches and equipment have been installed in most of the laboratory areas and the rooms for the electron cryo-microscopes in the basement are ready and waiting for the instruments to be installed. The building will go into its operational trial phase at the beginning of 2017. The first research groups are expected to move into the building in late spring of 2017 before the building's official opening ceremony takes place.

Our Research Strategy

CSSB research projects focus on how pathogens interact with the human hosts as well as the molecular machineries that control the secretion of toxic compounds from the pathogen to the host. The key approach used to address these questions is structural biology; using X-ray based research infrastructures such as the PETRA III synchrotron

operated by DESY and the European XFEL in Schenefeld as well as a new electron cryo microscopy facility in the CSSB building. These approaches will be complemented by a holistic investigation of the infection processes by a new research direction known as systems biology.

Fostering interdisciplinary collaboration between different research groups at the CSSB is a key element of our mission. We are very grateful to the Joachim Herz Stiftung, which is now supporting three collaborative research projects led by CSSB scientists. In 2016 the last of these three projects was offered to Thomas Marlovits (UKE) in collaboration with researchers from the Helmholtz Centre for Infection Research, Braunschweig and University of Vienna, Austria.

To foster cooperation with related research organisations and consortia the CSSB directorate organised several scientific working meetings:

- Symposium Structural Systems Biology: This joint symposium was held by DESY, the University of Kiel, and CSSB on 24-25 May, in Kiel.
- Meeting regarding the life science research activities on the Bahrenfeld campus, organised in cooperation with the HARBOR consortium, on 16 June. This and future related meetings will play a pivotal role in the establishment of a joint research strategy for the life sciences and biomedical research on the Bahrenfeld campus.
- Bilateral Meeting with a delegation from the medical faculty of Lund University (Sweden) on 15 September in Hamburg. It was agreed to consider concrete joint research projects and the exploration of external funding opportunities.

Recent research highlights from CSSB research groups are outlined in the CSSB Inaugural Report entitled 'We are taking off'.

Our Research Hotel

The CSSB Research Hotel was conceived to provide attractive research opportunities for junior investigators that effectively bridge the gap between postdoctoral research and independent senior investigator positions. CSSB has implemented its Research Hotel in an effort to facilitate this transition and to empower the next generation of scientists. Approximately 20 % of the CSSB building has been reserved for this purpose, with a capacity to host up to six research groups typically for five years. The Research Hotel will be open to small research groups from CSSB partner institutions as well as other external institutions irrespective of country of origin.



Figure 2

The outer shell of the CSSB Building is completed.

This year, CSSB has succeeded in recruiting Rainer Kaufmann (University of Oxford, United Kingdom) as a new Junior Group Leader at the CSSB. Rainer Kaufmann received a prestigious Freigeist-Fellowship from the Volkswagen Foundation to conduct independent research at CSSB. With this grant, he seeks to further our understanding of complex cellular processes by developing a new field of microscopy: super-resolution fluorescence cryo-microscopy. Rainer Kaufmann will move into the CSSB building when it opens in 2017. The University of Hamburg will act as his host institution.

Contact: Ina Plettner, ina.plettner@desy.de

Matthias Wilmanns, matthias.wilmanns@embl-hamburg.de

CSSB Partner Institutions

- Bernhard Nocht Institute for Tropical Medicine (BNITM)
- Deutsches Elektronen-Synchrotron (DESY)
- European Molecular Biology Laboratory (EMBL)
- Forschungszentrum Jülich (FZJ)
- Hannover Medical School (MHH)
- Heinrich Pette Institute (HPI)
- Helmholtz Centre for Infection Research (HZI)
- Research Center Borstel (FZB)
- Universität Hamburg (UHH)
- University Medical Center Hamburg-Eppendorf (UKE)

CSSB Investors

- Federal Republic of Germany
- Free and Hanseatic City of Hamburg
- Federal State of Lower Saxony
- Federal State of Schleswig-Holstein

The Helmholtz-Zentrum Geesthacht Outstation at DESY.

GEMS – Get Engineers to Make use of Scattering

Since January 2016 Martin Müller has taken over as Director of the Institute of Materials Research and of the German Engineering Materials Science Centre (GEMS) after the delegation of Andreas Schreyer as Director for Science to the European Spallation Source ESS in Lund, Sweden. He started with the implementation of a new GEMS structure with groups working in the fields of X-ray diffraction (led by Peter Staron) and imaging (led by Christina Krywka) at the DESY campus, as well as groups in the field of neutron scattering and new neutron instrumentation at the ESS.

In June 2016 the GEMS offices and laboratories have been moved to building 66 on the Bahrenfeld campus as an interim solution until GEMS will finally be accommodated in one wing of the new Photon Science building. Moreover, the former HARWI II beamline will be re-established at the P61.1 beamline in the PETRA III experimental hall 'Paul P. Ewald'.

The SFB 986 ('Tailor-Made Multi-Scale Materials Systems – M³', coordinated by Technical University Hamburg-Harburg, TU HH) was positively evaluated. GEMS will continue its successful work in the central project 'Investigation of multi-scale structured materials systems with synchrotron and neutron radiation' with two postdocs for four more years.

In the Röntgen-Angström-Cluster (RAC) project 'Synchro-Load' (Metallic Biomaterials, HZG, with University of Malmö) the mechanical stability and structural integration of different implant materials into bone will be studied by tomography techniques. This will help in the development of a knowledge-based design approach for bio-resorbable implants. The BMBF project 'MgBone' focusses on the nanostructure of the bone – implant interface to be investigated by scanning micro- and nanodiffraction.

Diffraction

In spring, the High Energy Materials Science beamline at PETRA III HEMS/P07 was successfully reviewed and classified 'world-leading' in its field and being highly requested in a 'widespread user community'. To further improve HEMS a powerful undulator as well as a fast and efficient detector (together with DESY) will be installed. The impact of *in situ* experiments applying high-energy X-ray diffraction to the development of engineering materials was recently documented in a review [1]. Two new *in situ* set-ups, a sputter chamber and a turning rig, which have been built in cooperation

with Linköping University (Sweden) within the framework of the project 'X-Cut' of the RAC, are now available to HEMS users. The important role of the quenching and deformation dilatometer as *in situ* sample environment is highlighted not only by the large number of users but also by a recent publication on nano-scaled modulated microstructures (Fig. 1, [2]). Also an *in situ* experiment on brazing of TiAl alloys was performed (Fig. 2). A new conical slit cell was successfully tested at the P07B side station in the framework of a cooperation with the company voestalpine Tubulars and Montanuniversität Leoben. The conical slit cell enables depth-resolved residual stress analysis also at the side station.

After more than 5 years of fruitful collaboration with EMBL the HZG engagement at the BioSAXS beamline (P12) ended in June 2016.

Imaging

The nanotomography station at the Imaging Beamline IBL/P05 at PETRA III has been equipped with new X-ray optics. A Fresnel zone plate (FZP) used for focusing and a mosaic prism optics developed at the Paul Scherrer Institute (PSI) serving as beam shaper yielded a resolution better than 100 nm (see Fig. 3). Nanotomography data were recorded from a nanoporous gold (NPG) sample, provided by the group of Erica Lilleodden ('Experimental Materials Mechanics', HZG). The experiment was performed at an energy of 14 keV with an effective pixel size of 17.4 nm. The square-shaped column was prepared using the GEMS focused-ion beam (FIB) milling machine. The 400 nm thick NPG filaments were nicely resolved.

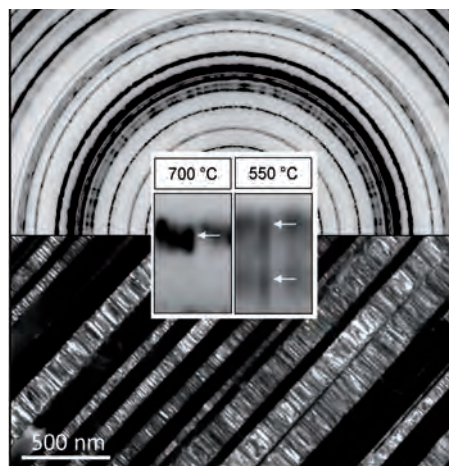


Figure 1

The image shows a diffraction pattern of a TiAl alloy observed with the quenching dilatometer from *in situ* measurements in the temperature range between 550 °C and 700 °C. The data reveals information on the balanced mechanical properties of nano-scaled modulated microstructures (lamellae with tweed substructure) [2].

Figure 2

In situ experiment on brazing of TiAl alloys. Brazing is done at 1110 °C in a vacuum chamber and under Ar atmosphere with induction heating (left). The *in situ* diffraction experiment shows the phase transformations going on in the joining region while a joint is formed. Scans over the joint region show the spatial distribution of phases as a function of time, e.g. after 5.5 h / 1110 °C (right).

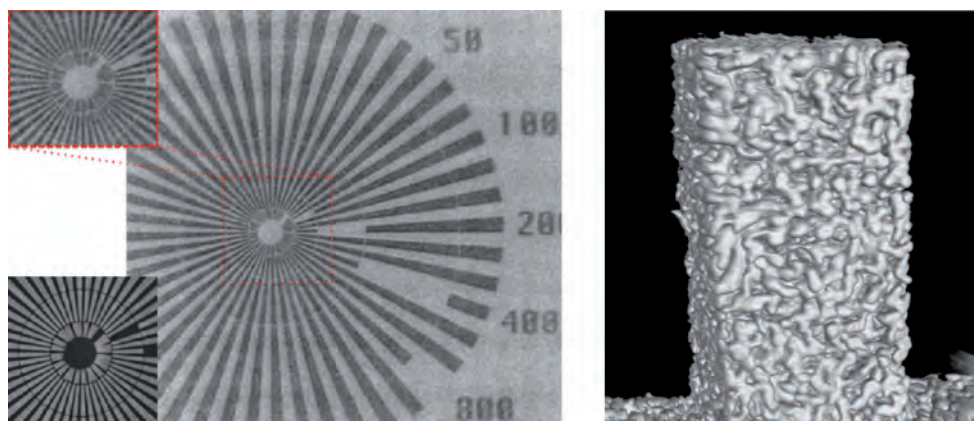
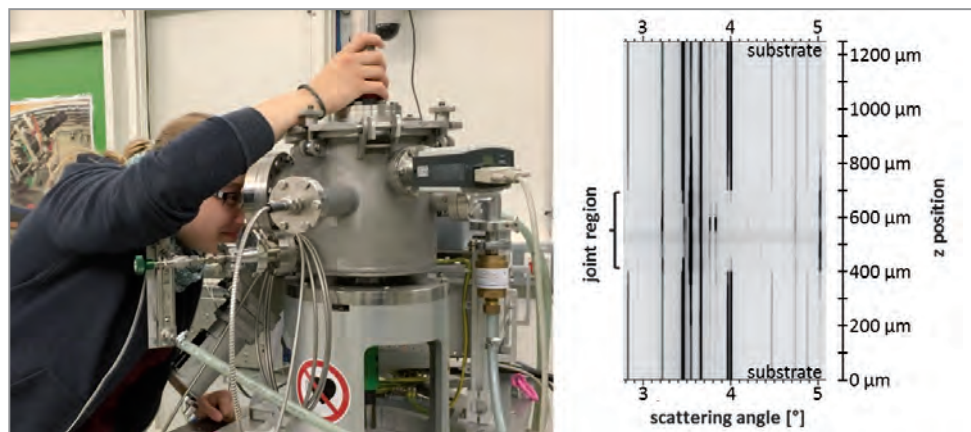


Figure 3

Left: X-ray microscopy image of an Xradia test pattern. The inner circle contains 50-100 nm lines, the 2nd circle contains 100-200 nm lines. Upper inset shows the magnified centre region. The SEM image, displayed in the lower left corner, reveals the partial collapse of the structures on the test pattern which is also visible in the X-ray microscopy data. Right: Volume rendering of a nanoporous gold sample (SFB 986). The square column has an edge length of 8 μm.

For the microtomography setup at IBL/ P05 another set of beam shaping optics was developed in the scope of the Virtual Institute 'New X-ray analytic methods in material science' by the Karlsruhe Institute of Technology (KIT). Here the goal was to increase the field of view by widening of the X-ray beam. First successful experiments were performed and the beam profile was enlarged in the vertical direction from 1.8 mm to 5 mm.

At the microtomography station at high-throughput experiments on materials science and bio-medical topics were performed. A newly installed camera system, developed in collaboration with KIT, has been successfully used to record *in vivo* radiographs of hissing cockroaches to understand the mechanism of hissing. Owing to the high density and spatial resolution of the imaging setup, new insights into the evolution and geobiology of selected animal taxa were generated, based on studies of 54 Ma and 100 Ma old amber inclusions (see highlight section of this report: Oliveira et al. as well as Stebner et al. [3]).

The grating-based phase-contrast microtomography setup at HEMS/P07 has been further developed towards higher spatial resolution. Currently, a resolution of 5 μm is possible using a single-grating interferometer with a 10 μm grating period. This setup was used to perform user experiments investigating the interface between a jaw bone and a titanium implant (at 60 keV) and for the investigation of calcified coronary arteries (at 40 keV).

The Nanofocus Endstation of the Micro- and Nanofocus X-ray Scattering Beamline at PETRA III (MINAXS/P03), operated by HZG in co-operation with DESY, was evaluated within the beamline evaluation of P03. Both the experimental setup as well as its strong focus on materials science related research received an outstanding positive feedback from the reviewers. Among the many *in situ* sample environments available, the custom-built nanoindentation device evolved into being the apparatus with the highest demand by users of the Nanofocus endstation. Next to 'classical' applications, such as the nanoindentation of extremely hard surfaces [4] the device has also been used by users from the KTH Royal Institute of Technology, in Stockholm to record indentation strain fields in individual, microscopic cellulose fibres.

Contact: Christina Krywka, christina.krywka@hzg.de
Peter Staron, peter.staron@hzg.de
Martin Müller, martin.mueller@hzg.de

References

1. P. Erdely et al., *Metals* 6, 17–21 (2016).
2. M. W. Rackel et al., *Acta Mater.*, accepted.
3. F. Stebner et al., *Scientific Reports* 6, 34352 (2016).
4. A. Zeilinger et al., *Scientific Reports* 6, 22670 (2016).

The DESY NanoLab provides nano-characterization, spectroscopy and nano-structuring methods, which are complementary to the photon based techniques available for users at DESY X-ray facilities PETRA III and FLASH. The access to the DESY NanoLab is granted for external users either through regular PETRA III or FLASH proposals (via DOOR), or through the submission of a proposal to the European user platform Nano Foundries Fine Analysis (NFFA Europe, www.nffa.eu). The characterization of samples for industrial users, who are liable to pay costs, has been offered by DESY NanoLab since 2016.

In collaboration with the University of Bayreuth an important tool for nano-structuring and nano-machining was put into operation in 2016: a dual focused ion beam (FIB). This exceptional instrument allows one to cut three-dimensional objects out of bulk samples with nanometre precision using a focused gallium ion beam with only a few nanometres in diameter. The cutting process can be directly imaged by a built-in high resolution scanning electron microscope (Fig. 1). Using a platinum containing precursor gas, very small samples can be glued to tips for X-ray tomography and transferred to the PETRA III X-ray imaging beamlines. In addition, the instrument is used to prepare secondary anvils and samples for ultra-high pressure experiments in the double stage diamond anvil cells at the PETRA III beamline P02.2 (Extreme Conditions Beamline). This new tool for nano-machining opens up new research possibilities for the X-ray investigation of

selected, individual nano-objects, as well as for the controlled nano-structuring of surfaces and nano-membranes.

Furthermore, a system for measurement of physical properties in external fields up to 14 T within a temperature range between 1.6 K and 400 K will be installed in the DESY NanoLab in 2017. This system, which is cryogen-free for convenient operation, will offer a series of different options for measurement of condensed-matter properties. Static and dynamic magnetic properties can be determined via vibrating-sample magnetometry (VSM) and ac-susceptibility, respectively. Electrical transport properties can be characterised via ac- and dc-resistivity as well as Hall-effect measurements. Moreover, the measurement of thermal transport properties and heat capacity will facilitate the detection and characterization of phase transitions in quantum condensed matter. A flexible layout of the measurement system allows for later installation of customized measurement options.

The DESY NanoLab instrumentation is temporarily located in building 3 on the DESY campus until the new Photon Science building is ready. Its construction will start in 2017 and the finalization is foreseen for 2019. The Photon Science building will host the DESY NanoLab, other DESY groups and outstations from the Helmholtz-Zentrum Geesthacht and the University of Kiel.

Contact: *Andreas Stierle, andreas.stierle@desy.de*

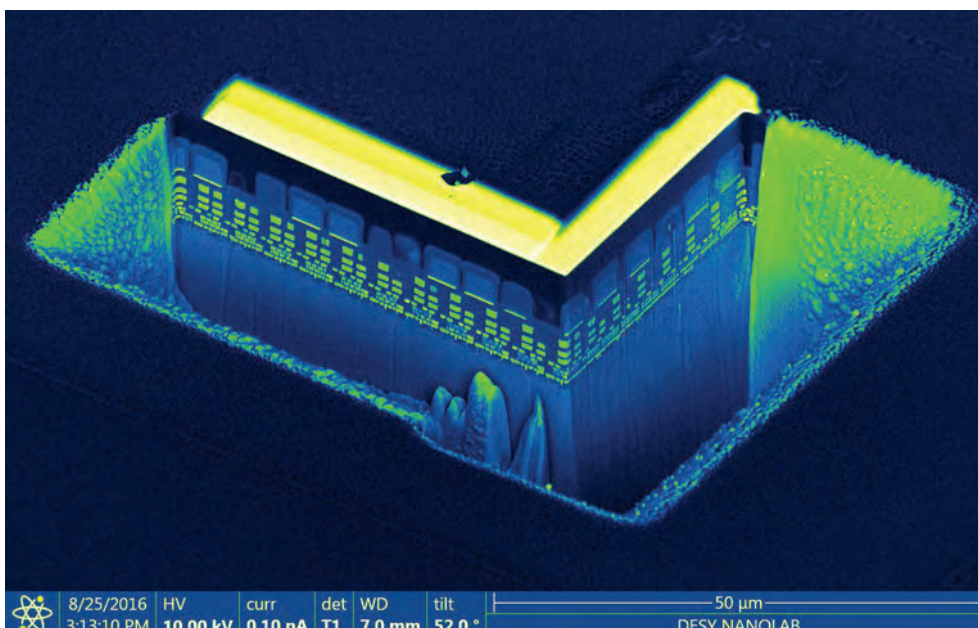


Figure 1
3D FIB cut through a semiconductor chip imaged with the built-in scanning electron microscope.

From the vacuum chamber into the car.

Transferring knowledge from the laboratory to society

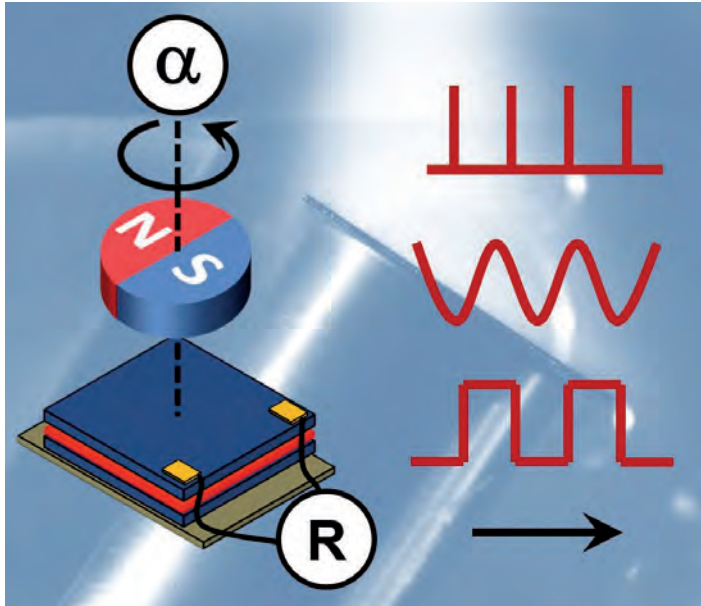


Figure 1

A new deposition procedure in oblique incidence allows scientists from DESY to freely adjust and to create new magneto-resistive sensor functionalities. The example shows a magneto-resistive tri-layer and corresponding sensor characteristics (field dependent change in electrical resistance), which can be realized with the new technology.

Magnetic sensors surround us everywhere in our daily life, for example in cars, computers and smartphones. Today's market for these sensors spans 2 billion USD and the annual growth rate amounts presently to 5 – 10 %. Industry demands continuously new sensor concepts to broaden their application fields and to open up new key markets. The growing markets can only partially be covered by conventional magneto-resistance sensors, because the variability of their functionalities is intrinsically limited.

To address this demand, the DESY research team around Ralf Röhlsberger applied for funding from the Helmholtz Validation Fund (HVF) for a new invention. They were strongly supported by the DESY department for Innovation and Technology Transfer (ITT). The HVF, financed by funds from the Helmholtz President's Initiative and Networking Fund, aims to bridge gaps between scientific findings and their commercial applications, and between public research and private investment.

The validation project comprises an invention by the DESY scientist Kai Schlage and coworkers. They used the technique of oblique incidence deposition (OID) to customize magneto-resistive properties of ultrathin films, thus enabling the

production of magneto-resistance sensors with a full suite of new functionalities (Fig. 1). This directly addresses the existing demand from industry. The aim of the project is the validation of the industrial compatibility of the OID procedure developed at DESY.

This project constitutes a good example of classical technology transfer. The DESY researchers found the basic principle of the new technology during a calibration measurement for another project – the analysis of the evolution of magnetic order in iron nano-stripes formed by *in-situ* deposition at oblique incidence onto nano-faceted sapphire substrates. They discovered that the properties of the magnetic material completely changed compared to deposition at normal incidence. This observation initialized the sensor project, which led to an invention disclosure and subsequent patent application.

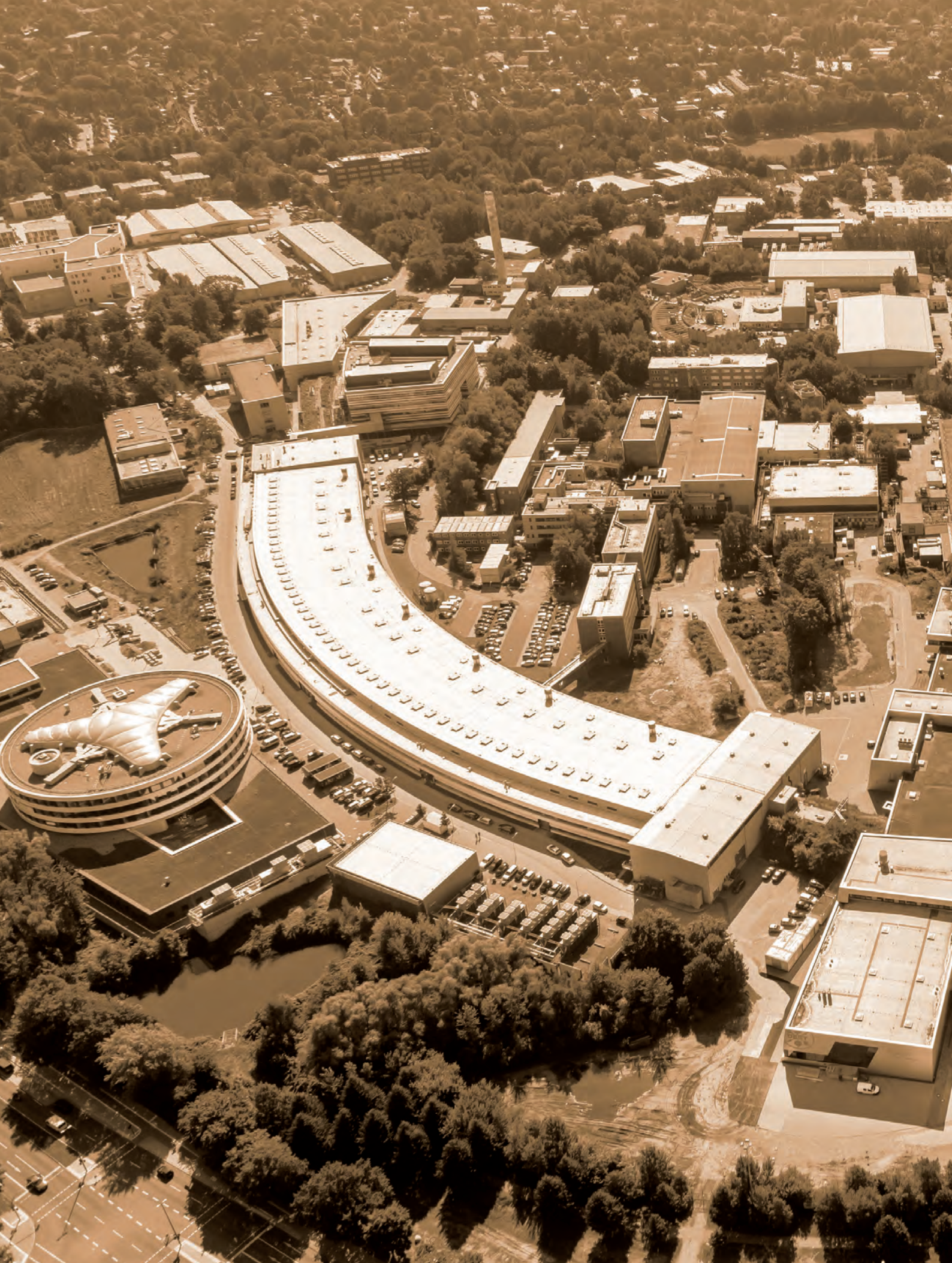
With the support of the DESY-ITT department, market research and exploratory discussions with potentially interested companies were undertaken, resulting in the cooperation with a strong partner from the automotive sector. The corresponding scientific work is featured in the highlight section of this report.

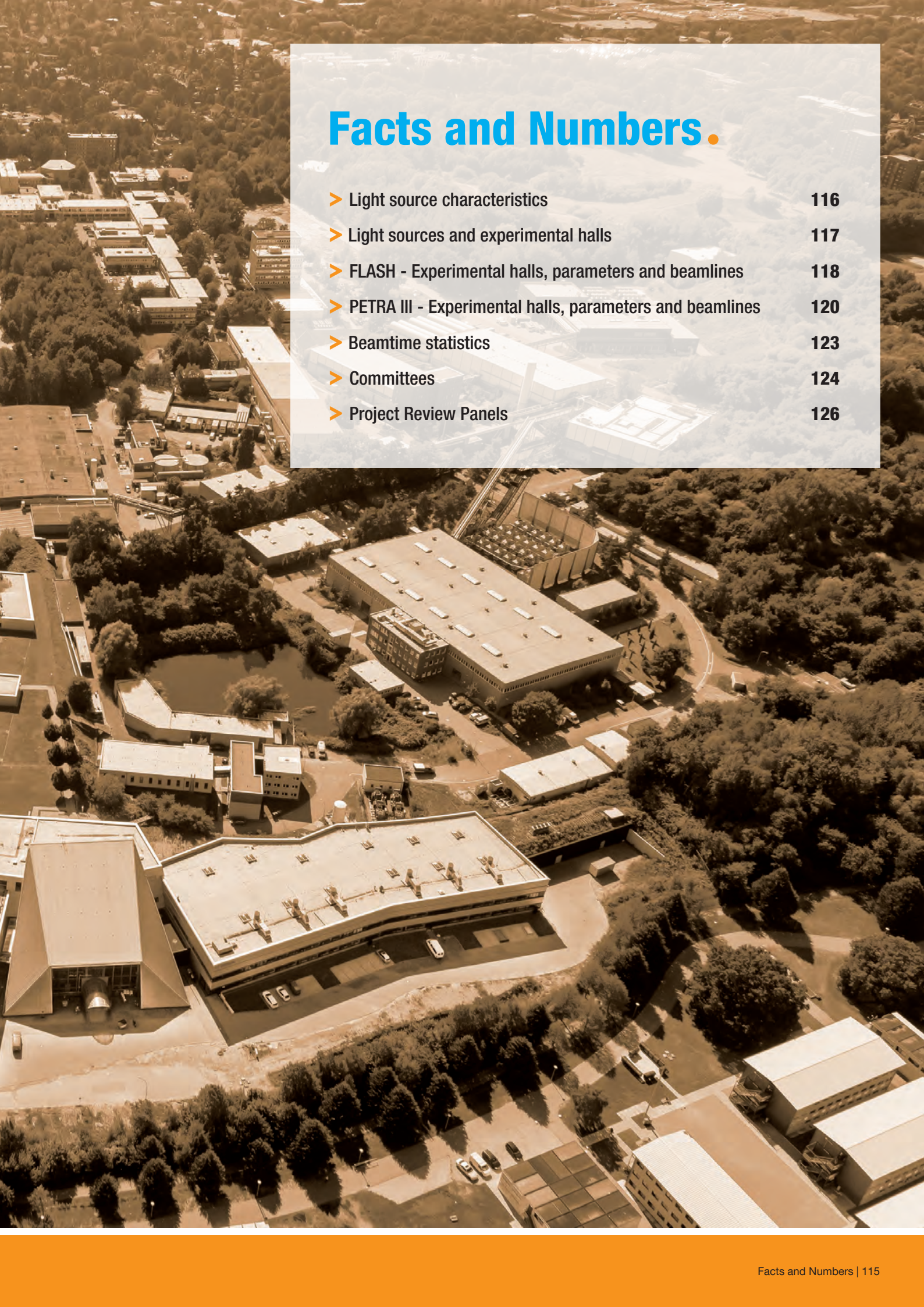
Approximately half of the total project costs (ca. 1.8 Mio Euro) will be covered by Helmholtz funding and the remaining half by DESY and a partner from industry. The project will start in 2017 and run for 2 years.

This is the second validation project that has been applied for by a DESY group together with the ITT department and been granted validation funding by the Helmholtz Association. The ITT department supports various kinds of funding applications for promising technologies, ideas and projects as well as for building up spin-offs. In the context of innovation and technology transfer at DESY, the development of the new Innovation Centre took the next step towards realization. End of October the partners DESY, the University of Hamburg and the City of Hamburg signed the foundation contract. These signatures are the starting point for the construction of the new building planned next to the CFEL building. Start of operation is planned for December 2018.

Contact: Arik Willner, arik.willner@desy.de

Involved scientists and engineers from DESY Photon Science: Kai Schlage, Lars Bocklage, Svenja Willing, Andrey Siemens, and Ralf Röhlsberger.

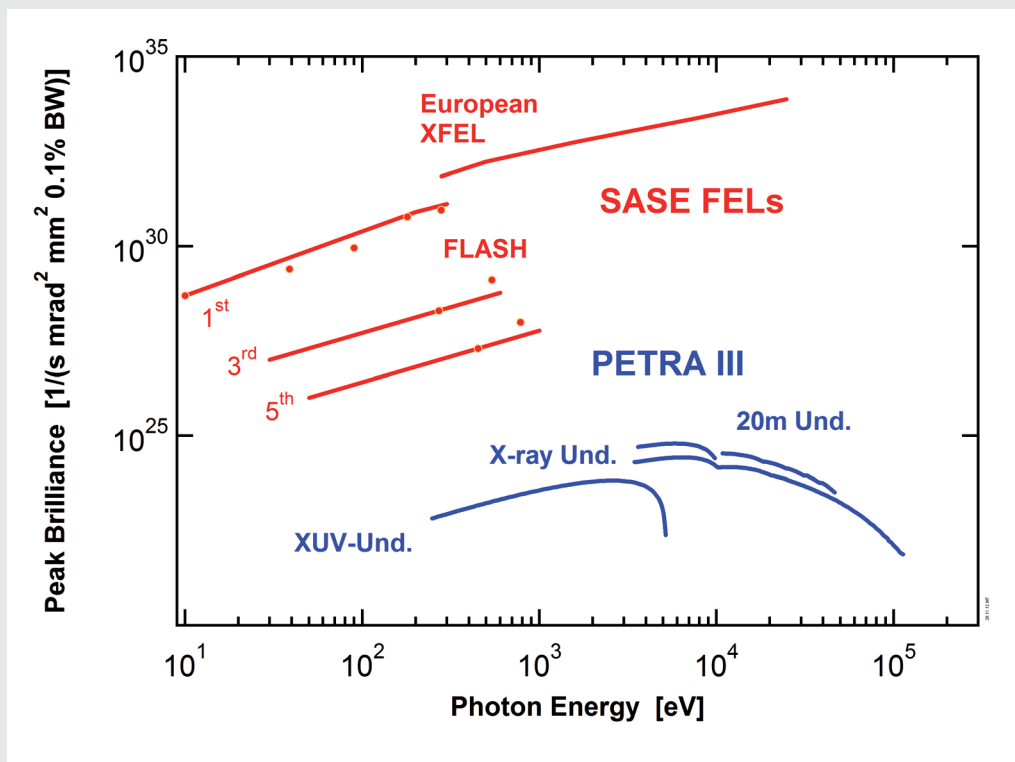
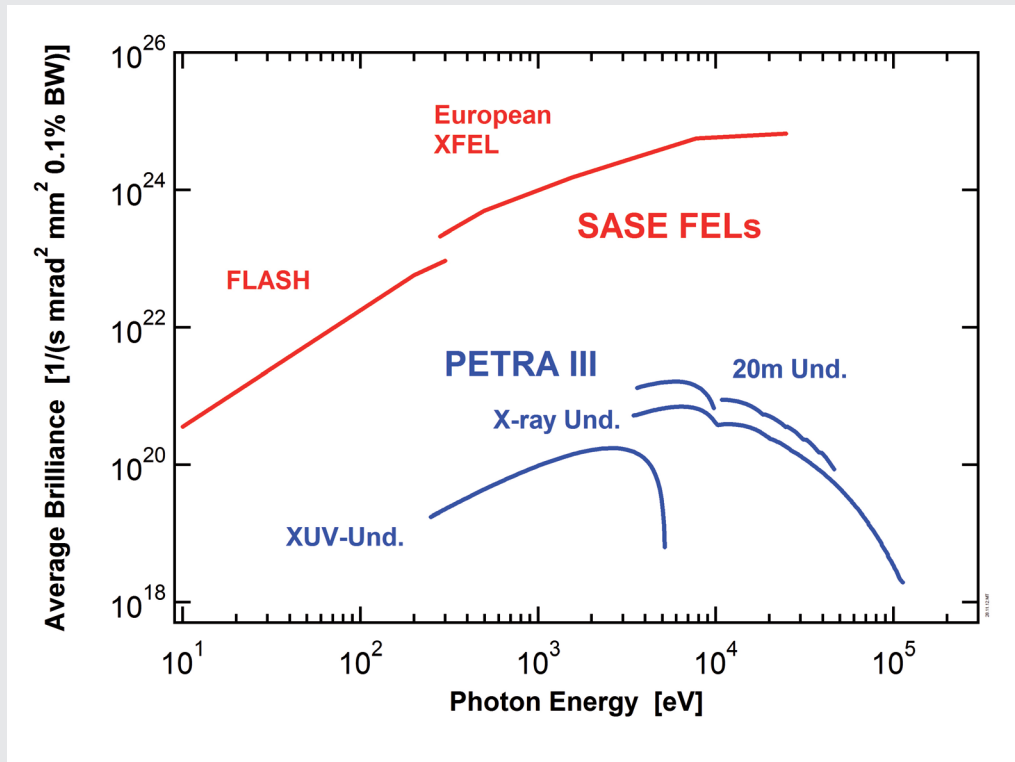




Facts and Numbers.

> Light source characteristics	116
> Light sources and experimental halls	117
> FLASH - Experimental halls, parameters and beamlines	118
> PETRA III - Experimental halls, parameters and beamlines	120
> Beamtime statistics	123
> Committees	124
> Project Review Panels	126

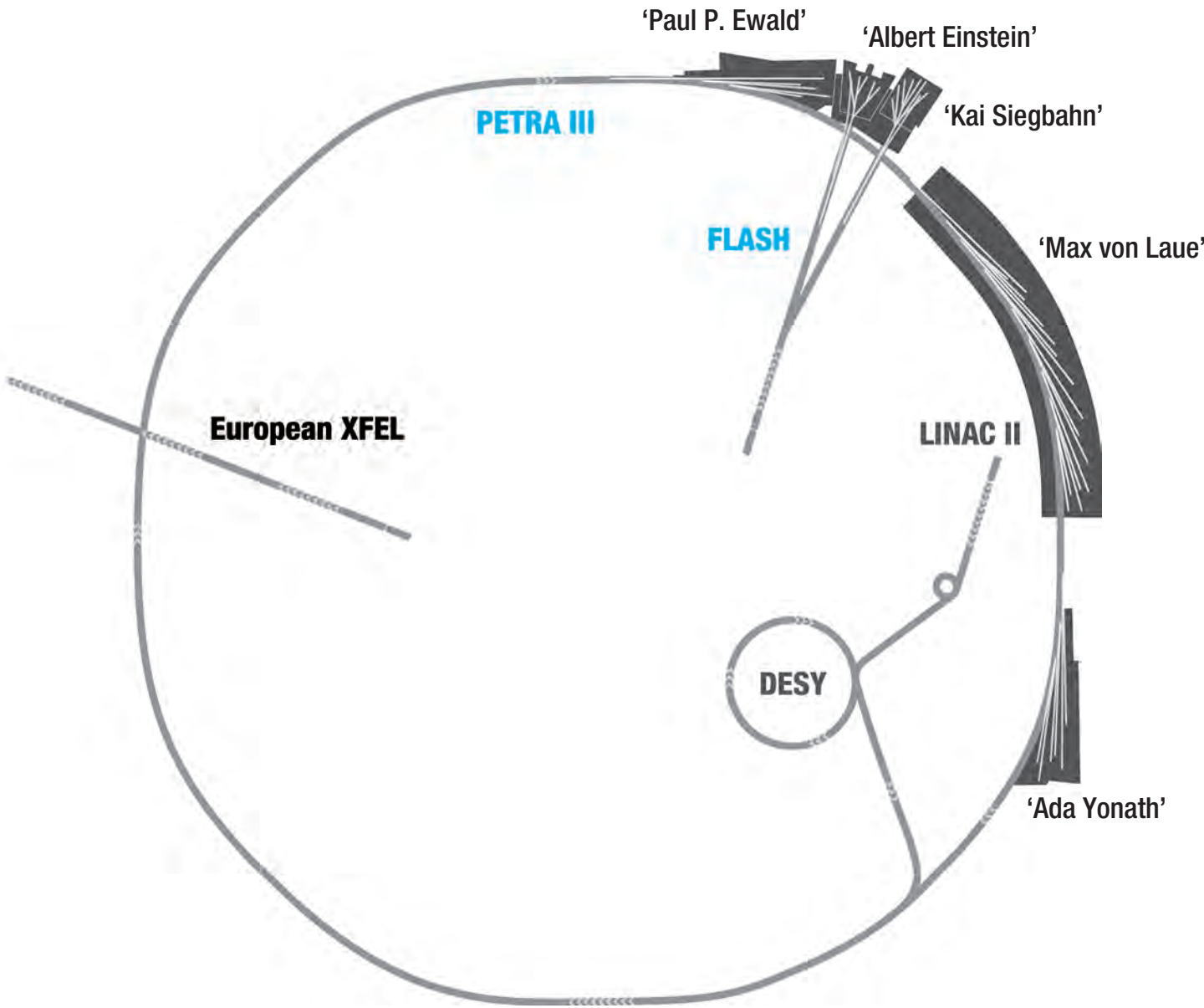
Light source characteristics.

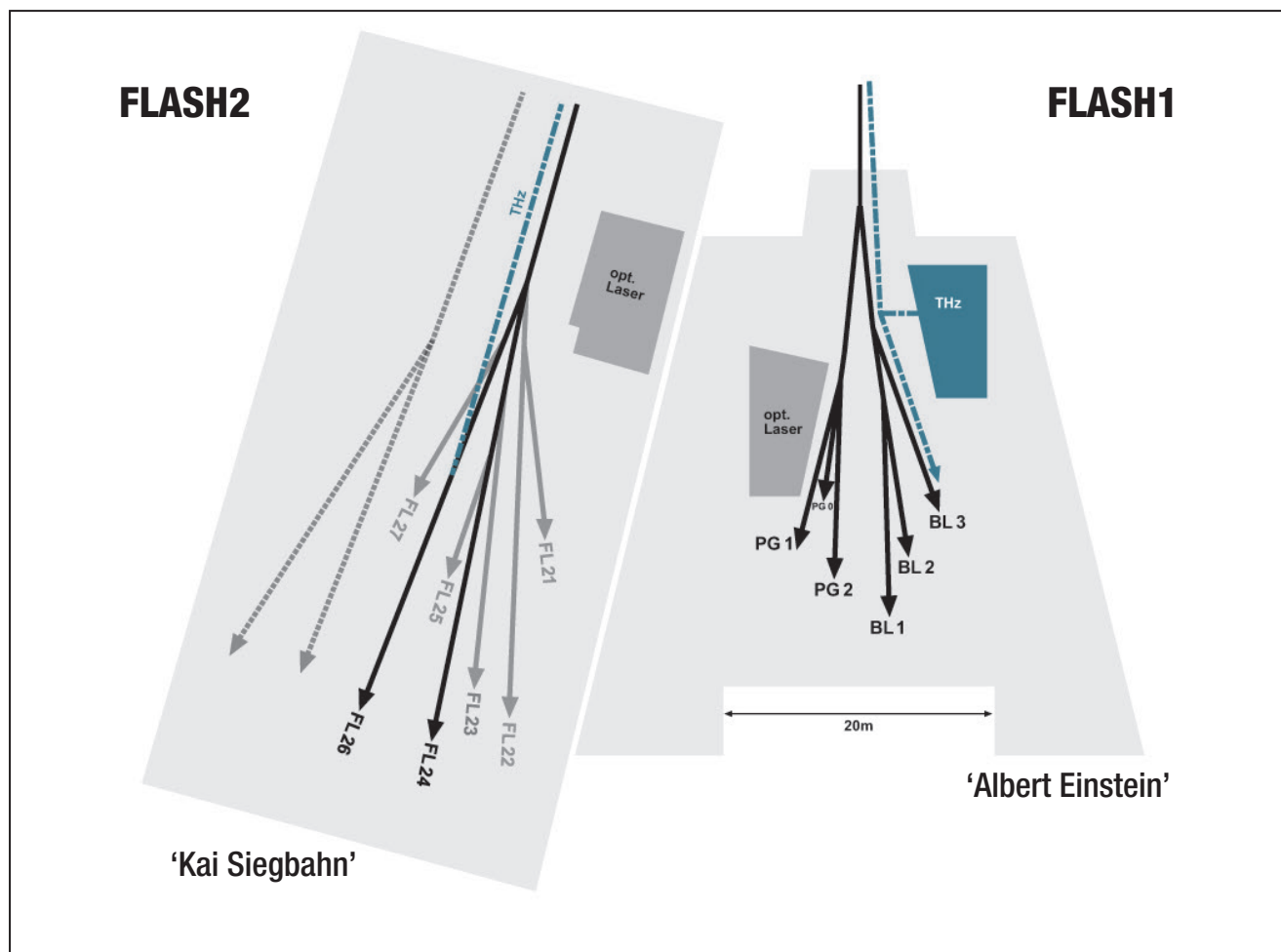


Average and peak brilliance values for FLASH, PETRA III and European XFEL. Peak brilliance values are given for the optimum bunch charge at the respective photon energies. Dots represent experimentally measured values at FLASH.

Light sources and experimental halls.

Experimental halls





Machine parameters FLASH

	FLASH1	FLASH2
Electron energy range	0.35 – 1.25 GeV	0.4 – 1.25 GeV
Normalised emittance at 1 nC (rms)	1.4 mm mrad	1.4 mm mrad
Energy spread	200 keV	500 keV
Electron bunch charge	0.1 – 1.2 nC	0.02 – 1 nC
Peak current	1 – 2.5 kA	1 – 2.5 kA
Electron bunches per second (typical/maximum)	300 / 5000	300 / 5000

FLASH lasing parameters

	FLASH1	FLASH2
Photon energy fundamental	24 – 295 eV	14 – 310 eV
Wavelength fundamental	51 – 4.2 nm	90 – 4 nm
Photon pulse duration (FWHM)	30 – 200 fs	10 – 200 fs (estimated)
Peak power	1 – 5 GW	1 – 5 GW
Single photon pulse energy (average)	1 – 500 μ J	1 – 1000 μ J
Spectral width (FWHM)	0.7 – 2 %	0.5 – 2 %
Photons per bunch	$10^{11} - 10^{14}$	$10^{11} - 10^{14}$
Peak brilliance photons/sec/mm ² /mrad ² /0.1%	$10^{28} - 10^{31}$	$10^{28} - 10^{31}$

FLASH1 beamlines

BL 1	non-monochromatic FEL photons Kirkpatrick-Baez (KB) focusing optics, FEL focal spot of $\sim 7 \mu\text{m} \times 8 \mu\text{m}$ (FWHM) split-and-delay unit for XUV pump - XUV probe experiments (under commissioning, -30 ps to 650 ps delay) optional pump - probe experiments using FLASH1 optical laser system permanent end station: multipurpose CAMP chamber with pnCCD detectors, electron and ion spectrometers and collinear incoupling optics for optical laser,	TU Berlin*
BL 2	non-monochromatic FEL photons focused to $\sim 20 \mu\text{m}$ /unfocussed beam size $\sim 5\text{-}10 \text{ mm}$ (FWHM, depending on wavelength) XUV beam splitter with variable time delay (-3 ps to 15 ps) for photon diagnostics and XUV pump - XUV probe experiments optional pump-probe experiments using FLASH1 optical laser system about 3 x 4 m footprint for user-provided end station	Univ. Münster*
BL 3	non-monochromatic FEL photons, spectral range: $>4.5 \text{ nm}$ (carbon coated optics) focused to $\sim 20 \mu\text{m}$ /unfocussed beam size $\sim 5\text{-}10 \text{ mm}$ (FWHM, depending on wavelength) optional pump - probe experiments using FLASH1 optical laser system optional pump - probe experiments using THz radiation (unique to BL3): - tunable: 10 – 230 μm ; up to 150 μJ /pulse; $\sim 10\%$ bandwidth - broadband at 200 μm , up to 10 μJ /pulse; $\sim 100\%$ bandwidth - synchronized and phase stable to X-ray pulses (down to 5 fs) - delivered to the experiment via vacuum beamline as: (i) ultra-high vacuum ($\sim 10^{-8}$ mbar), shorter delay between THz and X-ray ($\sim 4 \text{ m}$ path difference), can accommodate up to 0.3 m wide setup (ii) high vacuum ($\sim 10^{-6}$ mbar), longer delay between THz and X-ray ($\sim 7 \text{ m}$ path difference); can accommodate up to 2 m wide setup about 3 x 4 m footprint for user-provided end station	
PG1	high resolution plane grating XUV monochromator (SX 700 type, $<10^{-4}$ bandwidth, carbon coated optics): - variable combination of photon flux and resolution (from high flux to high resolution) - controlled temporal-spectral properties at moderate resolution for pump - probe experiments - high photon flux with harmonic filtering Kirkpatrick-Baez (KB) refocusing optics, FEL focal spot of 5 μm (vertically) permanent end station: in commissioning two-stage VUV-Raman spectrometer for high-resolution measurements close to Rayleigh line	Univ. Hamburg* Univ. Hamburg*
PG2	uses the same monochromator as PG1 50 μm focus XUV beam splitter with variable time delay ($\pm 6 \text{ ps}$) for time resolved studies optional pump - probe experiments using FLASH1 optical laser system about 3 x 4 m platform for user-provided end station	Univ. Hamburg*

FLASH1 optical / NIR laser system for pump - probe experiments

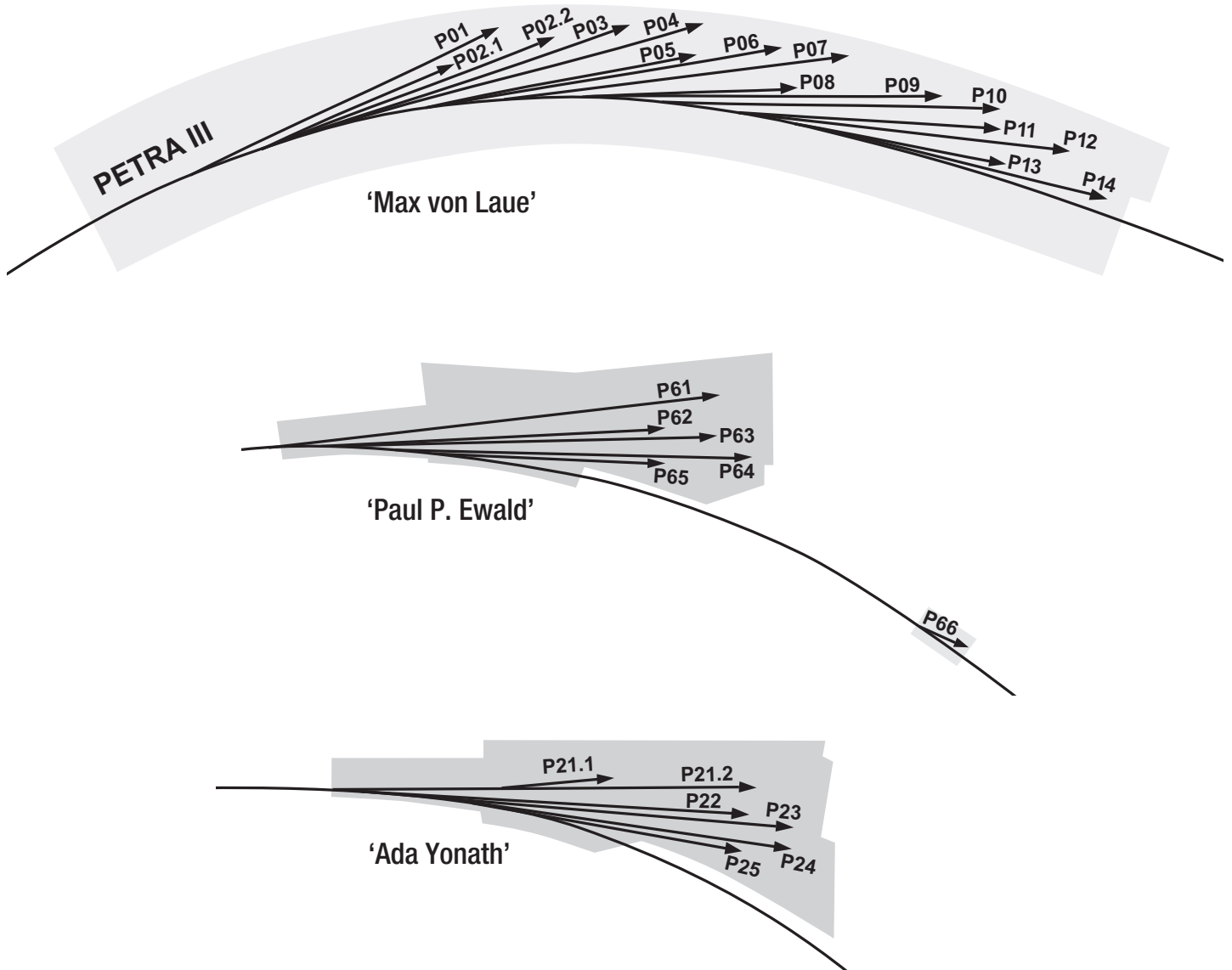
10 Hz single pulse	a) compressed pulse transported over beamline 1.5 mJ, 60 fs synchronization to FEL better than 60 fs r.m.s., corrected for drifts b) stretched pulse (chirped) transported over beamline pulse compressor must be included in experimental set-up 15 mJ, 200 ps uncompressed 10 mJ, 60 fs with external pulse compressor synchronization to FEL better than 60 fs r.m.s., corrected for drifts
Burst-mode	up to 400 pulses / burst 20 μJ per single pulse, 120 fs synchronization to FEL better than 60 fs r.m.s.

FLASH2 beamlines - under commissioning -

FL24	wavelength range: 4 – 16 nm for the fundamental with 6σ acceptance, for harmonics down to 0.8 nm, Kirkpatrick-Baez (KB) focusing optics (to be installed in early 2017) grazing incidence (1.8°) split-and-delay unit with $\pm 12 \text{ ps}$ time delay (to be installed 2017)	Univ. Münster*
FL26	wavelength range: 6 – 40 nm with 6σ , up to 80 nm with 3σ acceptance permanent end station: - split multilayer mirror & reaction microscope (REMI) for time-resolved spectroscopy - grazing incidence delay-line and refocusing optics for a second experiment in-line behind the REMI (under development)	MPI-K Heidelberg

All FLASH beamlines provide online photon diagnostics for intensity, wavelength, and beam position; fast shutter, aperture and filter sets.

*We would like to acknowledge all contributions to instrument development and operation provided within the framework of BMBF Verbundforschung.



Machine parameters PETRA III

Electron energy	6.08 GeV
Circumference of the storage ring	2304 m
Number of bunches	960, 480, 60, and 40
Bunch separation	8 ns, 16 ns, 128 ns, and 192 ns
Electron beam current	100 mA (top-up)
Horizontal electron beam emittance	1.2 nmrad
Vertical electron beam emittance	0.01 nmrad
Electron beam energy spread (rms)	0.1%
Horizontal x vertical beam size (rms) at 5 m undulator (high β section) and 10 keV photon energy	141 μm x 5.2 μm
Horizontal x vertical beam size (rms) at 5 m undulator (low β section) and 10 keV photon energy	36 μm x 5.7 μm

PETRA III experimental hall 'Max von Laue'

Beamline and instruments		Operated by
P01	High resolution dynamics 10 (20) m U32 4.5 – 40 keV	DESY
	Nuclear resonant scattering	DESY
	Non-resonant IXS	DESY / MPG
	X-ray Raman scattering	DESY / MPG
P02.1	Powder diffraction 2 m U23 60 keV	DESY
	Standard & Time resolved powder diffraction	DESY
	High resolution powder diffraction	DESY
P02.2	Extreme conditions 2 m U23 10 – 62 keV	DESY
	Laser heated diamond anvil cells	DESY
	General purpose high pressure	DESY
P03	Micro- and Nano-SAXS / WAXS 2 m U29 8 – 23 keV	DESY
	Micro-small and wide angle scattering	DESY
	Nano-beam scattering and diffraction	DESY
P04	Variable polarization soft X-rays 5 m UE65 200 – 3000 eV	DESY
	UHV diffractometer	DESY
	Photon-Ion spectrometer (PIPE)	DESY
	Ultra-high resolution photoelectron spectroscopy (ASPHERE)	DESY
	Soft X-ray absorption spectrometer	DESY
	Nano focus apparatus for spatial and time resolving spectroscopy	DESY
P05	Micro- and nano-imaging 2 m U29 8 – 50 keV	HZG
	Micro-tomography	HZG
	Nano-tomography	HZG (in commissioning)
P06	Hard X-ray Micro/Nano-Probe 2 m U32 5 – 100 keV	DESY
	Microprobe	DESY
	Nanoprobe	DESY
P07	High energy X-ray materials science 2 m U29 (planned: 4 m U19) 50 – 200 keV	HZG
	Multi-purpose triple-axis diffractometer	DESY
	Heavy load diffractometer	HZG
	Grain mapper	HZG
	High energy tomography	HZG
P08	High resolution diffraction 2 m U29 5.4 – 29.4 keV	DESY
	High resolution diffractometer	DESY
	Liquid surface diffraction	DESY
P09	Resonant scattering and diffraction/HAXPES 2 m U32 2.7 – 50 keV	DESY
	High precision psi-diffractometer	DESY
	Heavy load diffractometer	DESY
	Hard X-ray photoelectron spectroscopy	DESY
P10	Coherence 5 m U29 4 – 20 keV	DESY
	X-ray photon correlation spectroscopy (4 – 20 keV)	DESY
	Vertical rheometer (8.388 keV)	DESY
	Coherent imaging (8 – 15 keV)	DESY
	Multi-purpose diffractometer (8 – 20keV)	DESY
P11	Bio-imaging and diffraction 2 m U32 2.4 – 30 keV	DESY
	Imaging of biological samples (2.4 – 10 keV)	DESY (in commissioning)
	Macromolecular crystallography (5.5 – 30 keV)	DESY / MPG / HZI

PETRA III experimental hall 'Max von Laue' continued

Beamline and instruments		Operated by
P12	Bio SAXS 2 m U29 4 – 20 keV	EMBL / HZG
	Solution small-angle scattering	EMBL
P13	Macromolecular crystallography I 2 m U29 4 – 16 keV	EMBL
	Macromolecular crystallography	EMBL
P14	Macromolecular crystallography II 2 m U29 10 keV	EMBL
	Macromolecular crystallography	EMBL

PETRA III experimental hall 'Ada Yonath'

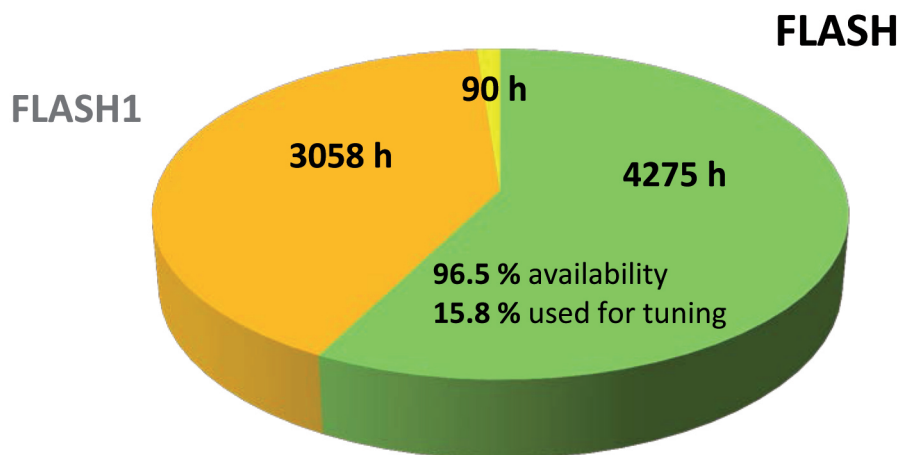
Beamline and instruments		Operated by
P21	Swedish high-energy materials science beamline 4 m IVU21 40 – 150 keV side branch: 2 m U29 50, 80, 100 keV	Swedish institution / DESY
	Diffraction and imaging Broad band diffraction	Swedish institution / DESY (commissioning 2017)
P22	X-ray spectroscopy 2 m U33 2.4 – 15 keV	DESY
	Hard X-ray photoelectron spectroscopy (relocated from P09)	DESY (commissioning 2017)
P23	Russian-German nano-diffraction beamline 2 m U32 5 – 35 keV	DESY
	Nano-XRD, in situ and complex environments	DESY (commissioning 2017)
	2 nd hutch instrument t.b.d.	not yet funded
P24	Chemical crystallography 2 m U29 8, 15 – 45 keV	DESY
	Single crystal diffraction in complex sample environments	DESY (operation planned 2017)
	Small molecule crystallography	DESY (operation planned 2017)
P25	t.b.d.	not yet funded

PETRA III experimental hall 'Paul P. Ewald'

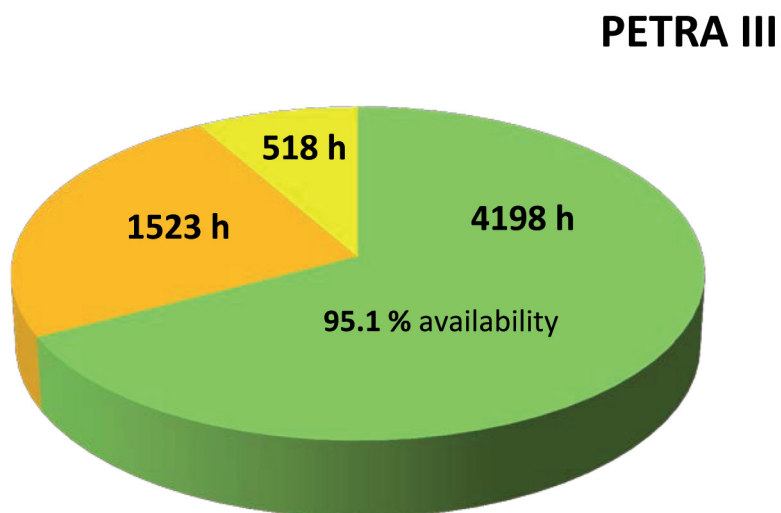
Beamline and instruments		Operated by
P61	High-energy materials science 40 m damping wiggler 50 – 200 keV / pink beam	DESY
	High-energy engineering materials science	HZG
	Extreme conditions in the large volume press	DESY (commissioning 2018)
P62	Small-angle X-ray scattering undulator energy t.b.d.	DESY
		(operation planned >2018)
P63	Instrument t.b.d.	DESY (not yet funded)
P64	Time-resolved X-ray absorption 2 m U32 4 – 44 keV	DESY
	Time-resolved <i>in situ</i> XAFS, QEXAFS, bioXAFS	DESY (operational from Spring 2017)
P65	Applied X-ray absorption Short U32 4 – 44 keV	DESY
	<i>Ex situ</i> and <i>in situ</i> XAFS of bulk samples	DESY
P66	Superlumi Bending magnet 4 – 40 eV	DESY
	Time-resolved luminescence spectroscopy (<i>separate bldg</i>)	DESY (commissioning 2018)

We would like to acknowledge all contributions to instrument development and operation provided within the framework of BMBF-Verbundforschung, the Röntgen-Ångström-Cluster (RAC), the Ioffe-Röntgen-Institute (IRI), and the Ruprecht-Haensel-Laboratory (University of Kiel).

Beamtime statistics 2016.



FLASH2 1570 h user beamtime



- User beamtime
- Machine studies/test runs/user experiment preparation
- Maintenance

Operation periods 2016

FLASH FLASH1: 01.01. - 31.12.2016
not included: shutdowns and commissioning (1361 h)
FLASH2: 01.01. - 31.12.2016

PETRA III 07.04. - 08.08.2016
29.08. - 23.12.2016
not included: user beamtime after 12.12.2016 (planned 216 h)

Committees 2016.

Photon Science Committee PSC — advises the DESY Photon Science management

Christian David (chair)

Melissa A. Denecke (vice chair)

Stefan Eisebitt

Gwyndaf Evans

Martina Havenith-Newen

Simo Huotari

Maya Kiskinova

Arwen Pearson

Thomas Pfeifer

Henning Friis Poulsen

Harald Reichert

Anthony J. Ryan, OBE

Bernd Schmitt

Andrea Somogyi

Julian Stangl

Stefan Vogt

Hermann Franz (PSC secretary)

PSI, Villigen, CH

University of Manchester, UK

MBI and Technische Universität Berlin, DE

Diamond Light Source Ltd., Didcot, UK

Ruhr-University Bochum, DE

University of Helsinki, FI

Elettra-Sincrotrone, Trieste, IT

CUI, Universität Hamburg, DE

MPI for Nuclear Physics, Heidelberg, DE

DTU Fysik, Lyngby, DK

ESRF, Grenoble, FR

University of Sheffield, UK

PSI, Villigen, CH

Synchrotron SOLEIL, Saint-Aubin, FR

Johannes Kepler Universität, Linz, AT

Argonne National Laboratory, Lemont, US

DESY, Hamburg, DE



PSC Members (second half 2016) from the left:

1st row: Melissa A. Denecke (vice chair), Maya Kiskinova,

Andrea Somogyi, Julian Stangl, Christian David (chair).

2nd row: Simo Huotari, Gwyndaf Evans, Bernd Schmitt.

3rd row: Harald Reichert, Stefan Vogt, Arwen Pearson.

4th row: Thomas Pfeifer, Stefan Eisebitt, Henning Friis Poulsen.

Here absent: Martina Havenith-Newen

Laser Advisory Committee LAC — shared between DESY and the European XFEL

Uwe Morgner (chair)	Leibniz Universität Hannover, DE
Giulio Cerullo	Politecnico di Milano, IT
Miltcho Danailov	Elettra-Sincrotrone, Trieste, IT
Mike Dunne	SLAC, Menlo Park, CA, US
Patrick Georges	CNRS, FR
Alfred Leitenstorfer	Universität Konstanz, DE
Robert W. Schoenlein	LBNL, Berkeley, US
William E. White	SLAC, Menlo Park, US
Andreas Galler (LAC secretary)	European XFEL GmbH, Hamburg, DE
Oliver D. Mücke (LAC secretary)	CFEL-DESY, Hamburg, DE

DESY Photon Science User Committee DPS-UC — represents the user community

Peter Müller-Buschbaum (Chair)	Technische Universität München, DE
Thomas Möller	Technische Universität Berlin, DE
Julian Stangl	Johannes Kepler Universität, Linz, AT
Gregor Witte	Ludwig-Maximilians-Universität München, DE
Joachim Wollschläger	Universität Osnabrück, DE

Komitee Forschung mit Synchrotronstrahlung KFS representative body of the German SR and FEL user community

Stefan Eisebitt (chair)	MBI and Technische Universität Berlin, DE
Bridget Murphy (vice chair)	Christian-Albrechts-Universität Kiel, DE
Peter Albers	AQura GmbH, DE
Ronald Frahm	Universität Wuppertal, DE
Jan-Dierk Grunwaldt	KIT Karlsruhe, DE
Christian Gutt	Universität Siegen, DE
Birgit Kanngießer	Technische Universität Berlin, DE
Lutz Kipp	Christian-Albrechts-Universität Kiel, DE
Tim Salditt	Universität Göttingen, DE
Hermann Schindelin	Universität Würzburg, DE
Andreas Schreyer	European Spallation Source ERIC, Lund, SE

Project Review Panels 2016.

PRP VUV- and Soft X-Ray

Lucia Aballe	CELLS-ALBA Barcelona, ES
Stephan Fritzsche	Helmholtz Institut Jena, DE
Michael Meyer	European XFEL GmbH, Schenefeld, DE
Luc Patthey	PSI, Villigen, CH
Jens Viefhaus (PRP Secretary)	DESY, Hamburg, DE

PRP X-Ray Spectroscopy

Iztok Arčon	University of Nova Gorica, SL
Matthias Bauer	Universität Paderborn, DE
Ralph Claessen	Julius-Maximilians-Universität Würzburg, DE
Jörg Evers	MPI für Kernphysik, Heidelberg, DE
Raphael Hermann	Oak Ridge National Laboratory, US
Greg Hughes	Dublin City University, IE
Marco Moretti	ESRF, Grenoble, FR
Maarten Nachtegaal	PSI, Villigen, CH
Håkan Rensmo	Uppsala University, SE
Svetoslav Stankov	Karlsruher Institut für Technologie KIT, DE
Max Wilke	Universität Potsdam, DE
Wolfgang Drube (PRP secretary)	DESY, Hamburg, DE

PRP High Pressure and Extreme Conditions

Denis Andrault	Blaise Pascal University, Clermont-Ferrand, FR
Leonid Dubrovinsky	Bayerisches Geoinstitut, Bayreuth, DE
Diego Gatta	University of Milan, IT
Sébastien Merkel	Lille University, FR
Ulrich Schwarz	MPI für Chem. Physik fester Stoffe, Dresden, DE
Sergio Speziale	GFZ, Potsdam, DE
Hanns-Peter Liermann (PRP Secretary)	DESY, Hamburg, DE

PRP Engineering Materials Science

Jens Gibmeier	Karlsruher Institut für Technologie KIT, DE
Patrick Huber	Technische Universität Hamburg-Harburg, DE
Jozef Keckes	Montanuniversität Leoben, AT
Svea Mayer	Montanuniversität Leoben, AT
Walter Reimers	Technische Universität Berlin, DE
Guillermo Requena	DLR and RTWH Aachen, DE
Gerold Schneider	Technische Universität Hamburg-Harburg, DE
Carsten Siemers	Technische Universität Braunschweig, DE
Axel Steuerer	University of Malta, MLT
Martin Müller (PRP secretary)	HZG, Geesthacht, DE
Dieter Lott (PRP secretary)	HZG, Geesthacht, DE
Ulrich Lienert (DESY representative)	DESY, Hamburg, DE

PRP Soft Condensed Matter – Bulk

Stephan Förster	Universität Bayreuth, DE
Christian Gutt	Universität Siegen, DE
Thomas Hellweg	Universität Bielefeld, DE
Uwe Klemradt	RWTH Aachen, DE
Michael Paulus	Technische Universität Dortmund, DE
Daniel Söderberg	KTH, Stockholm, SE
Joachim Wagner	Universität Rostock, DE
Rainer Gehrke (PRP secretary)	DESY, Hamburg, DE

PRP Soft Condensed Matter – Surfaces and Interfaces

Gerald Brezesinski	MPI Kolloid- u. Grenzflächenforsch., Potsdam, DE
Moshe Deutsch	Bar-Ilan University, Ramat Gan, IL
Tiberio A. Ezquerra	CSIC, Madrid, ES
Thomas Gutsmann	Leibniz-Zentrum Borstel, DE
Hyunjung Kim	Sogang University, Seoul, KR
Markus Mezger	Universität Mainz, DE
Frank Schreiber	Universität Tübingen, DE
Tobias Unruh	Technische Universität München, Garching, DE
Andreas Zumbühl	University of Fribourg, CH

PRP Imaging (full-field, scanning, coherent)

Oliver Bunk	PSI, Villigen, CH
Peter Cloetens	ESRF, Grenoble, FR
Julia Herzen	Technische Universität München, DE
Koen Janssens	University of Antwerp, BE
Hendrik Küpper	University of South Bohemia, České Budějovice, CZ
Stephan Peth	Universität Kassel, DE
Sebastian Schoeder	Synchrotron SOLEIL, Saint-Aubin, FR
Stefan Vogt	Argonne National Laboratory, Lemont, US
Frank Witte	Charité - Universitätsmedizin Berlin, DE
Gerald Falkenberg (PRP secretary)	DESY, Hamburg, DE
Felix Beckmann (HZG representative)	HZG, Geesthacht, DE

PRP Methods and Instrumentation

Yngve Cerenius	MAX IV Laboratory, Lund University, SE
Rolf Follath	PSI, Villigen, CH
Tim Salditt	Universität Göttingen, DE
Anatoly Snigirev	I. Kant Baltic Federal University, Kaliningrad, RU
Horst Schulte-Schrepping (PRP secretary)	DESY, Hamburg, DE

PRP Hard Condensed Matter – Surface and Coherent Scattering

Johan Gustafson	Lund University, SE
Václav Holý	Charles University, Prague, CZ
Alexander Komarek	MPI CPfS, Dresden, DE
Dieter Lott	HZG, Geesthacht, DE
Bogdan Sepiol	Universität Wien, AT
Julian Stangl	Johannes Kepler Universität Linz, AT
Peter Wochner	MPI für Festkörperforschung, Stuttgart, DE
Michael Sprung (PRP Secretary)	DESY, Hamburg, DE

PRP Hard Condensed Matter – Bulk (diffraction and scattering)

Johan Chang	University of Zurich, CH
Robert Dinnebiele	MPI für Festkörperforschung, Stuttgart, DE
Lars Ehm	Stony Brook University, Stony Brook, NY, US
Jochen Geck	IFW Dresden, DE
Hermann Gies	Ruhr-Universität Bochum, DE
Markus Huecker	Weizmann Institute of Science, Rehovot, IL
Helen Walker	ISIS, Didcot, GB
Xiaodong Zou	Stockholm University, SE
Jörg Stempfer (PRP secretary)	DESY, Hamburg, DE

PRP Soft X-Ray – FEL Experiments (FLASH)

Katharina Al-Shamery	Universität Oldenburg, DE
Michael Bonitz	Universität Kiel, DE
Christoph Bostedt	Argonne North Western University, US
Chris Jacobsen	APS, Argonne, US
Steven Johnson	ETH Zürich, CH
Claudio Masciovecchio	Elettra Sincrotrone Trieste, IT
Ronald Redmer	Universität Rostock, DE
Robert W. Schoenlein	SLAC Nat. Accelerator Laboratory, US
Kiyoshi Ueda	Tohoku University, Sendai, JP
Marc Vrakking	MBI, Berlin, DE
Martin Weinelt	FU Berlin, DE
Josef Feldhaus (PRP secretary)	DESY, Hamburg, DE
Elke Plönjes-Palm (PRP secretary)	DESY, Hamburg, DE
Rolf Treusch (PRP secretary)	DESY, Hamburg, DE

PEC: EMBL Life Science beamlines P12-P14 / PRP Bio-crystallography at P11

Pau Bernadó	CBS/CNRS, Montpellier, FR
Kristina Djinovic-Carugo	Universität Wien, AT
Gwyndaf Evans	Diamond Light Source, Didcot, GB
Robert Fischetti	Argonne National Laboratory, US
Mariusz Jaskolski	Adam Mickiewicz University of Poznan, PL
Javier Pérez	Synchrotron SOLEIL, Saint-Aubin, FR
Savvas Savvides	Ghent University, BE
Zehra Sayers	Sabancı University, Istanbul, TR
Joel Sussman	Weizmann Institute of Sciences, Rehovot, IL
Maria Vanoni	University of Milan, IT
Bente Vestergaard	University of Copenhagen, DK
Gregor Witte	Ludwig-Maximilians-Universität München, DE
Christian Schroer (DESY observer)	DESY, Hamburg, DE

Photographs and Graphics:

Wes Agresta, ANL
Gesine Born, Berlin
Fred Dott, European XFEL
DESY
EMBL
European XFEL
Sven Festersen, CAU
hammeskrause architekten
HZG
Gisela Köhler, Hamburg

Hanns-Peter Liermann, DESY
Dirk Nölle, DESY
Marta Mayer, DESY
MPG
Frank Poppe, European XFEL
Eberhard Reimann, DESY
Royal Society
Reimo Schaaf, Hamburg
Kai Schlage, DESY
Edgar Weckert, DESY

Figures of the Research Highlights were reproduced by permission from authors or journals.

Acknowledgement

We would like to thank all the authors and all those who have contributed to the realisation of this Annual Report. ●

Imprint

Publishing and Contact:

Deutsches Elektronen-Synchrotron DESY
A Research Centre of the Helmholtz Association

Hamburg location:

Notkestr. 85, 22607 Hamburg, Germany
Tel.: +49 40 8998-0, Fax: +49 40 8998-3282
desyinfo@desy.de

Zeuthen location:

Platanenallee 6, 15738 Zeuthen, Germany
Tel.: +49 33762 7-70, Fax: +49 33762 7-7413
desyinfo.zeuthen@desy.de

Photon Science at DESY

Tel.: +49 40 8998-2304, Fax: +49 40 8998-4475
photon-science@desy.de
photon-science.desy.de

www.desy.de

ISBN 978-3-945931-09-7

Online version:

photon-science.desy.de/annual_report

Realisation:

Tim Laarmann, Wiebke Laasch, Ralf Röhlsberger, Daniela Unger

Editing:

Sadia Bari, Martin Beye, Lars Bocklage, Rainer Gehrke,
Daniel Horke, Wiebke Laasch, Tim Laarmann,
Wolfgang Morgenroth, Nele Müller, Elke Plönjes,
Ralf Röhlsberger, Hans-Christian Wille,
Daniela Unger, Martin von Zimmermann

Layout: Sabine-Kuhls Dawideit, Büro für Grafik und Design,
Halstenbek

Printing: EHS Druck GmbH, Schenefeld

Copy deadline: December 2016

Reproduction including extracts is permitted subject
to crediting the source.



Deutsches Elektronen-Synchrotron A Research Centre of the Helmholtz Association

The Helmholtz Association is a community of 18 scientific-technical and biological-medical research centres. These centres have been commissioned with pursuing long-term research goals on behalf of the state and society. The Association strives to gain insights and knowledge so that it can help to preserve and improve the foundations of human life. It does this by

identifying and working on the grand challenges faced by society, science and industry. Helmholtz Centres perform top-class research in strategic programmes in six core fields: Energy, Earth and Environment, Health, Key Technologies, Structure of Matter, Aeronautics, Space and Transport.

www.helmholtz.de